INTERNATIONAL DOCTORAL SCHOOL OF THE USC

Xaniar
Esmailzadeh Gameshgoli

PhD Thesis

Nanoheater-induced plasmonic hyperthermia: Role of light irradiation conditions, and their effects on protein biocorona formation and biological cell responses.

Santiago de Compostela, 2025

Doctoral Programme in Materials Science

ESCOLA DE DOUTORAMENTO
INTERNACIONAL DA USC

DOCTORAL THESIS

NANOHEATER-INDUCED PLASMONIC HYPERTHERMIA: ROLE OF LIGHT IRRADIATION CONDITIONS, AND THEIR EFFECTS ON PROTEIN BIOCORONA FORMATION AND BIOLOGICAL CELL RESPONSES

Author

Xaniar Esmaeilzadeh Gameshgoli

Supervisors: Dr. Alberto Pardo Montero

Dr. Adriana Cambon Freire

Tutor: Dr.Pablo Taboada Antelo

PHD PROGRAM IN MATERIAL SCIENCE

SANTIAGO DE COMPOSTELA

I declare no conflicts of interest in conducting this research, and I am committed to maintaining objectivity, integrity, and transparency throughout the process.

I dedicate this thesis to my dear parents, **Sadegh** and **Soda**, whose enduring support and guidance have shaped my path. To **Saeedeh**, my loving wife, whose unwavering support and deep understanding were vital in overcoming the many challenges along the way. And to my sweet son, **Daniel**, whose laughter and light brought balance and inspiration to my life.

Xaniar Esmaeilzadeh Gameshgoli

In Memoria

Acknowledgements

“Sometimes we believe we move forward alone, but every path that leaves a mark is also shaped by gentle shadows, unseen hands, and hearts that sustain us without asking for anything in return.”

I would like to express my deepest gratitude to all those who have accompanied me throughout this journey.

First and foremost, my boundless gratitude goes to my wife, Dr. Saeedeh Khazaei. Her love, understanding, patience, and strength have been the cornerstone that has supported me throughout these years of work and dedication. She has stood by my side through every stage of this process—celebrating the successes, encouraging me during the challenges, and offering unwavering support. Her selflessness and constant belief in me have been a never-ending source of inspiration. This thesis would not have been possible without her presence, her dedication, and her wholehearted commitment, both personally and professionally.

To my family—especially my father, Sadegh Esmaeilzadeh, and my mother, Soda Mohammadi—for their constant support and sacrifices. To my siblings, for always being there. And to our son, Daniel, whose very existence has brought light, joy, and meaning to every step of this journey.

I am sincerely thankful to Dr. Pablo Taboada for admitting me into his laboratory and guiding this thesis. His support and trust have played a crucial role in shaping both my research and academic growth. I would like to express my deepest gratitude to Dr. Adriana Cambón Freire for her constant support and invaluable help throughout my PhD journey. Her readiness to assist and her kind guidance have been a great source of strength.

I extend my heartfelt thanks to Dr. Alberto Pardo. Working with him has been a true privilege—not only as an outstanding academic advisor but also as a dedicated and generous mentor. His scientific rigor, thoughtful guidance, and unwavering encouragement were essential to the development of this thesis. His trust in me provided a solid foundation throughout this work, and I am deeply grateful for the opportunity to learn from him.

I also extend my gratitude to all the members of the Colloid and Polymer Physics group: Dr. Gerardo Prieto, Dr. Silvia Barbosa, Dr. Antonio Topete, Dr. Lilia Arellano, Dr. Victoria Marcos,

Dr. Vicente Domínguez, Dr. Brenda Velasco, Dr. Juan Sabín, Alba Costa, Óscar Abelenda, Dr. Mariangel Luna, Alejandro Varela Dopico, and Alejandro Ogando. A special mention goes to Dr. Osvaldo Beltrán, who, beyond being my lab partner, I consider one of my best friends.

I am deeply grateful to the institutions that supported this research: the University of Santiago de Compostela and the University of Tehran, both of which have been my academic homes throughout this process.

I gratefully acknowledge the financial support provided by the Agencia Estatal de Investigación (AEI) through projects PID2019-109517RB-I00 and PID2022-142682OB-I00, as well as the Xunta de Galicia through action ED431C 2022/18.

Finally, to all the people who, in one way or another, made this thesis possible, I thank you. Your constant support, valuable insights, and encouraging words were essential to the completion of this work.

Resumo

A nanociencia e a nanotecnoloxía son disciplinas interdisciplinares centradas no estudo e manipulación da materia a escala nanométrica. A primeira enfócase típicamente no estudo das propiedades e comportamentos de estruturas entre 1 e 100 nm, aínda que pode abarcar rangos algo máis amplos dependendo do contexto específico. Así, nalgúns casos pódese falar de nanomateriais que teñen dimensións de menos de 1 nm ou ata 500 nm, por exemplo. Pola súa parte, a nanotecnoloxía emprega este coñecemento para desenvolver materiais, dispositivos e aplicacións prácticas. Como campo que combina ciencia básica e enxeñaría aplicada, a nanotecnoloxía explora as propiedades únicas dos nanomateriais, tales como condutividade, reactividade ou resposta óptica, para resolver retos tecnolóxicos e industriais. Nas últimas décadas, observouse un crecemento notable nestes ámbitos, motivado polos avances en técnicas de síntese e caracterización. Ademais, progresouse significativamente na comprensión das propiedades eléctricas, ópticas e magnéticas de nanoestruturas compostas por semiconductores, metais e/ou polímeros, o que abre novas vías de innovación en diversos sectores científicos e industriais.

Nesta escala nanométrica, os materiais amosan propiedades diferentes das observadas nas súas versións macroscópicas, debido principalmente a efectos cuánticos e superficiais. O confinamento cuántico pode modificar os comportamentos electrónicos, magnéticos e catalíticos, permitindo que metais como o ouro ou o paladio exhiban propiedades magnéticas e actividade catalítica melloradas cando son preparados en forma de nanoclústeres. Pola súa banda, os efectos superficiais derivan da elevada proporción de átomos na superficie, alterando este feito diversas propiedades fisicoquímicas dos materiais.

As técnicas avanzadas de caracterización, tales como poden ser a microscopía electrónica nas súas diferentes formas, a cristalografía ou os métodos espectroscópicos, resultan fundamentais para determinar as propiedades dos nanomateriais. Deste xeito, a nanociencia e a nanotecnoloxía seguen ofrecendo amplas oportunidades para innovar no deseño, síntese, caracterización e aplicación práctica de nanosistemas.

A nanomedicina é un campo emerxente dentro da área da nanotecnoloxía que aínda se atopa nunha fase relativamente inicial de desenvolvemento. Mediante a integración de enfoques multidisciplinares da medicina e da enxeñaría, busca innovar no diagnóstico, tratamento e

prevención de enfermidades a nivel molecular, empregando nanomateriais tales como nanopartículas (NPs) orgánicas e inorgánicas, dendrímeros, estruturas de carbono, ou plataformas de sílice, entre outros.

Entre os diversos nanomateriais, as NPs metálicas, e dentro destas moi particularmente as compostas por ouro, recibiron unha atención considerable debido ás súas excepcionais propiedades, entre as que se atopan unha elevada reactividade superficial, propiedades ópticas modulables e unha alta biocompatibilidade. Dentro deste grupo, as nanoestruturas con morfoloxía anisótropa, como as nanobarras (AuNRs) e as nanoestrelas (AuNSs), amosan capacidades funcionais superiores ás NPs de ouro con formas esféricas. En particular, as AuNRs presentan dous modos distintos de resonancia de plasmón superficial localizado (LSPR), sendo o modo lonxitudinal axustable á rexión do infravermello próximo (NIR). Isto converte ás AuNRs en ferramentas con potencial aplicación no eido das terapias fototérmicas (PTT), permitindo a ablación selectiva de células tumorais, como nas neoplasias mamarias. Pola súa banda, as AuNSs, grazas á súa morfoloxía con múltiples puntas de extremos afiados, son capaces de producir campos electromagnéticos de moi alta intensidade na súa superficie, sendo así útiles como axentes para espectroscopía Raman mellorada pola superficie (SERS), biosensores, ou ferramentas para terapia fotodinámica. Tanto as AuNRs como as AuNSs son habitualmente funcionalizadas con polietilenglicol (PEG) e ligandos específicos de recoñecemento, mellorando así a súa biocompatibilidade, o tempo de circulación sistémica, e a captación celular específica. Deste xeito, ambas tipoloxías de NPs poden ser usadas non só como axentes terapéuticos, senón tamén como ferramentas de diagnóstico, dando lugar así a nanoplataformas multifuncionais con potencial uso no eido da teranóstica. Con todo, aínda existen multitude de retos relacionados coa síntese a gran escala das NPs ou o seu comportamento unha vez incorporadas en sistemas biolóxicos complexos, entre outros moitos factores.

Esta tese ten como obxectivo investigar as propiedades fototérmicas das AuNRs e as AuNSs como potencias ferramentas para o tratamento mediante PTT do cancro de mama, avaliando dous métodos de irradiación láser na xanela do NIR diferentes: irradiación de onda continua (CW) e pulsada. Tamén se pretende avaliar como o grupo funcional terminal das cadeas poliméricas de PEG usadas para o recubrimento superficial das NPs modula a súa interacción coas células, incluíndo a súa internalización celular, citotoxicidade, e mecanismos de morte

celular inducidos polo efecto fototérmico. Ademais, o impacto do quecemento plasmónico sobre a composición da coroa proteica formada arredor das NPs, clave para definir a súa identidade biolóxica e potencial terapéutico, tamén se analizará.

Este estudo preséntase en catro capítulos ben diferenciados. O **Capítulo I** ofrece unha introdución exhaustiva ao eido dos nanomateriais, comezando por unha visión histórica da nanotecnoloxía e nanociencia e posteriormente detallando os diferentes tipos de nanosistemas existentes. Aínda que elaborado dende un punto de vista xeral, este primeiro capítulo enfócase nas NPs inorgánicas, con especial atención ás AuNRs e AuNSs, profundando nos métodos de síntese máis habitualmente empregados para a súa preparación e nas súas propiedades fisicoquímicas. Analízanse tamén as interaccións das NPs con sistemas biolóxicos, incluíndo a formación da coroa proteica, citotoxicidade, biodegradación e impacto das propiedades fisicoquímicas na súa identidade biolóxica. O capítulo conclúe cunha revisión das principais aplicacións biomédicas das NPs de ouro con morfoloxía anisótropa en campos como a bioimaxe, liberación controlada de fármacos, terapia fototérmica, ou terapia fotodinámica.

O **Capítulo II** describe os materiais utilizados para a síntese de AuNRs e AuNSs, así como para o estudo das súas propiedades e do seu comportamento biolóxico en cultivos celulares *in vitro*. Ademais, este capítulo describe técnicas experimentais empregadas para a caracterización físicoquímica e biolóxica das NPs, incluíndo dispersión dinámica de luz (DLS), medicións do potencial zeta, microscopía electrónica de transmisión (TEM) e confocal, espectroscopía UV-Vis e de fluorescencia, ou citometría de fluxo.

O **Capítulo III** presenta un estudo exhaustivo sobre a síntese, caracterización e propiedades fototérmicas das NPs de ouro anisótropas ao ser irradiadas tanto con láser CW como con láser pulsado. O capítulo tamén avalía a estabilidade fototérmica das NPs despois da exposición a cada tipo de láser. Ademais, a estabilidade coloidal das AuNRs e AuNSs, funcionalizados con diversas cadeas PEG terminais, é analizada en medios tampón, salinos e ricos en proteínas. Tras a caracterización das NPs, analízanse as respostas celulares das células MDA-MB-231 e Balb/c 3T3 cando son incubadas na presenza dos nanosistemas deseñados.

Ambos tipos de NPs foron sintetizadas mediante métodos establecidos de crecemento mediado por sementes. No caso das AuNRs, sintetizáronse pequenas sementes (*ca*. 3 nm de diámetro) mediante a redución de $HAuCl_4$ con $NaBH_4$ en presenza de bromuro de

cetiltrimetilamónio (CTAB). Estas foron engadidas a unha disolución de crecemento con CTAB e $AgNO_3$, promovendo un crecemento anisótropo. As AuNRs resultantes foron funcionalizadas con poli(4-estirensulfonato de sodio) (PSS) para estudos fototérmicos e recubertas con PEG de cara á súa avaliación en cultivos celulares *in vitro*. A análise TEM mostrou NPs monodispersas cunha forma de barra ben definida e con lonxitude e anchura medias de 39.1 ± 4.7 e 9.3 ± 1.3 nm, respectivamente. A espectroscopía UV-Vis revelou bandas LSPR características a 510 nm (transversal) e 795 nm (lonxitudinal), cun desprazamento azul na banda lonxitudinal tras o recubrimento con PSS.

De xeito análogo, as AuNSs foron sintetizadas empregando sementes de *ca*. 15 nm de diámetro. A polivinilpirrolidona (PVP) actuou como axente estabilizante, mentres que a dimetilformamida funcionou como disolvente e axente redutor. As AuNSs presentaron un diámetro de 123 ± 11 nm nas imaxes de microscopía obtidas, así como un pico LSPR intenso arredor de 835 nm no seu espectro UV-Vis. Deste xeito, ambas tipoloxías de NPs amosaron bandas LSPR dentro da ventá biolóxica, posibilitando unha conversión fototérmica eficiente para terapias oncolóxicas de tecidos profundos.

Tras a caracterización fisicoquímica das AuNRs e AuNSs, avaliouse a súa resposta fototérmica mediante irradiación con láser CW a 808 nm, rexistrando o aumento de temperatura ata acadar o equilibrio térmico. O efecto fototérmico débese á LSPR das NPs metálicas, onde a oscilación colectiva dos electróns superficiais permite converter a luz en calor. Neste estudo, realizáronse dispersións de AuNRs-PSS e AuNSs-PVP a distintas concentracións, que foron sometidas a diferentes densidades de potencia de láser. Observouse unha correlación directa entre a concentración de NPs e o incremento de temperatura acadado, así como entre este último e a densidade de potencia de láser empregada. A baixas concentracións e/ou densidades de potencia reducidas, tanto as AuNRs como as AuNSs xeraron incrementos térmicos moderados (< 10 °C), considerados axeitados para aplicacións como a hipertermia localizada ou a potenciación da eficacia da quimioterapia mediante sensibilización térmica. En cambio, concentracións máis elevadas de NPs e/ou densidades de potencia superiores deron lugar a aumentos de temperatura superiores aos 10 °C, superando o limiar da ablación térmica necesario para a destrución dirixida de células malignas.

As nanoestruturas de ouro sintetizadas amosaron unha excelente estabilidade fronte a diferentes condicións de irradiación con láser CW, tal e como demostraron as medicións

realizadas mediante espectroscopía UV-Vis, DLS e TEM, mantendo intactas tanto a súa estrutura coma a súa funcionalidade. Esta fotoestabilidade destaca o potencial das AuNRs e AuNSs deseñadas como candidatas prometedoras para aplicacións biomédicas baseadas en ciclos repetidos de quecemento e arrefriamento inducidos por luz. A súa elevada resistencia á fotodegradación avala o seu uso en áreas avanzadas como a terapia fototérmica, a detección óptica ou outras innovacións da nanotecnoloxía. Ademais, como se comentou anteriormente, as dispersións de AuNRs-PSS e AuNSs-PVP tamén se irradiaron cun láser pulsado cunha duración de pulso na orde dos 10^{-15} s (fs), co obxectivo de comparar ambos réximes de iluminación. A irradiación co láser fs provocou cambios mínimos de temperatura macroscópica, de entre 2 e 6 °C, en contraste co quecemento máis acusado observado co láser CW. Esta diferenza atribuíuse á curta duración dos pulsos do láser fs, inferior ao tempo de difusión térmica do medio circundante, o que garante confinamento térmico e evita efectos acumulativos. Pola contra, o láser CW fornece enerxía de maneira continua, provocando acumulación de calor e o observado aumento máis pronunciado da temperatura.

A estabilidade fototérmica das NPs despois de irradiacións con láser de fs tamén foi avaliada, observándose mediante espectroscopía UV-Vis un desprazamento cara ao azul no LSPR de ambos tipos de NPs, sendo este máis pronunciado nas AuNRs-PSS que nas AuNSs-PVP. Esta modificación espectral foi confirmada mediante observacións por TEM, que amosaron un remodelado morfolóxico nas AuNRs, mais non nas AuNSs. Ademais, as medicións por DLS indicaron unha pequena diminución no tamaño hidrodinámico dos nanosistemas en ambos casos.

A continuación, as nanoestruturas avaliadas foron funcionalizadas con moléculas de PEG que presentaban diferentes grupos terminais, co obxectivo de ver a influencia destes en reducir as interaccións inespecíficas cos compoñentes do soro, limitar a adsorción de proteínas, evadir a eliminación rápida polo sistema fagocítico mononuclear e mellorar a biocompatibilidade e a estabilidade coloidal. Empregáronse tres tipos de PEGs con funcionalidades terminais distintas: metoxi (mPEG), carboxilo (PEG-CM) e amino (PEG-NH_2). A modificación exitosa da superficie tanto das AuNRs como das AuNSs con estas variantes de PEG foi confirmada mediante múltiples técnicas de caracterización fisicoquímica. A funcionalización levada a cabo induciu un lixeiro desprazamento cara ao vermello nos picos LSPR nos espectros UV-Vis de ambos tipos de nanoestruturas, sen afectar significativamente á anchura espectral. Ademais,

o recubrimento con PEG tamén deu lugar a un incremento notable do diámetro hidrodinámico tanto das AuNRs como das AuNSs, atribuíble á presenza das cadeas poliméricas estendidas na superficie das NPs cando estas se dispersan en medio acuoso. Cómpre salientar que o grupo terminal do PEG desempeñou un papel clave na modulación da carga superficial das nanoestruturas, observándose potenciais zeta negativos, positivos e case neutros en auga nas NPs modificadas con PEG-CM, PEG-NH_2 e mPEG, respectivamente.

A estabilidade coloidal e a preservación das propiedades plasmónicas das NPs de ouro anisótropas sintetizadas avaliáronse tras a súa dispersión en diversos medios, incluíndo auga, tampón PBS (pH 7.4), tampón de acetato (pH 5.5), solucións de NaCl, e fluídos biolóxicos ricos en proteínas como DMEM e FBS ao 10-100%. Tanto as AuNRs como as AuNSs recubertas con mPEG, PEG-CM ou PEG-NH_2 mostraron boa estabilidade en múltiples medios. As AuNRs mantiveron un tamaño hidrodinámico estable en auga, PBS e tampón de acetato, malia lixeiros desprazamentos do LSPR, pero experimentaron alteracións significativas en tamaño e propiedades plasmónicas en condicións de alta salinidade. Pola súa banda, as AuNSs presentaron desprazamentos menores do LSPR segundo o medio, con aumentos de tamaño relevantes só en altas concentracións salinas. En xeral, o tamaño das NPs mantívose por baixo dos 200 nm tras seis días de incubación, o que favorece a súa aplicación biomédica.

Este Capítulo III inclúe tamén unha avaliación *in vitro* detallada das NPs recubertas coas tres tipoloxías de PEGs anteriormente descritas, tras a incubación con células de cancro de mama MDA-MB-231 e fibroblastos de rato Balb/c 3T3. As análises biolóxicas abrangueron o estudo da viabilidade celular, tanto na presenza como na ausencia de irradiación cos dous tipos de láser, estudos de internalización celular, e a análise dos mecanismos de morte celular inducidos polas AuNRs e as AuNSs. A microscopía confocal confirmou a internalización das AuNSs en ambas liñas celulares. Pola contra, as AuNRs non foron detectadas mediante esta técnica, probablemente debido ao seu menor tamaño e sinal de dispersión máis débil. Con todo, as imaxes de TEM adquiridas permitiron observar a internalización das AuNRs e AuNSs, mentres que a análise por ICP-MS estableceu unha maior captación celular de AuNSs fronte ás AuNRs, especialmente nas MDA-MB-231. No referente ao efecto do recubrimento, as NPs funcionalizadas con PEG-NH_2 presentaron os maiores niveis de internalización celular, segundo evidenciaron tanto a caracterización das mostras mediante ICP-MS como as imaxes de TEM adquiridas.

O ensaio de viabilidade celular revelou que, na ausencia de irradiación láser, tanto as AuNRs como as AuNSs presentaron unha elevada biocompatibilidade, manténdose a viabilidade celular por riba do 90 % nas dúas liñas celulares estudadas. Sen embargo, tras a exposición a irradiación láser CW, observouse unha diminución dependente da concentración na viabilidade celular, sendo as NPs con morfoloxía de estrela máis citotóxicas, probablemente debido a unha maior internalización celular e unha resposta fototérmica máis intensa que as AuNRs. No tocante ao efecto do tipo de PEG empregado para a funcionalización, destacou a maior citotoxicidade das NPs recubertas con PEG-NH_2, atribuíble ás máis intensas interaccións electrostáticas destas coas membranas celulares que favorecen un maior grao de internalización celular. Por outra banda, as células MDA-MB-231 mostraron maior sensibilidade aos efectos fototérmicos cas Balb/c 3T3. Curiosamente, as células MDA-MB-231 irradiadas co láser pulsado na presenza de AuNRs e AuNSs amosaron maior viabilidade que aquelas expostas ao láser CW coa mesma enerxía. Isto explícase polas diferenzas nos mecanismos de entrega enerxética: os láseres CW producen calor acumulativo, causando danos térmicos severos, mentres que os pulsos láser de moi curta duración promoven confinamento térmico, limitando o quecemento e reducindo o dano celular.

As medidas de citometría de fluxo revelaron mecanismos diferenciados de morte celular entre as dúas liñas celulares tras o tratamento con nanoestrutura de ouro e irradiación con láser de CW. Así, as células Balb/c 3T3 experimentaron maioritariamente apoptose, mentres que as células MDA-MB-231 mostraron predominantemente necrose. A irradiación das células MDA-MB-231 incubadas con AuNRs e AuNSs mediante pulsos láser de fs incrementou a taxa de apoptose. As diferenzas nos mecanismos de morte celular entre ambos láseres atribúense probablemente aos efectos de confinamento térmico anteriormente discutidos.

Finalmente, no **Capítulo IV** avaliouse a composición e comportamento da coroa proteica formada sobre as AuNRs e AuNSs tras a súa incubación en albumina sérica bovina (BSA) e fibrinóxeno (Fib). Esta análise, centrada no efecto do quecemento plasmónico, realizouse en tres condicións: sen irradiación, irradiación simultánea (durante a formación da coroa) e irradiación secuencial (despois da formación). Deste xeito, no estudo das AuNRs, observouse unha maior afinidade coas proteínas no caso das NPs recubertas con PEG-NH_2 en comparación coas recubertos con PEG-CM, debido probablemente ás máis favorables interaccións electrostáticas existentes, especialmente baixo condicións de quecemento plasmónico. A

adsorción da BSA na superficie das AuNRs provocou alteracións moderadas na estrutura proteica, caracterizadas principalmente por unha diminución do contido de estruturas α-hélice, efectos que se intensificaron coa irradiación simultánea fronte á secuencial. Pola súa parte, no caso de AuNRs incubadas en Fib e posteriormente sometidas a irradiación láser, observouse unha maior sensibilidade térmica, tendencia á degradación proteica e unha maior agregación das NPs. Estes efectos atribuíronse a un despregamento extensivo da proteína, cunha perda case completa das estruturas α-hélice e un aumento correspondente de follas β antiparalelas. A análise de atenuación da fluorescencia proporcionou información adicional sobre estas interaccións: os AuNRs recubertos con PEG-NH_2 provocaron unha maior atenuación da fluorescencia da BSA, indicando unha maior afinidade e proximidade espacial. Os estudos baseados nas ecuacións de Stern-Volmer e Hill revelaron que a unión da BSA aos AuNRs-PEG-NH_2 presentaba cooperatividade positiva, mentres que nos recubertos con PEG-CM esta foi negativa.

Pola súa banda, as AuNSs recubertas con PEG-CM incubadas en BSA non amosaron cambios significativos nin na posición da LSPR nin no tamaño hidrodinámico en ausencia de irradiación. Pola contra, a incubación con Fib resultou nunha diminución da intensidade da absorbancia UV-Vis e nun incremento do diámetro hidrodinámico en todas as modalidades de formación da coroa proteica. O quecemento plasmónico inducido mediante irradiación láser provocou alteracións nas conformacións das proteínas adsorbidas, particularmente en Fib, caracterizadas por unha perda substancial de contido α-helicoidal e un incremento notable na proporción de estruturas β-lámina antiparalelas.

Estes resultados poñen de manifesto a relevancia de factores como a morfoloxía das NPs, a súa química superficial ou a exposición a aumentos de temperatura na modulación do proceso de formación da coroa proteica e na integridade estrutural das proteínas adsorbidas. En conxunto, o estudo subliña a complexidade das interaccións entre os sistemas nanoestruturados deseñados e entidades biolóxicas e salienta a importancia de comprender os mecanismos moleculares subxacentes para o deseño racional de nanomateriais con aplicacións biomédicas seguras e eficaces.

A tese doutoral finaliza cun breve capítulo no que se presentan as principais conclusións extraídas do traballo experimental realizado, en particular da síntese, caracterización e avaliación biolóxica dos diferentes nanosistemas plasmónicos deseñados e analizados ao

longo do estudo. As conclusións abranguen os aspectos máis relevantes do comportamento das diferentes tipoloxías de AuNRs e AuNSs sintetizadas nos contextos biolóxicos avaliados, proporcionando unha visión detallada do seu potencial e limitacións, así como das perspectivas futuras para a súa aplicación en biomedicina, en particular no tratamento fototérmico do cancro de mama.

Table of Contents

List of Figures

List of Tables

1. Introduction

1.1 Nanoscience and Nanomaterials

1.1.1 What is Nanoscale and Nanotechnology?

The prefix “nano” is derived from a Greek word that denotes “dwarf” or “extremely tiny”. In science and technology context, “nano” has been adopted to represent a scale of one billionth of a unit. For example, in terms of dimensions, a nanometer is one billionth of a meter (1 nm = 10^{-9} m), being roughly the size scale of many viral structures (*ca*. 10-150 nm in diameter) or the radius of DNA double helices (*ca*. 1 nm) (Figure 1.1 A). From an atomic perspective, a nanometer can also be visualized as the length of a chain comprising five silicon atoms or ten hydrogen atoms.

Although there are different conventions, in the most accepted standard, materials must display at least one of their spatial dimensions below 100 nm to be considered nanomaterials, nanostructures or nanoparticles (NPs).[1] Interestingly, when the dimensions of materials are decreased to the nanoscale range, they often exhibit physicochemical properties and/or biological behavior that differ significantly from their bulk counterparts.

In this context, it is important to differentiate between nanoscience and nanotechnology. Nanoscience focuses on the study of structures and molecules within the nanometer scale, spanning from 1 to 100 nm. On the other hand, nanotechnology aims to promote the practical application of nanoscience by developing nanodevices for diverse purposes. In other words, nanotechnology is the branch of science and engineering devoted to the design, production and application of structures and devices with dimensions in the nanoscale. The use of nanomaterials has been documented for centuries, with early examples based on the capability of metallic NPs to display different colors depending on the angle of the incident light, which were exploited for ornamental purposes. Examples of these decorative applications of nanomaterials can be observed on the stained glasses of gothic churches throughout Europe or on the Lycurgus Cup from Roman culture. The latter, now housed in the British Museum, is considered one of the earliest well-known examples of dichroic glass, a term that refers to a glass whose color varies depending on the illumination conditions (Figure 1.1 B). More specifically, the cup appears green when illuminated from the front (reflected light) and shifts to a red-purple hue when illuminated from behind (transmitted light).[2] In

1990, scientists investigated the dichroism phenomenon of the cup through electron microscopy techniques, thus being established that the apparent color change of the object was attributable to the presence of silver (70%) and gold NPs (30%), ranging in size from 50 to 100 nm, in the internal structure of the cup. The reddish-purple color results from light absorption by gold NPs, whereas the green tint is associated with the scattering of light by silver NPs larger than 40 nm.[2]

In 1959, Richard Feynman delivered his famous lecture *There is Plenty of Room at the Bottom* at the California Institute of Technology (Caltech) during the annual meeting of the *American Physical Society*. Although the lecture did not have a huge impact at the time, it is now recognized as one of the earliest conceptual endorsements of nanotechnology, especially since the research in this field began to grow dramatically in the 1990s. In his talk, Feynmann discussed scientific insights related to both the micro- and nanoscale, offering a visionary outlook on the topic. For instance, he hypothesized the possibility of eventually storing the contents of 24 volumes of the British encyclopedia into a device smaller than the head of a pin, and he imagined a future in which extremely small machines could be constructed, ultimately reaching the molecular level. However, although Feynmann is considered the father of nanotechnology for this pioneering and visionary speech, [2] it is worth mentioning that the term “nanotechnology” was first coined by Norio Taniguchi in 1974. He defined it as the field devoted to the processing, separation, consolidation, and deformation of materials at the atomic or molecular scale.[2]

1.1.2 Materials at the Nanoscale: Physics and Classification

When particles are synthesized with dimensions ranging from *ca*. 1 to 100 nm, their properties can differ significantly from those observed in larger-scale materials with the same composition. Two primary factors responsible for these differences between nanomaterials and their bulk counterparts are quantum and surface effects, which will be briefly discussed here. [5] Depending on the specific type of material, this range can be extended, with some nanomaterials displaying dimensions below 1 nm or even up to several hundred nm.

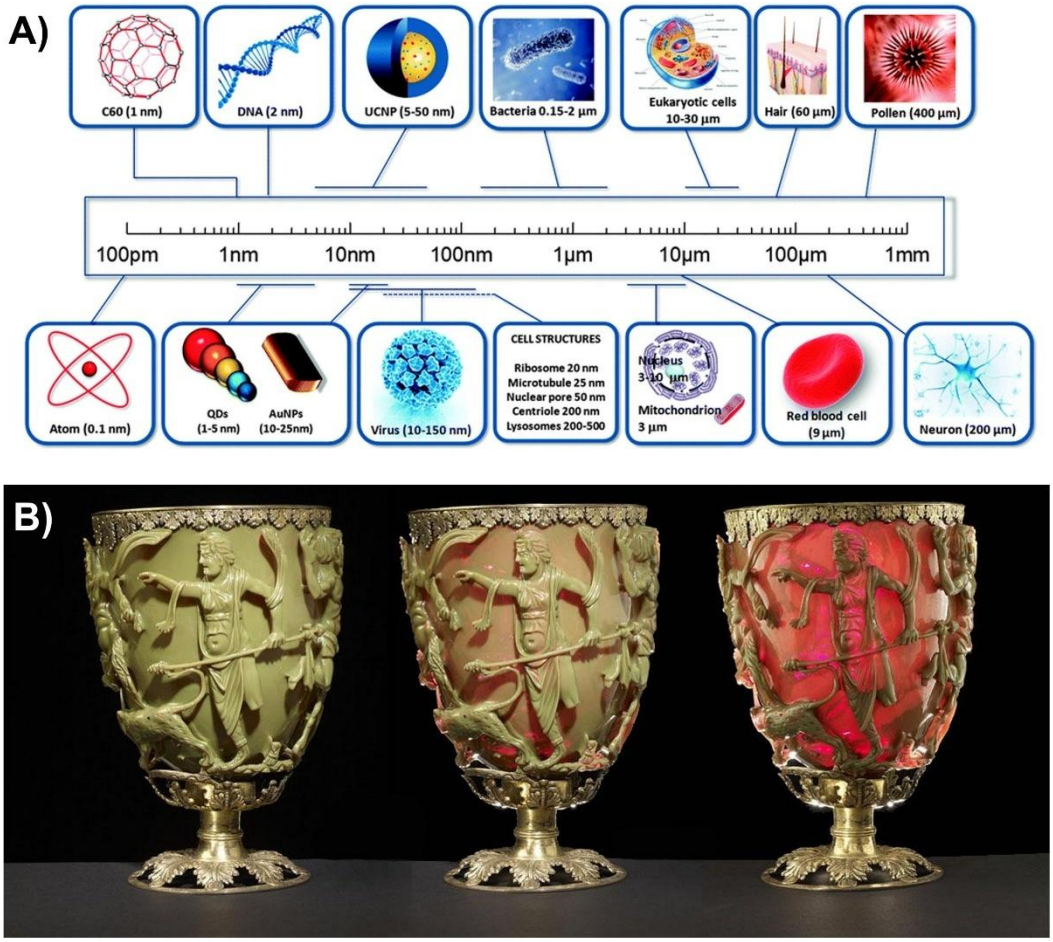

Figure 1.1. A) Representative examples of systems with dimensions ranging from the nanometric to the micrometric scale.[3] B) The Lycurgus Cup appears green under reflected light and red purple under transmitted light.[4]

Regarding quantum effects, when the dimensions of a material are reduced to the nanoscale, approaching the asymptotic exciton Bohr radius, the influence of atomic quantum confinement becomes increasingly significant and plays a key role in its final properties.

For instance, quantum effects are responsible for the magnetic behavior exhibited by certain elements at the nanoscale, such as gold or palladium, which are non-magnetic in their bulk form.[6,7] Moreover, quantum confinement can also lead to notable changes in the capability of materials to accept or donate electrical charges, which is directly correlated with the enhanced catalytic properties of various nanomaterials, such as platinum nanoclusters.[8]

On the other hand, the unique surface effects of nanomaterials compared to their bulk counterparts arise from their high surface-to-volume ratio. Because of their reduced dimensions, the percentage of atoms located at the surface of the nanomaterials increases and they have fewer neighboring atoms. For instance, spherical NPs with 30 nm in diameter have *ca*. 10% of their atoms located on the external surface, while this value increased up to *ca*. 50% in the case of nanostructures with 3 nm in diameter.[9,10] This results in lower binding energies per atom in nanomaterials, being this the cause of, for instance, the much lower melting temperature of gold NPs compared with bulk gold. Moreover, the increased surface area per unit volume of NPs also enhances their reactivity, promotes efficient interactions, and facilitates processes such as catalysis and chemical reactions. Additionally, it also enables higher degrees of surface modification, making nanomaterials highly versatile for a wide range of applications ranging from electronics, energy storage, or environmental remediation to biomedicine.[11]

Materials with dimensions at the nanoscale can be classified according to various criteria, including their composition, dimensionality, porosity, or origin, among other factors (Figure 1.2). Thus, on the basis of their composition, nanomaterials can be primarily divided into organic, inorganic, carbonaceous, and composite (hybrid) NPs. Organic nanostructures are derived from organic compounds and include polymeric or lipid-based NPs, which are often used in drug delivery and biosensing applications. Inorganic nanomaterials, such as metal oxides and noble metal NPs, are known for their unique optical and catalytic properties, making them ideal for use in electronic and environmental applications. On the other hand, composite or hybrid nanomaterials combine organic and inorganic components to enhance functionality, resulting in nanosystems with tailored properties for diverse applications in biomedicine, energy, or engineering.[12] Interestingly, carbon-based nanostructures, such graphene NPs or carbon nanotubes, exhibit exceptional mechanical and electrical properties, and they are typically not considered as purely organic or inorganic nanomaterials. Since they are allotropes composed entirely of carbon atoms, their unique structure and properties set them apart from both traditional organic-inorganic classification.

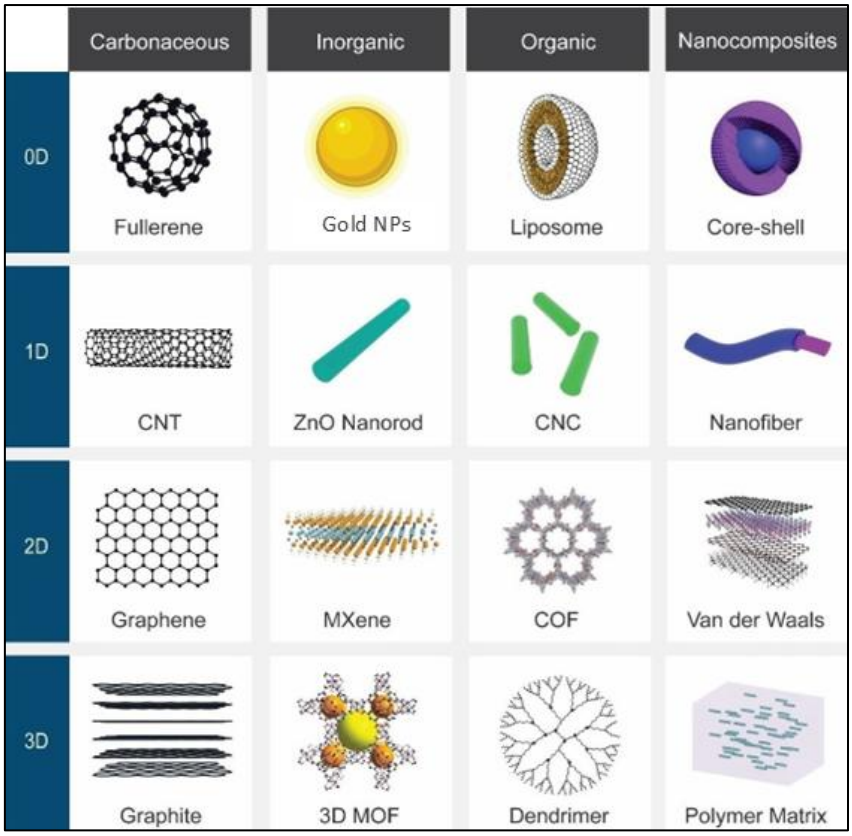

Figure 1.2. Classification of nanomaterials based on their dimensionality and chemical composition, including representative examples. CNT: carbon nanotubes; CNC: cellulose nanocrystals; COF: covalent-organic frameworks; MOF: metal-organic framework.[13] Under creative commons license CC-BY-NC license.

Nanomaterials can also be categorized based on the number of dimensions that fall within the nanoscale range. This classification includes zero-dimensional (0D) NPs, which are spherical or quasi-spherical nanostructures with all dimensions at the nanoscale, such as gold NPs. One-dimensional (1D) NPs, such as nanofibers and nanotubes, feature one dimension significantly larger than the nanoscale, while two-dimensional (2D) materials, such as graphene and nanosheets, possess nanoscale thickness while extending laterally. Finally, 3D nanomaterials consist of structures with interconnected macro- and mesopores, which prevent aggregation and restacking, offering the highest accessible surface area among nanomaterials.[14] Moreover, the NPs can also be divided into porous and non-porous, with the first ones displaying structures with internal voids. These pores can vary in size and allow for the storage or transport of different cargoes, which makes porous NPs useful in various

applications such as drug delivery, catalysis, or sensor development. Depending on the size of the pores, NPs can be divided into microporous (pore size less than 2 nm), mesoporous (pore size between 2 and 50 nm), and macroporous (pore size greater than 50 nm). Lastly, the origin-based classification of NPs distinguishes between natural, which are derived from biological processes or natural sources, and synthetic nanomaterials, which are artificially engineered for targeted applications in fields such as medicine, energy, and electronics.[15,16]

1.1.3 Overview of Nanomaterials Applications

Due to their unique physicochemical properties, nanomaterials have found applications across a wide range of fields, including biomedicine, energy, electronics, environmental protection, and industrial manufacturing, among others (Figure 1.3).

For example, in the biomedical area, nanomaterials have shown transformative potential in both diagnostic and therapeutic technologies. Different types of nanostructured materials, including liposomes, dendrimers, or polymeric nanocarriers, enable targeted drug delivery to specific tissues or cells, thereby minimizing side effects and improving the efficacy and specificity of the treatments. Nanomaterials also play a pivotal role in modern bioimaging and diagnostic procedures, in which quantum dots, gold NPs, or magnetic NPs have been proposed to improve resolution and sensitivity in techniques such as magnetic resonance imaging (MRI) and fluorescence imaging. Additionally, nanomaterials have also found application in emerging biomedical fields such as tissue engineering and regenerative medicine, where the incorporation of different types of NPs has been proposed to modulate the mechanical properties, architecture, or stimuli-responsiveness of the designed scaffolds.[17]

In electronics, nanomaterials are essential for the development of smaller, faster, and more efficient devices. Materials such as carbon nanotubes, graphene, or quantum dots are used for the design of high-performance transistors, sensors, and memory components, providing them with exceptional electrical conductivity and mechanical strength. Interestingly, the use of these same nanomaterials also enables innovations in the fabrication of flexible and wearable electronics. Moreover, the use of nanostructured electrodes has been also critical in the last advancements to maximize the performance of batteries and supercapacitors, increasing both their energy capacity and charging speed. In optoelectronics, NPs are used in

light-emitting diodes (LEDs), photovoltaic cells, and displays to boost efficiency and color quality.[17,18]

Furthermore, the energy sector has also greatly benefited from the most recent advances in the field of nanotechnology. For example, quantum dots and perovskite NPs are being used for the development of next-generation solar cells, offering improved light absorption and conversion efficiency. On the other hand, nanostructured catalytic materials are used in fuel cells and hydrogen production, accelerating chemical reactions and boosting overall energy output. Additionally, thermoelectric nanomaterials are being explored to convert waste heat into usable energy, with the final aim of providing sustainable solutions for energy recovery.[19]

In terms of their application for environmental purposes, the use of nanomaterials has demonstrated a potential high impact to improve current remediation and sensing technologies. For instance, systems such as nanoscale membranes and titanium dioxide NPs are effective for filtering contaminants, pathogens, and heavy metals in wastewater treatment processes. For air purification, photocatalytic nanomaterials can degrade pollutants, while nanosensors provide high-sensitivity detection of gases, toxins, and hazardous substances. Furthermore, nanomaterials are being explored for soil remediation and waste management, providing innovative solutions to clean up environmental pollutants.[20]

In the industrial sector, nanomaterials have shown their capability to significantly enhance the performance and functionality of a wide range of products. For instance, they have been incorporated into coatings and paints to impart properties such as scratch resistance, self-cleaning, and UV protection. In textiles, nanostructured materials are used to produce fabrics with antibacterial, water-repellent, and flame-retardant properties. Moreover, the use of nanostructures such nano-silica and nano-clay has been proposed in construction, where these can be exploited to improve the durability, strength, and thermal insulation of building materials. Furthermore, nanocomposites are increasingly used in the aerospace and automotive sectors to produce lightweight, high-strength components, leading to improved fuel efficiency and reduced emissions.[21]

In conclusion, nanomaterials have become a cornerstone of modern science and technology, with applications spanning medicine, energy, electronics, environment, or industry. Their unique properties are driving innovations that address critical global challenges, from

healthcare and clean energy to sustainability and advanced manufacturing. As research in nanotechnology continues to evolve, the potential of nanomaterials to shape a smarter, more efficient, and sustainable future remains immense.

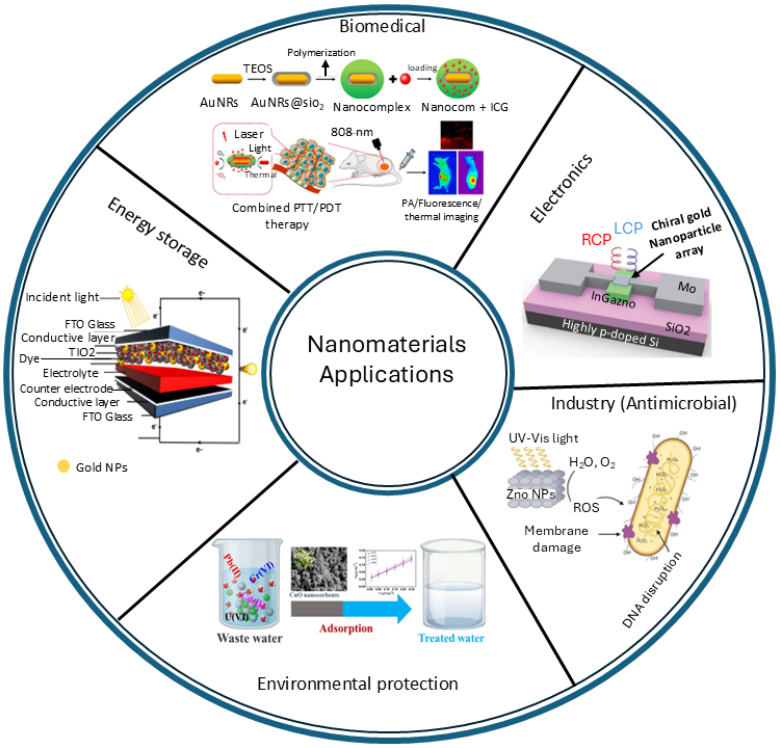

Figure 1.3. Schematic illustration of the applications of nanomaterials across various fields, including biomedicine, energy storage,[22] electronics, environmental protection,[23] and industrial processes. Biomedical, electronic and industrial application images are reproduced from ref. 24–26. Under creative commons CC-BY-NC 4.0 license.

1.2 Brief Introduction to Inorganic NPs

Given that the ultimate goal of this work is the synthesis, characterization, and evaluation of the potential biomedical application of a specific type of inorganic nanosystems, namely gold-based nanostructures, this section provides a brief overview of the main characteristics of inorganic NPs. The following sections will delve into the particular interest of anisotropic gold NPs, as well as the various synthesis and functionalization methods, characterization techniques, physicochemical properties, and the most relevant biomedical applications of both inorganic NPs in general and gold NPs in particular.

As previously mentioned, nanostructured inorganic materials are among the most extensively evaluated systems in the field of nanotechnology owing to their unique properties in terms of catalytic activity, stimuli responsiveness, optical behavior, or mechanical strength, among others. These NPs are composed of non-carbon-based materials, often derived from metals, metal oxides, ceramics, or other inorganic compounds (Figure 1.4). Inorganic nanostructures can be categorized into several subgroups depending on their composition and properties, with the most relevant being metal and metal oxide NPs, quantum dots, ceramic NPs, and other inorganic compounds such as carbides and nitrides.[12]

Among these, inorganic NPs based on metallic elements have been undoubtedly the most extensively designed and studied over the past decades due to their broad application potential. In the most typical approach, the synthesized nanostructures consist of a single metallic element, with gold, silver, or platinum, being the most frequently studied; however, the design of bi-metallic and more complex poly-metallic NPs *via* doping strategies or the growth of core-shell structures has also been extensively explored.[15] Gold and silver NPs, in particular, exhibit distinctive chemical, optical, and electrical properties when compared to their bulk counterparts. One of their standout features is the so-called localized surface plasmon resonance (LSPR), an optical phenomenon responsible for their unique light absorption and scattering properties, which will be discussed in detail in subsequent sections. Additionally, metallic NPs often display excellent electrical conductivity and thermal stability. Their physicochemical properties and optical responses are strongly influenced by a wide variety of design parameters, including their composition, size, morphology, or structure, thus allowing the tailored synthesis of nanostructures with the desired behavior for specific applications.[27]

On the other hand, metal oxide-based nanostructures are formed through the combination of metal elements with oxygen, resulting in materials with distinctive optical, electrical, and/or magnetic responses. Common examples include various forms of iron oxide (*e.g.* magnetite, maghemite, hematite), titanium dioxide, zinc oxide, or cerium oxide, among others. These NPs are known for their high stability and biocompatibility, supporting their use in different biomedical applications. By controlling their composition, metal oxide-based NPs can be provided with remarkable photocatalytic activity (*e.g.* titanium oxide), semiconductor behavior (*e.g.* tin oxide), or magnetic responsiveness (*e.g.* magnetite). This last type of

magnetically-responsive NPs are particularly intriguing nanostructures because of their ability to be controlled by remote magnetic stimuli.[28] Although magnetic NPs based on non-oxidized metals have been designed, in most cases they are composed of iron oxide in their different forms. Their behavior under static or alternating magnetic fields can be finely tuned through precise control over their physical and chemical characteristics. Thus, the magnetic moment induced in these nanostructures can be exploited to control their arrangement/displacement within complex biomaterials or living organisms, the generation of heat, and/or their magnetic relaxation profile. In this way, magnetic NPs have been evaluated as contrast agents for MRI, stimuli-responsive nanocarriers for drug delivery, or magnetothermal tools for hyperthermia treatments.[29,30]

Another category of inorganic nanostructures is formed by ceramic NPs, which are based on inorganic, non-metallic materials such as silicates, alumina, zirconia, and carbides. These materials are recognized for their high mechanical strength, thermal stability, and resistance to wear. Their robustness makes them suitable for use under extreme conditions, including high temperatures or corrosive environments. In this way, the use of ceramic NPs has been proposed for demanding industrial activities, but also for more sophisticated applications in the biomedical field such as enhancing the mineralization of hard tissue engineered scaffolds.[30]

Finally, the last typology of nanostructures that we want to highlight in this short discussion about the different inorganic NPs is quantum dots. These are a distinct class of semiconductor NPs, typically composed of materials such as cadmium selenide, cadmium sulfide, or lead sulfide. These nanostructures are characterized by their extremely low dimensions, with diameters ranging from 1 to 10 nm, which strongly influences their electronic and optical properties. Quantum dots exhibit size-tunable fluorescence, meaning they can emit different colors of light depending on their dimensions. Their high photostability, quantum efficiency, and resistance to photobleaching, make them highly suitable for diverse applications, including solar energy conversion, light-emitting diodes, or their biomedical use as contrast agents in bioimaging techniques.[31]

In the following sections, we will provide a detailed discussion on various aspects related to the synthesis, characterization and application of inorganic NPs. However, as mentioned above, this thesis will be particularly focused on the study of gold NPs with anisotropic

morphologies, such as gold nanorods (AuNRs) and gold nanostars (AuNSs). Therefore, special emphasis will be placed on the properties and behavior of these specific nanostructures throughout the general discussion.

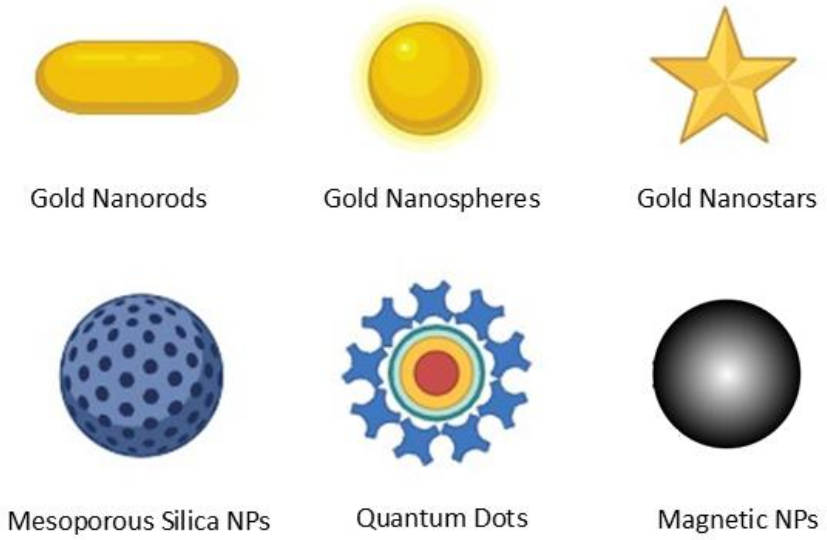

Figure 1.4. Schematic representation of gold NPs with different morphologies, along with representative examples of other commonly synthesized inorganic nanostructures (not in scale).

1.3 The Particular Interest of Anisotropic Gold-Based Nanostructures

Nanostructured materials based on noble metals have attracted considerable attention owing to their unique optoelectronic properties, which are highly dependent on the composition, size, and morphology of the NPs. Among the different noble metals used for the synthesis of nanoparticulated systems, including silver, platinum, or palladium, gold stands out as a particularly attractive option for biomedical applications because of its excellent biocompatibility and low chemical reactivity.[32–35]

These exceptional optoelectronic properties of metallic NPs are primarily governed by the LSPR phenomenon, which arises from the collective oscillation of conduction electrons on metallic surfaces and their interaction with incident electromagnetic fields at specific wavelengths.[36] This interaction leads to the scattering of some photons in multiple directions, while others are absorbed and converted into lattice vibrations, resulting in light absorption. Consequently, LSPR produces an extinction (absorption + scattering) peak, with its resonant

frequency influenced by various factors such as the physicochemical properties of plasmonic NPs, the interparticle spacing, and the refractive index of the surrounding medium. Unlike metals such as lead, mercury, or cadmium, which exhibit plasmonic frequencies in the UV range, noble metals like gold show plasmonic frequencies displaced to longer wavelengths, thus allowing the tunning of the LSPR peaks of gold NPs into the visible and NIR regions of the spectrum.

These highlighted properties of gold NPs, including high chemical stability and biocompatibility along with structural-dependent LSPR, make this kind of nanostructure particularly promising for various applications in the biomedical field.[37] Moreover, although this property is more pronounced in other typologies of NPs such as those based on silver, gold NPs also exhibit notable antibacterial properties against both animal and foodborne pathogens, broadening their applicability in areas such as cancer photothermal therapy, bioimaging, biosensing, or pharmacokinetics.[38]

A particularly critical feature of gold NPs in these applications is the controllable tunability of their scattering-to-adsorption ratio.[39] Although this ratio can be adjusted through variations on the size of the gold nanostructures or the incorporation of low amounts of other elements, such as silver, the most efficient strategy is the design of gold NPs with complex anisotropic morphologies, such as AuNRs and AuNSs.

1.3.1 Gold Nanorods

Gold nanostructured materials with rod-like morphologies are characterized by displaying two different LSPR bands on their extinction spectra upon interaction with an incident electromagnetic field.[40] The first, known as the transverse plasmon resonance peak, arises from electrons oscillation across the width of the AuNRs and is consistently centered at a wavelength of *ca*. 520 nm. The second one is the longitudinal plasmon band, which results from electrons oscillation along the longer axis of AuNRs and can be modulated by adjusting the aspect ratio (*i.e.* the length-to-width ratio) of the rod-like NPs. As the aspect ratio of AuNRs increases, the longitudinal plasmon band undergoes a red-shift, meaning it moves toward longer wavelengths. This shift is responsible for the observable color changes in colloidal dispersions of AuNRs: those with low aspect ratio appear red, while those with higher aspect ratios appear blue (Figure 1.5 A-C).[41]

This tunable optical behavior can be theoretically explained on the basis of Gans' theory (equation 1), which allows the quantitative calculation of the extinction coefficient (γ):

$$\gamma = \frac{2\pi NV\varepsilon_m^{3/2}}{3\lambda}\sum\frac{\left(\frac{1}{P_j^2}\right)\varepsilon_2}{(\varepsilon_1+\frac{1-P_j}{P_J}\varepsilon_m)^2+\varepsilon_2^2} \quad (1)$$

where N denotes number of particles, V the volume occupied by a single particle, λ the wavelength of the incident light, P_j stand for depolarization factors for three axes of the nanorods, $\mathcal{E}$ the complex dielectric constant of the metal, which consists of both real and imaginary components; and $\mathcal{E}_m$ the dielectric constant of surrounding medium.

By building upon Gans' theory, Link *et al*. established a direct linear relationship between the longitudinal LSPR absorption peak and the aspect ratio of AuNRs dispersed in aqueous solutions (equation 2).[42]

$$\lambda_{max} = 95 \cdot R + 420 \quad (2)$$

where λ_{max} represents the wavelength of the longitudinal LSPR, and R the aspect ratio of the AuNRs.[41] In this way, when the aspect ratio of the AuNRs increases, the position of the longitudinal LSPR absorption peak shifts towards longer wavelengths.

However, it is important to note that Gans' theory is specifically formulated for short, rod-like metallic NPs, and it only accounts for dipole oscillations. In the case of AuNRs with broader ranges of aspect ratios, the discrete dipole approximation (DDA) is more frequently used and appropriate. DDA is a robust approach that integrates electrodynamics with numerical techniques to calculate the optical properties of nanostructured materials with diverse morphologies and compositions.[43] In this model, solving Maxwell's equations becomes more straightforward, and the extinction cross-section coefficient (σ_{ext}) calculated following equation 3:

$$\sigma_{\text{ext}} = \frac{24\pi^2 R^3 \epsilon_d^{3/2}}{\lambda}\frac{\epsilon_2}{(\epsilon_1+2\epsilon_d)^2+\epsilon_2^2} \quad (3)$$

where λ is the wavelength of incident light, R the average aspect ratio of the nanorods, ϵ_d represent the real dielectric function of the medium, and $\in=\in_1+ i \in_2$, the complex dielectric function of the metal.[44]

In this method, the NPs are modeled as a 3D array of individual point dipoles, each of which interacts with both the external electric field of incident light and fields generated by neighboring dipoles. Starting from an initial estimation of the dipole moment, DDA enables accurate predictions of how the size and morphology of metallic NPs influence the LSPR absorption, scattering, and overall extinction. For example, El-Sayed *et al*. used DDA simulations to investigate AuNRs with varying aspect ratios, establishing that the scattering component of LSPR increases with aspect ratio of NPs (Figure 1.5 D).[45] Their findings were consistent with Gans' theory, observing a linear relationship between aspect ratio of AuNRs and the wavelength of their longitudinal LSPR band (Figure 1.5 E, top). Moreover, they observed that while scattering efficiency increases, quantum yield decreases due to enhanced adsorption at higher aspect ratios, attributed to an increase in the imaginary component of metal's dielectric constant (Figure 1.5 E, bottom).[41]

1.3.2 Gold Nanostars

Gold NPs with spiky star-shaped morphologies represent a particularly interesting class of plasmonic nanostructures with unique optical properties, primarily stemming from their anisotropic structure, which features a central core surrounded by sharp, protruding tips. Under light irradiation, these sharp tips of AuNSs function as "hot spots" in which electromagnetic fields are significantly enhanced. This property underpins the high potential of AuNSs in applications such as surface-enhanced Raman scattering (SERS) spectroscopy, allowing for substantial amplification of weak Raman signals from nearby molecules.[46]

The optical response of AuNSs is strongly influenced by their specific morphological features, thus allowing their tunability for a broad range of applications such as sensing, imaging, and photothermal therapy. Owing to their star-like morphology, AuNSs support multiple plasmonic modes: the core typically resonates at shorter wavelengths (visible region), while the tips produce resonances at longer wavelengths (NIR region). This resonance in the NIR region (650-900 nm), known as the biological transparency window, is essential for exploiting the potential biomedical application of AuNSs due to the reduced absorption of light with these wavelengths by biological tissues.[47]

Key structural factors that govern the plasmonic behavior of AuNSs include core size, tips length and sharpness, number of tips, or the ratio between tip length and core diameter.

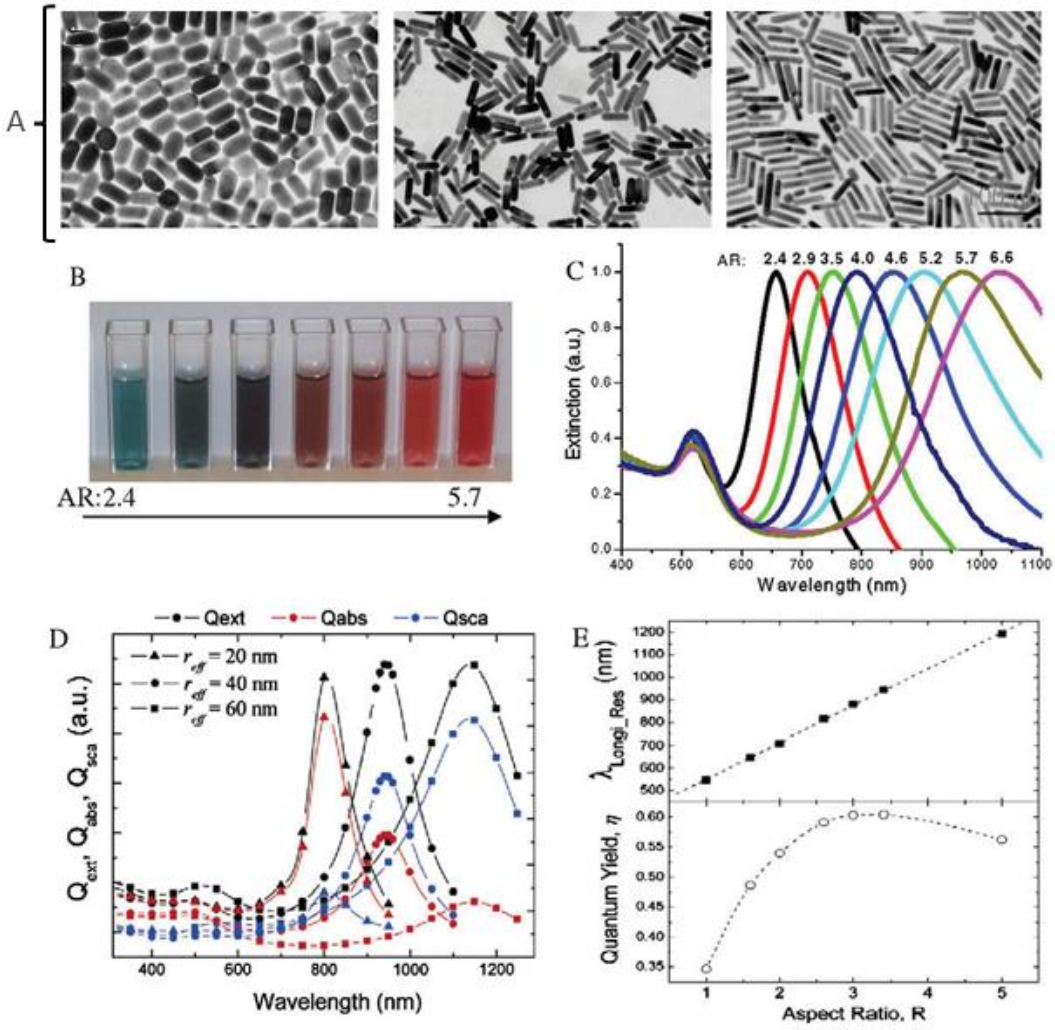

Figure 1.5. A) TEM images of AuNRs with different aspect ratios. B) Color change and C) LSPR red shifting of AuNRs dispersions with different aspect ratios between 2.4 and 6.6.[41] D) DDA simulation of AuNRs with different sizes. E) Correlation between the aspect ratio of AuNRs and their LSPR wavelength (top) and scattering yield (down).[41] Under creative commons CC BY-NC-ND 3.0 license.

In general, smaller AuNSs typically exhibit plasmonic peaks in the visible range, whereas larger AuNSs with longer tips shift their resonances into the NIR region. On the other hand, sharper tips enhance local electric fields intensity, contributing to red-shifted and intensified plasmonic peaks. Interestingly, although a larger number of tips can also enhance the overall electromagnetic field, they may also induce plasmonic coupling effects that broaden and

dampen LSPR peaks. Another remarkable effect is the displacement of LSPR peaks towards longer wavelengths observed in AuNSs with high tip-to-core ratio (Figure 1.6 A-C).[48]

In addition to morphology, the local environment and surface chemistry also play a vital role in the plasmonic response of AuNSs. Their sensitivity to the dielectric constant of the surrounding medium enables LSPR shifts in response to changes in refractive index, making them ideal for sensing applications.[49] Moreover, the surface functionalization of star-shaped gold NPs with different coatings can further modulate their optical responses while enhancing colloidal stability in different environments.

A precise control over the physicochemical properties of AuNSs and, consequently, over their plasmonic response, can be achieved through careful control of synthetic procedures. In this regard, seed-mediated growth methods enable a tailored manipulation of the dimensions and morphological features of the obtained AuNSs by adjusting concentrations of gold precursors, reducing agents, and surfactants. In addition, modifying reduction kinetics can influence tip growth, resulting in either sharp or blunt tips, which directly affect the optical properties of the nanostructures.[47] Furthermore, post-synthesis treatments, such as chemical etching or thermal annealing, provide additional control over tip geometry and plasmonic behavior.

Due to this wide range of design strategies available to control their optical response, AuNSs are highly adaptable for their application in various biomedical areas. Tunable LSPR peaks within the NIR range have led to the evaluation of AuNSs as potential nanotools for targeted photothermal therapies and *in vivo* imaging. Moreover, as previously stated, their intense local field enhancement has been exploited for ultra-sensitive molecule detection *via* SERS, as well as in other biosensing platforms for detecting environmental contaminants, pathogens, and biomolecules. Beyond biomedical use, AuNSs have also shown promise in plasmon-driven catalysis, including CO_2 reduction and water splitting, owing to their capacity for localized light energy concentration.[50–52]

In a study conducted by de Puig *et al.*, experimental extinction coefficients were compared with the obtained simulation values to evaluate the impact of various design parameters of AuNSs.[53] Simulations were carried out using the DDA method, with the extinction coefficients (C_{ext}) calculated following equation 4:

$$\varepsilon = \frac{C_{ext} N_A}{\ln 10} = N_A \left(\frac{10^{-17}}{\ln 10}\right)\left(\frac{9\pi}{16}\right)^{\frac{1}{3}} V^{\frac{1}{3}} Q_{ext} \quad (4)$$

where Q_{ext} and V represent the maximum extinction cross-section and the volume of AuNSs, being N_A de Avogadro´s number.

Interestingly, both experimental and simulated results demonstrated a linear correlation between ε and $V^{2/3}$, as well as between the maximum LSPR and $V^{2/3}$. Furthermore, both parameters were found to be linearly dependent on the tip-to-core diameter ratio, highlighting its critical role in modulating the optical behavior of AuNSs.[53]

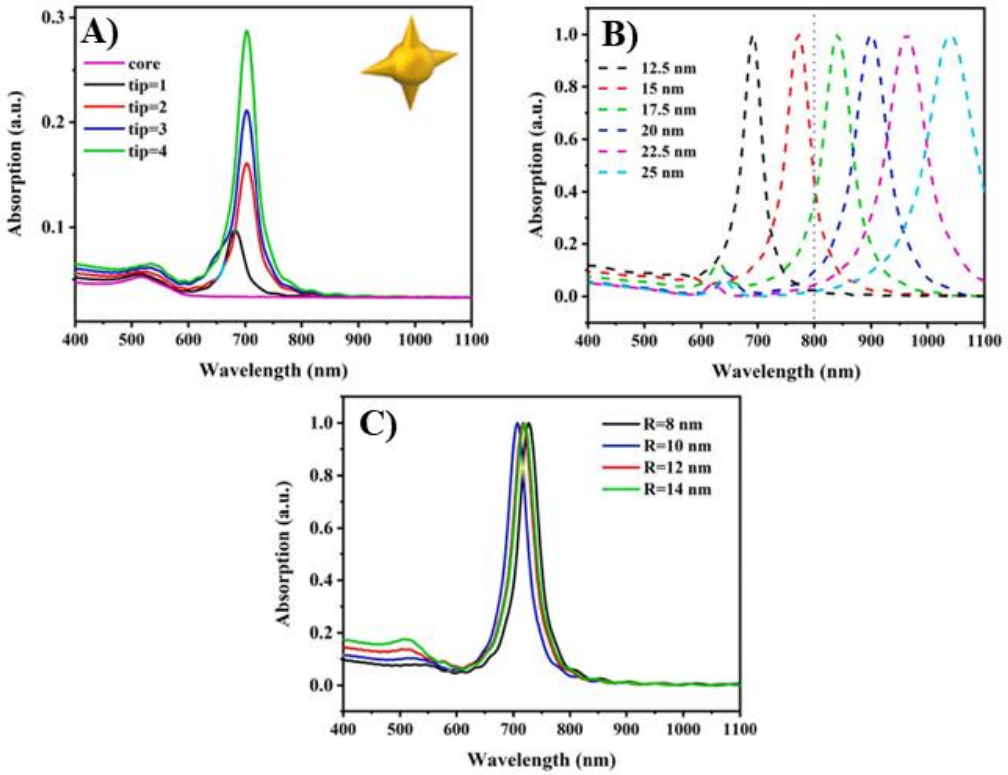

Figure 1.6. Representative UV-Vis absorbance spectra illustrating the key influence of structural characteristics of AuNSs on their plasmonic response, including A) number of tips, B) tip length, and C) diameter of the central core.[54]

1.4 Synthesis of Inorganic Nanostructures

This section provides a brief overview of the main existing synthetic methods used for the preparation of nanostructured inorganic systems. It begins with a general discussion of the most common approaches for synthesizing various types of metallic NPs, followed by a more

focused description of those strategies typically applied for the design of gold-based nanosystems, which constitutes the primary goal of this research work.

In general, synthetic methodologies for nanostructured materials can be broadly classified into two main categories: top-down and bottom-up approaches (Figure 1.7). Top-down strategies involve the breakdown of bulk materials into smaller, nano-sized particles through mechanical, chemical, and/or physical techniques. Commonly used top-down methods include photolithography, electron beam lithography, mechanical milling, anodization, and plasma etching. A major limitation of top-down methods is the lack of precise control over the characteristics of the obtained NPs, such as their size or morphology, often resulting in highly polydisperse nanosystems. On the other hand, bottom-up strategies are based on the controlled assembly of atoms or molecules into nanostructured materials through chemical or biological processes. Examples of such methods for the synthesis of NPs include self-assembly of monomer/polymer molecules, chemical or electrochemical precipitation, sol–gel processing, laser-induced pyrolysis, chemical vapor deposition, thermal decomposition, and bio-assisted synthesis.[55] Bottom-up strategies generally allow for more precise control over the physicochemical properties of the resulting NPs than top-down approaches, making them highly suitable for the rational design of nanomaterials tailored to specific applications.

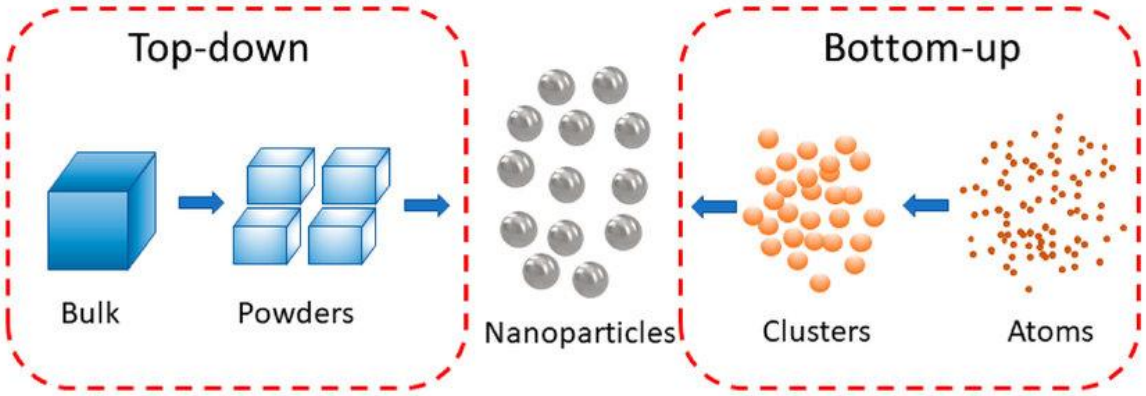

Figure 1.7. Schematic representation of the top-down and bottom-up synthetic methodologies used for the preparation of nanostructured materials.[56] Under Creative Commons CC BY-NC 4.0 license.

1.4.1 Most Relevant Methods for the Synthesis of Metallic NPs

This section briefly discusses five widely employed methods for the synthesis of inorganic metallic nanostructures (Figure 1.8). Several of these strategies are commonly used for the synthesis of gold NPs, which is the primary focus of this study, while others, such as thermal decomposition, are more frequently applied for the preparation of magnetic nanostructures. Following this more general overview, section 1.4.2 will delve specifically into the three most prevalent approaches for synthesizing gold NPs with controlled physicochemical properties.

1.4.1.1 Chemical Reduction

Chemical reduction is one of the most established bottom-up methods for the synthesis of metallic NPs. In this process, metal ions or complexes are reduced to their metallic state through electron transfer from reducing agents involved in the reaction (Figure 1.8 A). Typical metallic precursors include metal salts or compounds that contains the element to be reduced (*e.g.* Ag^{+}, Au^{3+}, or Cu^{2+} ions), while commonly used reducing agents range from sodium borohydride and ascorbic acid to hydrazine, sodium citrate, or even natural agents such as plant extracts or microorganisms.[57]

Different stabilizers are often included in synthetic processes to prevent the aggregation of formed NPs and control their size and morphology. The physicochemical properties and monodispersity degree of the resulting metallic NPs are highly sensitive to various synthetic parameters, including the composition and concentration of metal ions, the used reducing and stabilizing agents, or the molar ratios between the different precursors. Moreover, external reaction conditions such as the used solvent, pH, temperature, or reaction time can significantly affect the dimensions, morphology, stability and/or aggregation of the designed nanosystems.[57] As an example, Iqbal *et al*. investigated the influence of $NaBH_4$ concentration on the characteristics of gold NPs obtained by chemical reduction. They observed that low to moderate reducing agent concentrations yielded uniform NPs, whereas excessive $NaBH_4$ led to larger, aggregated NPs with broader size distributions.[58]

1.4.1.2 Laser Ablation

Laser ablation in liquid environment, commonly referred to as laser ablation synthesis in solution (LASiS), is a versatile top-down technique that enables the production of metallic

nanostructures with relatively high control over their characteristics. The method involves focusing a high-energy laser beam onto a bulk metal immersed in a liquid medium. The laser ablates atoms from the metal surface, which subsequently nucleate and grow into NPs within the surrounding solution (Figure 1.8 B). The physicochemical properties of the obtained nanosystems can be widely tuned by adjusting laser parameters, such as its wavelength, energy, or pulse duration, as well as the properties of the surrounding liquid medium. In this way, LASis has been effectively applied to synthesize inorganic NPs formed by transition and noble metals, including copper, iron, silver, platinum, or gold.

In a representative example of the synthesis of gold NPs, Mafune *et al.* used 640 and 532 nm lasers to irradiate gold plates immersed in aqueous SDS solutions, employing a 250 mm focal length lens. They demonstrated that the dimensions of the NPs are highly dependent on the amount of SDS, obtaining smaller nanostructures with increasing concentrations of the surfactant.[59] Another study reported the laser-assisted synthesis of gold NPs in aqueous solution using an 800 nm pulsed laser, observing that the NPs were partially oxidized by the oxygen present in the solution and acquired slightly negative surface charges. The study also highlighted that adding salts such as KCl, NaCl, or NaOH is an effective strategy to modulate the size of the synthesized gold nanostructures.[60]

The primary advantages of LASiS lie in its operational simplicity, adaptability to different environments, and the absence of chemical reducing agents. These render the method especially attractive for applications requiring high-purity NPs, such as biomedicine, catalysis, and nanoelectronics. However, challenges remain in controlling NPs size distribution and improving the cost-effectiveness of large-scale production.[61,62]

1.4.1.3 Green or Eco-Friendly Synthetic Routes

The so-called green methods represent an environmentally conscious approach for the controlled design of metallic NPs, leveraging biological compounds as both reducing and stabilizing agents (Figure 1.8 C). These biological agents, derived from plants, bacteria, fungi, or algae, serve as sustainable alternatives to conventional and potentially toxic chemical reagents. This approach aligns with the principles of green chemistry, aiming to minimize ecological impact while promoting safer and more energy-efficient synthetic practices.

In this processes, bioactive molecules from plant extracts or microorganisms interact with metal ions, reducing them to their elemental state and facilitating the formation of NPs. These processes are typically conducted under mild conditions (ambient or slightly elevated temperatures), thus reducing energy demand and production costs. Metallic nanostructures produced *via* green methods have shown promise across diverse applications such as biomedicine, environmental remediation, catalysis, or electronics. Interestingly, there are some representative studies that explored the use of green chemistry for the synthesis of anisotropic gold NPs such as those intended in this work. For example, Parial *et al.* proposed the use of the cyanobacterium *Nostoc ellipsosporum* for the synthesis of AuNRs with tunable aspect ratios and optical responses.[63] In another interesting work, bovine serum albumin was incorporated into the one-pot synthetic procedure of gold NPs with star-like morphology under acidic conditions. Remarkably, the obtained inorganic nanostructures displayed pH-dependent optical properties, with the absence of protein leading to a lack of particle formation, thus underscoring its critical role in the synthetic process.[64]

1.4.1.4 Thermal Decomposition

Thermal decomposition is a widely explored method for synthesizing metallic NPs through the high-temperature breakdown of metal precursors. Typically carried out in the presence of surfactants or stabilizing agents, this strategy involves the controlled heating of metal complexes until they decompose, releasing zero-valent metal atoms that nucleate and grow into NPs (Figure 1.8 D). The physicochemical properties of the resulting NPs can be precisely controlled by carefully regulating various synthetic parameters, such as temperature, reaction time, inert atmosphere, or the type of stabilizing agents.[65–67] Common precursors include metal carbonyls and salts such as $Fe(CO)_5$, $AgNO_3$ or $HAuCl_4$. For example, Otto *et al*. prepared spherical-shaped gold NPs through the controlled thermal decomposition of $HAuCl_4$ in different heating steps up to 320 °C. [68] In another representative study, octahedral gold NPs were obtained by thermally treating $HAuCl_4$-loaded polystyrene-*b*-poly(2-vinylpyridine) for 5 min at 250 °C in air.[69] Despite these examples, the availability of more cost-effective and low-hazardous alternative synthetic routes to produce gold NPs with well-defined physicochemical characteristics has led to thermal decomposition being less frequently used for their preparation.

1.4.1.5 Electrochemical Deposition

Electrochemical deposition is a synthesis method wherein metal ions are electrochemically reduced to form solid metal atoms, which then aggregate into nanostructures. This process occurs in an electrochemical cell through the application of an external voltage between an anode and a cathode immersed in an electrolyte containing metal ions (Figure 1.8 E).

The size, shape, and distribution of the resulting NPs can be controlled by adjusting various parameters, such as the applied potential and current density, temperature, electrolyte concentration, or deposition time, among others. Once the desired size and morphology of NPs are achieved, the deposition process is halted, and the nanosystems can either remain attached to the substrate or be harvested by scraping or dissolving the substrate. This approach offers an environmentally favorable alternative to traditional chemical reduction methods, avoiding the use of harsh reagents and high-temperature conditions. Electrochemical deposition has been widely explored for the fabrication of functional nanostructures used in sensors, energy storage devices, or catalysis.[70]

1.4.2 Fundamental Approaches for the Synthesis of Gold NPs: a Focus on the Turkevich, Brust-Schiffrin, and Seed-Mediated Growth Methods

In previous section 1.4.1, we provided a general overview of common methodologies for the synthesis of inorganic NPs, many of which have been applied for the preparation of gold NPs. Among these, chemical reduction methods remain the most extensively studied and foundational strategies for the synthesis of gold nanostructures, owing to their simplicity, scalability, and high degree of control over NPs morphology. In particular, here we discussed in detail the Turkevich, Brust-Schiffrin, and seed-mediated growth methods, which have become cornerstone synthetic techniques in gold NPs research due to their reproducibility and tunability.

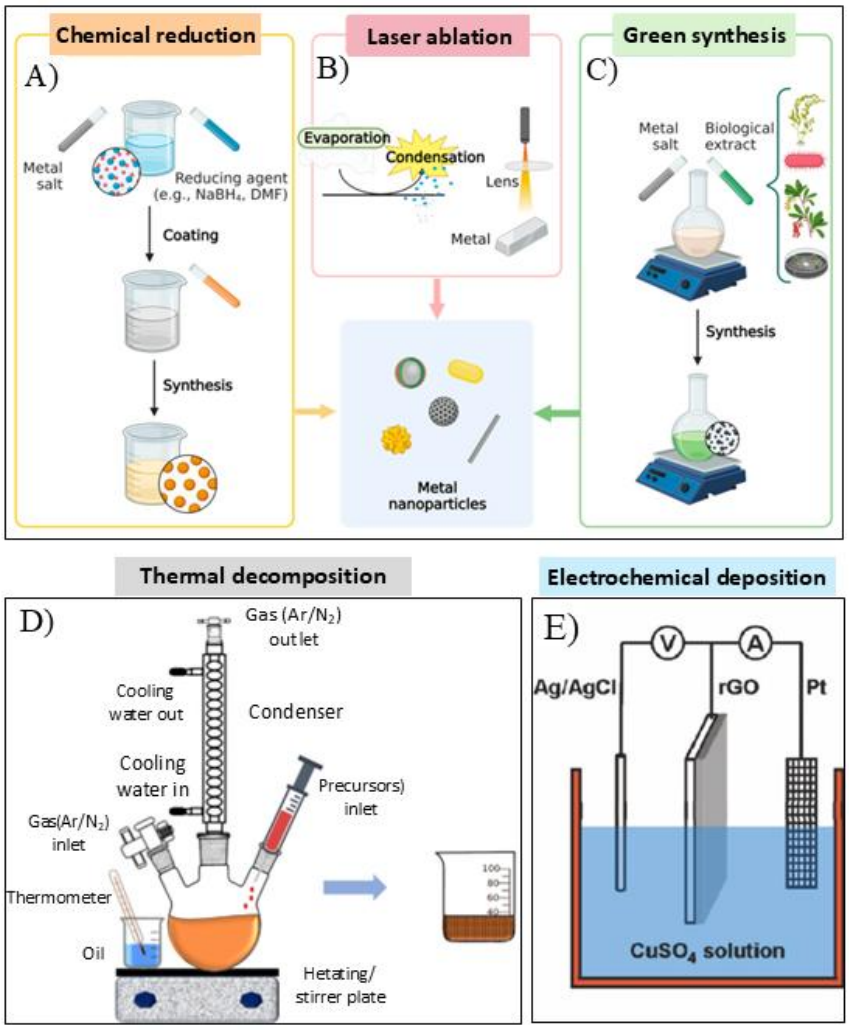

Figure 1.8. Schematic representation of the main synthetic methods for metallic NPs, including A) chemical reduction, B) laser ablation, C) green synthesis,[71] D) thermal decomposition,[72] and E) electrochemical deposition.[73] Under Creative Commons CC BY-NC 4.0 license.

These approaches rely on the reduction of gold ions in solution, leading to their nucleation followed by controlled growth to form nanostructures. Stabilizing agents are incorporated into the reactions to modulate the physicochemical properties and prevent the undesired aggregation of NPs throughout the synthetic processes. Typical reducing agents include sodium borohydride, formaldehyde, hydroxylamine, or citric acid, while polymers and surfactants are frequently employed as stabilizers.

Over the years, several modifications to these protocols have been developed to control the size, morphology, or surface chemistry of gold-based nanostructures. This section outlines the fundamental principles, experimental procedures, and typical characteristics of gold NPs synthesized *via* the Turkevich, Brust-Schiffrin, and seed-mediated growth methods, with each one offering distinct advantages in terms of simplicity, scalability, and/or tunability.

1.4.2.1 Turkevich Method

The Turkevich method, first introduced in 1951, is a classical approach for synthesizing spherical gold NPs through the reduction of $HAuCl_4$ by trisodium citrate in boiling aqueous solutions (Figure 1.9 A). In this protocol, the incorporated citrate ions assume a dual role, acting both as reducing and stabilizing agents for the controlled formation of NPs. Upon addition of citrate to the boiling gold precursor solution under vigorous stirring, the reaction mixture undergoes a rapid color change from pale yellow to deep red, indicating gold NPs formation. The resulting gold nanostructures typically exhibit well-defined spherical morphologies, and average diameters close to *ca*. 20 nm.[74]

The synthetic strategy proposed by Turkevich was subsequently modified to synthesize gold NPs in the size range of 15 to 150 nm, being this objective achieved by adjusting the ratio between trisodium citrate and gold precursors.[74] After that, numerous research groups have implemented further modifications to this method to refine the synthetic process of gold nanostructures with controlled physicochemical characteristics. For instance, Kimling *et al*. demonstrated the crucial role of the concentration of citrate over the dimensions and morphologies of the obtained NPs. More specifically, higher citrate concentrations promote the formation of smaller, spherical gold NPs, while lower concentrations tend to induce the aggregation of metallic precursors, resulting in the formation of larger nanostructures.[75] Both theoretical and experimental analyses have demonstrated that sodium citrate can significantly alter the pH of the precursor solutions, which has been identified as a key factor in determining the characteristics of the formed gold NPs.[76] Furthermore, altering the sequence of reagent addition, that is, adding gold precursor into a boiling sodium citrate solution, leads to the formation of smaller gold NPs with narrower size distributions.[77]

1.4.2.2 Brust-Schiffrin Method

The Brust-Schiffrin method represents a pivotal advance in the synthesis of thiol-functionalized gold NPs in organic media. This biphasic reduction process involves the transfer of tetrachloroaurate ions from an aqueous solution into toluene using a phase transfer agent, typically tetraoctylammonium bromide (TOAB), followed by reduction with sodium borohydride in the presence of alkanethiols such as dodecanethiol (Figure 1.9 B). The addition of the reducing agent induces a characteristic change in the color of the organic phase, shifting from orange to a deep brown.

This technique produces highly stable, monodisperse NPs with controllable core diameters (typically 1-5 nm). NPs size is largely governed by the thiol-to-gold ratio: higher concentrations of thiol result in smaller particle diameters due to stronger surface passivation. Among the key advantages of this synthetic approach are its operation under ambient conditions, the high stability and low aggregation degree of the obtained nanostructures, and the ability to precisely control NPs size by adjusting the amount of alkanethiol incorporated in the synthetic process.[78]

1.4.2.3 Seed-Mediated Growth Method

The seed-mediated growth approach is a two-step strategy that provides exceptional control over the size and morphology of the resulting gold NPs. Initially, small gold seeds are formed by the rapid reduction of gold precursors, typically using sodium borohydride. These seeds then serve as nucleation sites for further growth in a secondary solution containing additional gold precursor and a mild reducing agent, such as ascorbic acid (Figure 1.9 C).

This method enables the synthesis of NPs with controllable sizes and morphologies, exhibit dimensions ranging from *ca*. 5 to 200 nm. The physicochemical characteristics of the resulting gold NPs are primarily influenced, among other factor, by the seed-to-precursor ratio and the concentration of surfactants, being cetyltrimethylammonium bromide (CTAB) the most typically used. Surfactants preferentially adsorb onto specific crystallographic facets, thereby guiding the directional growth of NPs into rods, cubes, or other non-spherical forms.[79]

Murphy *et al*. performed a comprehensive analysis of the seed-mediated growth synthesis of gold NPs, examining in detail how seed concentration, reducing agent type, and the rate of

reducing agent addition influence NPs size and stability.[80] Interestingly, they found that slower addition of the reducing agent favored enlargement of existing seeds, while rapid addition promoted nucleation of new seeds and the formation of smaller gold NPs. The study also examined the effect of different reducing agents, demonstrating that the incorporation of hydrazine and SDS in the seed-mediated reaction led to the formation of smaller NPs in comparison with the non-seeded approach. Conversely, when sodium borohydride was used as the reducing agent, smaller NPs were obtained through the unseeded method, suggesting that growth dominated over nucleation.

Further comparative studies, such as those by Natan *et al*., have shown that seed-mediated methods significantly reduce nanoparticle polydispersity compared to direct chemical reduction, particularly when larger seeds are employed.[81] These findings highlight the importance of precise control over synthetic conditions for tailoring NPs characteristics.

1.5 Functionalization and Colloidal Stability of Inorganic Nanostructures

Inorganic NPs, including gold-based nanostructures, possess unique physicochemical properties that make them attractive for a wide range of applications, particularly in biomedicine. However, a major limitation to their effective use in biological environments lies in their frequently poor colloidal stability. This instability is especially pronounced when the syntheses of NPs are performed in organic solvents, resulting in nanostructures with highly hydrophobic behavior and prone to aggregation under physiological conditions. Even those NPs synthesized in aqueous media, which are inherently hydrophilic, may still lack high colloidal stability in complex biological environments due to nonspecific interactions with surrounding biomolecules. When introduced in biological environments, NPs tend to adsorb a large number of proteins and other compounds onto their surfaces, a phenomenon that can lead to aggregation and/or significant alterations in their behavior and functionality.[83] Thus, and despite their high potential for a wide range of applications within the biomedical field, inorganic nanostructured materials face a significant challenge regarding their colloidal stability which may limit their applicability. Consequently, surface functionalization is essential to preserve colloidal stability and ensure predictable behavior of NPs in biological systems.[84]

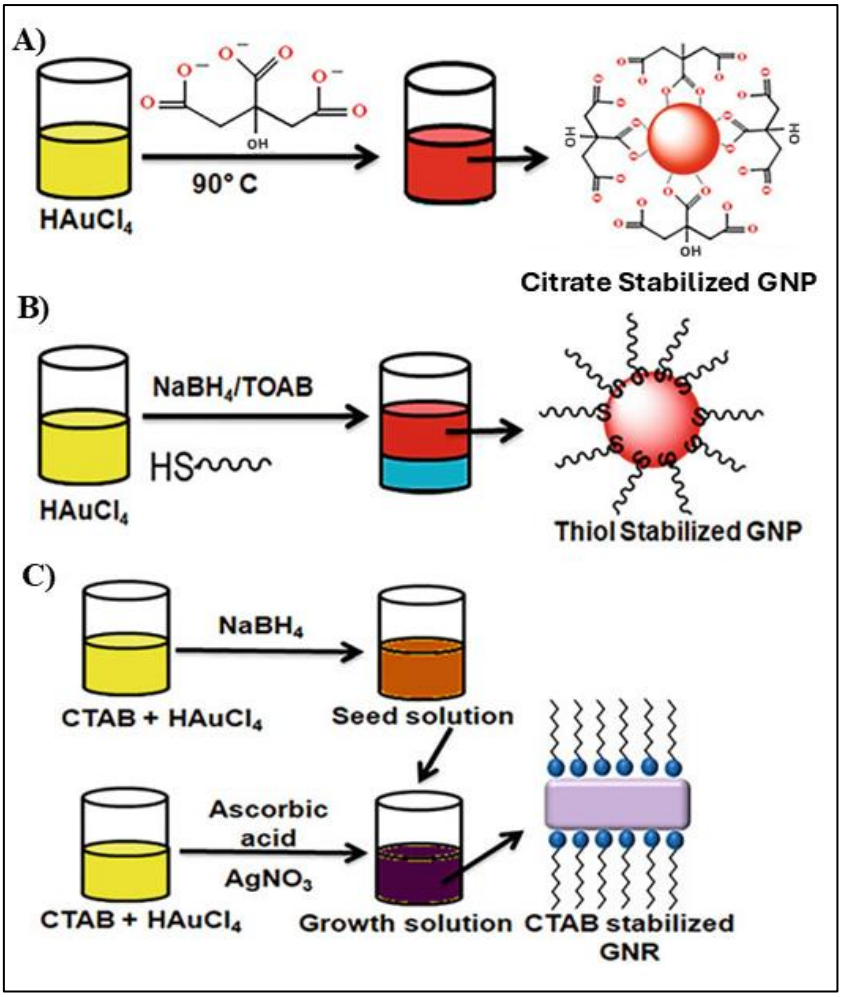

Figure 1.9. Schematic illustration of the three fundamental chemical reduction strategies for the synthesis of gold NPs: A) Turkevich, B) Brust-Schiffrin, and C) seed-mediated growth methods.[82]

Several strategies have been developed to render inorganic nanostructures colloidally stable in biological media, with the most relevant being ligand exchange, polymer coating, encapsulation within organic particles, or the formation of silica nanoshells wrapping the NPs.[85] The ligand exchange strategy involves the replacement of original surface ligands with hydrophilic moieties that exhibit stronger binding affinities to the NPs surface, while polymer coating is based on the adsorption or covalent attachment of biocompatible polymers to provide a steric barrier and prevent aggregation (Figure 1.10). On the other hand, encapsulation and silica coating approaches involve the enclosure of NPs within organic shells, such as liposomes, or silica layers, respectively, thus enhancing dispersibility and reducing

surface reactivity. Among these, ligand exchange and polymer coating are the most widely employed techniques due to their versatility and straightforward implementation. Polymer-based functionalization is particularly attractive because polymers can be engineered with specific functional groups, charges, or responsive elements to meet the requirements of diverse applications.[86]

It is important to note that surface functionalization of inorganic NPs not only confers colloidal stability but also plays a pivotal role in modulating the biological identity, biodistribution, and clearance of NPs. Proper functionalization can reduce toxicity, minimize off-target effects, enhance biocompatibility, and enable active targeting strategies. This surface modification is particularly critical for NPs that are highly reactive and prone to oxidation, as these can undergo rapid degradation, lose their functionality, or even pose health risks by aggregating or occluding microvasculature during *in vivo* administration.

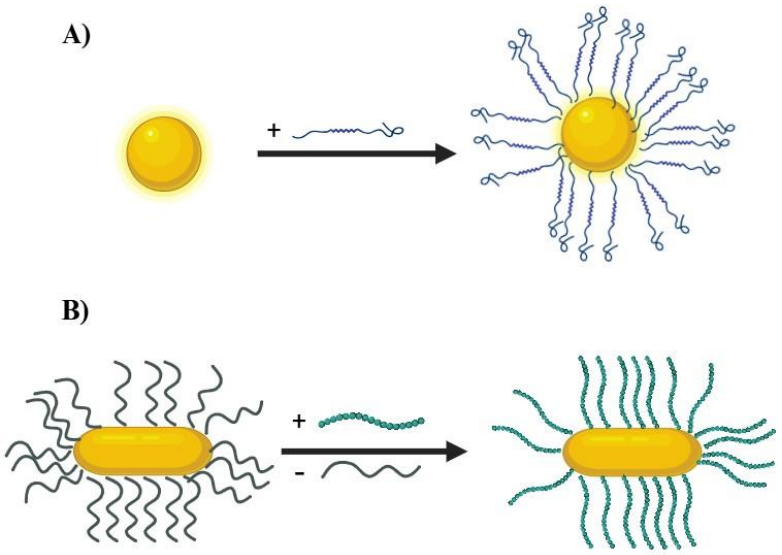

Figure 1.10. Graphical representation of the two most commonly used strategies for the functionalization of inorganic NPs: A) polymer coating and B) ligand exchange.

1.5.1 PEGylation

Among the various surface functionalization strategies that have been explored to enhance the biostability of inorganic NPs and prolong their circulation time *in vivo*, those based on the conjugation of hydrophilic polymer chains have proven particularly effective. Polymers such as poloxamers (pluronics), poloxamines, and chitosan have been extensively studied for this

purpose.[87] However, polyethylene glycol (PEG), also known as macrogol, is undoubtedly the most commonly adopted polymer for the functionalization of inorganic NPs.

PEG is a highly hydrophilic, biocompatible polyether derived from ethylene oxide. Its attachment to the surface of inorganic NPs prevents the adsorption of hydrophobic functional groups of proteins and minimizes non-specific biological interactions, making it particularly suitable for the application of PEG-coated NPs in biomedical areas such as drug delivery, photothermal therapy, or bioimaging. The surface modification of NPs with PEG, commonly referred to as PEGylation, forms a hydration shell that increases colloidal stability and extends circulation time by reducing recognition and clearance by the mononuclear phagocyte system. This ability of PEGylated nanomaterials to be invisible to the immune system, known as the "stealth effect", enhances their biocompatibility and targeting capability.[88]

Currently, many different types of PEGs are available for NPs functionalization, differing in both terminal functional groups and molecular weights. Examples of terminal groups include thiols (-SH), amines (-NH_2), carboxylic acids (-COOH), N-hydroxysuccinimides (NHS), or maleimides, among others (Figure 1.11 A). On the other hand, the molecular weight of PEG typically ranges from 2 kDa (comprising *ca.* 45 monomer units) to 20 kDa (*ca.* 454 units).[89] Both characteristics of PEG molecules have a strong influence over the physicochemical properties of NPs upon PEGylation: the terminal group determines the binding affinity and surface charge, while longer polymer chains confer greater steric flexibility and hydrophilicity.[90]

Another critical factor that dictates the NPs behavior post-PEGylation is the grafting density of PEG chains on their surfaces. Depending on this density, PEG molecules can adopt either a mushroom or a brush conformation (Figure 1.11 B). When the spacing between chains exceed the Flory radius (the typical end-to-end distance of a polymer chain in a good solvent) (equation 5), the so-called mushroom conformation is formed. In contrast, when the density of PEG chains is high enough to have interdistances smaller than the Flory radius, steric crowding forces the chains into an extended brush-like configuration.[91]

$$F = 0.6 \cdot \alpha \cdot n \quad (5)$$

where *F* is the Flory radius, *n* is the number of monomers in each PEG, and α is the length of the monomers in Å. For PEG monomer, α = 3.5 Å.

These conformational regimes of PEG molecules have a significant influence on the stability and biological performance of PEGylated NPs. Thus, at lower grafting densities (mushroom conformation), the limited steric hindrance can lead to weaker stabilization and increased aggregation of NPs. In contrast, higher grafting densities (brush-like conformation) result in densely packed PEG chains that provide NPs with substantial steric repulsion, preventing aggregation and enhancing their colloidal stability in physiological environments. The choice between mushroom or brush-like PEG configurations depends on the intended application of PEGylated NPs. While brush-like configurations improve circulation and stealth properties of NPs, mushroom-like ones enhance their cellular uptake capability and even improve the efficiency of cargo release in drug delivery applications.[92] The efficacy of PEGylation to reduce non-specific protein adsorption by enhancing hydrophilicity and promoting steric repulsion have been extensively validated across a broad spectrum of nanomaterials, including gold NPs, magnetic NPs, or quantum dots.[93–100] This minimization of protein adsorption leads to reduced opsonization, lower complement activation, and decreased NPs hepatic uptake, thereby extending their circulation half-life (*i.e.* the time during which >50% of the injected dose remains in circulation), improving the likelihood of NPs reaching target sites by avoiding clearance by the reticuloendothelial system. In this way, PEGylation has been demonstrated as an efficient functionalization strategy for improving the biological performance of inorganic NPs in view of their potential application for biomedical purposes.[90]

1.6 Main Experimental Techniques for the Physicochemical Characterization of Nanostructured Materials

A comprehensive understanding of the physicochemical properties of inorganic NPs is crucial for predicting and optimizing their behavior accross diverse applications. This section provides a detailed overview of the most widely employed experimental techniques for the physicochemical characterization of inorganic nanostructured materials. These approaches offer valuable insights into key NPs attributes such as size, morphology, surface charge, optical properties, and colloidal stability—factors essential for ensuring their effective performance in intended applications. When combined, these complementary techniques enable accurate and reliable assessment of nanosystems.

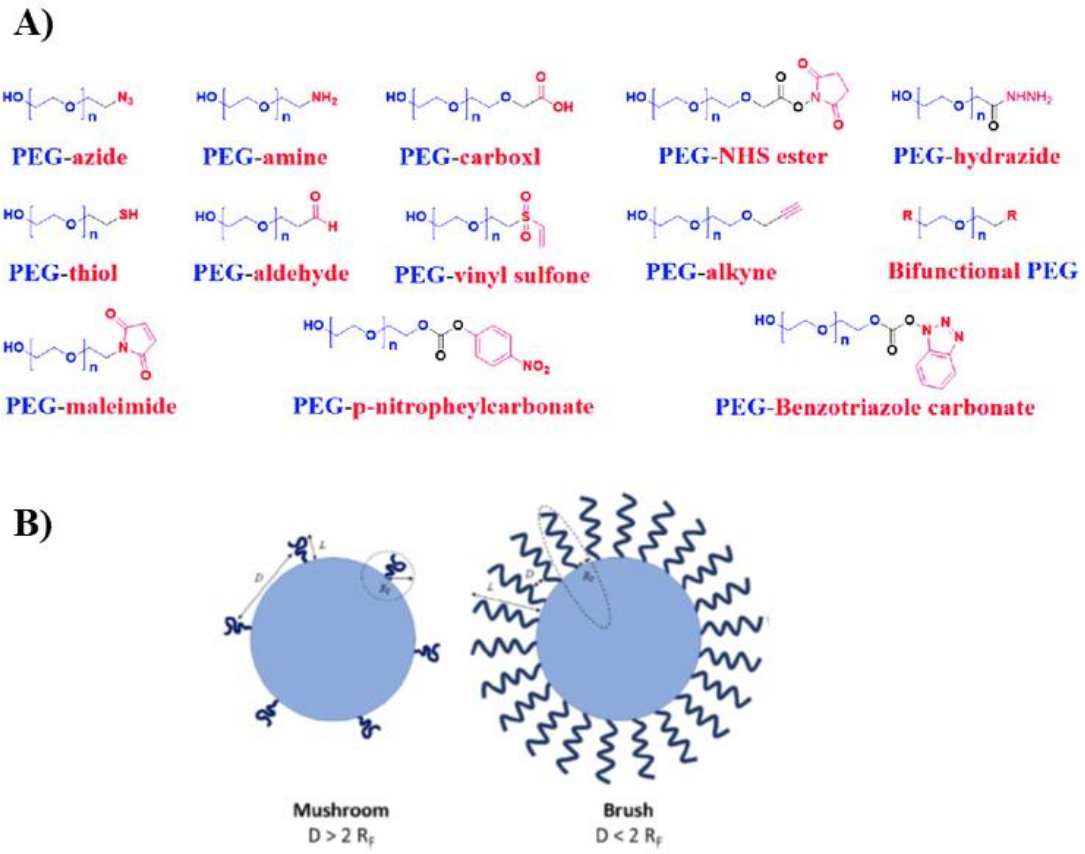

Figure 1.11. A) Chemical structures of PEG molecules bearing different terminal functional groups commonly used for NPs surface functionalization.[88] Under creative commons attribution-noncommercial 3.0 license. B) Schematic representation of PEG conformations on NPs surfaces depending on grafting density: low-density "mushroom" and high-density "brush" configurations.[89] Under creative commons CC BY-NC 4.0 license.

1.6.1 Dynamic Light Scattering

Dynamic light scattering (DLS) is a widely used technique to measure the hydrodynamic diameter of particles in colloidal suspensions, particularly when they display dimensions within the sub-micrometer range. The principle of DLS relies on the Brownian motion of small particles dispersed in a solvent, where they move randomly in all directions due to collisions with surrounding molecules. When a laser beam is directed to colloidal dispersion, the NPs scatter the light, and this scattered radiation fluctuates in intensity as the particles move. A detector measures these intensity fluctuations at a specific angle, typically 90 or 173 degrees from the laser beam, and the rate at which the intensity fluctuates is related to the speed of

the NPs motion, which in turn is determined by their size. Smaller particles move more quickly, causing rapid fluctuations, while larger particles move slower, resulting in slower fluctuations.

The data obtained from DLS are processed through an autocorrelation function which analyzes the fluctuations in light intensity. Initially, this function is linear and constant, indicating that the NPs remain stationary, but when particle movement occurs the correlation function starts to decay exponentially, reflecting the diffusion of the NPs. Smaller particles exhibit swift movement, resulting in rapid decay, while larger particles move at a slower pace and cause a delayed decay in the correlation function (Figure 1.12).[101] The correlation function allows the calculation of the so-called translational diffusion coefficient of the nanostructures, being used to determine their hydrodynamic size through the Stokes-Einstein equation (equation 6), which correlates the diffusion coefficient and hydrodynamic size to the solvent viscosity and temperature.[102]

$$D = K_B\, T/(6\pi \cdot \eta \cdot R_H) \qquad (6)$$

where D is the translational diffusion coefficient, K_B is the Boltzmann constant, T and η are the temperature and viscosity of the solvent, and R_H is the hydrodynamic radius of the NPs.[102]

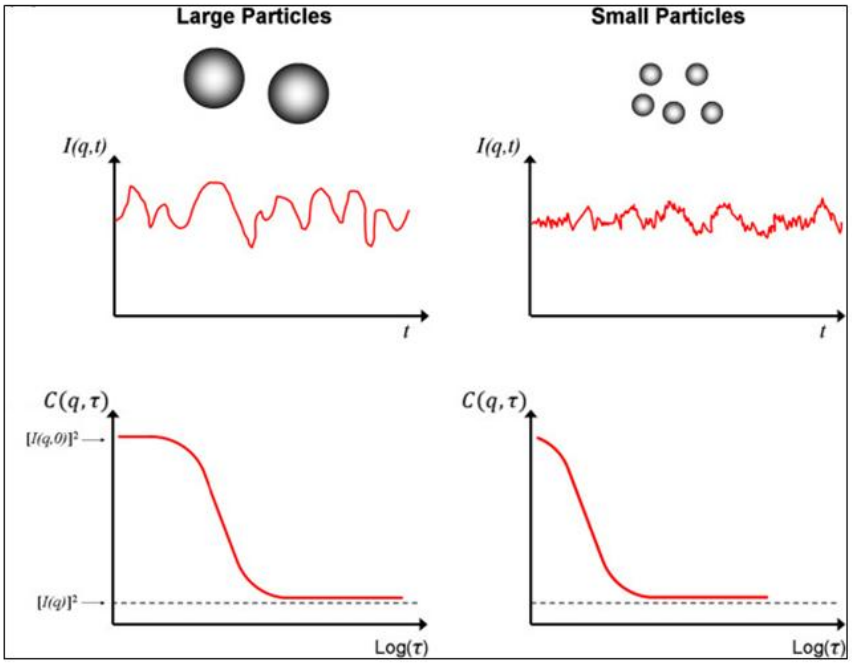

Figure 1.12. Illustrative diagrams show the intensity of the scattered light over time and the corresponding autocorrelation functions of colloidal dispersion formed by particles with different hydrodynamic sizes.[101] Under creative commons CC BY-NC 2.0 license.

Typically, DLS software can be configured to calculate the hydrodynamic size of the dispersed NPs by averaging data based on different parameters, including the number of particles, their volume, or the intensity of the scattered light, among others. Importantly, a key limitation of DLS is the assumption of spherical-shaped NPs when calculating their hydrodynamic size. Thus, for non-spherical nanostructures, the hydrodynamic diameter obtained from DLS may not accurately reflect their true dimensions, as NPs morphology influences the rate of Brownian motion.

1.6.2 Nanoparticle Tracking Analysis

Nanoparticle tracking analysis (NTA) is a diffusion-dependent technique in which dispersed NPs are introduced into a chamber before a laser beam passes through. A video of the light scattered by the nanostructures is recorded by a high precision camera, thus enabling a precise tracking of their Brownian motions within the sample.[102] In a similar way than for DLS characterization, if the temperature and viscosity of the colloidal dispersion is known, the hydrodynamic diameter can be derived from the diffusion coefficient using the Einstein-Stokes equation.

An interesting work conducted by Jiskoot *et al*. compared NTA and DLS by analyzing standard polystyrene beads ranging from 60 to 1000 nm through both characterization techniques. The results demonstrated that, in general, NTA provides more accurate and reliable hydrodynamic size distributions.[103] This finding corroborates previous studies that emphasized the challenges of interpreting DLS results, particularly for samples with low degree of monodispersity. In contrast, NTA can more effectively distinguish between different hydrodynamic size populations within a sample. This difference arises from the fact that NTA tracks individual particles, whereas DLS analyzes a collective group, often leading to a bias toward larger particles in the sample.[104] In any case, none of the methodologies consider the shape of the NPs.

1.6.3 Zeta Potential Measurement

When colloidal particles are dispersed in a liquid, the so-called electric double layer is formed around them. This consists of a tightly bound layer of counter-ions near the particle surface

(Stern layer) and a more diffuse layer of ions farther away (diffuse layer). The slipping plane is the boundary between these two layers, where the fluid moves relative to the particle (Figure 1.13).

The zeta potential is the electrical potential measured at the slipping planes of the dispersed NPs, thus reflecting the difference in charge between the particle and the surrounding medium. The value of this magnitude is highly influenced by several factors, including the size and surface chemistry of the NPs, their concentration, or the pH, temperature, and ionic strength of the medium, among others.[102] In this way, the zeta potential is a crucial parameter to assess the stability of colloidal dispersions. As a general rule, particles with a strong positive or negative charge exhibit high repulsion between them, thus preventing aggregation and leading to stable colloidal dispersions (zeta potential values greater than ± 30 mV), while lower values are typically characteristic of electrostatically non-stable colloidal systems.[104]

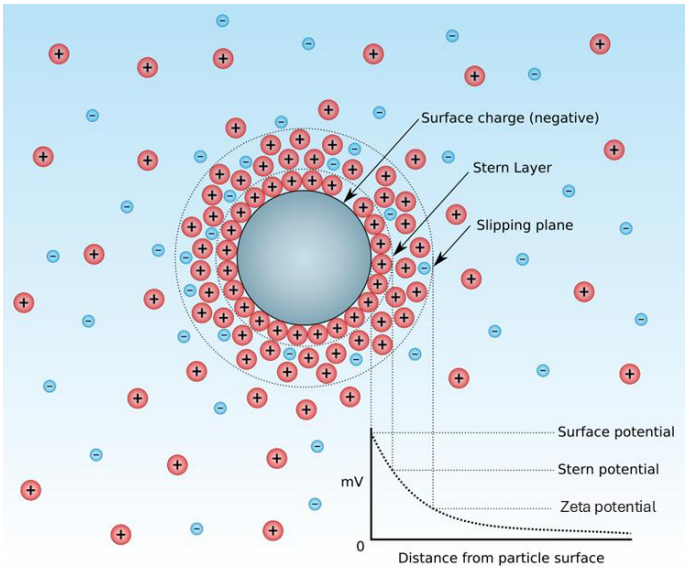

Figure 1.13. Schematic representation of the electrical double layer around a colloidal particle. The Stern layer and the slipping plane are indicated, as well as the different potential levels. Graph on the bottom right illustrates potential decay with distance from particle surface, highlighting the zeta potential at the slipping plane.[105] Under creative commons CC BY-NC 3.0 license.

1.6.4 UV-Vis Spectroscopy

Ultraviolet-Visible (UV-Vis) spectroscopy is a widely used, rapid, and robust experimental technique for the optical characterization of nanostructured materials. This analytical method enables the study of the interaction between electromagnetic radiation and optically active NPs within the ultraviolet and visible regions of the spectrum, typically ranging from *ca*. 200 to 800 nm. As previously described, plasmonic NPs exhibit unique optical features arising from the collective oscillation of free electrons on their surfaces when excited by an incident light, a phenomenon known as LSPR. Consequently, the extinction spectra of plasmonic nanostructures display characteristic absorption peaks that correspond to the resonance frequency of these surface plasmons. The position, intensity, and width of these peaks provide valuable information about the physical and chemical properties of the dispersed NPs, including their size, shape, composition, and aggregation state. Moreover, shifts in the peak position or changes in spectral features can indicate variations in the local environment or surface modifications of the nanoparticles, making UV-Vis spectroscopy an essential tool for monitoring NPs stability and functionalization (Figure 1.14 A).

For instance, increasing the size of plasmonic NPs and decreasing the interparticle distance both result in a red-shift of their characteristic absorption peaks (Figure 1.14 B-C).[106] This shift occurs due to changes in the plasmonic coupling between particles and alterations in their resonance conditions. In this way, UV-Vis spectroscopy can be effectively employed not only to qualitatively monitor these spectral changes but also to quantitatively determine the number of metallic atoms present in dispersions of plasmonic NPs. For example, the concentration of silver NPs has been precisely determined by monitoring the LSPR peak intensity over time and fitting the obtained data to the calibration curve derived from well-characterized standard solutions.[107,108] In a similar way, it was also established that variations in shape affect the distribution of electron oscillations on NPs surfaces, leading to distinct spectral signatures that can be used to infer morphological details of plasmonic NPs and assess sample homogeneity (Figure 1.14 D).

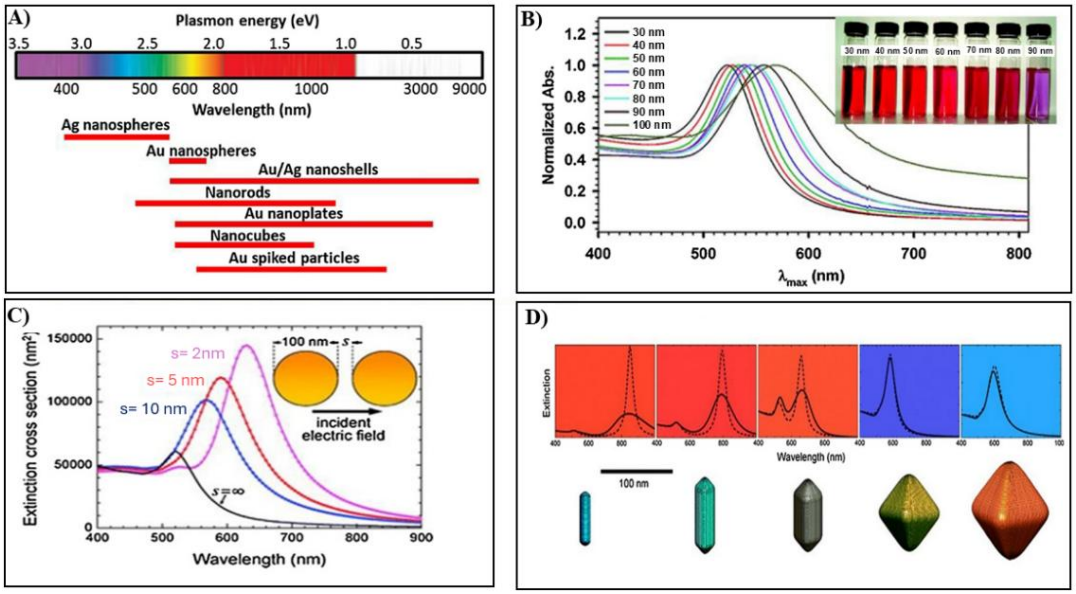

Figure 1.14. A) Energy and LSPR position of plasmonic NPs with different morphologies and compositions.[106] B) Position of LSPR in gold NPs with different sizes.[109] C) Plasmonic response (LSPR position and extinction cross-section) of two gold spherical NPs interacting as a function of their interparticle distance.[110] D) LSPR position of gold NPs with different sizes and morphologies.[110]

1.6.5 Microscopy Techniques

Scanning and transmission electron microscopy (SEM and TEM), together with confocal laser scanning microscopy (CLSM), are among the most widely used techniques for the visualization and physicochemical characterization of inorganic NPs. These microscopy methods are essential for accurately determining the dimensions, morphology and structural properties of the analyzed NPs, parameters that play a key role in their performance in the intended application. In this section, each technique will be briefly discussed, highlighting their operation principles and key advantages for the characterization of different types of nanosystems (Table 1.1).

SEM operates on the principle of scanning a focused electron beam across the surface of samples. The electron beam, controlled by specific lenses, strikes the sample and causes the ejection of high-energy primary scattered electrons and low-energy secondary electrons from the surface of the specimen. These ejected electrons generate signals that are subsequently converted into images, thus allowing the physicochemical characterization of the analyzed

NPs. Besides analyzing individual NPs, this technique can also provide information about the dispersion of the nanostructures within a sample, revealing their distribution within various matrices, such as polymeric networks or biological tissues.[15]

On the other hand, TEM operates by transmitting an electron beam through a specimen to obtain high-resolution images. Upon the interaction of electrons with the sample, some of them pass through and form the image, while others are either elastically or inelastically scattered. The amplitude of this interaction and, consequently, the obtained image, is influenced by various factors, including the dimensions, density, and elemental composition of the sample.[104] TEM has been widely applied, for instance, to evaluate the distribution and physical properties of metallic-based NPs upon their internalization into cells, thus determining with high precision their aggregation and degradation degrees after their endocytosis.[104] Moreover, TEM is also valuable to characterize alterations in subcellular structures, such as the formation of apoptosis-related vacuoles in melanoma cells during magnetic hyperthermia treatments using iron oxide NPs,[111] or to assess the NPs penetration across various tissues.[112]

Finally, in contrast to the electron beam-based SEM and TEM techniques described above, CLSM is an optical imaging method that enhances resolution and contrast by excluding out-of-focus light. This method was patented by Marvin Minsky in the 1950s, and it is based on the use of pinhole apertures on both the illumination and detection sides at the conjugate image plane, making the system "confocal".[113] In CLSM, a laser scans the sample using galvanometer mirrors, directing the beam both horizontally (x-direction) and vertically (y-direction) within the field of view. A key feature of confocal microscopy is the so-called Z-stack, which consists of a series of images taken at different focal planes along the optical axis (Z-axis) of the specimen, enabling 3D visualization of the sample. [113] Such capability allows for precise imaging of cellular structures, organelles, and dynamic processes in living cells over time, establishing CLSM as a powerful tool for studying cell biology.[114]

Table 1.1. Summary of key aspects of TEM, SEM and CLSM microscopy techniques, including their resolution, dimensionality of the acquired images, or their main advantages and disadvantages.

	TEM	SEM	CLSM
Source	Electron beam	Electron beam	Laser light
Resolution	High resolution (< 0.2 nm)	High resolution (1-10 nm) for surface features	Moderate resolution (200 nm lateral, 500 nm axial)
Image type	2D	3D	2D and 3D
Specimens	Dead, thin	Dead, thin or thick	Alive or dead, thin or thick
Advantage	Very high resolution for internal details	Detailed surface morphology in 3D	Real-time 3D imaging of live samples
Disadvantage	Extensive sample preparation	Limited to surface imaging	Fluorescent labeling required

1.7 Interactions of Inorganic NPs with Biological Environments

1.7.1 Protein Corona Formation. Impact on the Biological Behavior of Nanosystems

When inorganic NPs are incubated in physiological fluids, they spontaneously interact with biomolecules, leading to the formation of a new dynamic biological coating known as the *biomolecular corona*. This consists primarily of proteins (protein corona), but it can also include lipids, sugar moieties, nucleic acids, and metabolites, all of which bind to the surface of the nanomaterials. The composition of this biocorona critically impacts the subsequent fate of the nanosystems, and it is strongly influenced by the physicochemical properties of NPs, including their size, morphology, or surface charge. Additionally, environmental factors such as protein source and concentration, ionic strength, pH, incubation time and temperature, and the distinction between *in vitro* and *in vivo* conditions, also affect the dynamics of the formed corona.

The uncontrolled nature of protein corona formation can lead to unexpected alterations in the biological behavior of NPs, impacting processes such as cellular uptake, immune responses, and toxicity, posing a challenge for the successful biomedical application of nanostructured

materials. [115] In this regard, the corona composition can include molecules that reduce the reactivity of NPs or mask cell membrane receptors, thereby hindering cellular internalization. Conversely, the corona may shield NPs from opsonization, enhancing their circulation time and stability compared to pristine counterparts. The mechanisms governing protein corona formation are increasingly studied in biomedicine to optimize cell internalization and improve the *in vivo* performance of theranostic systems based on nanostructured materials.

A distinctive "fingerprint" of the protein corona can be generated by identifying plasma proteins, especially rare proteins and glycoproteins, adsorbed onto the surface of NPs. This fingerprint can be utilized to identify biomarkers individually and supports the study of post-translational modifications, contributing to risk assessment, prognosis, and illness identification.[115] Interestingly, data-driven approaches, including artificial intelligence, have facilitated the analysis of NPs-biological interactions. Machine learning algorithms can leverage personalized protein corona profiles to predict disease states by identifying the critical variables that govern protein corona formation on different types of NPs.[115] Protein adsorption onto NPs may also induce conformational changes, influenced by both NPs properties and environmental factors.[116] These changes can alter protein function; for instance, lipoproteins adsorbed on two-dimensional graphene flakes were found to expose multiple epitopes capable of binding hepatic receptors.[117]

The protein corona is typically categorized into two layers: the hard corona, composed of tightly bound proteins that remain associated under physiological conditions, and the soft corona, consisting of loosely bound, rapidly exchanging proteins in dynamic equilibrium with the biological environment (Figure 1.15).[118–120] Discriminating between these layers is essential for understanding the dynamic nature of NPs-protein interactions and their implications in the biological response of the nanostructures, including their cellular uptake, biodistribution, or cytocompatibility. Protein binding is driven by noncovalent forces—including hydrogen bonding, electrostatic and hydrophobic interactions, and π–π stacking—with thermodynamically favorable conditions promoting competitive adsorption.[121] Interestingly, many proteins found in the soft corona also contribute to the hard corona, suggesting a continuum of binding affinities.[122]

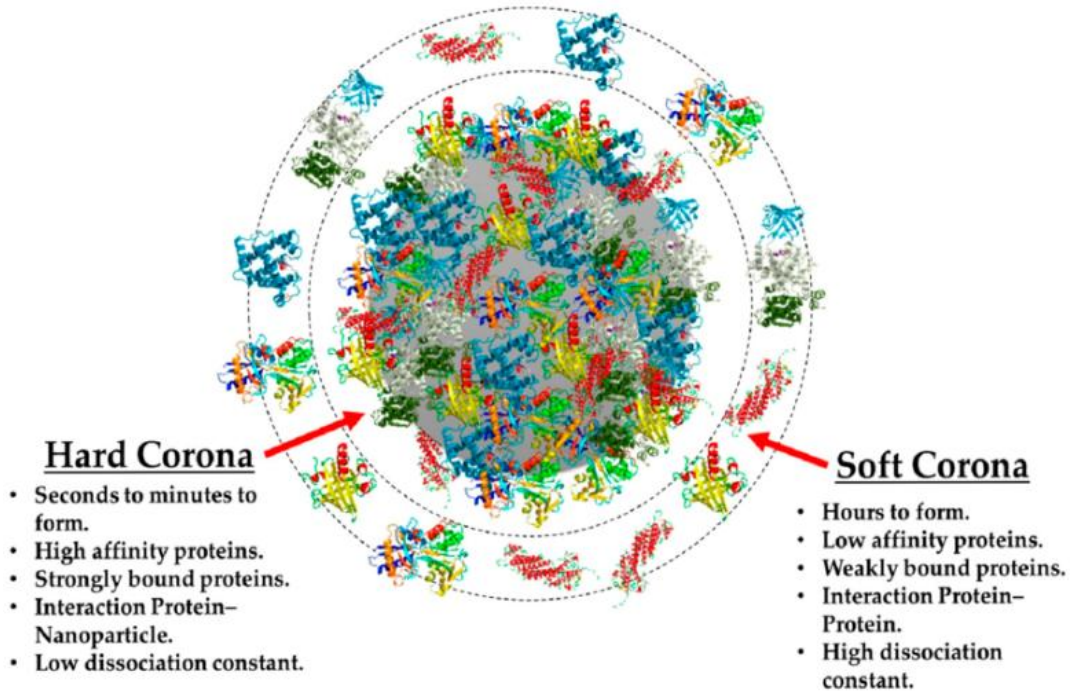

Figure 1.15. Schematic illustration of the protein corona formed around NPs upon their incubation in biological fluids. Key characteristics distinguishing the hard and soft corona layers are highlighted.[123] Under creative commons CC BY-NC 4.0 license.

1.7.2 Cytotoxicity and Biodegradation

Biodegradation is the process by which materials break down into smaller components when they are dispersed or incubated in biological fluids, enabling them to be either metabolized or excreted by the body. Many nanostructured materials, particularly those of inorganic origin, are not readily biodegradable and may accumulate in tissues, potentially leading to long-term toxicity.[124] Inorganic NPs are primarily internalized by cells primarily *via* endocytosis, a process where the nanostructures are engulfed by the cell membrane. During this process, the pH of the surrounding medium varies from a neutral value in the extracellular environment to a mildly acidic pH in early endosomes and further decreasing to a more acidic pH of *ca*. 5 in lysosomes. These pH changes have a strong influence over the stability, dissolution, and eventual degradation of the NPs.

During cellular internalization, NPs encounter enzymes such as cathepsin L, which is capable of degrading the majority of bio-NPs conjugates. Subsequent exposure to the acidic environments can lead to acid-etching of the NPs surface, releasing, for example, free metallic

ions that formed the NPs. These metal ions can potentially impact cellular functions and homeostasis by interacting with proteins and genes, contributing to increasing toxicity (Figure 1.16).[125]

In this regard, an interesting study by Xia *et al*. revealed that the intracellular biodegradation of zinc oxide NPs in RAW 264.7 cells disrupt zinc homeostasis, damage lysosomes and mitochondria, and ultimately induce cell death.[126] In a similar way, cadmium selenide release Cd^{2+} ions upon degradation, which bind sulfhydryl groups in mitochondrial proteins, leading to cell apoptosis.[127] Gold NPs have also been shown to release gold ions that impair mitochondrial enzyme activity, disturb redox balance, generate reactive oxygen species (ROS), and trigger apoptosis (Figure 1.16).[124,128,129] Interestingly, it has been demonstrated that, under certain conditions, gold ion release may exert beneficial effects. For example, the presence of gold ions released from metallic NPs in extracellular surroundings reduces microgliosis and neuronal apoptosis, while promoting an enhanced response of neural stem cells following a localized brain injury.[130]

To mitigate the biodegradation of inorganic NPs and the associated cytotoxicity in view of their potential application as biomedical nanotools, several strategies have been developed. The most common approach is the surface functionalization of the NPs with biocompatible coatings, such as PEG or albumin. This improves the stability of the nanostructures, minimizes their degradation and ultimately leads to a higher biocompatibility of the designed nanosystems. Alternatively, the development of hybrid NPs, in which the inorganic cores are incorporated within organic nanocapsules made of materials such as polymers or lipids, has been also proposed to reduce biodegradation. More advanced approaches based on the doping of inorganic nanostructures with biodegradable elements such as magnesium can also enhance biocompatibility of NPs without compromising their functionality.[124,131]

In summary, the biodegradation of inorganic nanosystems in biological environments is a complex multifactorial process governed by both the intrinsic physicochemical properties of the NPs and external conditions. Addressing these aspects to minimize the biodegradation mechanisms is essential for the rational design of safe, effective nanomaterials for biomedical use.[124]

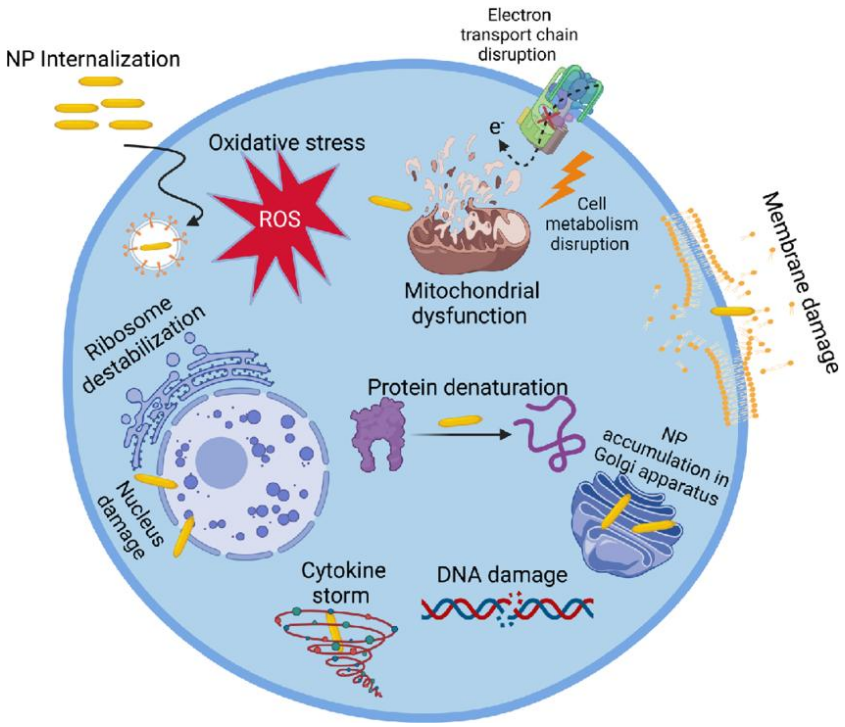

Figure 1.16. Schematic representation of different cellular mechanisms affected by NPs internalization, including ROS generation, DNA and nuclear damage, and other forms of cellular disruption.[132] Under creative commons CC BY-NC 3.0 license.

1.7.3 The Role of Physicochemical Properties in the Biological Fate of Nanosystems: Emphasis on Gold NPs

The reticuloendothelial system (RES), also known as the mononuclear phagocyte system, is the body's primary defense mechanism against foreign invaders such as bacteria, fungi, and viruses. Upon exposure to exogenous substances, a type of proteins known as opsonins rapidly recognize and mark these foreign materials, facilitating their uptake and clearance by macrophages. Because of their nanoscale dimensions and surface properties, most NPs readily activate the RES, which can significantly limit their ability to reach their intended site of action.[133] As mentioned, the behavior of NPs in biological media is highly influenced by their physicochemical properties, including size, morphology, surface charge, or porosity, among others (Figure 1.17). Below, we briefly discuss how these properties influence RES recognition and clearance, with a particular focus on gold NPs similar to those we aim to design in this work.

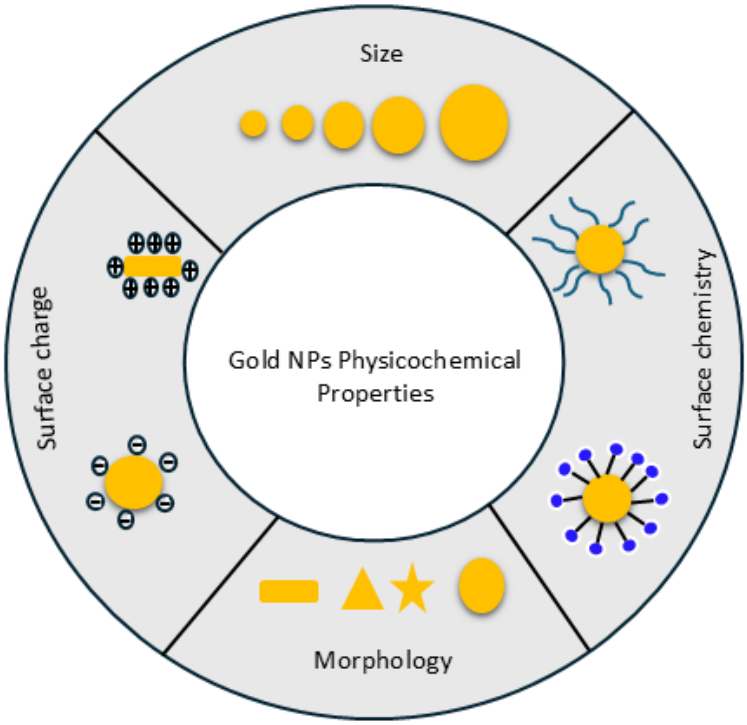

Figure 1.17. Diagram illustrating the key physicochemical properties of gold NPs that most critically influence their interactions with biological systems.

1.7.3.1 Hydrodynamic Size and Morphology

The hydrodynamic size and morphology of NPs critically affect their interaction with biological systems, influencing protein corona formation, immune evasion, cellular internalization pathways, membrane adhesion, or cargo delivery efficiency, among other processes. In a representative study, Yohan *et al.* investigated the influence of hydrodynamic size on the internalization of spherical gold nanostructures by MCF-7 and MDA-MB-231 tumor cell lines, under both monolayer and multilayer culture conditions. In monolayers, 20 nm gold NPs showed lower cellular uptake compared to 50 nm NPs, but this trend reversed in tissue-like cell multilayers, where smaller NPs penetrated more efficiently than larger ones. This behavior was attributed to reduced surface area and receptor interaction in smaller NPs, which require less energy for internalization at the monolayer level.[134]

On the other hand, the effect of NPs morphology on their intracellular uptake has also been extensively evaluated. In a representative work analyzing this influence, it was observed that rod-shaped gold NPs exhibited lower uptake than their spherical counterparts. Specifically,

spherical gold NPs with diameters of 74 nm and 14 nm exhibited 500% and 375% higher uptake, respectively, compared to 74×14 nm AuNRs (Figure 1.18 A).[135] In another study, Xie *et al*. evaluated the internalization of AuNRs, AuNSs, and gold nanotriangles (AuNTs) by RAW 264.7 cells using TEM and ICP-MS. Their results revealed the highest uptake for AuNTs, followed by AuNRs and AuNSs (Figure 1.18 B-E). Interestingly, while all three types of nanostructures were internalized *via* endocytosis, they followed distinct pathways: AuNSs were primarily internalized through clathrin-mediated uptake, AuNRs through both clathrin- and caveolae/lipid raft-mediated endocytosis, and AuNTs through multiple routes, including clathrin-mediated endocytosis and a dynamin-dependent pathways.[136]

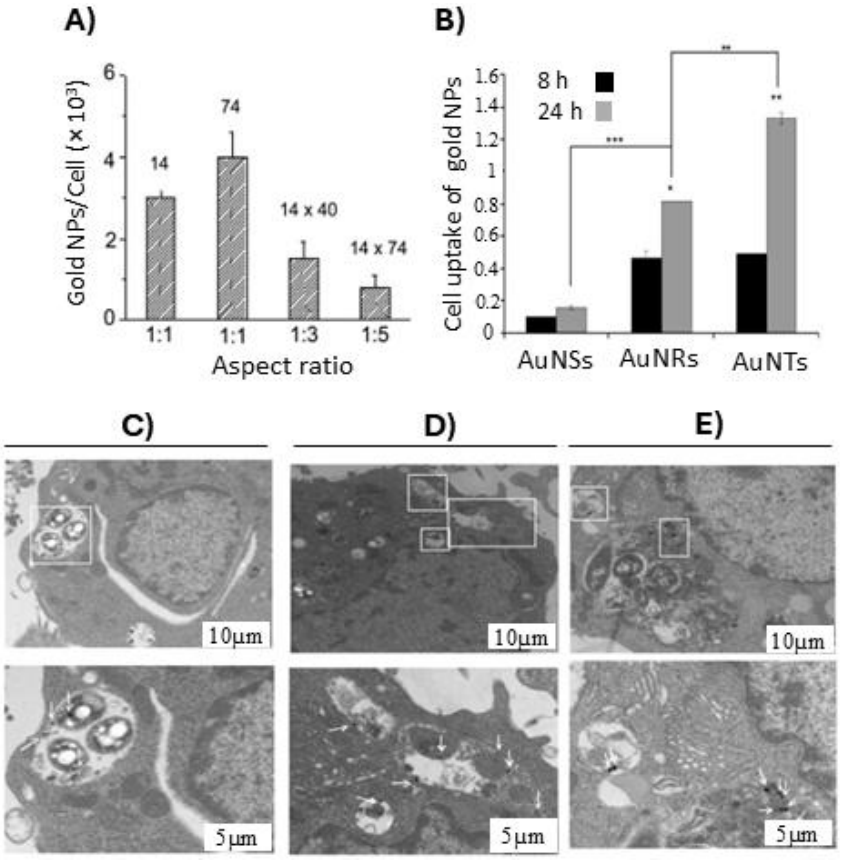

Figure 1.18. A) Comparative cellular uptake study showing greater internalization of spherical gold NPs with 14 and 74 nm in diameter compared to rod-shaped NPs with 14 x 40 and 14 x 74 nm dimensions.[135] B) Time-dependent uptake of gold NPs with different morphologies by RAW 264.7 cells, demonstrating higher internalization degree of AuNTs, followed by AuNRs and AuNSs.[136] TEM images from this last study, showing RAW 264.7 cells incubated with C) AuNSs, D) AuNRs, and E) AuNTs.[136] Under creative commons CC BY-NC 4.0 license.

1.7.3.2 Surface Charge

The surface chemistry of nanostructured materials, particularly their electrical surface charge, plays a crucial role in determining their biological fate by influencing cellular uptake, biodistribution, circulation time, and clearance. Positively charged NPs tend to interact more readily with negatively charged cell membranes, leading to enhanced cellular uptake but also increased cytotoxicity and faster clearance *via* RES (Figure 1.19 A). In contrast, negatively charged NPs typically exhibit lower cellular internalization degrees while showing prolonged circulation times owing to their reduced opsonization and uptake by macrophages. Neutral or zwitterionic NPs generally show minimal protein adsorption, reduced immune recognition, and enhanced stability in biological fluids, positioning them as promising candidates for various biomedical applications. Therefore, optimizing surface charge is essential for tailoring NPs behavior to specific biomedical uses, balancing their efficient cellular interaction with reduced cytotoxicity.[137]

The impact of surface charge on the biological behavior of inorganic NPs has been extensively analyzed. Focusing on the specific case of gold-based nanostructures, several studies evaluated the influence of their coating and, consequently, their surface charge, over their biological fate. For example, it was found that the surface charge of AuNRs significantly influenced the generated immune responses. Specifically, AuNRs coated with negatively charged carboxyl groups promoted the expression of pro-inflammatory proteins, while those coated with positively charged amino groups induced the upregulation of anti-inflammatory markers (Figure 1.19 B-C).[138] These findings highlight the potential for surface modification to modulate immune responses, enabling the design of NPs that selectively enhance or suppress inflammation as needed. Such control over immunomodulation is particularly valuable for developing nanomedicine strategies for inflammatory diseases, autoimmune disorders, and targeted drug delivery systems.

In vivo studies further emphasize the key role of surface charge on the biological fate of nanostructured materials. A comprehensive study involving lipid-based NPs intravenously injected into mice revealed that positively charged NPs caused significant liver toxicity, weight loss, and an increased pro-inflammatory response. In contrast, neutral or negatively charged NPs caused fewer adverse effects, underscoring the critical role of surface charge in NPs biodistribution and toxicity in physiological environments.[139]

In conclusion, surface charge is a fundamental factor in the design of nanostructures for biomedical applications. Here, it is important to note that upon dispersion/incubation into extremely complex biological environments, the surface charge of NPs is not static; interactions with biological fluids can cause fluctuations, potentially leading to unforeseen effects and altering NPs performance. Therefore, careful assessment and control of surface charge dynamics are also essential to ensure the desired outcomes in the intended application. [137]

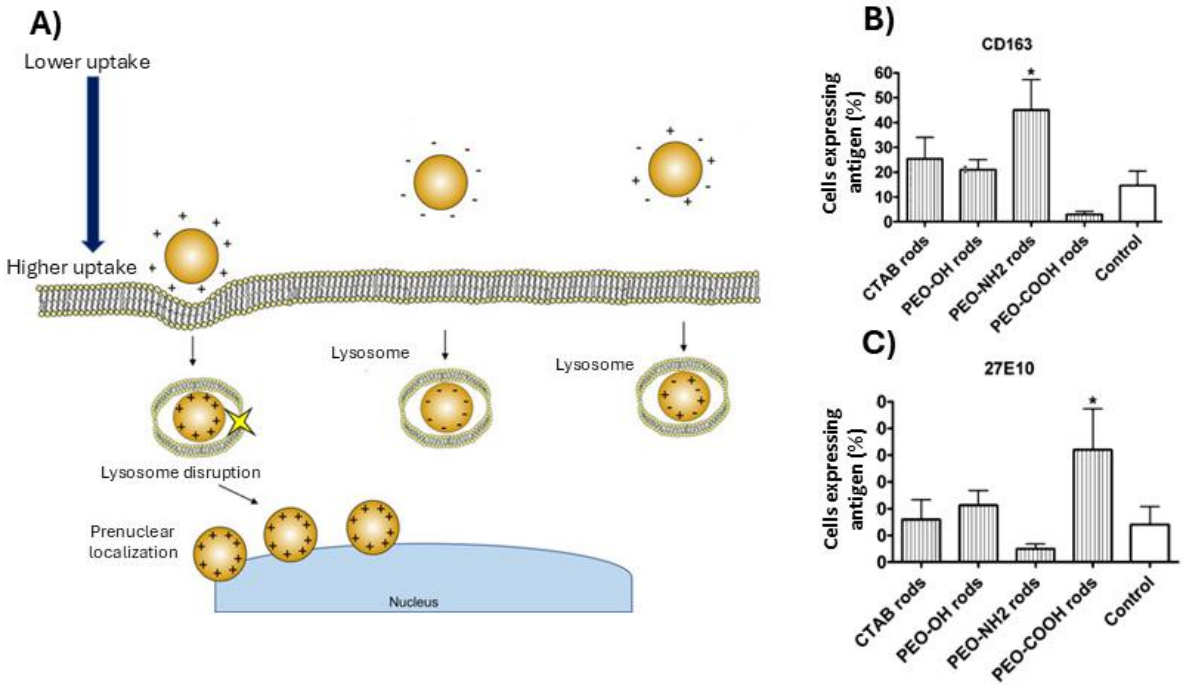

Figure 1.19. A) Schematic representation of the effect of surface charge on the cellular uptake of positively, negatively, and neutrally charged NPs. Expressions of B) CD163, indicative of an anti-inflammatory response, and C) 27E10, associated with a pro-inflammatory phenotype, obtained through the flow cytometry analysis of macrophages after 7 days of incubation with different functionalized AuNRs.[138]

1.7.3.3 Hydrophobicity and Hydrophilicity

The hydrophilic or hydrophobic nature of NPs, largely governed by their surface chemistry and charge discussed above, strongly dictates their biological fate. Hydrophilic NPs, commonly modified with polymers such as PEG, are known to exhibit enhanced colloidal stability, prolonged systemic circulation, and reduced immune recognition, making them ideal for

applications such as systemic drug delivery. Conversely, hydrophobic NPs often display increased cellular uptake due to stronger interactions with lipid membranes, but they are more prone to rapid clearance by the immune system because of their reduced colloidal stability. Despite this apparent limitation for biomedical purposes, hydrophobic NPs offer advantages for specific applications, such as the delivery of water-insoluble therapeutic compounds. For instance, succinobucol, a water-insoluble inhibitor of vascular cell adhesion molecule, was effectively encapsulated in triblock polymer NPs *via* intermolecular hydrophobic interactions, facilitating its controlled release.[140]

The interplay between hydrophobicity and biological performance was further illustrated in a study on glutathione-coated luminescent gold NPs. Functionalizing these NPs with hydrophobic octanethiol dramatically enhanced their membrane affinity and accelerated cellular uptake by over an order of magnitude. [141] These findings underscore the importance of carefully tuning NP surface properties to balance biological compatibility and functional performance in biomedical applications.[142]

1.8 Biomedical Applications of Inorganic Nanostructures: A Focus on Anisotropic Gold NPs

The biomedical use of inorganic NPs has garnered significant attention in recent decades due to the unique physicochemical properties that emerge from their nanoscale dimensions. These characteristics have enabled their application across a wide range of biomedical fields, ranging from bioimaging and biosensing to hyperthermia treatments and targeted drug delivery, among others. For example, various types of nanosystems, including quantum dots, iron oxide, or gold NPs have been widely proposed to enhance bioimaging contrast in modalities such as MRI, computed tomography or fluorescence microscopy. These NPs can also be exploited for biosensing applications, enabling highly sensitive biomarker detection for disease diagnostics by leveraging their optical, plasmonic, or electrochemical properties.

In addition, certain inorganic nanomaterials, including silver and copper oxide NPs, exhibit strong antimicrobial activity, facilitating their use in application like infection control or wound healing. Other nanomaterials, such as gold NPs or carbon nanotubes, have been demonstrated as efficient nanotools for photothermal (PTT) and photodynamic therapies (PDT), enabling localized tumor ablation or ROS generation upon light irradiation.

Among all the inorganic nanostructures mentioned, gold NPs, particularly those with anisotropic morphologies, stand out due to their tunable LSPR within the biological window, which significantly enhances their performance for bioimaging, therapeutic, or biosensing purposes (Figure 1.20). This section discusses the specific advantages of anisotropic gold NPs in the most relevant applications in which they have been proposed as potential nanotools.[17,143]

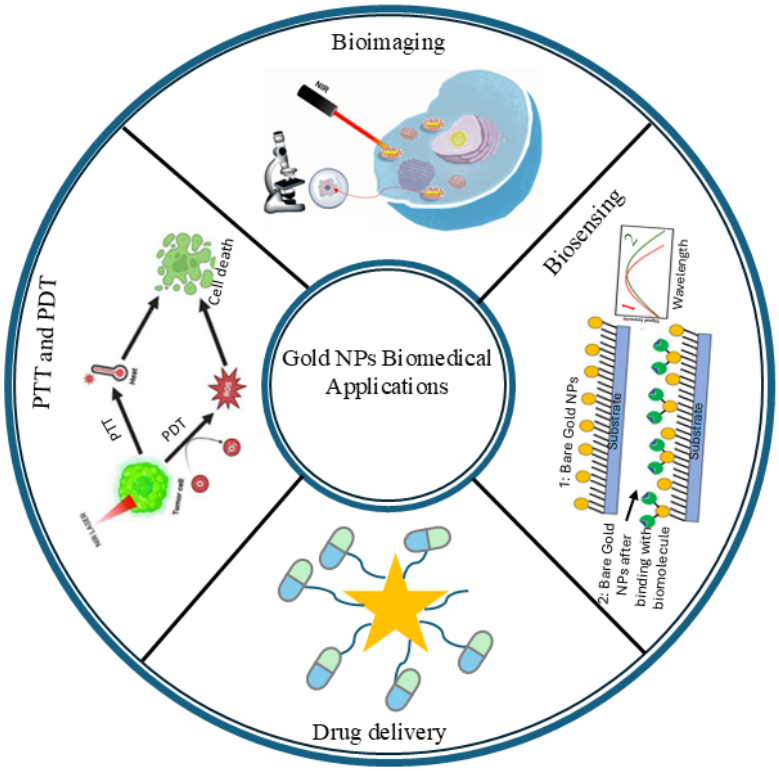

Figure 1.20. Graphical representation of the main biomedical applications of anisotropic gold NPs, including bioimaging, targeted drug delivery, biosensing, PTT and PDT.[144,145] Under creative commons CC BY-NC 4.0 license.

1.8.1 Bioimaging and Diagnostics

The unique physicochemical properties of various types of inorganic NPs, particularly their high sensitivity and responsiveness to external stimuli, have been leveraged for their use as contrast agents in a broad range of bioimaging applications. For example, gadolinium-based or magnetic NPs have been extensively proposed as contrast agents in MRI, enabling enhanced visualization of target tissues and facilitating the early detection of various diseases.

These diagnostic capabilities can be integrated with therapeutic functionalities, such as the magnetothermal properties in the case of magnetic NPs, to engineer nanoplatforms with theranostic potential. Similarly, quantum dots have been used to enhance the contrast in fluorescence bioimaging owing to their excellent photostability and tunable emission profiles, which allow multiplexed imaging and long-term tracking. Functionalization with targeting ligands allows quantum dots to selectively bind to diseased tissues, making them valuable nanotools for cancer detection. Furthermore, they can be loaded with therapeutic cargos, also positioning quantum dots as promising candidates for integrated diagnostic and therapeutic applications.[146–149]

Moving to gold NPs, which are the primary focus of this work, these are undoubtedly among the most commonly evaluated for bioimaging purposes because of their above discussed exceptional biocompatibility, chemical stability, and highly tunable optical properties. These attributes, combined with ease of synthesis and functionalization, have made gold NPs highly attractive for theranostic applications in biomedicine. Specifically, the LSPR properties of gold nanostructures, governed by their size, shape, and morphology, enable fine-tuning of their light absorption and scattering behavior, facilitating their integration into a variety of bioimaging modalities.

Firstly, we can find several bioimaging techniques that exploit the scattering properties of gold NPs driven by their LSPR response. In some cases, gold nanostructures can exhibit scattering intensities up to 10^5 times higher than traditional fluorophores such as fluorescein.[150] Dark field confocal imaging (DFCI) and optical coherence tomography (OCT) are two prominent examples that capitalize on this property. Gold NPs have been widely used as DFCI probes for imaging a variety of intracellular biological events, including DNA damage, viral infection, cell division, and endocytosis, offering high-resolution, label-free contrast. On the other hand, OCT is an interferometric bioimaging technique that uses low-coherence NIR light to illuminate samples, benefits significantly from gold NPs-enhanced backscattering.[150] Gold nanostructures of various sizes and shapes, including AuNRs, AuNSs, nanoprisms, and nanodisks, have been thoroughly studied as OCT contrast agents. Among these, AuNRs are especially promising due to their easily tunable optical response, which can be precisely adjusted *via* their aspect ratio. A representative study demonstrated that large AuNRs (100x30 nm) generated OCT signals 32 times stronger than smaller counterparts (50x15 nm) (Figure

1.21 A-B), enabling enhanced imaging of tumor vasculature *in vivo* at previously inaccessible depths.[151,152]

Other LSPR-dependent bioimaging modalities leverage the absorption of light by gold nanostructures, particularly in photothermal (PT) and photoacoustic (PA) imaging. Upon light absorption, gold NPs convert photon energy into heat, leading to changes in the refractive index (detected in PT imaging) or thermoelastic expansion (producing acoustic waves detected in PA imaging). In these modalities, the gold NPs used imaging nanotools are typically significantly smaller than those employed in previously discussed scattering-based techniques.[150] For example, the potential of AuNSs as contrast agents for visualizing lymphatic systems *in vivo* through PA bioimaging was thoroughly analyzed in a recent study. Following intradermal injection into rat footpads, spectroscopic PA tomography enabled real-time tracking of the NPs biodistribution in lymphatic vessels. The results demonstrated that the designed gold nanostructures produce strong PA signals, with a detection limit of 1 ppm that enables an extremely high-resolution visualization of lymphatic structures (Figure 1.21 C-E).[153]

On the other hand, SERS-based imaging with gold NPs is a highly sensitive and powerful technique for biomedical diagnostics. Although SERS is widely known for its role in biosensing, that will be discussed later, its application for *in vivo* imaging has positioned it as a powerful modality within the broader field of bioimaging. When combined with gold NPs, SERS enables highly sensitive, high-resolution visualization of biological tissues and molecular features due to the strong local electromagnetic field enhancement driven by LSPR. Gold nanostructures serve as efficient SERS enhancers owing to their tunable morphology and plasmonic properties, which amplify Raman signals from surface-bound or nearby molecules. In bioimaging applications, these nanostructures are often designed to carry Raman reporters and engineered for stability and biocompatibility, enabling detailed, non-invasive mapping of pathological tissues.[150]

A landmark study published by Harmsen *et al.* demonstrated the utility of SERS-active AuNSs, featuring star-shaped gold cores, silica coatings, and NIR Raman reporters, for the real-time visualization of tumors *in vivo*. These NPs enabled accurate delineation of tumor margins, identification of microscopic invasion, and detection of regional tumors spread in multiple cancer models (pancreatic, breast, prostate, and sarcoma). Notably, their high Raman signal intensity yielded a detection sensitivity as low as 1.5 femtomolar, allowing the identification

of both malignant and premalignant lesions without requiring active targeting ligands. This capability underscores the bioimaging potential of SERS-gold NPs in applications such as image-guided surgery and early cancer diagnostics, particularly given their biocompatible gold-silica composition and broad tissue penetration in the NIR range.[154]

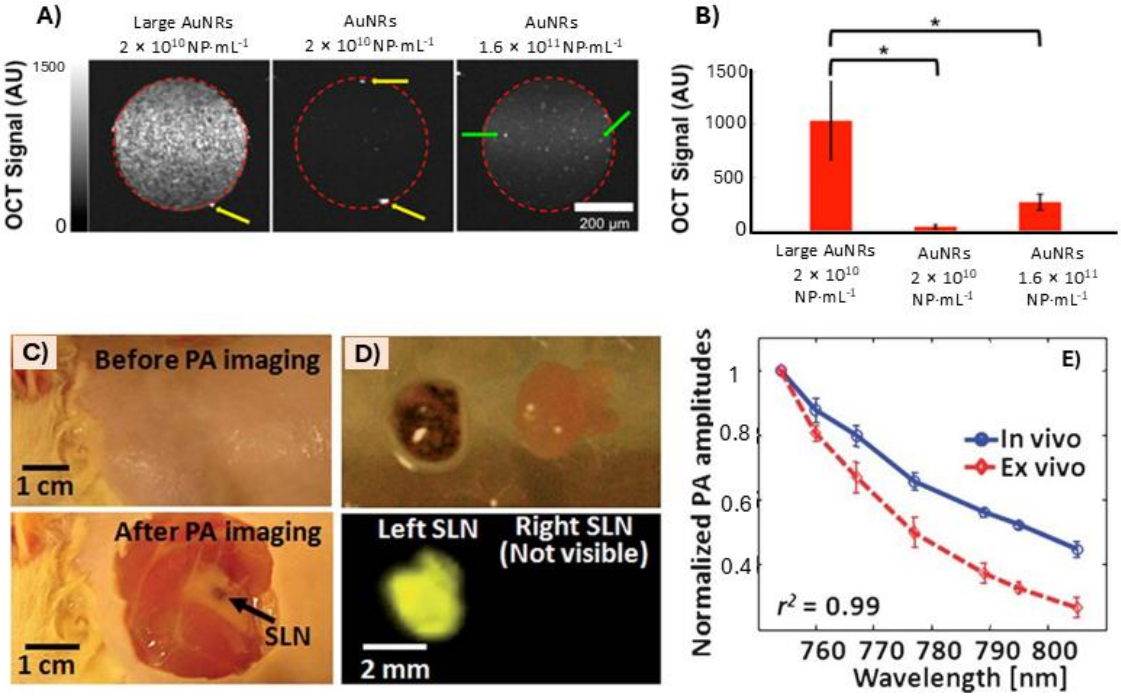

Figure 1.21. Representative example of the use of gold NPs for bioimaging: A) OCT signal intensity comparison between large AuNRs (100×30 nm) and two concentrations of small AuNRs (50×15 nm). B) Quantitative OCT analysis illustrating the enhanced scattering signal of large AuNRs relative to small AuNRs at both concentrations. C) *In vivo* PA imaging of the rat axillary region before (top) and after (bottom) AuNSs injection, showing selective accumulation in the sentinel lymph node (SLN). D) Photograph (top) and corresponding *ex vivo* PA image (bottom) of left and right SLNs, revealing a stronger PA signal on the side proximal to the injection site. E) Spectroscopic PA signal quantification *in vivo* and *ex vivo* within the SLNs, demonstrating robust AuNSs accumulation and signal retention.[152,153]

1.8.2 Biosensing

Inorganic nanostructures have emerged as versatile platforms for advanced biosensing across a broad spectrum of applications, ranging from medical diagnostics to environmental

monitoring and food safety.[150] The above discussed unique physicochemical properties, such as high surface-to-volume ratio, tunable optical behavior, and multifunctionality, enable sensitive, selective, and often multiplexed detection of biological targets. Among these, plasmonic nanomaterials, particularly gold and silver NPs, have shown exceptional promise due to their ability to enhance signal transduction in techniques such as SERS- and LSPR-based biosensors. On the other hand, quantum dots, with their high photostability and tunable fluorescence, allow for multiplexed readouts in fluorescence-based assays, while magnetic NPs offer targeted biosensing and sample manipulation through external magnetic fields, simplifying detection in complex biological matrices.[148]

Focusing on the specific case of gold with anisotropic morphologies, numerous studies have thoroughly examined their potential use as high-performance biosensing nanotools. Their shape-dependent optical properties, particularly their tunable LSPR features, enable precise spectral matching for enhanced signal output and facilitate multimodal sensing strategies. For example, AuNSs functionalized with Raman reporters and specific antibodies (anti-PDL1, anti-EGFR) have been designed for *in vivo* detection of breast cancer biomarkers. These AuNSs-based biosensors proved effective for the selective and simultaneous detection of both PD-L1, which is overexpressed in various types of tumors and contributes to immunosuppression, and EGFR, a receptor commonly associated with aggressive tumor growth.[155]

In another representative study, SERS-active AuNRs were utilized to monitor the expression of ICAM-1, a pro-inflammatory biomarker linked to early-stage disease. Murine macrophages were incubated with the SERS probes and then stimulated with lipopolysaccharides, enabling real-time, label-free detection of ICAM-1 expression. Notably, the SERS-based platform achieved biomarker quantification within one hour, significantly reducing the analysis time compared to conventional techniques like ELISA, which typically require 5 h or more. This substantial improvement in temporal resolution underscores the practical advantages of using plasmonic gold nanostructures for rapid biosensing (Figure 1.22 A-B).[156]

Furthermore, the potential of multifunctional biosensing platforms has been demonstrated through the design of silica-coated AuNSs encapsulating methylene blue, a photosensitizer capable of generating singlet oxygen under laser excitation.[157] These NPs were engineered to combine SERS-based molecular detection with photothermal capabilities. Upon light

activation, the system not only enabled molecular profiling of BT549 breast cancer cells *via* Raman signals, but also facilitated ROS generation, inducing significant cytotoxicity.

Together, these examples demonstrate the power of anisotropic gold nanostructures to enhance sensitivity, specificity, and functionality in biosensing, providing an essential bridge between fundamental nanoscience and translational biomedical applications.

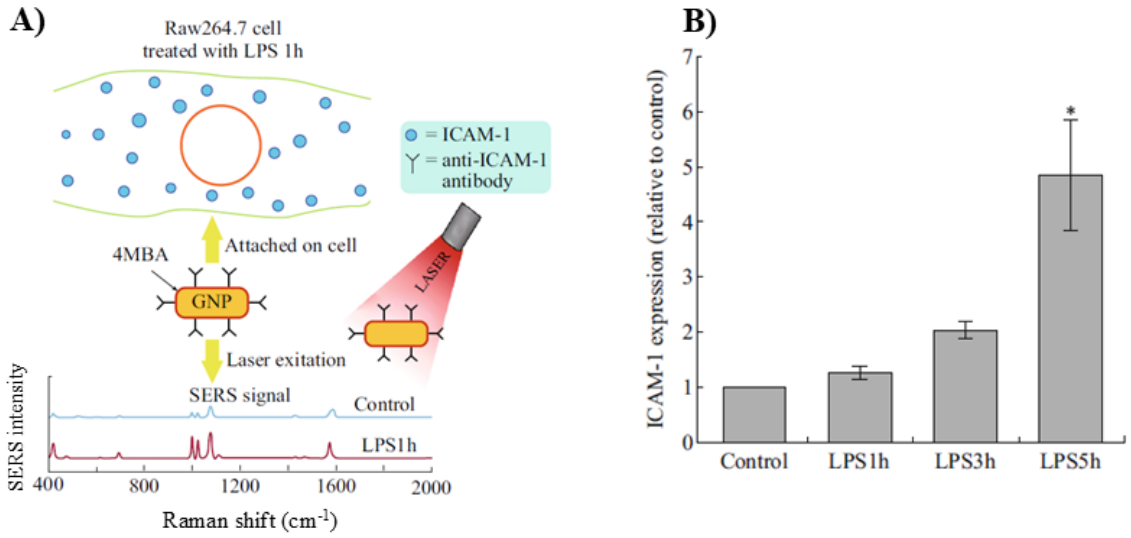

Figure 1.22. Representative example of the use of gold NPs for biosensing applications: A) schematic illustration of AuNRs-based SERS probes to identify adhesion molecules present on the surface of RAW 264.7 macrophages, and B) quantification of ICAM-1 expression levels in cells following stimulation with lipopolysaccharide for 1, 3, and 5 h, compared to untreated control cells.[156] Under Creative Commons CC BY-NC 4.0 license.

1.8.3 Drug Delivery

The high surface-to-volume ratio and structural versatility of inorganic NPs make them excellent candidates for drug delivery applications. Their architecture can often be tailored to include porous or hollow domains, enabling the encapsulation or adsorption of large amounts of bioactive molecules. Furthermore, these nanosystems can typically be easily functionalized to target specific regions of interest, and the stimuli-responsive properties of several inorganic NPs allow controlled or on-demand drug release in response to external or internal triggers.

A wide variety of inorganic nanostructures have been investigated for such applications, including mesoporous silica NPs, gold nanostructures, and iron oxide-based NPs. These

materials have been shown to protect loaded drugs from premature degradation, prolong circulation time, and enable precise release in response to triggers such as temperature, pH, light, or magnetic fields. Among them, mesoporous silica NPs are particularly attractive for drug delivery due to their high surface area, well-defined pore networks, and tunable pore size. These characteristics allow for the loading of a broad range of therapeutic agents, from small-molecule drugs to macromolecules like proteins and nucleic acids. For example, pore size can be optimized depending on the therapeutic cargo: while anticancer agents such as doxorubicin (DOX) can be effectively loaded into small-pore silica NPs, larger biomacromolecules require expanded pore architectures.[158] The key role of pore size of mesoporous NPs in drug delivery applications was well established by Vallet-Regí *et al.*, who effectively controlled the loading capability and kinetic release of ibuprofen in the designed silica nanostructures by adjusting the pore dimensions.[159] Beyond physical entrapment, mesoporous silica NPs also offer a chemically modifiable surface rich in silanol groups, which can be functionalized with targeting ligands or stimuli-responsive gatekeepers. This allows for site-specific delivery and triggered cargo release under physiological cues such as acidic tumor microenvironments or enzymatic activity.[158]

In contrast, the advantage of gold-based NPs for this specific application lies in their photothermal properties, which can be harnessed for light-triggered drug release. Upon NIR light irradiation, gold nanostructures, especially anisotropic forms like AuNRs, generate localized heating through LSPR, disrupting drug-NPs interactions or deforming the nanocarrier matrix to induce release. This light-mediated control allows for spatial and temporal precision in therapeutic delivery, making gold NPs attractive tools in on-demand nanomedicine.

A particularly innovative strategy combines the strengths of both material types by integrating AuNRs into silica nanocomposites. In one representative study, mesoporous silica shells were grown around AuNRs cores, creating a hybrid nanoplatform capable of high drug loading and photothermally activated release. The chemotherapeutic agent methotrexate (MTX) was successfully loaded into the silica pores, and NIR irradiation of the nanostructures enabled simultaneous drug delivery and localized hyperthermia in osteosarcoma cells, leading to significant cytotoxicity (Figure 1.23 A-B).[160] This multifunctional system illustrates the potential of combined photothermal and chemotherapeutic therapies within a single, finely tunable nanoplatform.

Altogether, these findings underscore the potential of inorganic nanostructures as the next-generation drug delivery systems, combining high loading efficiency, controlled release, and therapeutic synergy, thus opening new avenues for personalized and minimally invasive medicine.

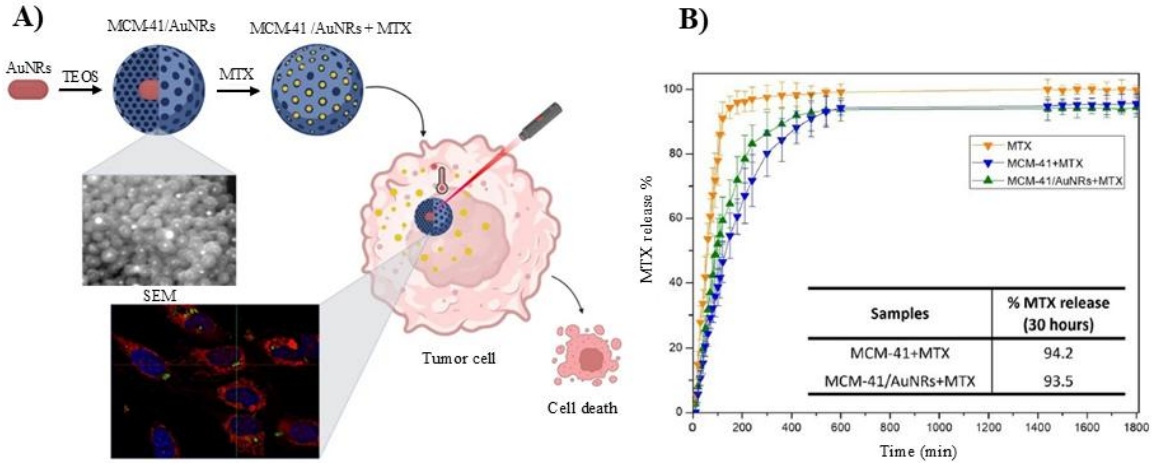

Figure 1.23. Representative example of the use of gold NPs for drug delivery applications: A) schematic illustration of the application of silica-coated AuNRs for the controlled delivery of MTX in cancer treatments. B) MTX release curves and percentage of MTX released over 30 h from the designed gold-based nanoplatforms.[160]

1.8.4 Photodynamic Therapy

Photodynamic therapy (PDT), also known as photochemotherapy, is a minimally invasive therapeutic modality that involves the localized generation of ROS, particularly singlet oxygen, to selectively destroy cancer cells. The therapeutic process is initiated when a photosensitizing agent absorbs light (typically in the visible or NIR region) and subsequently transfers energy to molecular oxygen, producing cytotoxic ROS. These species induce oxidative stress, damaging cellular membranes, proteins, and DNA, ultimately triggering cell death through apoptosis or necrosis.

In this context, inorganic nanostructures, and particularly anisotropic gold NPs, have emerged as promising platforms for enhancing PDT efficacy. Owing to their strong light absorption in the NIR region, excellent biocompatibility, and ease of surface functionalization, gold

nanostructures can serve both as carriers of photosensitizers and as agents that facilitate light-triggered therapy with spatial precision.

In a representative example of this strategy, AuNRs were functionalized with a clinically approved NIR photosensitizer such as indocyanine green. Moreover, hyaluronic acid was incorporated in the formulation of the gold-based nanoplatform as a targeting and stabilizing ligand, promoting the selective uptake of NPs by tumor cells overexpressing CD44 receptors. Upon NIR irradiation, this multifunctional nanosystem achieved ROS generation efficiency up to 80% relative to the positive control, resulting in cell death rates of approximately 70% in HeLa cells after only five min of light exposure.[161]

Remarkably, recent studies have revealed that anisotropic gold nanostructures can also act as intrinsic photosensitizers, eliminating the need for external photoactive molecules. For example, Vankayala *et al.* reported for the first time that folate-PEG-coated AuNRs, even in the absence of additional photosensitizers, were capable of generating substantial levels of singlet oxygen under low-dose LED or laser excitation.[162] These rod-shaped gold NPs simultaneously contributed photothermal and photodynamic effects, culminating in the complete eradication of solid tumors *in vivo*. Mechanistic studies confirmed the ROS generation *via* fluorescence assays, sodium azide quenching, and the upregulation of heat shock proteins, further validating their dual-function therapeutic potential.

Altogether, these findings underscore the significant promise of gold-based nanoplatforms in PDT applications, whether as carriers for conventional photosensitizers or as self-sufficient phototherapeutic agents. Their ability to combine tumor-targeted delivery and deep-tissue light penetration holds great potential for advancing cancer therapy toward more efficient and less invasive clinical interventions.

1.8.5 Photothermal Therapy

Inorganic nanomaterials have garnered considerable attention for photothermal therapy (PTT) due to their distinctive optical properties, high thermal stability, and excellent biocompatibility. Although various types of inorganic nanosystems have been proposed for PTT, gold NPs are by far the most widely explored for this specific application. This strong interest stems from their LSPR properties, which enable highly efficient absorption of NIR light and conversion into heat. Additionally, as described in the discussion of previous biomedical

applications of gold NPs, these can be easily functionalized with targeting ligands to enhance specificity and promote tumor accumulation *via* the EPR effect. Once concentrated in the target area, the generated heat can selectively destroy cancer cells while minimizing damage to surrounding healthy tissues.[41,106,163]

Among the various types of gold NPs, those with anisotropic morphologies, such as AuNRs or AuNSs, are particularly interesting for PTT applications. In these typologies of nanostructures, the LSPR can be finely tuned into the NIR window, allowing for deeper tissue penetration. Additionally, their morphology-dependent optical properties can be leveraged to optimize their interactions with tumor cells, potentially enhancing cellular uptake and retention, and ultimately increasing therapeutic efficacy.[106]

The pioneering study on the use of gold-based nanostructures for PTT was conducted by Halas *et al*. in 2003. Here, gold nanoshells with 10 nm in thickness were grown around silica nanocores, yielding plasmonic NPs with a LSPR band centered at 820 nm. These nanoshells were injected interstitially into the volume of superficial tumors in mice, after which they were irradiated at 4.0 $W \cdot cm^{-2}$ for 4-6 min using a NIR light source. The heat generated due to the photothermal properties of the designed NPs was shown to induce irreversible damage to the treated tumor tissues.[96]

Since this seminal work, numerous studies have explored the use of other typologies of anisotropic gold NPs for *in vivo* PTT, including AuNRs,[164] AuNSs,[165] gold nanoprisms,[166] or gold nanocages,[167] among others. All these plasmonic NPs have shown promising capabilities in targeting and eliminating solid tumors in preclinical models by exploiting their photothermal properties. However, their effective clinical translation still remains limited due to key challenges such as the long-term accumulation of gold nanostructures in the liver and spleen (raising toxicity concerns), or the limited tissue penetration depth of NIR light required for effective photothermal activation.[106]

To overcome these limitations, combining PTT with the previously discussed PDT has emerged as a synergistic strategy to enhance therapeutic outcomes. In a representative study that explored this approach, AuNSs were functionalized with calcium carbonate and ICG. At an acidic pH value of 6.4, typical of tumor environments, the calcium carbonate layers degrade, leading to the release of the photosensitizing agent. The performed *in vitro* and *in vivo* studies

demonstrated that the PDT activity of ICG, in combination with the heat generated upon laser irradiation of the gold nanoplatforms, resulted in a strong anticancer efficacy (Figure 1.24). Interestingly, the above discussed capability of gold NPs to enhance contrast in various bioimaging techniques facilitated the study of the biodistribution within the tumor using fluorescence microscopy.[168]

Following PTT or combined PTT/PDT treatments, tumor cell death may occur through various mechanisms, including apoptosis, necrosis, or thermal ablation. This last involves the exposure of cells to extremely elevated temperatures (55-100 °C), which destroys tissue integrity. Necrosis can result from moderate heating (40-50 °C), causing membrane rupture and potentially promoting inflammation and tumor recurrence. In contrast, mild hyperthermia (*ca*. 40 °C) can trigger apoptosis, a regulated form of cell death that also stimulates antitumor immune responses through phagocytosis. Therefore, optimizing PTT conditions to favor apoptosis over necrosis or ablation is key to improving therapeutic selectivity and immune modulation.[106]

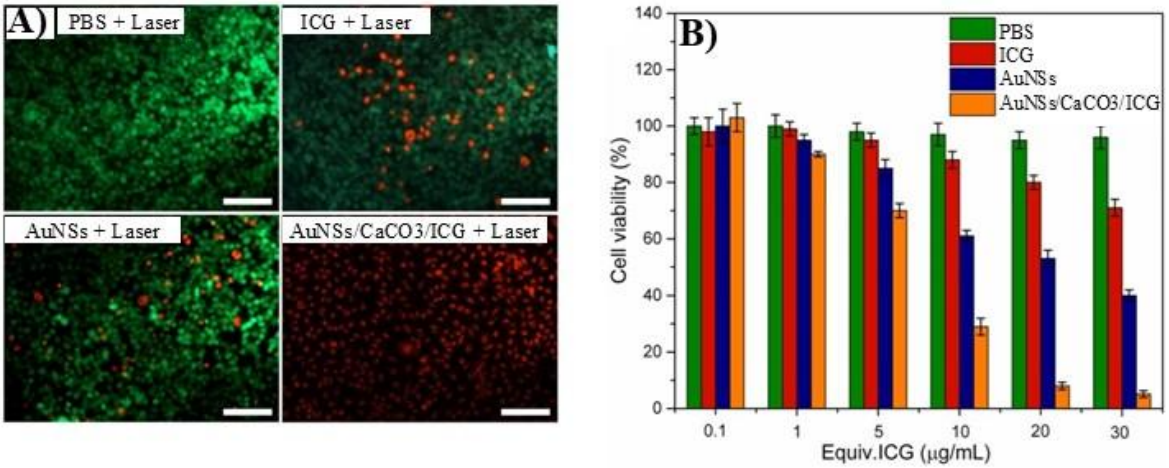

Figure 1.24. Representative example of the use of gold NPs for PDT/PTT applications: A) live/dead staining and B) graphical representation of the viability of MGC-803 cells after 24 h incubation with different concentrations of free ICG, AuNSs, and AuNSs coated with calcium carbonate loaded with ICG, followed by laser irradiation.[168] Under creative commons CC BY-NC 4.0.

1.9 Objectives

1.9.1 General Objective

The primary aim of this thesis is to investigate the photothermal potential of two types of anisotropic gold nanostructures—AuNSs and AuNRs—as candidates for PTT. Specifically, the study evaluates their behavior under various illumination conditions within the NIR-I region, with a particular focus on how surface functionalization with PEG terminated with methoxy, amine, or carboxylic groups affects their photothermal performance and biological interactions. Special emphasis is placed on understanding the biological fate of gold NPs, including cellular uptake, cytotoxicity, and the mechanisms of cell death induced by photothermal treatment.

In addition, this work analyzes how plasmon-induced hyperthermia modulates the composition of the protein corona formed surrounding AuNRs and AuNSs, an essential factor that determines the biological identity and therapeutic performance of the nanostructures. The study considers multiple parameters affecting photothermal efficiency, protein corona formation and composition, and cellular responses. These include the laser type (continuous *vs*. pulsed), irradiation conditions (power density, exposure time), NPs concentration and surface chemistry, and cell phenotype.

1.9.2 Specific Objectives

- **Synthesis and Characterization of NPs**
  - To synthesize anisotropic AuNSs and AuNRs and functionalize the NPs with PEG chains bearing terminal methoxy, amine, or carboxylic acid groups.
  - To characterize their physicochemical properties using appropriate techniques such as UV-Vis-NIR spectroscopy, TEM, or DLS.
- **Evaluation of Colloidal Stability**
  - To analyze the colloidal stability of PEG-functionalized AuNSs and AuNRs in different biological relevant media, including buffer solutions, high-salt environments, cell culture media, and protein-rich biological fluids.
  - To assess how different PEG coatings influence NPs dispersion and aggregation across incubation media.

- **Photothermal Performance Analysis in the NIR-I Window**
  - To quantify and compare the photothermal response (temperature increase) induced by AuNSs and AuNRs under NIR-I laser irradiation.
  - To evaluate the influence of key illumination parameters, such laser type (continuous *vs*. pulsed), power density, or irradiation time, on photothermal conversion efficiency.
  - To determine optimal NPs concentrations and irradiation conditions for achieving controlled and effective photothermal effects for therapeutic use.
- **Assessment of Biological Fate and Cellular Response**
  - To investigate the cellular uptake of AuNSs and AuNRs in different cell lines, evaluating the effect of morphology and surface functionalization on internalization.
  - To assess the impact of photothermal treatment on cell viability, considering different irradiation conditions and NPs doses.
  - To elucidate the predominant cell death pathways (apoptosis *vs*. necrosis) triggered by PTT using AuNSs and AuNRs, and to correlate them with NPs type and photothermal profile.
- **Analysis of Hyperthermia-Induced Changes in Protein Corona**
  - To characterize the protein corona formed on AuNSs and AuNRs before and after laser-induced heating, assessing hyperthermia-driven alterations in protein composition.
  - To study the role of PEG terminal chemistry in modulating protein binding and corona stability under photothermal conditions.

2. Materials and Methods

2.1 Materials for Synthesis and Characterization of Gold NPs

Cetyltrimethylammonium bromide (CTAB, biology grade), silver nitrate, tetrachloroauric (III) acid trihydrate, sodium borohydride, ascorbic acid, poly(sodium 4-styrenesulfonate) (PSS, molecular weight 70000 $g \cdot mol^{-1}$), and methanol were purchased from Sigma Aldrich (St. Louis, MO, USA). Polyvinylpyrrolidone K15 (PVP, molecular weight 10000 $g \cdot mol^{-1}$) and N, N-dimethylformamide (DMF) were obtained from Fluka (St. Louis, MO, USA). Heterobifunctional PEG thiol derivatives (mPEG-SH, NH_2-PEG-SH and CM-PEG-SH) were supplied by Laysan Bio Inc. (Arab, AL, USA). Absolute ethanol was obtained from Scharlau (Barcelona, Spain). Milli-Q water was used in all aqueous preparations. All reagents were of analytical grade and used without further purification.

2.2 Materials for Biological Studies

Mouse embryo fibroblasts (Balb/c 3T3) and MDA-MB- 231 human breast cancer cells used for *in vitro* studies were obtained from Sigma Aldrich (St. Louis, MO, USA). Bovine serum albumin (BSA), bovine fibrinogen (FIB), phosphate buffer saline (PBS), Triton™ X-100, and doxorubicin hydrochloride (DOXO) were also supplied by Sigma Aldrich. Dulbecco´s Modified Eagle Medium (DMEM), non-essential amino acids (NEAA), L-glutamine, sodium pyruvate, penicillin-streptomycin, and Trypsin-EDTA were purchased from ThermoFisher Scientific (Waltham, MA, USA). Fluorescent dyes 4',6-diamidino-2-phenylindole (DAPI, with ProLong Gold antifade reagent) and Alexa Fluor™ Phaloidin 647 were acquired from Invitrogen (USA). The Annexin V Cell Death Detection Kit and the CCK-8 Cell Counting Kit were provided by Dojindo (Kumamoto, Japan).

2.3 Synthesis and Functionalization of AuNRs

2.3.1 Preparation of AuNRs Seeds

A 0.2 M CTAB solution was prepared one day prior to synthesis to ensure complete solubilization. For the synthesis of seed NPs, 7.5 mL of this CTAB solution was gently mixed with 0.25 mL of 0.01 M $HAuCl_4$ in a water bath at 28 °C to prevent CTAB crystallization. Afterwards, an ice-cold 0.01 M $NaBH_4$ solution was freshly prepared and stored in the refrigerator for 3 min. Subsequently, 0.6 mL of this $NaBH_4$ solution was rapidly

injected into the $HAuCl_4$-CTAB mixture under vigorous magnetic stirring and kept for 2 min. The resulting yellow-brown solution was allowed to stand for 1.5 h to enable the decomposition of excess $NaBH_4$ (Figure 2.1).

2.3.2 Seed-Mediated Growth of AuNRs

AuNRs were synthesized *via* a seed-mediated growth method based on previously reported protocol with minor modifications.[163] Briefly, 850 µL of 0.01 M $HAuCL_4$ was added to 20 mL of 0.2 M CTAB in a water bath at 28 °C. The solution was gently stirred until a bright yellow color appeared. Subsequently, 246 µL of a freshly prepared 0.01 M $AgNO_3$ solution (protected from light) was added under stirring at 500 rpm. Next, 136 µL of 0.1 M ascorbic acid was added all in one, and the mixture was stirred at 500 rpm for an additional 4 min, resulting in a colorless solution. Finally, 220 µL of the gold seeds solution was added under continuous stirring for 2 min. The mixture was incubated in a 28°C water bath for 12 h, during which it acquired a reddish-pink color, indicating the successful formation of AuNRs (Figure 2.1). The synthesized AuNRs were purified by centrifugation at 14800 rpm for 30 min at 28 °C to remove excess of CTAB followed by resuspension in Milli-Q water. The centrifugation step was repeated to eliminate residual surfactant, and the final pellet was redispersed in 20 mL of Milli-Q water.

2.3.3 PSS Coating of AuNRs

To functionalize AuNRs to enhance their colloidal stability and enable subsequent analysis of their photothermal properties (laser irradiation), a 10 $mg \cdot mL^{-1}$ PSS solution was prepared in 12 mM NaCl. Once fully dissolved, 10 mL of this PSS solution was mixed with 10 mL of 12 mM NaCl and stirred at 450 rpm. Subsequently, 10 mL of AuNRs dispersion (OD ≈ 1) was added dropwise. After 1 h of PSS adsorption onto AuNRs, the mixture was centrifuged twice at 15000 rpm for 25 min each, and the resulting pellet was resuspended in Milli-Q water.

2.3.4 AuNRs PEGylation

To replace CTAB and improve their biocompatibility, the AuNRs were functionalized with thiol-terminated PEG molecules of 5 kDa molecular weight, including mPEG-SH, NH_2-PEG-SH and CM-PEG-SH. A total of 14130 PEG chains per particle (equivalent to 10 chains per nm^2) was used, based on the approximation of AuNRs as cylinders with dimensions of 40 nm in length and 10 nm in diameter.[169] PEGylation was performed in a two-step process. Initially, an

appropriate volume of a 10 mg·mL^{-1} PEG solution was added to a dispersion of AuNRs at concentration of 1.0 x 10^{12} NP·mL^{-1}, and the mixture was stirred overnight. The PEGylated AuNRs were then centrifuged at 14000 rpm and redispersed in 90% ethanol to remove residual CTAB. In the second step, the same volume of PEG solution was added to the ethanol-redispersed AuNRs and stirred for an additional 5 h.[169] Finally, the AuNRs were thoroughly washed, redispersed in sterilized distilled water, and stored at 4°C for further use.

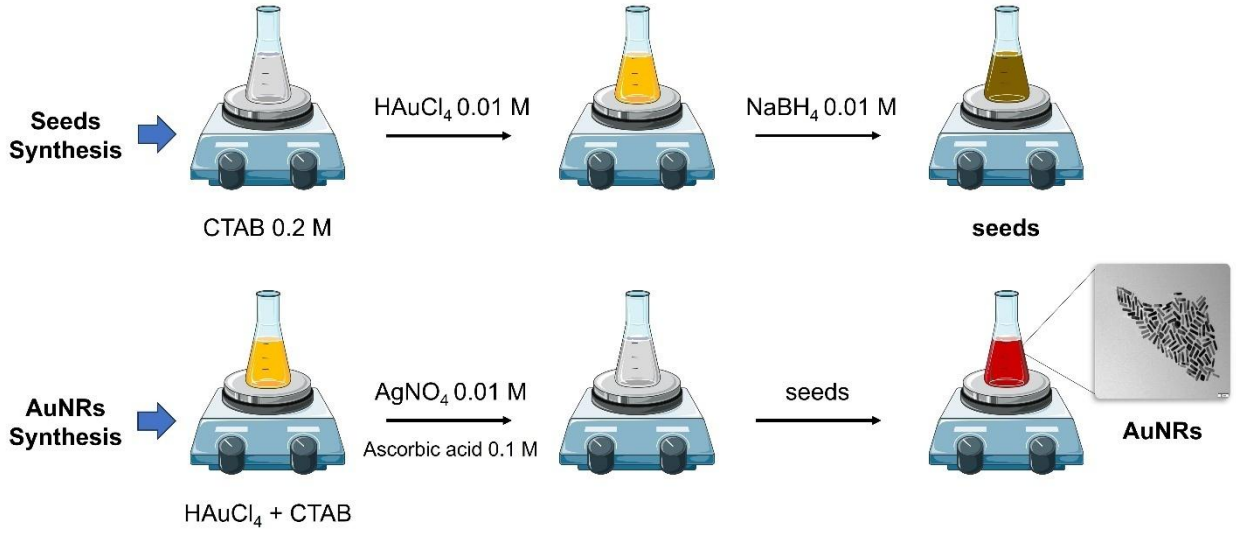

Figure 2.1. Schematic illustration of AuNRs synthesis *via* a seed-mediated growth method, including seed preparation and growth in a solution containing $AgNO_3$ and ascorbic acid.

2.4 Synthesis and Functionalization of AuNSs

2.4.1 Preparation of AuNSs Seeds

Gold seeds for the synthesis of AuNSs were prepared using a classical citrate reduction protocol, as previously described.[170] In brief, 100 mL of 50 mM $HAuCl_4$ was heated under continuous stirring. Once bubbles appeared near boiling, 5 mL of a 1% (w/v) sodium citrate solution was rapidly added, and the reaction was maintained for 15 min, allowing the formation of the seeds. Subsequently, 5 mL of an aqueous PVP solution—corresponding to a surface coverage of 60 PVP molecules per nm² of gold NPs surface—was added dropwise, and the mixture was left to react overnight (Figure 2.2). Finally, the solution containing gold seeds was centrifuged at 4000 rpm for 90 min, and the collected NPs were redispersed in ethanol.

2.4.2 Seed-Mediated Growth of AuNSs

AuNSs were synthesized *via* a seed-mediated growth method based on a previously reported procedure. [171] First, PVP was dissolved in water at a concentration of 10 mM and sonicated for 30 min. Then, 546 µL of 50 mM $HAuCl_4$ was added to 100 mL of this PVP solution under continuous stirring at room temperature. After 8 min (an optimized time to allow reduction of Au^{3+} to Au^{+}), 73 µL of the previously prepared gold seeds dispersion was added (Figure 2.2). After 24 h reaction, the resulting PVP-functionalized AuNSs were washed through three centrifugation cycles at 6000 rpm for 12 min each.

2.4.3 AuNSs PEGylation

Surface modification of PVP-stabilized AuNSs was performed using the same three types of PEG derivatives employed for the functionalization of AuNRs. A total of 530660 PEG chains per particle, equivalent to 10 PEG chains per nm^2, was used to ensure full surface coverage.[169] This calculation was based on the approximation of considering the designed AuNSs as nanospheres with a diameter of 132 nm, yielding a surface area of 53066 nm^2. PEGylation was carried out in a two-step procedure. First, a defined volume of a 10 $mg \cdot mL^{-1}$ PEG solution was added to a dispersion of AuNSs at 1.50 x 10^9 $NP \cdot mL^{-1}$ and stirred overnight. The PEGylated AuNSs were then centrifuged at 6000 rpm and redispersed in water. In the second step, the same volume of PEG solution was re-added to the AuNSs dispersion and stirred for an additional 5 h. Finally, the AuNSs were washed thoroughly, resuspended in sterile distilled water, and stored at 4 °C for further use.

2.5 Physicochemical Characterization of Anisotropic Gold NPs

2.5.1 UV-Vis Spectroscopy

The optical properties of gold NPs were analyzed using a Cary Bio 100 UV-Vis spectrophotometer (Agilent Technologies, USA). Measurements were performed with 1 cm quartz cuvettes using 2 mL of NPs. For each measurement, NPs dispersions were added to a 2 mL cuvette, and spectra were recorded over the 400-900 nm range. Each sample was measured in triplicate to confirm stability, and the average spectrum was used for analysis. All measurements were repeated three times to ensure nanoparticle stability, and the results were averaged to obtain the final spectrum.

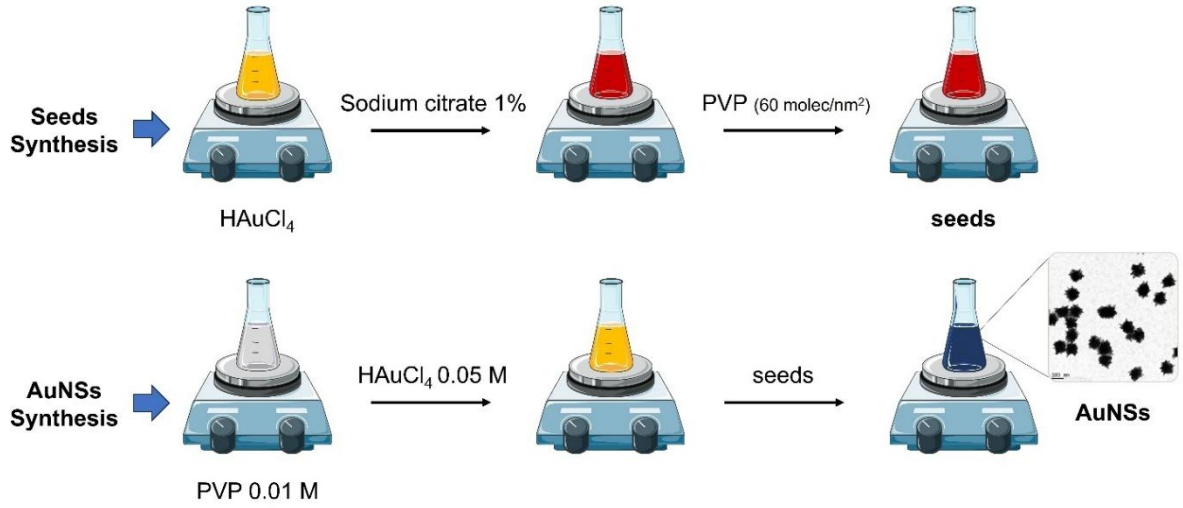

Figure 2.2. Schematic illustration of AuNSs synthesis *via* a seed-mediated growth protocol, including citrate seed preparation and PVP-mediated growth.

2.5.2 DLS Characterization

Hydrodynamic dimensions and polydispersity index of AuNRs and AuNSs were determined using a ZetaSizer Nano ZS (Malvern Instruments, UK). Measurements were carried out at 25 °C using a 532 nm laser source and a scattering angle of 90°. Diluted gold NPs dispersions were analyzed with a 120 s acquisition time per measurement. All experiments were performed in triplicate, and the mean values were reported.

2.5.3 Zeta Potential Measurement

Zeta potential measurements were also conducted using the Zetasizer Nano ZS (Malvern Instruments, UK), equipped with a 633 nm He-Ne laser. The samples were equilibrated at 25 °C prior to analysis and measured in disposable zeta cells. The electrophoretic mobility was converted to zeta potential using the Smoluchowski approximation. Results were expressed in millivolts (mV) and averaged from three independent measurements.

2.5.4 ICP-MS Characterization

Gold content in AuNRs and AuNSs dispersions was quantified by ICP-MS using a Varian 820-MS equipment (Agilent Technologies, USA). For digestion, 1 mL of gold NPs dispersion was mixed with 0.3 mL of concentrated HCl (37%) and 0.1 mL of HNO_3 (70%), followed by dilution

with deionized water to a final volume of 2 mL. The gold concentration was determined by comparing emission intensities with a standard calibration curve.

2.5.5 TEM Characterization

The size and morphology of the designed plasmonic NPs were characterized by TEM using a JEOL JEM-2010 microscope (Tokyo, Japan) operating at an acceleration voltage of 120 kV. The samples were prepared by drop-casting 20 µL of NPs dispersion onto a 400-mesh copper grid coated with a 3-4 nm amorphous carbon film, followed by air-drying at room temperature.

2.6 Stability and pH Responsiveness of PEGylated AuNRs and AuNSs

The colloidal stability of AuNRs and AuNSs functionalized with the three different types of PEG derivatives was assessed over six days under various physiological and challenging conditions. DLS and UV-Vis spectroscopy were employed to monitor changes in hydrodynamic diameter and LSPR, respectively. Stability was evaluated in the following media: Milli-Q water, PBS buffer (pH 7.4), acetate buffer (pH 5.5), NaCl solutions (0.01, 0.05, 0.10 and 0.20 M), FBS (at 10%, 50%, and 100%), and DMEM cell culture medium supplemented with 10% (v/v) FBS. The samples were incubated at 37 °C and analyzed at predetermined time points (0, 1, 3, and 6 days) to assess stability *via* LSPR peak shifts and hydrodynamic size distribution changes.

2.7 Laser Irradiation Experiments

2.7.1 Continuous Wave Laser Irradiation

Photothermal experiments were conducted using a continuous wave (CW) fiber-coupled diode laser with an emission wavelength of 808 nm (50 W Oclaro, Inc., San Jose, CA) powered by a Newport 5700-80 laser diode driver (Newport Corporation, Irvine, CA). The laser output was delivered through a 200 µm core optical fiber. Laser power density ($W \cdot cm^{-2}$) received by the samples was calculated by measuring the output power using a power meter and dividing it by the irradiated surface area, which was estimated from a laser spot radius of 0.7 mm (area = 0.38 cm^2).

To investigate the heat generation capability of the designed gold NPs, dispersions of AuNRs (1.50×10^8 - 1.50×10^{11} $NP \cdot mL^{-1}$) and AuNSs (1.50×10^6 - 1.50×10^9 $NP \cdot mL^{-1}$) were prepared in 6 mL volumes and placed in 12-well plates. Samples were irradiated vertically at a 30 cm distance from the fiber output. Temperature changes were monitored in real-time using a

digital thermometer until a plateau was reached. The laser was then turned off, and the cooling phase was recorded to generate complete temperature-time profiles. To assess photothermal stability (heating-cooling cycles), 3 mL of each nanoparticle type was irradiated in a quartz cuvette in the horizontal direction. For the calculation of photothermal conversion efficiency, the same sample volume was irradiated vertically under identical conditions.

2.7.2 Femtosecond Pulsed Laser Irradiation

Photothermal experiments using ultrashort pulsed laser illumination were carried out with the STELA system (Santiago TErawatt Laser), which emits pulses at a central wavelength of 800 nm. For these experiments, a low-energy output setting (1 mJ per pulse) was used, with a pulse duration of 100 femtoseconds (fs) and a repetition rate of 1 kHz. The laser beam was focused to a spot size of 0.38 cm^2, matching that of the CW laser setup.

AuNP dispersions (6 mL) of AuNRs (1.50×10^{11} $NP \cdot mL^{-1}$) and AuNSs (1.50×10^{9} $NP \cdot mL^{-1}$) were placed in a 12-well plate positioned 30 cm from the laser output. Temperature changes were monitored using a digital thermometer throughout the irradiation process, which was continued until a thermal plateau was reached.

2.7.3 Photothermal Conversion Efficiency

The photothermal conversion efficiency (η) of AuNRs and AuNSs was determined using the method described by Roper *et al*.[172] Briefly, gold NPs dispersions (3 mL) were irradiated vertically in a quartz cuvette using an 808 nm CW laser, and the temperature evolution was recorded until thermal equilibrium was reached. After switching off the laser, the cooling profile was recorded.

The system time constant (τ_s) was extracted by fitting the cooling data to a linearized form of the temperature decay expression (equation 7).

$$-Ln\ \theta = \frac{t}{\tau_s} \tag{7}$$

where θ is a dimensionless temperature parameter based on the ambient and maximum temperatures. Photothermal conversion efficiency was then calculated using the following equation 8.

$$\eta = \frac{hA(T_{max} - T_{amb}) - Q_0}{I(1 - 10^{-A_\lambda})} \quad (8)$$

where I is the laser power, A_λ is the absorbance of NPs at 808 nm, T_{max} is the equilibrium temperature, h is the convective heat transfer coefficient, and A is the surface area of the quartz cell. Q_o represents the baseline heat absorbed by the solvent and cuvette, which was calculated based on known heat capacities of the system components (quartz and water). All measurements were repeated in triplicate, and average values were used for efficiency calculations.

2.8 *In Vitro* Cellular Assays

2.8.1 Cell Viability

The biocompatibility of the synthesized gold NPs was assessed in MDA-MB-231 and Balb/c 3T3 cells using the CCK-8 assay following the manufacturer´s protocol. Cells were seeded at a density of 1.0×10^4 cells per well in 96-well plates (100 µL per well) and allowed to adhere for 24 h at 37 °C in a humidified 5% CO_2 incubator. Subsequently, cells were exposed to AuNRs at concentrations ranging from 3.2 x 10^9 to 4.0 x 10^{11} NP·mL^{-1}, or AuNSs at 1.0 x 10^8 to 5.0 x 10^9 NP·mL^{-1}, in both cases with gold NPs dispersions prepared in DMEM supplemented with 10% (v/v) FBS and 1% (v/v) penicillin/streptomycin. After 24 h of incubation, cells were washed twice with PBS and 100 µL of 10% (v/v) CCK-8 solution in DMEM was added to each well. Plates were incubated for 1-2 h in the dark at 37 °C, and absorbance was recorded at 450 nm using a microplate reader (Bio-Rad Model 680). For assessing cell viability in the presence of AuNRs and AuNSs after laser irradiation, non-internalized gold NPs were removed, added fresh DMEM and the cells were then irradiated with a CW laser at 2.0 W·cm^{-2} for 5 min, followed by 24 h incubation before applying the CCK-8 protocol as described. In the case of pulsed laser irradiation experiments, cells were exposed to power densities of 1.0 or 3.0 W·cm^{-2} for 2 or 4 min, respectively, using the fs laser system.

2.8.2 Cellular Internalization Study of Gold NPs by TEM

Internalization of AuNRs and AuNSs by Balb/c 3T3 and MDA-MB-231 cells was analyzed by TEM. For this, cells were seeded in 6 well-plates (2 mL, 1.0 x 10^5 cells per well) and incubated for 24 h under standard culture conditions. After washing with 150 µL of PBS 1X, 2 mL of AuNRs (3.0×10^{11} NPs·mL^{-1}) or AuNSs (3.0×10^9 NPs·mL^{-1}) dispersions were added to each well

and incubated for an additional 24 h. The cells were then washed three times with PBS 1X, trypsinized, and centrifuged at 1500 rpm for 4 min. The cell pellet was fixed with 500 µL of 2.5% glutaraldehyde, embedded in agar, and post-fixed with 1% (w/v) osmium tetroxide in 0.1 M cacodylate buffer. The samples were dehydrated, embedded in Eponate resin (Ted Pella Inc., Redding, CA, USA), and sectioned using an ultramicrotome (UltraCut S, Leica Microsystems GmbH, Germany). The resulting ultrathin sections were examined using a JEOL JEM 1011 TEM microscope (JEOL Ltd., Japan).

2.8.3 Cellular Internalization Study of Gold NPs by Confocal Microscopy

Balb/c 3T3 and MDA-MB-231 cells were seeded at 1.50 x 10^5 cells per well in 6-well plates (300 µL DMEM) and incubated for 24 h. After washing with 150 µL of PBS 1X, 2 mL of AuNRs (3.0×10^{11} NPs·mL^{-1}) or AuNSs (3.0×10^{9} NPs·mL^{-1}) dispersions were added to each well and incubated for an additional 24 h. Post-incubation, the supernatant was removed, and cells were washed three times with 200 µL of PBS. Fixation was performed with 4% (w/v) paraformaldehyde for 10 min, followed by permeabilization using 100 µL of 0.25% (w/v) Triton X-100. Actin cytoskeleton was stained with Alexa Fluor™ Phalloidin 647 (0.5%, Invitrogen, MA, USA), and nuclei were stained with DAPI using ProLong Gold Antifade Mountant. Samples were stored at –20 °C for 24 h prior to imaging. Visualization was performed using a Leica SP5 confocal microscope with a 63X objective. DAPI fluorescence was observed in the blue channel (λ_{ex} = 350 nm), actin in the red channel (λ_{ex} = 647 nm), and gold NPs were visualized using reflectance mode, appearing as yellow dots.

2.8.4 Quantitative Cellular Uptake Analysis by ICP-MS

Balb/c 3T3 and MDA-MB-231 cells were seeded in 6-well plates (1.0×10^5 cells per well) in 2 mL of growth medium and incubated under standard cell culture conditions for 24 h. Following incubation, the cells were washed with 1X PBS before adding gold NPs dispersed in complete DMEM. The concentration of AuNRs was varied between 1.0 x 10^{11} and 12.0 x 10^{11} NP·mL^{-1}, while in the case of AuNSs it ranged from 1.5 x 10^9 and 15.0 x 10^9 NP·mL^{-1}. After 24 h, the cells were washed three times with 1 mL of PBS to remove non-internalized gold NPs and trypsinized with 500 µL of 0.25X trypsin. Cell counts were obtained using a Beckman Coulter Multisizer 3 cell counter. The cells were then centrifuged, the supernatant was discarded, and the remaining cell pellets were used for quantification of internalized gold NPs by ICP-MS.

2.8.5 Analysis of Cell Death Mechanism by Flow Cytometry

Balb/c 3T3 and MDA-MB-231 Cells were seeded in 96 well-plates (1.25 x 10^4 cells per well) and incubated for 24 h under standard conditions. Then, AuNRs (3.0×10^{11} NP·mL^{-1}) or AuNSs (3.0×10^9 NP·mL^{-1}) dispersions were added and incubated for an additional 24 h. Gold NPs were dispersed in phenol red-free DMEM to avoid interference with optical readings. Three controls were included in flow cytometry assays: 5.0 µM DOXO as apoptosis control, 0.5% Triton X-100 as necrosis control, and untreated cells (not incubated with gold NPs) as negative control (live cell baseline). After 24 h incubation with gold NPs or control agents, the medium was removed and replaced with fresh DMEM. The cells were then irradiated using either a CW laser at 2.0 W·cm^{-2} for 5 min, or a pulsed laser at 3.0 W·cm^{-2} for 2 or 4 min.

Following irradiation, the cells were incubated for an additional 24 h to allow the onset of photothermal-induced cell death. Then, cells were washed with 1X PBS, trypsinized, and centrifuged at 1000 rpm for 4 min at 37 °C. The supernatant was discarded, and the cell pellets were resuspended in 200 µL of binding buffer containing 5 µL Annexin V-FITC and 5 µL propidium iodide. The cells were then incubated at room temperature for 15 min in the dark. Flow cytometry characterization was performed using a Luminex Guava easyCyte 12HT (Luminex Corp., Texas, USA) to distinguish live, early apoptotic, late apoptotic, and necrotic cells based on fluorescence signals from Annexin V and propidium iodide staining.

2.9 Protein Corona Formation on AuNRs and AuNSs

The formation of protein corona on AuNRs and AuNSs was investigated under three different experimental conditions: i) without laser irradiation (control), where proteins were incubated with gold NPs allowing natural corona formation without external stimulation; ii) simultaneous irradiation, where the gold NPs-protein dispersions were irradiated immediately after mixing, evaluating corona formation under active plasmonic heating; and iii) sequential irradiation, where AuNRs and AuNSs were first incubated with proteins for 2 h to allow protein corona formation prior to laser irradiation.

2.9.1 UV-Vis Spectroscopy and DLS Characterization of Protein-Coated Gold NPs

To evaluate the dynamics of protein corona formation and the influence of laser irradiation, defined amounts of BSA (15.2 µM), and Fib (2.94 µM), were added to dispersions of AuNRs-PEG-NH_2, AuNRs-PEG-CM (5.0 x 10^{11} NP·mL^{-1}) or AuNSs-PEG-CM (5.0 x 10^9 NP·mL^{-1}). The final

protein concentration in all samples was adjusted to 2 µM in PBS (pH 7.4), corresponding to the saturation concentration for both BSA and Fib. UV–Vis spectra were recorded over the range of 400-900 nm for non-irradiated protein-coated gold NPs nanostructures subjected to simultaneous and sequential irradiation conditions. The same AuNRs and AuNSs dispersions were used for hydrodynamic size analysis by DLS. The bioconjugates were irradiated by CW laser intensity of 2 $W \cdot cm^{-2}$ until the temperature reached 45 °C. In all cases, laser-irradiated samples were exposed to a CW laser at 2.0 $W \cdot cm^{-2}$ until the temperature reached 45 °C.

2.9.2 Fluorescence Spectroscopy Analysis of Protein Corona

The interaction between BSA and AuNRs was investigated by monitoring fluorescence quenching of the intrinsic aromatic residues—tryptophan, tyrosine, and phenylalanine—using a Cary Eclipse fluorescence spectrophotometer (Varian Instruments Inc, Agilent Technologies, USA) equipped with a temperature controller and multicell sample holder. For this, AuNRs functionalized with PEG-NH_2 or PEG-CM were mixed with BSA (2 µM) in PBS pH 7.4 in a quartz cuvette. The concentration of AuNRs dispersions was varied from 0 to 1.0×10^{12} $NP \cdot mL^{-1}$, and emission spectra were recorded in the range of 300-400 nm following excitation at 280 nm. To assess the influence of plasmonic heating on fluorescence quenching, samples were irradiated with a CW laser at power densities of 1.0 and 3.0 $W \cdot cm^{-2}$ for 5 min, and fluorescence was measured before and after irradiation.

2.9.3 Circular Dichroism Spectroscopy of Protein-Gold NPs Interactions

The secondary structural changes of proteins upon interaction with gold NPs were characterized by circular dichroism (CD) spectroscopy. Spectra were recorded at room temperature using a Jasco-715 spectropolarimeter equipped with a PTC-343 Peltier thermostated cell holder (Jasco, Japan). Measurements were performed in quartz cuvettes with a 1 mm path length, and the spectral bandwidth was set to 1 nm. Data were collected over the far-UV range (190-250 nm), and PBS (0.01 M, pH 7.4) was used as the blank.

BSA and Fib (each at 2 µM) were analyzed in the presence and absence of AuNRs (5.0×10^{11} $NP \cdot mL^{-1}$) and AuNSs (5.0×10^{9} $NP \cdot mL^{-1}$) without laser irradiation and under simultaneous and sequential irradiation modes. To quantify the protein secondary structure, CD spectra were processed using the Beta Structure Selection (BeStSel) method.

3. Photoresponsive Behavior of Functionalized Gold Nanostructures

3.1 Synthesis and Characterization of AuNRs

AuNRs were synthesized through a seed-mediated growth method following the experimental procedure detailed in Chapter 2. Briefly, gold NPs with 2-3 nm in diameter were used as seeds in synthetic processes assisted by silver nitrate, in which CTAB was incorporated as stabilizing agent.[163] The temperature of the solution during the synthetic procedures was maintained at 27°C to prevent the crystallization of CTAB, which can compromise the stabilization and the intended rod-like morphology of the designed nanostructures.[173] Finally, the obtained AuNRs were coated with PSS in order to provide them with long-term stability.

As can be observed in TEM image (Figure 3.1 A), the as-synthesized AuNRs were highly monodisperse and displayed well-defined rod-like morphologies. The population distribution of the length and width of the AuNRs were measured from the obtained TEM images, being established average values of 39.1 ± 4.7 and 9.3 ± 1.3 nm, respectively (Figure 3.1 B-C). The UV-Vis spectrum of the CTAB-capped nanostructures was also obtained, displaying two differentiated adsorption bands derived from the oscillation of free electrons along the length and width of AuNRs when they were exposed to different light wavelengths (Figure 3.1 D).[174] The first peak, located at *ca*. 510 nm, corresponds to the transversal localized surface plasmon resonance (LSPR), which occurs due to the collective oscillation of electrons along the short axis (width) of the AuNRs. On the other hand, the second absorption peak corresponds to the longitudinal LSPR, which arises from electron oscillations along the long axis (length) of the nanostructures. This longitudinal LSPR band shifts to longer wavelengths, at *ca*. 795 nm, thus coinciding with the first biological window (650-950 nm).[175] After modifying the surface of AuNRs with PSS, the longitudinal LSPR band exhibited a slight blue shift, this being attributed to the lower refractive index of PSS compared to the original CTAB layer surrounding the AuNRs (1.380 *vs*. 1.435) (Figure 3.1 D).[176]

The AuNRs were also characterized through DLS measurements before and after their PSS coating, being observed in both cases two peaks on the hydrodynamic size population distributions that arise from the morphological asymmetry of this typology of NPs (Figure 3.1 E). The peaks located at a lower hydrodynamic size correspond to the rotational diffusion coefficient, while the second ones correspond to the translational diffusion coefficient.[177]

Here, it is worth mentioning that the DLS analysis is based on the Stokes-Einstein relationship, which assumes that the analyzed nanostructures display spherical morphologies. Therefore, in the case of rod-shaped NPs the hydrodynamic sizes obtained by DLS just represent the average values of widths and lengths in all possible orientations of the dispersed particles in solution.[178]

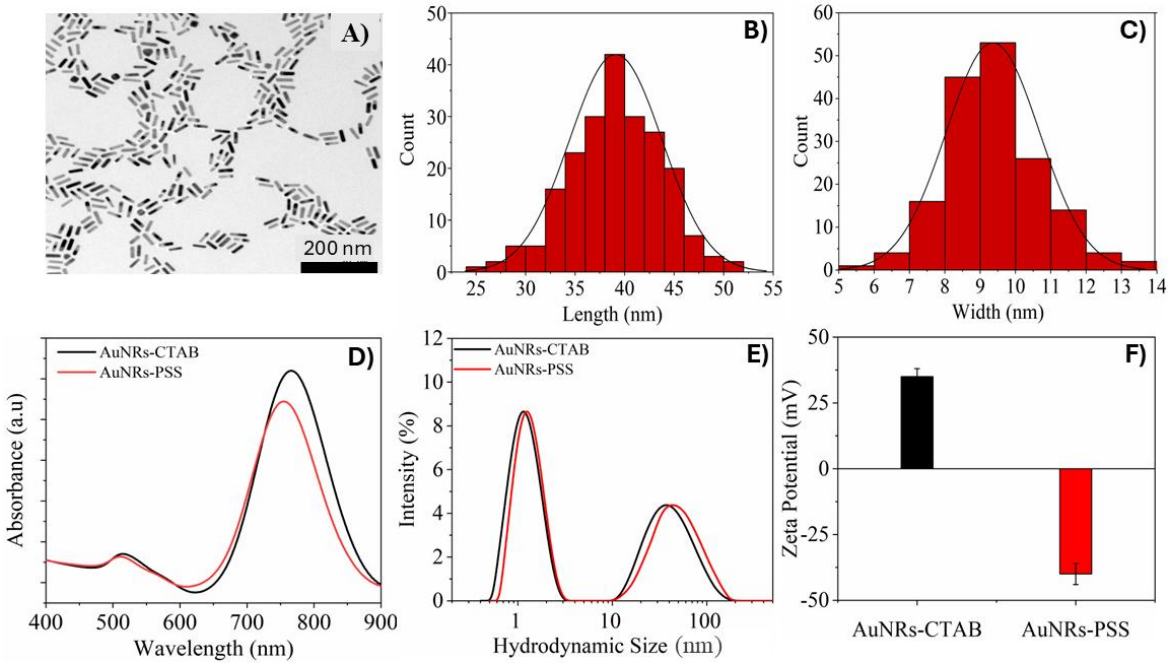

Figure 3.1. A) TEM image of AuNRs-CTAB. B) Length, and C) width statistical distributions of AuNRs-CTAB. D) UV-Vis spectra, E) hydrodynamic size distributions, and F) zeta potential measurements of AuNRs before and after their surface coating with PSS.

However, the presence of two narrow and well-differentiated peaks confirms the high monodispersity and well-defined morphology of the synthesized nanostructures. It was observed that the coating of AuNRs@CTAB with a single layer of PSS increased their hydrodynamic length from 39.5 ± 1.3 to 47.5 ± 1.8 nm (Figure 3.1 E). Finally, the zeta potential of the obtained AuNRs was also evaluated, being determined a positive charge of 35.5 ± 2.5 mV for the AuNRs@CTAB, which was attributed to its cationic quaternary-ammonium head group.[179] After functionalizing the AuNRs with PSS, their zeta potential shifted to a negative value of -40.0 ± 3.7 mV, as expected due to the anionic nature of this polyelectrolyte (Figure 3.1 F).[180]

3.2 Synthesis and Characterization of AuNSs

AuNSs are a particularly interesting type of anisotropic metallic nanostructures because of their morphology with multiple pointed arms or spikes, which provide them with high potential as photothermal agents.[47] In a similar way that discussed above for the rod-shaped NPs, AuNSs were synthesized through a seed-mediated growth method that was detailed previously in Chapter 2.[171] Basically, AuNSs were grown using spherical gold NPs with 15.0 ± 2.3 nm in diameter as seeds, in the presence of PVP as stabilizing agent and DMF acting as both the solvent and reducing agent in the synthesis reaction.[181]

TEM analysis revealed that the synthesized AuNSs were highly monodisperse, with well-defined star-like morphologies (Figure 3.2 A). Similar to the case of AuNRs, no ungrown spherical gold seeds, NPs with undesired morphologies, or metallic aggregates were observed here. The size of the AuNSs was established from the obtained electronic microscopy images, displaying an average diameter of 123 ± 11 nm (measured between opposite tips) (Figure 3.2 B). On the other hand, the UV-Vis spectrum of AuNSs was also obtained, displaying a main absorption band centered at *ca*. 835 nm (Figure 3.2 C). The position of the LSPR peak was attributed to star-shaped morphology with sharp protruding spikes of the synthesized nanostructures, being in good agreement with previous studies that analyzed AuNSs with similar dimensions.[171,182] Interestingly, gold-based NPs with absorption peaks in the NIR region, such as the present designed AuNSs, hold great promise as plasmonic photothermal agents. The existence of LSPR bands within the biological window allows a more efficient conversion of light into heat upon light irradiation of the nanostructures, which can be exploited for the selective treatment of cancer cells in deep tissues.[183] Furthermore, the use of lasers with these wavelengths is generally less detrimental to healthy tissues compared to the use of irradiation with larger frequencies.

DLS measurements were also performed to evaluate the hydrodynamic diameter of the AuNSs. Remarkably, in this case the DLS data reflect more accurately the hydrodynamic diameter of the designed nanostructures, since AuNSs display similar diameters in all of their dimensions. The presence of only one narrow peak in the DLS spectrum confirmed the high monodispersity of the synthesized AuNSs, determining an average hydrodynamic diameter of 125.5 ± 6.3 nm (Figure 3.2 D). The larger value of the hydrodynamic diameter of AuNSs compared to the dimensions of the inorganic cores observed on microscopy images was

attributed to the presence of PVP chains and adsorbed water molecules on the surface of the nanostructures in dispersion, which are not visible in TEM characterization.[184]

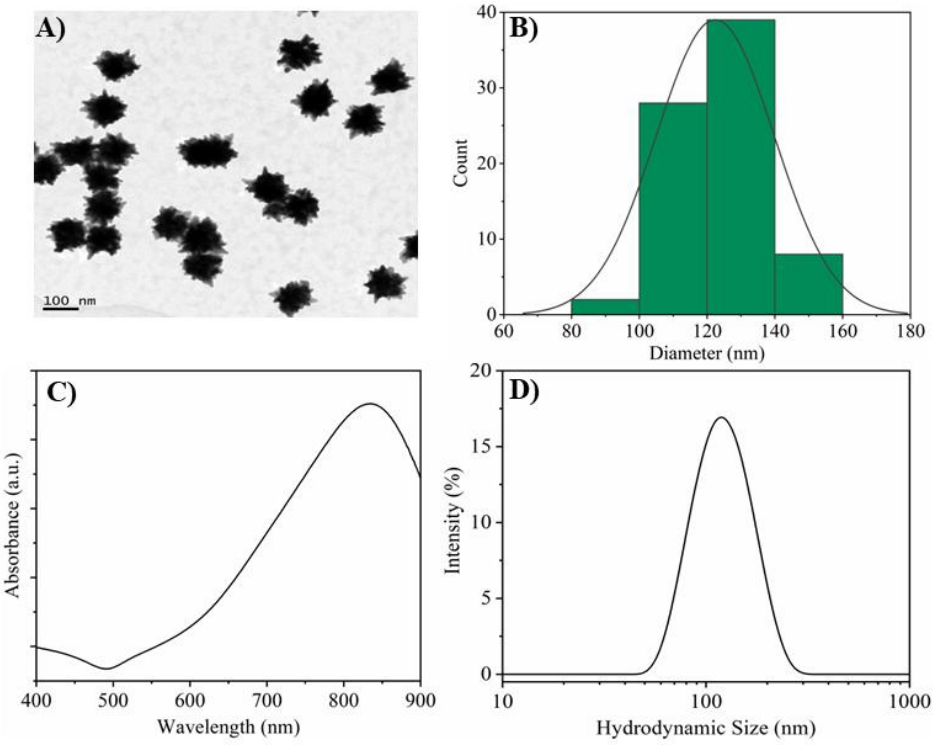

Figure 3.2. A) TEM image, B) diameter statistical distributions, C) UV-Vis spectrum, and D) hydrodynamic size distribution of the synthesized AuNSs.

3.3 Photothermal Properties of Plasmonic Gold NPs under CW Laser Irradiation

3.3.1 CW Laser-induced Temperature Increases in AuNRs and AuNSs Dispersions

In this section, we thoroughly analyze the photothermal properties of the two types of anisotropic gold nanostructures (AuNRs and AuNSs) that were previously synthesized. As outlined in the Introduction section, the photothermal effect arises from the oscillation of free electrons on the surface of metallic NPs upon their light-mediated excitation at specific wavelengths, enabling the conversion of photon energy into heat. The heat generation capability strongly depends on several factors, including the characteristics of the nanostructures and their concentration within the laser spot, as well as laser power, wavelength, and irradiation duration, among other factors. Controlled local temperature increases induced through the irradiation of gold-based NPs have been applied in various

biomedical fields, ranging from cancer photothermal therapy, biosensing, or antimicrobial treatments to complex drug delivery applications.[106]

The heat generation capability of the designed nanosystems was first evaluated in AuNRs and AuNSs dispersions whose concentrations were adjusted to achieve optical density (OD) values close to 1. Thus, based on the previously measured UV-Vis spectra of both typologies of gold NPs, these concentrations were set at 1.50 x 10^{11} and 1.50 x 10^{9} NP·mL^{-1} for AuNRs and AuNSs, respectively. The dispersions were irradiated with laser power densities ranging from 0.65 to 3.94 W·cm^{-2} for 30 min, using an 808 nm CW fiber-coupled diode laser. In this way, it was observed that AuNRs dispersions exhibited temperature increases of *ca*. 8.0, 16.6, 30.5, and 40.0 °C when irradiated at 0.65, 1.30, 2.60, and 3.94 W·cm^{-2}, respectively (Figure 3.3 A). On the other hand, the heating induced in AuNSs dispersions upon irradiation was slightly lower, with temperature increases of *ca*. 7.7, 15.0, 28.1, and 39.0°C at the same laser power densities (Figure 3.3 B). Interestingly, both AuNRs and AuNSs dispersions exhibited rapid temperature rises during the first 5-10 min of exposure to light source. After this initial phase, the heating rate slowed, and the temperature eventually stabilized at a constant value. The larger temperature increases in the dispersions irradiated with rising power densities were attributed to the enhanced absorption of photons by the plasmonic NPs and the subsequent conversion of photon energy into heat.

On the other hand, the influence of NPs concentration on the photothermal performance of both typologies of gold-based nanostructures was also analyzed. For this, the concentration of AuNRs was varied between 1.50 x 10^{8} and 1.50 x 10^{11} NP·mL^{-1}, while for AuNSs it ranged from 1.50 x 10^{6} to 1.50 x 10^{9} NP·mL^{-1}. To isolate the effect of concentration in this study, the samples were irradiated at a fixed power density of 2.60 W·cm^{-2} for 30 min, with temperature variations monitored until reaching thermal equilibrium and also during the cooling processes after turning off the laser. In this way, it was observed that both types of plasmonic NPs exhibited increased heat generation capability at higher concentrations (Figure 3.3 C-D). This was attributed to the larger number of particles available to absorb incident light and convert it into heat. Furthermore, at higher concentrations, plasmonic NPs are more likely to be in close proximity, which can lead to plasmonic coupling, enhancing local electromagnetic fields and increasing the efficiency of light absorption and heating. As the concentration of NPs

increases, the overall thermal energy produced rises, thereby elevating the temperature of the surrounding environment.[174]

Thus, the performed experiments allowed us to evaluate the effects of both laser power density and NPs concentration on the photothermal properties of the two types of designed nanostructures. Interestingly, several of the evaluated conditions resulted in temperature increases greater than 10 °C, thus reaching the thermal ablation threshold required for the selective destruction of malignant cells (above 45 °C). This elevated temperature was attained by irradiating AuNRs dispersions at 1.50 x 10^{11} NP·mL^{-1} with laser power densities of 1.30, 2.60, and 3.94 W·cm^{-2} (Figure 3.3 A). Lower concentrated AuNRs dispersions (1.50 x 10^{9} - 1.50 x 10^{10} NP·mL^{-1}) also reached similar temperature increases, but in these cases minimal laser power densities up to 2.60 W·cm^{-2} were required (Figure 3.3 C). Similarly, AuNSs dispersion at a concentration of 1.50 x 10^{9} NP·mL^{-1} also exhibited light-induced heating up to 10 °C when irradiated with laser power densities higher than 1.30 W·cm^{-2}. When the concentration of AuNSs was reduced to 1.50 x 10^{8} NP·mL^{-1}, at least 2.60 W·cm^{-2} irradiation was required to reach the thermal ablation threshold (Figure 3.3 B-D). Under the remaining conditions, at lower NPs concentrations and/or weaker laser power densities, both AuNRs and AuNSs nanoplatforms exhibited more moderate heating capabilities, with temperature increases below 10 °C. This behavior makes them suitable for applications like localized focused hyperthermia or thermal sensitization.[172]

Finally, photothermal conversion efficiency and the heat transfer rate were calculated using the heat transfer model developed by Roper *et al*. (described in Chapter 2).[172] The photothermal conversion efficiency represents the percentage of irradiated light energy converted into heat by plasmonic gold NPs, while the heat transfer rate refers to the characteristic time required for the system (comprising both the NPs and the surrounding medium) to reach thermal equilibrium after exposure to laser irradiation.[172] It is worth mentioning that conversion efficiency is an intrinsic property of the NPs, depending only on their physicochemical properties, whereas the heat transfer rate depends on the experimental configuration, particularly on the dimensions of the measurement cell and the volume of the dispersion. In this study, calculations were performed using the heating data of AuNRs and AuNSs dispersions at concentrations of 1.50 x 10^{11} and 1.50 x 10^{9} NP·mL^{-1}, respectively, both irradiated at 2.60 W·cm^{-2}. The calculated efficiency and heat transfer rate for AuNRs were

45.7% and 588 s, respectively, with these values decreasing to 46.8% and 357 s in the case of AuNSs. These findings align well with previous studies in which photothermal conversion efficiencies close to 50% and 55% were reported for AuNRs with dimensions of 26×7 nm (LSPR at 770 nm) and 44×13 nm (LSPR at 780 nm), respectively.[185,186] Additionally, the calculated heat transfer rates are also consistent with previously reported values by Almada *et al*., which ranged from 564 and 612 s for AuNRs coated chitosan-PVA-alginate.[187]

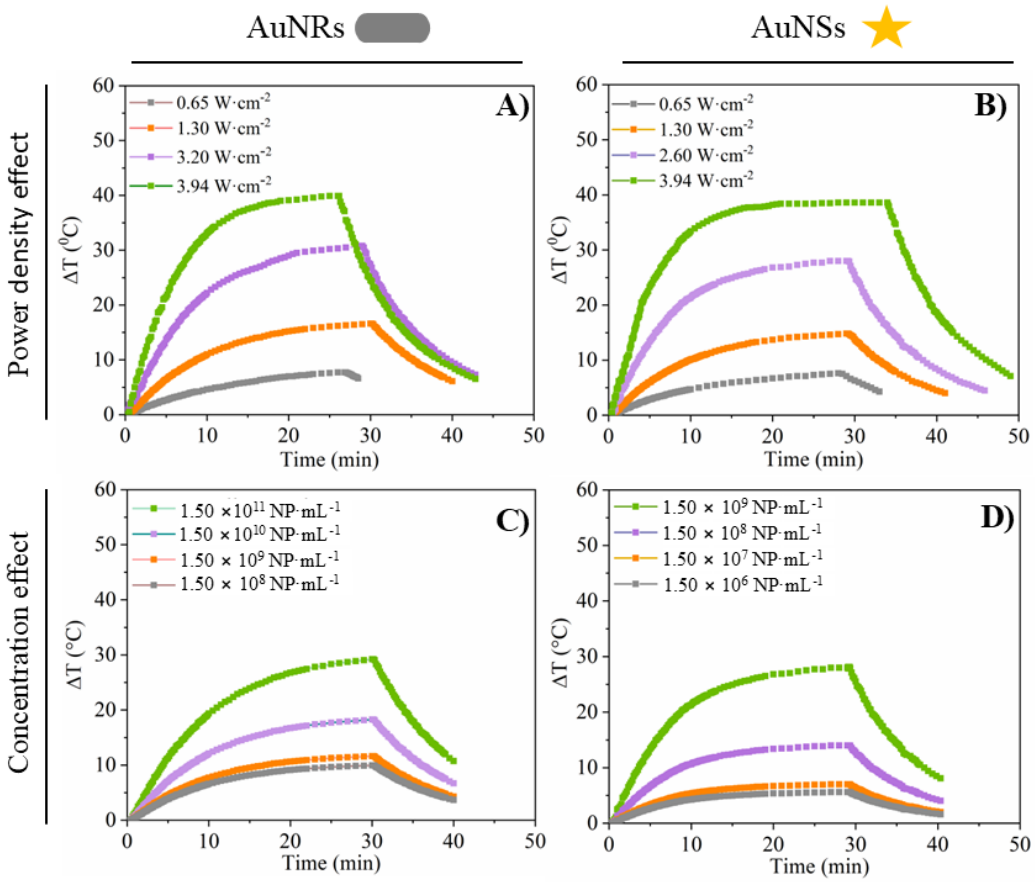

Figure 3.3. Temperature increases of A) AuNRs dispersions at 1.50 x 10^{11} NP·mL^{-1} and B) AuNSs dispersions at 1.50 x 10^{9} NP·mL^{-1} under different laser power densities. Temperature increases of C) AuNRs and D) AuNSs dispersions at different concentrations irradiated with a laser power density of 2.60 W·cm^{-2}.

3.3.2 Impact of Initial Temperature on Heat Generation Dynamics

In this experiment, colloidal dispersions of AuNRs and AuNSs at different initial temperatures were irradiated with a CW laser to investigate the effect of this parameter in the

thermoplasmonic response of the NPs. Specifically, the study aimed to compare the heating profiles when irradiation was initiated with the dispersions at room temperature (25 °C) or at physiological temperature (37 °C). By analyzing the influence of initial temperature on photothermal behavior, this experiment contributes to a deeper understanding of the temperature-dependent efficiency and stability of the designed NPs, which is essential in view of their potential biomedical application.

For this purpose, AuNRs and AuNSs dispersions at concentrations of 1.50 x 10^{11} and 1.50 x 10^{9} NP·mL^{-1}, respectively, were irradiated for 35 min with laser power densities of 2.60 and 3.20 W·cm^{-2}. As mentioned, irradiation was performed with the dispersions initially at either 25°C or 37°C. The results obtained showed that both AuNRs and AuNSs dispersions reached similar equilibrium temperatures, regardless of the initial value of this magnitude (Figure 3.4 A-D). This finding holds true for both laser power densities evaluated. However, the heating rate was faster for the samples with an initial temperature of 25 °C compared to those initially at physiological temperature. This different behavior can be explained on the basis of heat transfer dynamics and thermal equilibrium principles. When the initial temperature of the dispersions was 37 °C, the nanosystems were already close to thermal equilibrium with the surrounding medium, resulting in slower heating rates as the systems quickly balanced the heat generated by irradiation with the heat dissipated to the surroundings.

Therefore, it is important to note that when the designed AuNRs and AuNSs are dispersed in media at physiological temperature, their heating rates upon light irradiation are lower than those observed when irradiated at room temperature. This observation is crucial for optimizing potential photothermal therapies based on the use of these nanoplatforms.

3.3.3 Photothermal Stability of Plasmonic NPs under CW Laser Irradiation

High photothermal stability is a critical requirement for plasmonic nanostructures, especially in view of their potential use in high-precision biomedical applications. For example, in complex photothermal therapies that rely on this type of NPs, maintaining their stability is essential to ensure consistent heat generation without degradation and/or morphological changes, thereby optimizing therapeutic efficacy and minimizing adverse side effects.[188] In this study, AuNSs and AuNRs dispersions at the typical concentrations of 1.50 x 10^{9} and 1.50 x 10^{11} NP·mL^{-1}, respectively, were exposed to various laser power densities ranging from 0.65 to 3.95

W·cm^{-2} for 30 min. To evaluate the photothermal stability of the designed gold nanostructures, their UV-Vis spectra and their hydrodynamic sizes were measured both before and after irradiation.

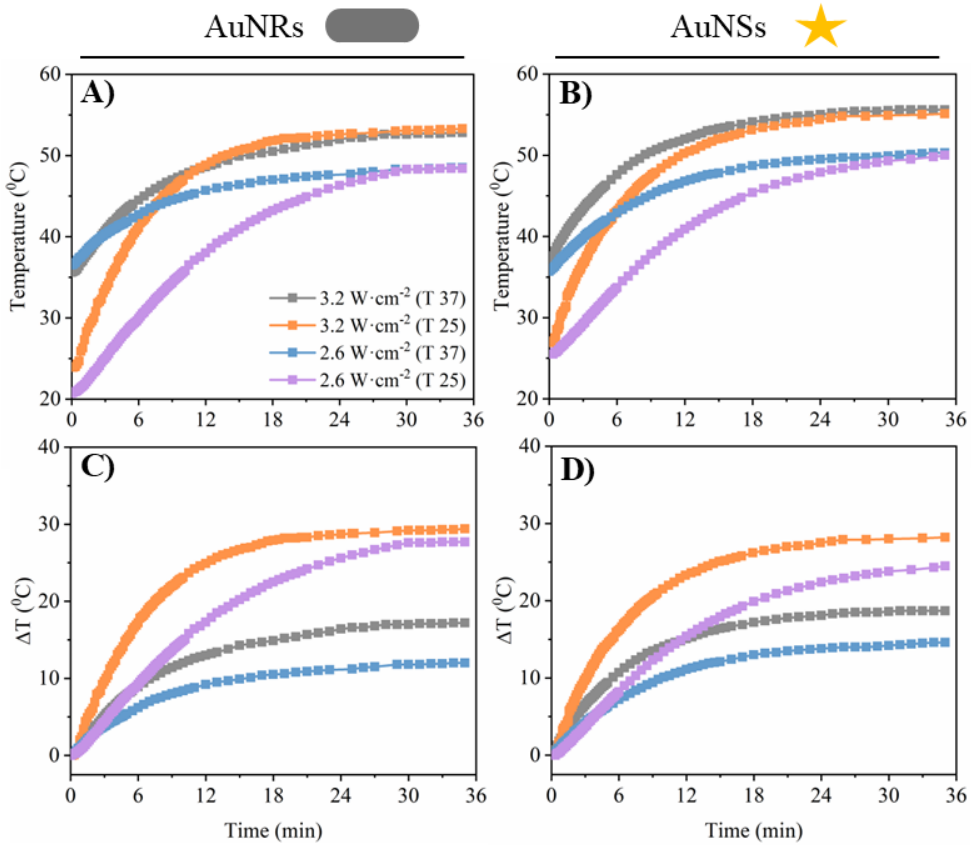

Figure 3.4. Temperature increases of A) AuNRs and B) AuNSs dispersions with initial temperatures of 25 and 37 °C during laser irradiation at 2.60 and 3.20 W·cm^{-2}. C) and D) show the variation in the global temperature (ΔT) of the dispersion during irradiation.

Additionally, their stability was assessed through four heating-cooling cycles at 2.60 W·cm^{-2}. After completing these cycles, TEM images were acquired to analyze morphological changes at the nanoscale, providing further insights into the structural integrity and resilience of the samples under these experimental conditions.

In this way, the performed UV-Vis measurements indicated that laser irradiation did not significantly affect the plasmonic properties of the NPs, with only negligible shifts in the position of the LSPR peaks for both AuNRs and AuNSs (Figure 3.5 A). Furthermore, DLS data

confirmed the exceptional stability of the designed gold nanostructures in terms of hydrodynamic size across varying laser intensities (Figure 3.5 B).

On the other hand, both AuNRs and AuNSs dispersions exhibited similar temperature profiles across the performed four heating-cooling cycles (Figure 3.5 C). In the first irradiation, the dispersions exhibited a pronounced temperature increase during the initial minutes, followed by a slower heating rate and a sharp decline once the laser was turned off. This pattern was repeated in the subsequent cycles, with temperature values reaching similar levels in all cases and exhibiting nearly identical heating/cooling profiles. These results demonstrated the high photothermal stability of both AuNRs and AuNSs, correlating with the absence of significant degradation or morphological changes in the NPs, as confirmed by TEM images (Figure 3.5 D-E).

In conclusion, the synthesized gold nanostructures exhibited remarkable stability under various CW laser irradiation conditions, maintaining their structural and functional integrity. This resilience highlights the robustness of the designed AuNRs and AuNRs, making them potential biomedical nanotools for applications that require repeated light-mediated heating and cooling cycles. Thus, the established high resistance against photo-degradation can allow the use of the nanoplatforms in sophisticated fields such as photothermal therapy, optical sensing, or other nanotechnology-driven innovations.

3.4 Photothermal Properties of Gold NPs under Pulsed Laser Irradiation

Laser pulses with durations in the order of fs can generate extremely high intensities with minimal energy input and have gained significant attention for the precise and highly localized deposition of energy in biological samples. Their use is particularly advantageous due to the extremely short pulse duration, which minimizes excessive heat transfer and prevents the initiation of inflammatory responses in biological tissues. In addition to their high peak powers, fs lasers induce the generation of free electrons *via* nonlinear absorption interactions, distinguishing them from CW or long-pulsed lasers that rely on linear photon absorption (one photon at a time). This linear adsorption mechanism of CW and long-pulsed lasers results in greater heat accumulation and an increased risk of collateral damage.[189] Leveraging these advantages, fs lasers have been proposed for various biological applications, including dental procedures, ear and cataract surgeries, or cancer photothermal therapy.[189]

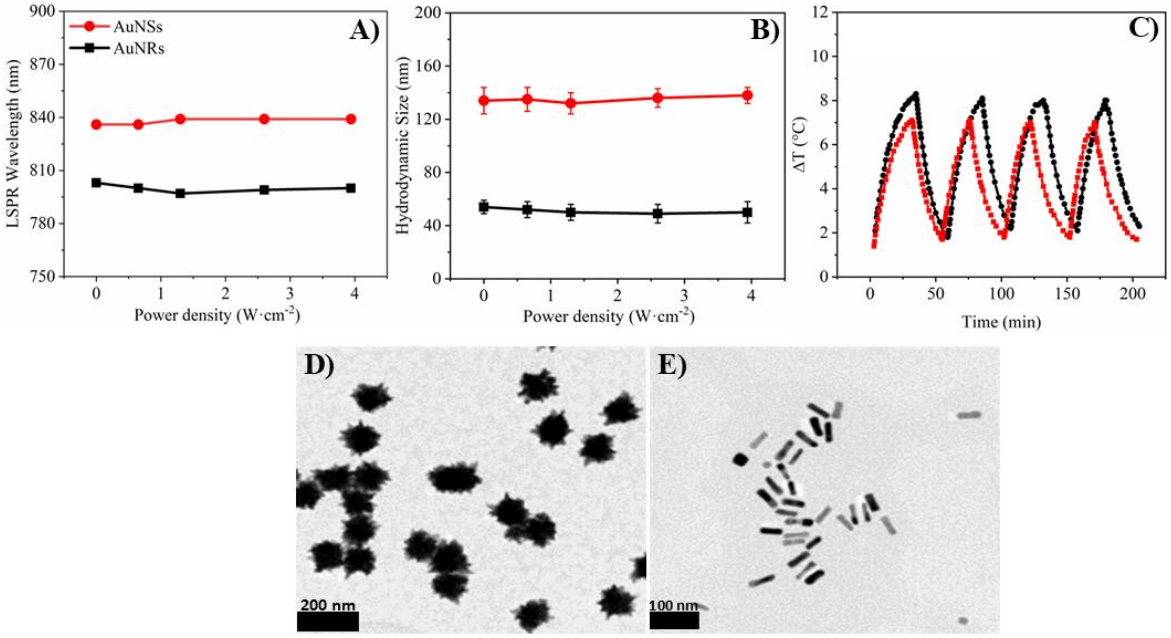

Figure 3.5. A) Position of LSPR peaks and B) hydrodynamic sizes of AuNRs and AuNSs after 30 min of irradiation of the dispersions at different laser power densities. C) Temperature profiles of AuNRs and AuNSs dispersions during four successive irradiation cycles at 2.60 $W \cdot cm^{-2}$. TEM images of D) AuNSs and E) AuNRs after four irradiation cycles at 2.60 $W \cdot cm^{-2}$.

3.4.1 Pulsed Laser-Induced Temperature Increases in AuNRs and AuNSs Dispersions

In this section, we assess the heat generation capabilities of the designed AuNRs and AuNSs under the application of fs laser pulses. For this purpose, gold NPs dispersions at varying initial temperature were irradiated for 30 min with an 800 nm pulsed laser (100 fs pulse duration, 1 kHz frequency), evaluating the effect of different laser power densities ranging from 0.30 to 0.90 $W \cdot cm^{-2}$. These irradiation conditions, in terms of time and intensity, were selected to be energetically equivalent to those used in previous experiments with a CW laser (Section 3.3.1). Additionally, the power densities were chosen to ensure that the laser energy remained below the threshold for air ionization (10^{13} $W \cdot cm^{-2}$), thereby preventing plasma formation and minimizing potential disruptions to the experimental conditions.

When they showed an initial temperature of 25 ˚C, both AuNRs and AuNSs dispersions exhibited temperature increases lower than 6.0 ℃ following 30 min of pulsed laser irradiation. Specifically, in the case of AuNRs dispersions the temperature increased between 2.4 and 5.7

˚C depending on the applied laser power density (Figure 3.6 A), while for AuNSs dispersions these values ranged from 1.9 to 5.9 ˚C (Figure 3.6 B).

The heat generation capabilities of the nanoplatforms were also evaluated in dispersions with initial temperatures of 37 ˚C. As anticipated from earlier experiments using a CW laser, the temperature increases were lower compared to those observed at an initial temperature of 25 ˚C. Thus, AuNRs dispersions exhibited a maximum temperature increase of 3.2 ˚C under the highest laser power density evaluated (Figure 3.6 C), while for AuNSs the maximum increase was 3.1 ˚C (Figure 3.6 D). As described before, this reduced heating at physiological temperatures is attributable to heat transfer dynamics and the principles of thermal equilibrium.

When comparing the NIR-induced heating of gold NPs dispersions under CW and pulsed laser irradiation, temperature increases were significantly lower in the experiments with pulsed light (Figure 3.3). This can be attributed to the extremely short pulse duration (100 fs) of the non-continuous laser, which allows electrons on the surface of the plasmonic NPs to absorb energy, but the transfer of this energy to the crystal lattice and the subsequent heating occurs over longer timescales. Given the brief duration of the pulses and the relatively long intervals between them (1 ms), the heat generated by each pulse dissipates before the next one arrives, thus preventing significant temperature increases in the gold NPs dispersions.[190]

In conclusion, irradiation of AuNRs and AuNSs dispersions using a pulsed laser did not induce significant macroscopic temperature increases, in contrast to the larger heating observed under CW laser irradiation. This lower heating effect under pulsed light was likely due to the short duration of the pulses, which facilitated rapid energy dissipation and prevented substantial heating. In contrast, the continuous energy delivery of CW lasers results in heat accumulation over time, leading to higher macroscopic temperature increases.

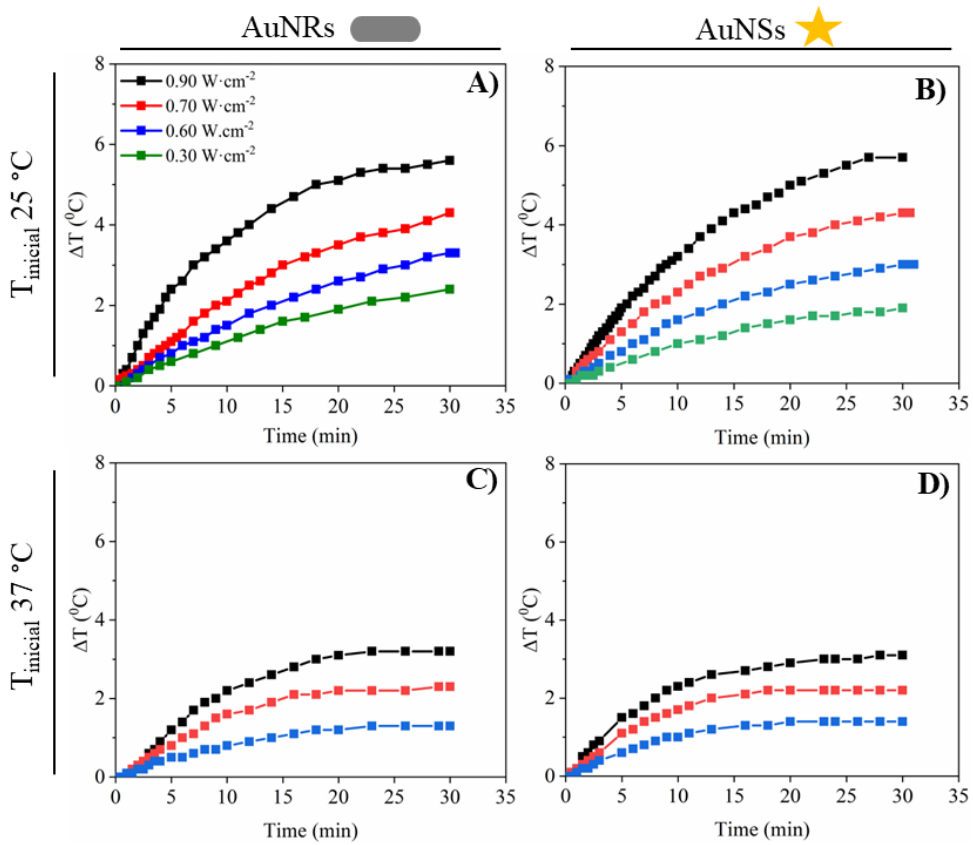

Figure 3.6. Temperature increases in A) AuNRs and B) AuNSs dispersions at 1.50 x 10^{11} and 1.50 x ·10^{9} NP·mL^{-1}, respectively, with initial temperature of 25 ℃, upon pulsed laser irradiation at different laser power densities. Temperature increases in C) AuNRs and D) AuNSs dispersions at 1.50 x 10^{11} and 1.50 x ·10^{9} NP·mL^{-1}, respectively, with initial temperature of 37 ℃, upon pulsed laser irradiation at different laser power densities.

3.4.2 Photothermal Stability of Plasmonic NPs under Pulsed Laser Irradiation

After evaluating the heat generation capability of AuNRs and AuNSs under pulsed laser irradiation, we next investigated the photothermal stability of the nanoplatforms after light exposure. The experimental conditions used to assess the photothermal capability of the nanosystems in previous section were maintained in this stability analysis. Thus, AuNRs and AuNSs dispersions at concentrations of 1.50· x 10^{11} and 1.50 x 10^{9} NP·mL^{-1}, respectively, were irradiated with pulsed laser power densities ranging from 0.30 to 0.90 W·cm^{-2} for 30 min. Subsequently, UV-Vis and DLS measurements were performed, also acquiring TEM images of both nanostructures upon their irradiation at the highest evaluated laser intensity.

As shown in Figure 3.7 A, both AuNRs and AuNSs exhibited blue shifts in their main LSPR peaks upon pulsed laser irradiation, with these displacements becoming more pronounced at higher laser power densities. For AuNRs, the longitudinal LSPR shifted from 805 nm to 730 nm at the highest pulsed laser intensity evaluated. This significant blue shift in the longitudinal LSPR can be attributed to the light-induced degradation of the AuNRs and the well-known dependence of the plasmonic response of rod-shaped gold nanostructures on their aspect ratio. Additionally, a partial removal of the PSS coating, which could alter the refractive index of the surrounding environment and affect the plasmonic response of the AuNRs dispersion, cannot be excluded. In the case of AuNSs dispersions, the LSPR peak shifted only from 848 to 828 nm after irradiation at 0.90 $W \cdot cm^{-2}$ for 30 min, representing a significantly lower displacement compared to AuNRs. This limited variation of the plasmonic response of AuNSs is likely due to their complex multi-branched morphology, in which pulsed irradiation may cause slight melting or shortening of the sharp tips (hot spots), but the overall core structure remains largely intact. Since the primary LSPR of star-shaped gold NPs is dominated by the core, these subtle morphological changes do not result in drastic spectral shifts.

On the other hand, hydrodynamic size measurements before and after the pulsed irradiation of gold NPs dispersions further supported the UV-Vis results. In the case of AuNRs, the hydrodynamic size decreased from 55.0 ± 4.5 to 43.0 ± 3.4 nm, while for AuNSs this variation was from 130 ± 10 to 117.3 ± 8.6 nm (Figure 3.7 B). This observation correlates with the larger shift in the LSPR wavelength of AuNRs previously established through UV-Vis spectroscopy, which, as already discussed, can be attributed to changes in aspect ratio and/or partial removal of surface coating. In the case of AuNSs, the slight decrease in their hydrodynamic size reflects the loss of parts of their sharp tips or desorption of their surface coating, both of which may be caused by the high energy delivered by fs laser pulses.

The results obtained for AuNSs are also consistent with the minimal degradation observed in TEM images, indicating that they successfully retain their characteristic star-like morphologies upon irradiation (Figure 3.7 C-D). It is important to note that extremely short laser pulses generate intense, ultrafast bursts of energy that can induce high localized heating and mechanical stress on the tips of AuNSs, which are particularly susceptible to melting or fragmentation. Despite this, the obtained data demonstrated the high photothermal stability of the designed AuNSs, which retained their structural integrity after pulsed laser exposure.

In the case of AuNRs, TEM images revealed that the intense localized heating induced by pulsed laser irradiation caused a subtle reshaping of AuNRs, slightly reducing their aspect ratio and leading to the aforementioned blue-shift of the longitudinal LSPR peak (Figure 3.7 E-F); the morphological variations in the AuNRs are highlighted by red circles.

In conclusion, the comparative study of AuNRs and AuNSs dispersions under fs laser irradiation revealed distinct photothermal response and stability of these two types of gold-based nanoplatforms. The pronounced blue-shift in the longitudinal LSPR and the significant reduction in the hydrodynamic size observed for AuNRs demonstrate their susceptibility to structural changes, which are driven by the variation of their high-aspect-ratio under intense localized heating. In contrast, AuNSs displayed only minor spectral shifts and lower hydrodynamic size variations, reflecting the resilience of their multi-branched structure under pulsed laser irradiation. TEM imaging supported these findings, being observed significant morphological changes in AuNRs but minimal alteration in AuNSs. These results emphasize the critical role of geometry and structural features in determining the photothermal stability of plasmonic NPs, providing valuable insights for optimizing the design of nanomaterials in view of their use in applications that require high durability of the nanoplatforms under high-energy laser exposure.

3.5 Surface Functionalization of AuNRs and AuNSs Using Different PEGs

Surface functionalization of inorganic nanostructures with PEG is a widely used strategy to reduce nonspecific interactions with serum components, thereby minimizing protein adsorption on their surfaces, preventing rapid clearance by the mononuclear phagocyte system, and enhancing biocompatibility, stability, and circulation time *in vivo*. This approach, known as PEGylation, is crucial for improving the targeting ability of NPs, thus reducing potential harmful effects and enhancing their efficacy for various biomedical applications.[191]

In this work, the synthesized AuNRs were initially coated with CTAB, a stabilizing agent incorporated in the synthetic process of the NPs which is known for its high cytotoxicity. Therefore, efficient removal of CTAB from the surface of the nanostructures is essential in view of their use for biomedical purposes. To achieve this, the AuNRs were functionalized with PEG *via* ligand exchange procedures, in which a significant portion of CTAB was replaced by PEG

through the formation of Au-thiol bonds. Three types of PEGs with different terminal groups were evaluated: methoxy (mPEG), carboxyl (PEG-CM), and amine (PEG-NH_2).

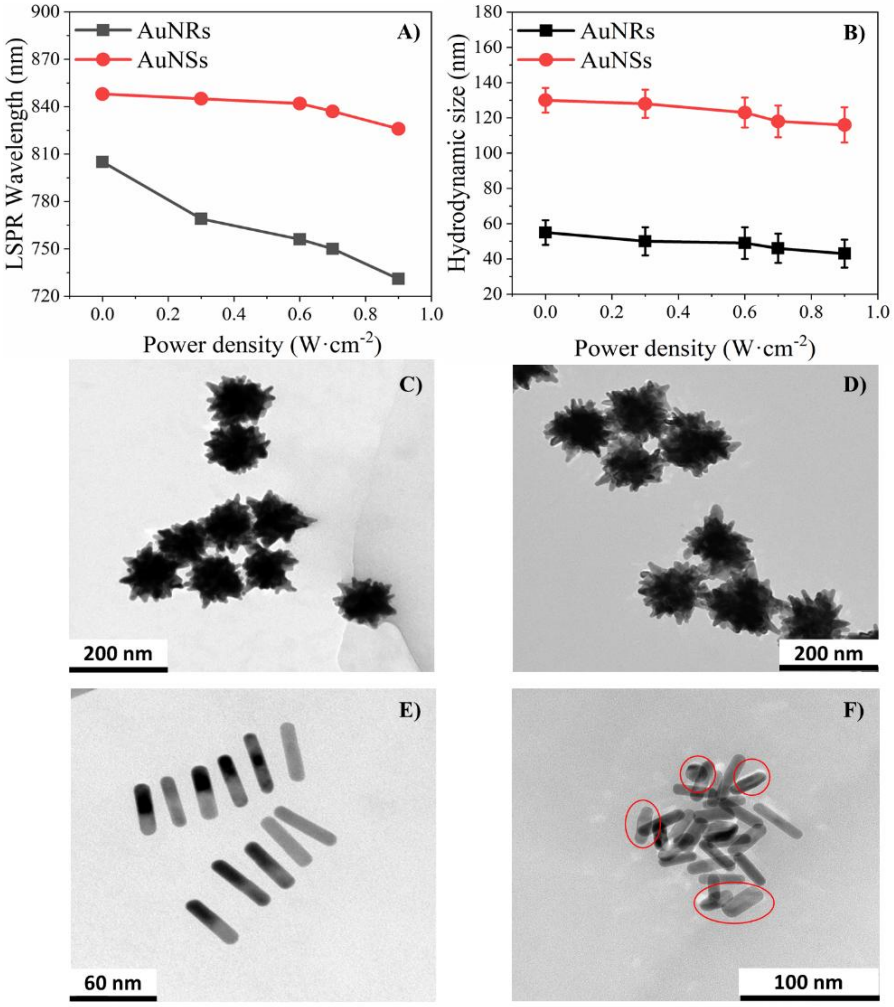

Figure 3.7. A) LSPR shift and B) hydrodynamic size changes of AuNRs and AuNSs upon their pulsed laser irradiation at different power densities. TEM images of AuNSs C) before and D) after 30 min of pulsed laser irradiation at 0.90 W·cm^{-2}. TEM images of AuNRs E) before and F) after 30 min pulsed laser irradiation at 0.90 W·cm^{-2}. Morphological variations of AuNRs upon light exposure are highlighted with red circles in F).

On the other hand, although CTAB was not involved in the synthesis of AuNSs, the designed star-shaped NPs were also functionalized with the same types of PEG to enhance their colloidal stability and biocompatibility. Based on previously reported coating studies, the amount of polymer used in the PEGylation processes was calculated to have a density of 16 PEG chains per nm² of NPs surface, thus ensuring a complete coverage of the

nanostructures.[169] The volume and mass of the NPs were determined form their morphologies and dimensions obtained through TEM images, with AuNRs and AuNSs modeled as cylinders and spheres, respectively. The successful functionalization of both typologies of plasmonic NPs was evaluated through UV-Vis, DLS, and zeta-potential measurements.

In this way, the optical characterization of AuNRs revealed slight red shifts in their longitudinal LSPR peak, from *ca*. 770 nm to 779 nm, following modification with the three different PEGs (Figure 3.8 A). These displacements were attributed to the sensitivity of free electrons oscillations to changes in the refractive index of the surrounding environment, which resulted from the growth of the different PEG layers. Interestingly, the transversal LSPR peak of the AuNRs remained unchanged at *ca*. 515 nm regardless of the type of PEG used in the functionalization process. These findings are consistent with previous studies that analyzed the PEGylation of similar rod-shaped gold nanostructures.[192,193] The successful PEGylation of AuNRs was further confirmed by increases in their hydrodynamic dimensions after the functionalization procedures. Thus, the initial hydrodynamic size (length) of 45.2 ± 2.5 nm for as-synthesized CTAB-capped AuNRs increased up to 78.3 ± 5.3, 73.6 ± 3.8, and 76.3 ± 4.2 nm after coating with mPEG, PEG-CM, and PEG-NH_2, respectively (Figure 3.8 B). These increments were derived from the larger size of the PEG chains attached to the surface compared to the CTAB molecules they replaced. Given that a single ethylene glycol monomer weighs *ca*. 44 Da and has a length of 0.35 nm, the contour length of a fully extended PEG chain with a molecular weight of 5 kDa would be around 40 nm. The observed increases in hydrodynamic size of AuNRs, from 28.4 to 33.1 nm, depending on the type of PEG terminals, correspond to a capping thickness of *ca*. 16.5 nm, thus suggesting that the PEG chains on AuNRs surfaces were not fully extended and adopted a coiled, folded, or twisted conformation.[194,195]

Zeta potential measurements were also performed to confirm the successful attachment of PEG chains to the surface of AuNRs. The surface charge of as-synthesized CTAB-capped AuNRs, 35.5 ± 2.5 mV, was found to change to -5.3 ± 1.5, -18.6 ± 5.8, and 30.2 ± 3.9 mV after functionalization with mPEG, PEG-CM and PEG-NH_2, respectively (Figure 3.8 C). These different values of zeta potential can be explained by the ionization state of the functional groups exposed on the surface of AuNRs functionalized with the three PEG derivatives (dispersions at pH 6). Thus, PEG-CM coated nanostructures exhibited a highly negative surface charge due to the partial deprotonation of the exposed carboxyl groups (-COOH) to form

carboxylate anions (-COO^-). In contrast, mPEG-functionalized AuNRs displayed slightly negative zeta potential, since their surfaces lack ionizable groups, with only minor negative contributions from the adsorption of hydroxide ions or residual charges. Meanwhile, PEG-NH_2-coated AuNRs exhibited highly positive surface charges resulting from the protonation of amine groups to -NH_3^+ under mildly acidic conditions.[196]

Following the same characterization procedure performed for PEG-coated AuNRs, the functionalization of AuNSs with different PEGs was also analyzed by monitoring changes in the LSPR position, hydrodynamic size, and zeta potential values. As shown in Figure 3.8 D, PEGylation caused slight red shifts in the LSPR peak of AuNSs, similar to what was observed for AuNRs, which can be attributed to variations of the refractive index of the surrounding media. DLS measurements further confirmed the successful functionalization of the star-shaped nanostructures, showing hydrodynamic size increases of *ca*. 10-15 nm for all three PEG types (Figure 3.8 E). On the other hand, zeta potential values varied from the -15.2 ± 2.7 mV of as-synthesized PVP-coated AuNSs to -5.1 ± 2.3, -25.2 ± 3.6, and 23.2 ± 2.8 mV after coating with mPEG, PEG-CM and PEG-NH_2, respectively (Figure 3.8 F). These variations were fully consistent with those observed in the functionalization of AuNRs with the same PEGs.

In conclusion, the successful surface functionalization of both AuNRs and AuNSs with the three different PEGs was confirmed through multiple characterization techniques. The results indicated that PEGylation caused a slight red-shift in the LSPR wavelength of both typologies of gold-based nanostructures, with no significant changes in spectral bandwidths. Moreover, PEGylation led to substantial increases in the hydrodynamic sizes of AuNRs and AuNSs due to the high length of PEG chains attached to their surfaces. Additionally, the type of PEG used was found to be crucial to establish the surface charge of the nanostructures, with PEG-CM, PEG-NH_2 and mPEG imparting negative, positive, and near-neutral charges, respectively.

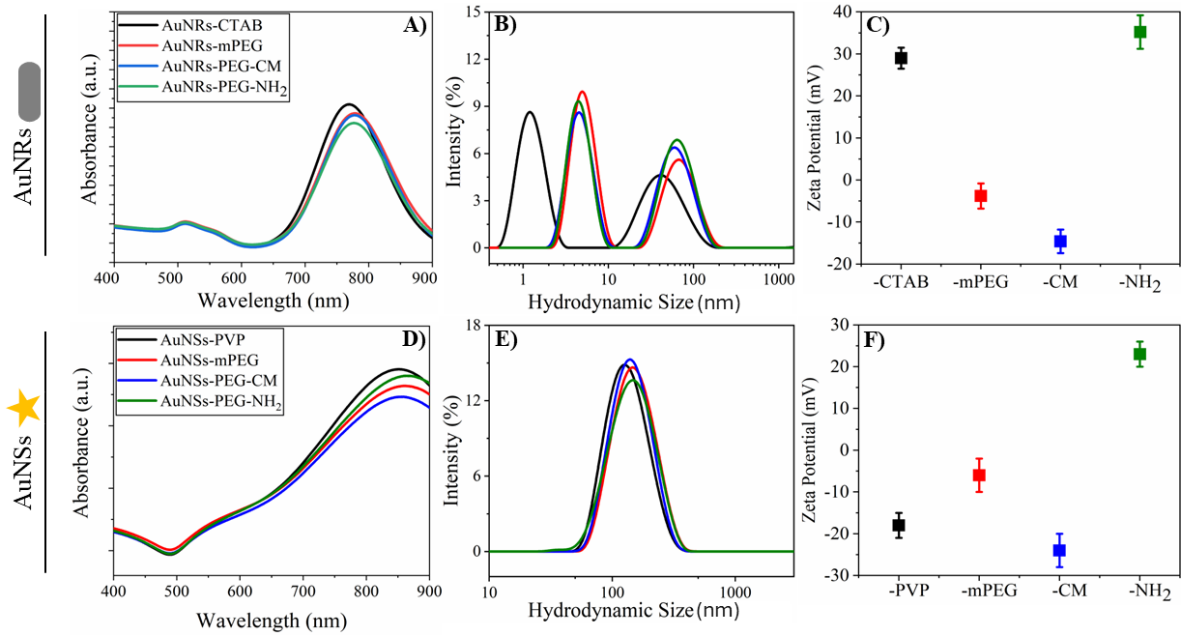

Figure 3.8. A) UV-Vis spectra, B) hydrodynamic size distribution, C) zeta potential values of PEG-coated AuNRs. D) UV-Vis spectra, E) population hydrodynamic size distribution, and F) zeta potential values of PEG-coated AuNSs.

3.6 Colloidal Stability of AuNRs and AuNSs in Relevant Physiological Media

The colloidal stability of gold NPs, particularly the ability to maintain a consistent hydrodynamic size, is a crucial factor in view of their *in vitro* evaluation and potential *in vivo* biomedical application. For instance, it has been demonstrated that NPs with dimensions ranging from 20 to 200 nm exhibit reduced blood clearance *via* the reticuloendothelial system (RES) and can effectively target tumor tissues. In contrast, NPs with hydrodynamic sizes larger than 200-300 nm are typically phagocytosed and retained by the RES, thus hindering their desired targeting.[197] Additionally, the preservation of the plasmonic properties of gold NPs upon dispersion in complex physiological media is also an essential aspect for their effective use as nanotools in various biomedical applications. In this section, we evaluate the colloidal stability and resistance to degradation of the designed PEG-coated gold NPs in different physiologically relevant media.

3.6.1 Evaluating the Stability of AuNRs and AuNSs NPs in Buffered and Saline Media

The colloidal stability and the retention of plasmonic properties of gold NPs functionalized with mPEG, PEG-CM, or PEG-NH_2 were evaluated upon dispersion in water, PBS 1X (pH 7.4), acetate buffer (pH 5.5), and NaCl solutions (0.01-0.20 M). For this, PEG-coated AuNRs and AuNSs were dispersed at fixed concentrations of 1.50 x 10^{11} and 1.50 x 10^{9} NP·mL^{-1}, respectively, in the mentioned media, being their behavior monitored over a six-day period through UV-Vis and DLS measurements.

Initial analysis of AuNRs dispersions revealed slight variations in the behavior of the designed rod-shaped nanostructures depending on the type of PEG coating and dispersion medium. As shown in Figure 3.9 A, the longitudinal LSPR peak of AuNRs-mPEG incubated in water, acetate buffer (pH 5.5), and PBS (pH 7.4) exhibited a gradual blue shift over the six-day period. These shifts in LSPR wavelengths were minimal, in all cases lower than 10 nm, and were more pronounced in PBS, likely due to the presence of different ionic species in the medium. A similar trend was observed for AuNRs coated with PEG-CM, which also showed minor variations in their UV-Vis spectra upon incubation in buffered media (Figure 3.9 B). In the case of PEG-NH_2-coated AuNRs, they displayed almost negligible displacements on the position of their LSPR peak across all media during the incubation period (Figure 3.9 C).

DLS data further supported previous observations, with both AuNRs-mPEG and AuNRs-PEG-CM displaying reductions up to *ca*. 15 nm in their hydrodynamic sizes after incubation in buffered media, probably due to partial degradation of the polymeric coatings (Figure 3.9 D-E). In contrast, the hydrodynamic size of AuNRs-PEG-NH_2 remained nearly constant throughout the six-day incubation period in all cases (Figure 3.9 F). These results suggest excellent colloidal stability and preservation of plasmonic response for functionalized AuNRs, especially those coated with PEG-NH_2, in water, PBS, and acetate buffer.

Notably, the stability of PEGylated rod-shaped gold NPs was significantly affected when incubated in NaCl solutions. Both AuNRs-mPEG and AuNRs-PEG-CM exhibited similar trends in their UV-Vis spectra during incubation in saline media, with blue shifts in their longitudinal LSPR becoming more pronounced as the NaCl concentration increased. Specifically, the maximum blue shifts observed on the LSPR upon six days incubation in 0.20 M NaCl were *ca*. 8 and 10 nm for AuNRs-mPEG and AuNRs-PEG-CM, respectively (Figure 3.9 G-H). In the case

of AuNRs coated with PEG-NH_2, the UV-Vis spectra remained nearly unchanged (LSPR shift < 5 nm) during the analyzed six-day period, even at high NaCl concentrations (Figure 3.9 I). DLS measurements corroborated these UV-Vis results, revealing structural degradation in AuNRs-PEG-CM and AuNRs-mPEG that led to hydrodynamic size decreases of *ca*. 16 and 19 nm after six days in NaCl 0.20 M (Figures 3.9 J-K). Interestingly, despite the excellent preservation of plasmonic properties for AuNRs-PEG-NH_2, DLS measurements indicated a non-negligible decrease in their hydrodynamic size up to *ca.* 12 nm after six days in highly concentrated NaCl solutions (Figure 3.9 L).

The relatively low stability of AuNRs in NaCl solutions at concentrations above 0.10 M can likely be attributed to a combination of several factors. For example, High salt concentrations can induce a collapse, dehydration, or compaction of PEG chains on the surface of NPs due to osmotic pressure changes and ionic interactions. [198, 199] Additionally, increased salt concentration may facilitate the partial desorption of PEG from the NP surface as chloride ions compete for adsorption sites.

After analyzing the behavior of functionalized AuNRs in different buffered media and NaCl solutions, the stability and the preservation of the plasmonic response of PEG-coated AuNSs were assessed in the same manner. Interestingly, it was found that star-shaped nanostructures exhibited distinct behaviors compared to their rod-like counterparts coated with the same type of PEGs, both in saline and buffered media. As shown in Figure 3.10 A-C, all PEG-coated AuNSs displayed an increasing blue shift in their LSPR peak when incubated in PBS at pH 7.4, reaching maximum displacements close to 15 nm in the case of AuNSs-PEG-NH_2 after six days. However, when functionalized AuNSs were dispersed in water or acetate buffer at pH 5.5, the wavelength of LSPR peak tended to increase (red shift), with displacements of up to 10 nm observed upon six-day incubation. On the other hand, DLS data showed that all PEG-coated AuNSs experienced increases in their hydrodynamic sizes over the whole incubation period in water, acetate buffer, and PBS (Figure 3.10 D-F). The most significant changes were observed for AuNSs-mPEG in PBS and AuNSs-PEG-NH_2 in acetate buffer, with hydrodynamic sizes increasing from an initial value of *ca*. 150 nm to over 190 nm.

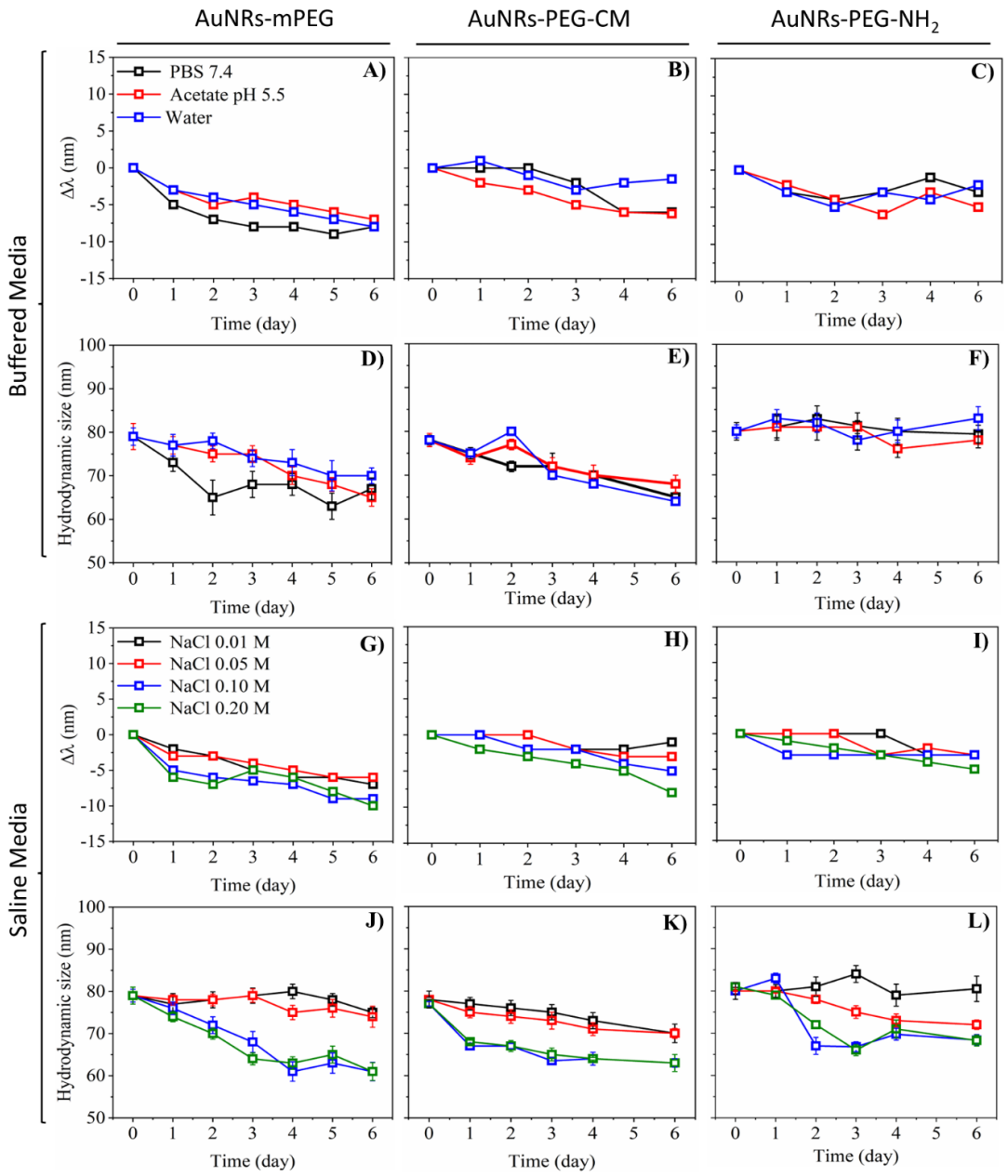

Figure 3.9. A-C) Displacements in the wavelength of the longitudinal LSPR peak (Δλ) of PEG-coated AuNRs, and D-F) evolution of their hydrodynamic size during six days of incubation in water, PBS, and acetate buffer. G–I) Displacements in the wavelength of the longitudinal LSPR peak (Δλ) of PEG-coated AuNRs, J–L) evolution of their hydrodynamic size during six days of incubation in NaCl solutions. The graphs in the first, second, and third column of the figure show data of AuNRs coated with mPEG, PEG-CM, and PEG-NH_2, respectively.

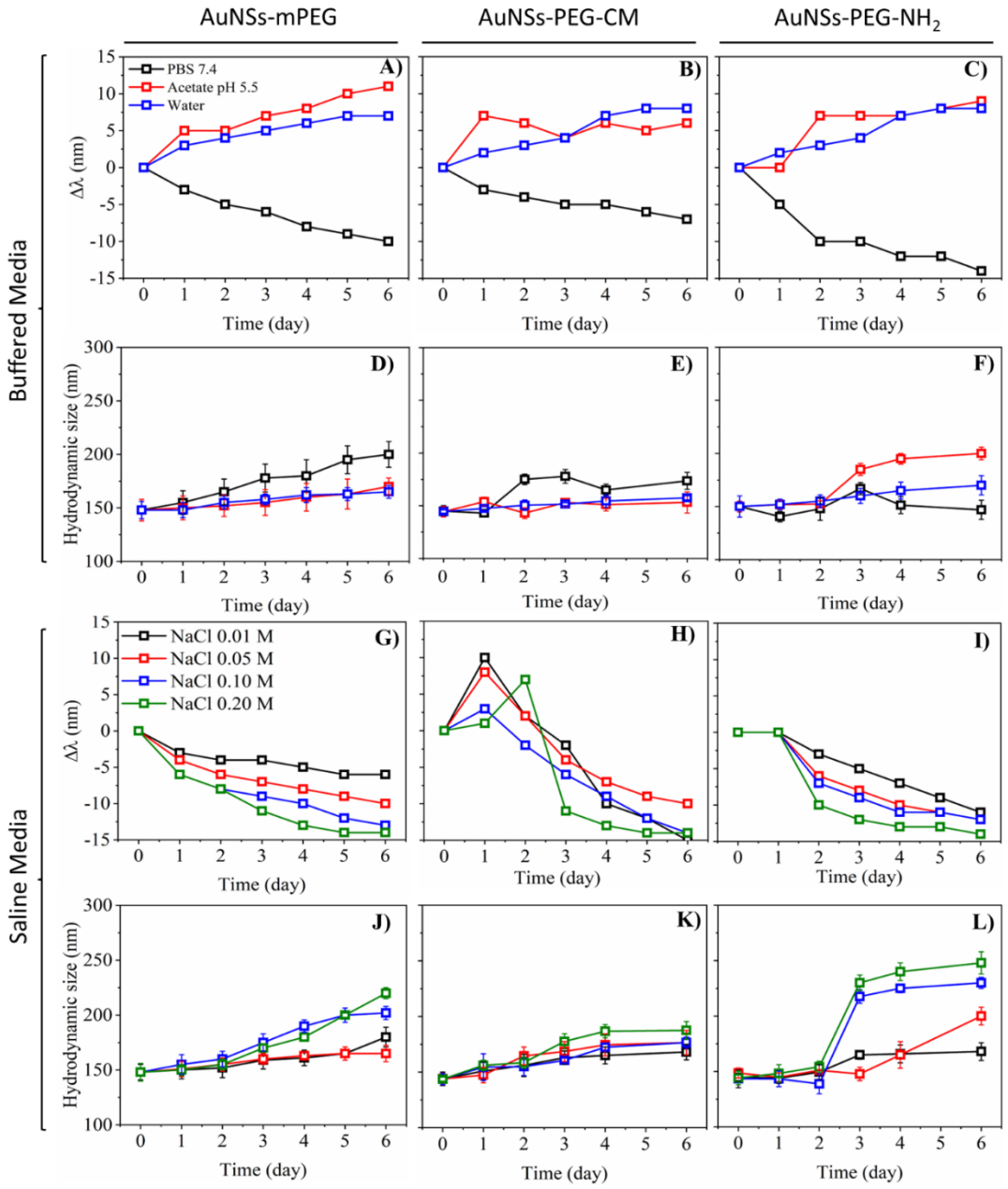

Figure 3.10. A-C) Displacements in the wavelength of the LSPR peak (Δλ) of PEG-coated AuNSs, and D-F) evolution of their hydrodynamic size during six days of incubation in water, PBS, and acetate buffer. G–I) Displacements in the wavelength of the LSPR peak (Δλ) of PEG-coated AuNSs, J–L) evolution of their hydrodynamic size during six days of incubation in NaCl solutions. The graphs in the first, second, and third column of the figure show data of AuNSs coated with mPEG, PEG-CM, and PEG-NH_2, respectively.

When the PEG-coated AuNSs were dispersed in NaCl solutions, relevant blue shifts between *ca*. 5-15 nm of their LSPR peak were observed upon 6 days of incubation (Figure 3.10 G-I). In

general, the shift of the LSPR wavelength was relatively progressive during the incubation period, with larger changes observed at the most concentrated NaCl solutions and a reduced influence of the PEG type used for functionalization. In terms of hydrodynamic size, the measured values remained nearly constant in most of the analyzed systems, with only minor increases over the six-day incubation period (Figure 3.10 J-L). However, AuNSs-mPEG and AuNSs-PEG-NH_2 incubated for six days in NaCl solutions with concentrations higher than 0.10 and 0.05 M, respectively, displayed very significant increases on their hydrodynamic sizes, exceeding values of 200 nm. These large size increases could be explained by the phenomenon of surface charge screening, in which the dispersion of charged NPs into physiological environments can reduce their surface charges and diminishes their electrostatic repulsion, increasing the likelihood of slight aggregation. Therefore, when PEG-coated AuNSs underwent charge screening under the aforementioned conditions, their effective hydrodynamic size may increase due to the formation of small aggregates or clusters.

In conclusion, the stability of both AuNRs and AuNSs coated with the three types of PEGs was demonstrated across various media. For AuNRs, their hydrodynamic size remained stable upon incubation in water, PBS, and acetate buffer, indicating robust colloidal stability despite minor blue shifts in their LSPR. However, when incubated in NaCl solutions, significant changes in the LSPR and hydrodynamic size were observed, particularly for AuNRs-mPEG and AuNRs-PEG-CM at higher salt concentrations. On the other hand, PEG-coated AuNSs exhibited a blue shift in their LSPR in PBS and saline media, while these shifts occurred toward larger wavelengths in water and acetate buffer. These shifts, ranging from 0 to 15 nm, were minimal due to the broad UV-Vis absorption band of AuNSs, resulting in no significant impact on their plasmonic properties. Similar to AuNRs, significant increases in the hydrodynamic size of AuNSs were only observed at high saline concentrations, with most systems remaining below 200 nm after the incubation period. As mentioned, nanostructures below this size threshold the NPs can be exhibit several advantageous properties, including improved cellular uptake and more favorable biodistribution.

3.6.2 Assessing the Impact of Protein-Rich Dispersion Media on the Stability of Gold NPs

The colloidal stability of nanoparticulated systems in protein-rich biological fluids is essential for their potential biomedical application, as uncontrolled particle aggregation and/or degradation can lead to adverse side effects. Therefore, extending the previous analysis of the

behavior of gold NPs in buffered media to include their stability in more complex biological environments is crucial for properly assessing their potential as biomedical nanotools. Upon dispersion in biological media, several proteins adsorb onto the external surface of the NPs, ultimately determining their identity and interaction with cells and other biological entities. Moreover, in the specific case of plasmonic NPs, maintaining stability is also crucial for preserving their optical properties, which are key to their subsequent performance as theranostic nanotools.[41]

Here, the colloidal stability of the previously designed PEG-coated gold NPs was evaluated in various relevant biological media. To do so, AuNRs and AuNSs dispersions at the typical concentrations of 1.50 x 10^{11} and 1.50 x 10^{9} NP·mL^{-1}, respectively, were incubated in DMEM and FBS at concentrations of 10%, 50%, and 100%, monitoring their behavior over a six-day period through DLS and UV-Vis measurements.

Starting with the analysis of rod-shaped gold NPs, it was observed that when dispersed in FBS 10%, all three PEGylated AuNRs maintained their LSPR peaks without significant shifts (Figure 3.11 A-C). Consistent with this, their hydrodynamic sizes remained stable, showing no signs of aggregation or dramatic size increase (Figure 3.11 D-F). This stability can be attributed to the formation of a protein corona around the NPs, which provides a steric barrier that prevents aggregation. The relatively low protein concentration in 10% FBS is sufficient to stabilize the AuNRs without excessive protein adsorption that could destabilize the system. However, PEG-coated AuNRs dispersed in DMEM or higher concentrations of FBS (50% and, more notably, 100%) exhibited notable red shifts in their longitudinal LSPR peaks, with displacements of up to 20 nm over the incubation period (Figure 3.11 A-C). The effect of the type of PEG used for functionalization on AuNRs stability was minimal again; for example, AuNRs-mPEG, AuNRs-PEG-CM, and AuNRs-PEG-NH_2 displayed similar longitudinal LSPR peak displacements of 27-29 nm after incubation in FBS 50% and 100%. These variations on the plasmonic properties of AuNRs were accompanied by substantial increases in their hydrodynamic sizes, which exceeded 200 nm in many cases (Figure 3.11 D-F). Specifically, AuNRs coated with mPEG, PEG-CM, and PEG-NH_2, which initial hydrodynamic size was *ca*. 70 nm, displayed final values of 205 ± 13, 212 ± 14, and 228 ± 16 nm upon incubation in DMEM.

These observations indicate significant aggregation of the functionalized AuNRs in DMEM and FBS 50-100%, likely due to insufficient stabilization provided by PEG coatings. The extensive

protein adsorption on the surface of AuNRs in these media reduced the electrostatic repulsion between the nanostructures, promoting uncontrolled aggregation and leading to the loss of colloidal stability and changes in their plasmonic response.[200]

Regarding the AuNSs, the behavior of the star-like nanostructures dispersed in DMEM and FBS media was notably different from that of their rod-shaped counterparts. In general, the designed AuNSs were more stable and showed better preservation of their plasmonic response. AuNSs coated with the three different PEGs displayed red shifts in their LSPR peaks of less than 17 nm in all cases. Specifically, AuNSs-mPEG maintained almost unchanged plasmonic behavior during the six-day incubation in the analyzed media, with maximum LSPR displacements of *ca*. 7 and 11 nm in FBS and DMEM, respectively. Slightly larger shifts were observed for AuNSs-PEG-CM and AuNSs-PEG-NH_2, with maximum LSPR displacements reaching the aforementioned *ca*. 17 nm (Figure 3.11 G-I). Interestingly, given the broad plasmon band of AuNSs, these small variations on the wavelength of the LSPR peaks resulted in only minor changes of the optical properties of the nanostructures. As expected, DLS data were in good agreement with previous observations, showing that AuNSs experienced much smaller relative increases in their hydrodynamic size compared to AuNRs when incubated in DMEM and FBS. In most cases, the final hydrodynamic size of AuNSs upon the incubation period of six days was below 200 nm, starting from an initial size over 140 nm. The most significant size increases were observed for AuNSs-PEG-NH_2, which reached hydrodynamic sizes between 209-230 nm after incubation in DMEM and FBS 50-100% (Figure 3.11 J-L).

In conclusion, the stability of PEGylated gold NPs varied significantly during incubation in DMEM and FBS (10-100%) media. In DMEM, both AuNSs and, more markedly, AuNRs exhibited pronounced LSPR red-shifts and increases in their hydrodynamic sizes, indicating aggregation due to the destabilizing components in the medium. In contrast, when the NPs were dispersed in FBS 10%, the observed minimal LSPR shifts, and stable hydrodynamic sizes suggested effective stabilization by the formed protein corona. However, at higher FBS concentrations, the established larger red-shifts of the LSPR peak and hydrodynamic size growth, particularly for AuNRs, indicated enhanced protein adsorption and potential aggregation of the nanostructures. The slight differences in the observed behaviors depending on the type of coating can be attributed to the varying terminal groups of the PEG chains, which lead to the adsorption of different amounts of proteins on the surface of AuNRs and

AuNSs. Overall, these results highlighted the importance of both medium composition and PEG chemistry in maintaining colloidal stability and resisting plasmonic degradation.

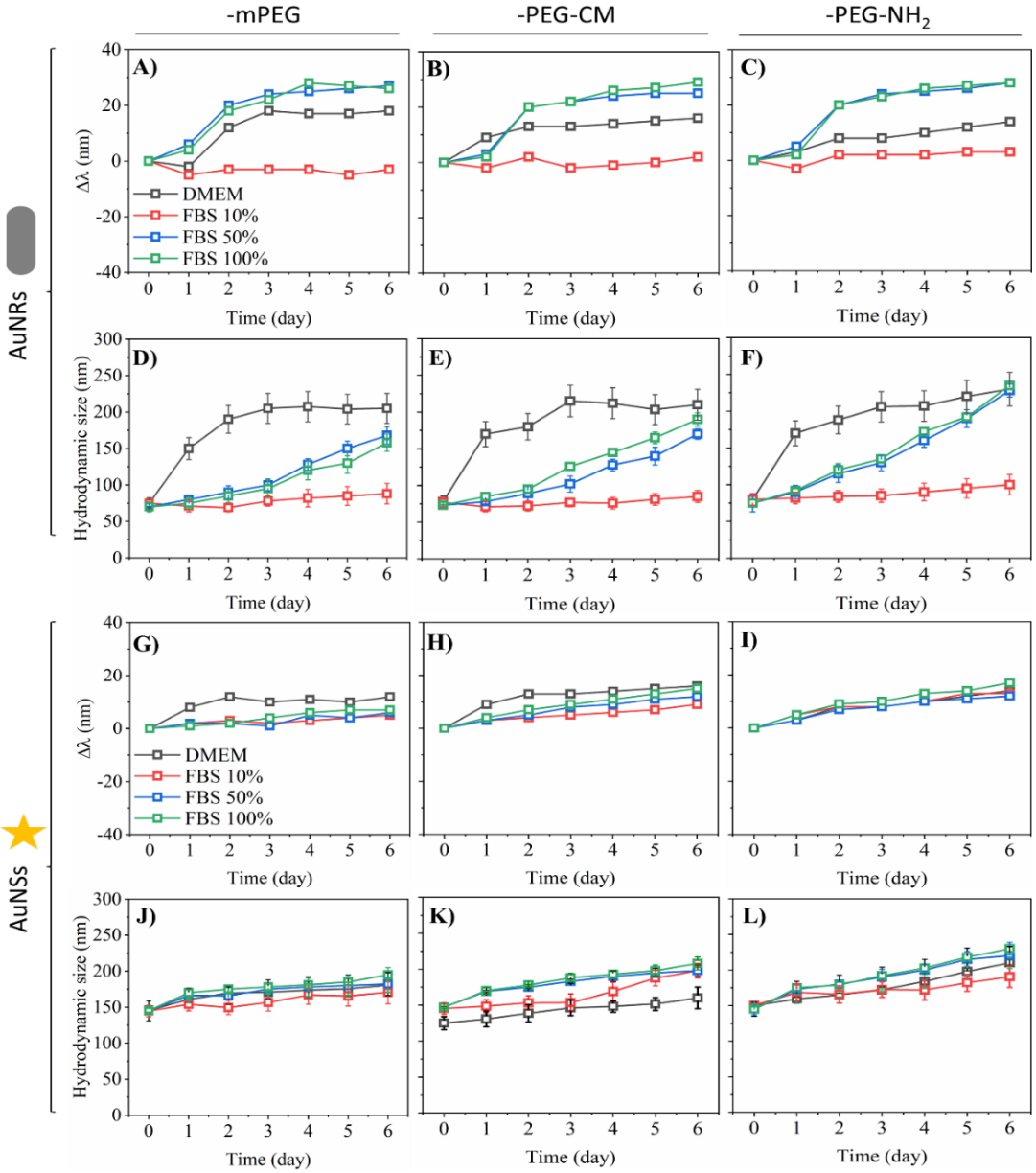

Figure 3.11. A-C) Displacements in the wavelength of the longitudinal LSPR peak (Δλ) of PEG-coated AuNRs, and D-F) evolution of their hydrodynamic size during six days of incubation in DMEM and FBS 10-100%. G–I) Displacements in the wavelength of the LSPR peak (Δλ) of PEG-coated AuNSs, and J–L) evolution of their hydrodynamic size during six days of incubation in DMEM and FBS 10-100%. The graphs in the first, second, and third column of the figure show data of AuNRs-AuNSs coated with mPEG, PEG-CM, and PEG-NH_2, respectively.

3.6.3 Effect of Dispersion Media pH on the Stability of Gold NPs

A comprehensive analysis on the pH effect on the stability of PEGylated gold NPs is crucial for optimizing their functionality and performance in various applications. Changes in the pH of the surrounding environments influence the surface charge of nanostructures, which in turn affects the electrostatic interactions between them and ultimately dictates their colloidal stability. Thus, understanding how pH affects the behavior of NPs is especially important in the biomedical field, where it can help to select the adequate functionalization to enhance targeting efficiency, optimize their function as drug release agents, or improve their therapeutic-diagnostic capabilities, among other attributes.[201]

In this study, the zeta potential values and hydrodynamic sizes of PEG-coated AuNRs and AuNSs were compared across dispersion media with pH values ranging from 2 to 12. Consistent with the previous colloidal stability experiments, the concentrations used were 1.50×10^{11} NP·mL^{-1} for AuNRs and 1.50×10^{9} NP·mL^{-1} for AuNSs.

As shown in Figure 3.12 A-B, both AuNRs and AuNSs coated with PEG-NH_2 exhibited higher zeta potential values than those functionalized with mPEG or PEG-CM across the entire pH range analyzed. The only exception occurred for AuNRs dispersed in media at pH 12, where those coated with PEG-CM showed a slightly higher surface charge (less negative) than AuNRs-PEG-NH_2. These higher zeta potential values of gold NPs functionalized with PEG-NH_2 can be attributed to the partial protonation of the terminal groups of the PEG chains, which results in the exposure of a positive charge on the surface of the nanostructures (-NH_3^+). This phenomenon is particularly significant in acidic dispersions, where PEG-NH_2-coated NPs acquired highly positive surface charges that ensure strong electrostatic repulsion between, thus enhancing their colloidal stability. The point of zero charge (PZC), defined as the pH at which the net surface charge of dispersed NPs is null, shifted from pH 3 for AuNRs-mPEG and AuNRs-PEG-CM to pH 7.7 for AuNRs-PEG-NH_2 (Figure 3.12 A). A very similar trend was observed for the star-shaped nanostructures, with PZC shifting from pH 3 for AuNSs-mPEG and AuNSs-PEG-CM to pH 8.3 for AuNSs-PEG-NH_2 (Figure 3.12 B). In both cases, the larger PZC of PEG-NH_2-coated nanostructures resulted from the aforementioned protonation of NH_2 terminal groups in acidic environments. The slight difference in the PZC between AuNSs-PEG-NH_2 and AuNRs-PEG-NH_2 may arise from the distinct stabilizing agents used in the synthesis of both types of NPs (PVP for AuNSs and CTAB for AuNRs), and how these interacted with PEG-

NH_2 chains during the coating process. Additionally, the extent of PEG-NH_2 coating on the NPs surface might also contribute to differences in the PZC between the two types of gold nanostructures.

On the other hand, the effect of the pH of the dispersion media over the hydrodynamic size of PEG-coated gold NPs was also evaluated. In this way, it was observed that AuNRs and AuNSs coated mPEG or PEG-CM remained highly stable in terms of their hydrodynamic size across the entire pH range of 2-12 (Figure 3.12 C-D). This stability was attributed to the steric hindrance provided by the PEG chains, which prevented aggregation of the nanostructures even when their zeta potential values were relatively low. mPEG contains a neutral, non-ionic methoxy group at its terminus, which makes surface interactions less sensitive to pH and minimizes the effect of charge variations across different pH conditions. In contrast, the carboxymethyl group at the end of PEG-CM chains can ionize depending on the pH, acquiring a negative charge at higher pH values that enhances the stability of coated NPs in basic media. However, the behavior of gold NPs coated with PEG-NH_2 was notably different, with both AuNRs and AuNSs displaying extremely high hydrodynamic sizes in the pH range 7-10. For instance, AuNRs-PEG-NH_2 reached a maximum hydrodynamic size up to 583 ± 47 nm when dispersed in medium at pH 9 (Figure 3.12 C), while this value was even higher, 630 ± 26 nm, in the case of AuNSs-PEG-NH_2 dispersed at pH 10 (Figure 3.12 D). This strong aggregation of PEG-NH_2-coated NPs likely stems from the previously established low surface charge of the nanostructures in the pH range 7-10, which reduces electrostatic repulsion between the NPs and ultimately promotes their uncontrolled aggregation. At pH values below 7, however, both AuNRs and AuNSs coated with PEG-NH_2 remained colloidally stable, with hydrodynamic sizes values consistent with the absence of aggregation. Interestingly, these nanosystems also showed reduced hydrodynamic sizes when dispersed in highly basic environments (pH 12), likely due to the precipitation of most NPs upon their aggregation, with only a small number of NPs remaining well-dispersed and measured by DLS.

In conclusion, this study demonstrated the significant role of PEGylation type in the surface charge and colloidal stability of both AuNRs and AuNSs across varying pH conditions. All the designed nanosystems exhibited a trend of becoming more negatively charged with increasing pH. The observed PZC shifts suggest that PEG-NH_2-coated nanostructures are more sensitive to pH changes, particularly in the neutral to basic range. This fact correlates with the large

aggregation degrees observed for AuNRs and AuNSs coated with PEG-NH_2 in media at 7-10 pH. In contrast, mPEG and PEG-CM coatings conferred a robust colloidal stability to gold NPs, maintaining consistent hydrodynamic sizes across the entire pH range analyzed.

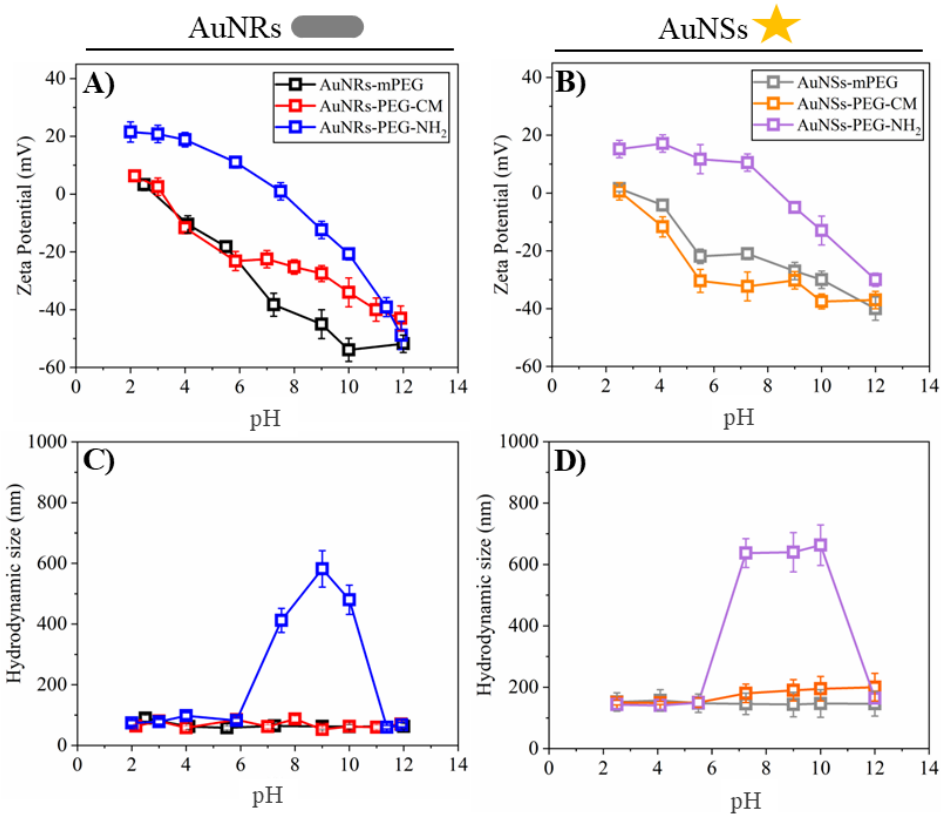

Figure 3.12. Zeta potential of PEG-coated A) AuNRs and B) AuNSs, and hydrodynamic size of PEG-coated C) AuNRs and D) AuNSs, upon dispersion in media with pH ranging from 2 to 12.

3.7 *In Vitro* Evaluation of Gold NPs Internalization, Biocompatibility, and Cell Death Mechanisms

This section investigates the biological response of MDA-MB-231 and Balb/c 3T3 cells incubated with AuNRs and AuNSs under various experimental conditions through a series of *in vitro* assays. First, cellular internalization of AuNRs and AuNSs will be investigated using confocal microscopy, TEM, and ICP-MS. These techniques will provide detailed insights into NPs uptake, biodistribution, and intracellular localization. Following internalization studies, cell viability will be assessed using the CCK-8 assay both before and after CW laser irradiation to evaluate the potential cytotoxic effects induced by treatments based on the designed gold NPs. This analysis will help to determine the influence of laser exposure on cellular

metabolism and survival. Next, the mechanisms underlying cell death triggered by CW laser illumination will be examined using flow cytometry, allowing for differentiation between apoptosis and necrosis. Finally, an additional study will assess both cell viability and death mechanisms after irradiating the NPs-incubated cells with a pulsed laser. This will offer a comprehensive understanding of the impact of ultrafast laser pulses on cellular behavior, which could be crucial for applications in photothermal therapy and nanomedicine.

3.7.1 Cell Internalization Studies by Confocal, TEM and ICP-MS

Cellular internalization of AuNRs and AuNSs was investigated through a combination of confocal microscopy, TEM, and ICP-MS to properly assess NPs uptake and intracellular distribution. Reflectance confocal microscopy, a label-free imaging technique, utilizes scattering properties to visualize NPs internalization in real time, providing valuable information about their localization and interaction with intracellular structures. On the other hand, TEM provides high-resolution ultrastructural details, enabling precise visualization of NPs morphology, intracellular positioning, and potential interactions with organelles. ICP-MS is a highly sensitive analytical technique that allows to determine the elemental composition of internalized NPs, providing accurate measurements of cellular uptake efficiency. By integrating these complementary techniques, a thorough understanding of NPs internalization and their intracellular fate can be obtained, facilitating the development of effective NPs-based strategies for various biomedical applications.

3.7.1.1 Confocal Microscopy Study of Gold NPs Internalization

Confocal microscopy technique plays a pivotal role in studying NPs internalization by providing high-resolution, nondestructive and three-dimensional imaging, enabling their precise localization within cells. By minimizing out-of-focus light, it effectively distinguishes internalized NPs from those bound to cell surface. Reflectance confocal microscopy, which leverages the intrinsic optical properties of metallic NPs, enables real-time tracking of NPs uptake and intracellular distribution.[202]

Here we analyzed the internalization of mPEG, PEG-CM and PEG-NH_2-coated AuNRs and AuNSs in MDA-MB-231 cells, while in Balb/c 3T3 cells the uptake study was restricted to mPEG-coated nanostructures. mPEG-coated NPs were tested in Balb-3T3 as a model cell line in order to assess the intrinsic biocompatibility of the polymer-coated metallic NPs and

decipher the potential presence of off-target effects produced by the nanoparticle entity itself by excluding any potential interference/effect provided by the presence of surface charge groups in the polymeric functionalizing layer. AuNRs and AuNSs dispersions at concentrations of 1.50×10^{11} and 1.50×10^{9} NP·mL^{-1}, respectively, were incubated with cells for 24 h, followed by staining with Phalloidin Alexa Fluor™ 647 and DAPI for microscopy characterization (see detailed procedure in chapter 2).

The obtained confocal microscopy images showed high degrees of internalization of AuNSs coated PEG-NH_2, PEG-CM and mPEG in MDA-MB-231 cells upon 24 h incubation (Figure 3.13 A-C). Additionally, the designed star-shaped gold nanostructures coated with mPEG were also successfully internalized when incubated with Balb/c 3T3 cells (Figure 3.13 D). However, the internalization of AuNRs coated with PEG-NH_2, PEG-CM and mPEG by both cell lines could not be confirmed by reflectance confocal microscopy (Figure 3.13 E-H). While the nuclei and cytoplasm of the cells were clearly visible, the expected reflectance from the rod-shaped gold nanoparticles was not detectable, either inside or outside the cells. Here, it is important to note that the reflectance mode of gold nanostructures depends on their ability to scatter light, which drastically diminishes below a certain size threshold. Thus, the lower contrast of the designed AuNRs upon their incubation and internalization within cells can be attributed to their smaller size compared to AuNSs. [202] In this way, it cannot be discarded that AuNRs were indeed internalized by the cells, and further investigations using TEM and ICP-MS will be conducted to confirm the internalization of this type of gold NPs (see next sections).

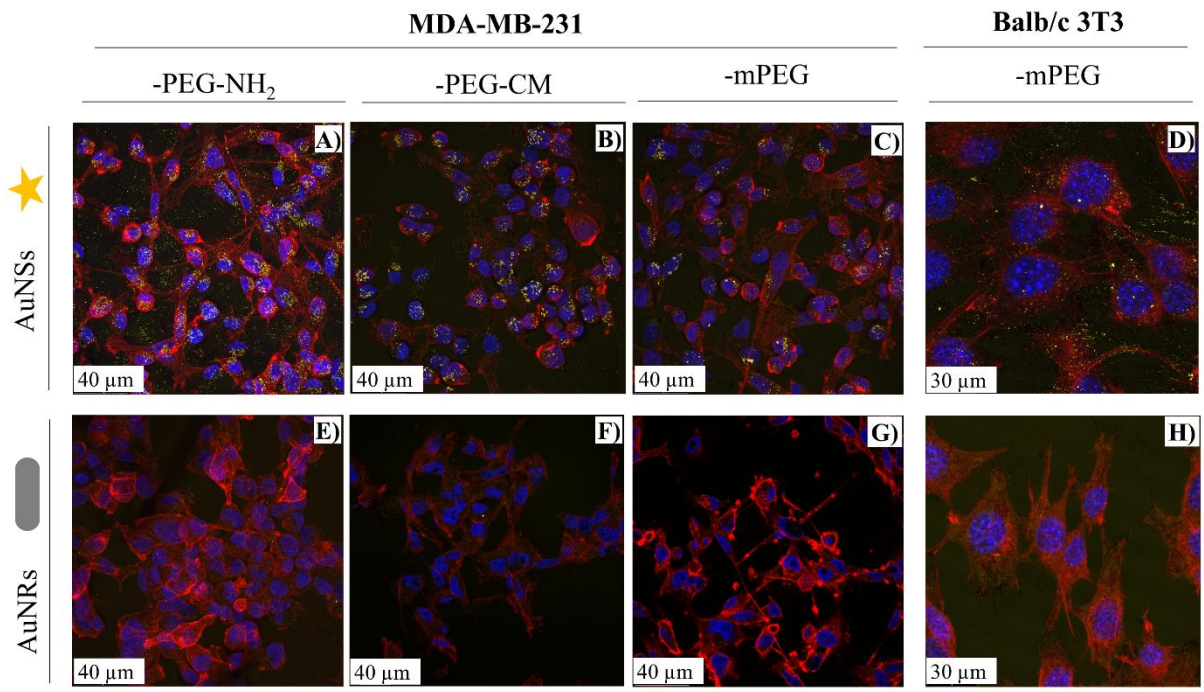

Figure 3.13. Reflectance confocal microscopy images of: MDA-MB-231 cells incubated with A) AuNSs-PEG-NH_2, B) AuNSs-PEG-CM, and C) AuNSs-mPEG. D) Balb/c 3T3 cells incubated with AuNSs-mPEG. MDA-MB-231 cells incubated with E) AuNRs-PEG-NH_2, F) AuNRs-PEG-CM, and G) AuNRs-mPEG. H) Balb/c 3T3 cells incubated with AuNRs-mPEG.

3.7.1.2 TEM Study of Gold NPs Internalization

To further confirm the internalization of AuNSs within the cells and assess whether AuNRs were successfully uptaken, TEM images were acquired. Moreover, this microscopy technique provides detailed insights into the internalization mechanism and intracellular distribution of nanostructured materials.

As in previous confocal experiments, PEG-coated AuNRs and AuNSs colloidal dispersions at concentrations of 1.50 x 10^{11} and 1.50 x 10^{9} NP·mL^{-1}, respectively, were incubated with both Balb/c 3T3 and MDA-MB-231 cell lines for 24 h before TEM characterization. As in the previous microscopy study, the internalization of gold NPs functionalized with mPEG, PEG-CM, and PEG-NH2 was evaluated in MDA-MB-231 cells, while the uptake by Balb/c 3T3 cells was only studied for the case of mPEG-coated nanostructures.

The obtained TEM images confirmed that MDA-MB-231 internalized AuNSs coated with the three different PEGs after 24 h incubation. The degree of internalization varied depending on the type of PEG used for functionalization, with AuNSs-PEG-NH_2 being internalized in greater amounts than AuNSs-PEG-CM and AuNSs-mPEG (Figure 3.14 A-F). Nevertheless, these latter two types of PEG-coated AuNSs were also clearly visible inside cells in the acquired images, indicating successful internalization in MDA-MB-231 cells. In the same manner, mPEG-coated AuNSs were also internalized by Balb/c 3T3 cells after 24 h incubation (Figure 3.14 M-N), corroborating confocal microscopy results and suggesting that both cell lines efficiently internalized PEG-coated star-shaped gold NPs under similar conditions.

On the other hand, TEM images provided a more detailed analysis AuNRs internalization, which could not be fully assessed by confocal microscopy because of the reduced size of the designed rod-shaped nanostructures. Thus, it was established that AuNRs were internalized by both types of cells, but in a significantly lower extent than AuNSs. This was particularly evident for mPEG-coated AuNRs, for which very few internalized nanostructures were observed in both MDA-MB-231 and Balb/c 3T3 cells (Figure 3.14 G-H and O-P). AuNRs-PEG-CM and, especially, AuNRs-PEG-NH_2, were internalized by MDA-MB-231 cells to a greater extent, though still at lower levels compared to their star-shaped counterparts (Figure 3.14 I-L).

The higher internalization degree of AuNSs compared to AuNRs by both cell lines can be attributed to their spike-like structure that replicates the typical morphology of viruses, thus potentially triggering cellular pathways involved in pathogen recognition and internalization. This observation aligns with the findings from Pakravan *et al*., who demonstrated that gold NPs with well-defined star morphologies were internalized in larger amounts than NPs with other shapes, such as rods, in MCF7 cells.[203] Similar effects have been observed with other nanomaterials, such as mesoporous silica NPs, which are internalized more efficiently when designed with virus-like shapes.[204]

Regarding the internalization mechanism and sub-cellular distribution of PEG-coated gold NPs, it was observed that all types of AuNSs were primarily localized in the cytoplasm of MDA-MB-231 cells, mostly within endosomal vesicles, suggesting endocytosis as the primary internalization pathway. AuNSs-mPEG were found in secondary lysosomes (Figure 3.14 A-B), while AuNSs-PEG-CM were detected within heterogeneous lysosomes (Figure 3.14 C) and

autophagosomes—structures formed when the cell engulfs organelles marked for degradation (Figure 3.14 D). In the case of AuNSs-PEG-NH_2, large amounts of these star-shaped nanostructures were observed in multivesicular bodies and secondary lysosomes within MDA-MB-231 cells (Figure 3.14 E, F). In the same manner, there was also substantial evidence that supported the cellular internalization of AuNRs by MDA-MB-231 *via* endocytosis. For example, in Figure 3.14 G-H, multivesicular bodies and a clathrin pit are clearly visible, supporting the hypothesis of clathrin-mediated endocytosis as the mechanism of AuNRs-mPEG uptake. Additional evidence was provided by the localization of AuNRs-PEG-CM within lysosomes (Figure 3.14 J), indicating potential lysosomal entrapment, while AuNRs-PEG-NH_2 were observed within endosomes (Figure 3.14 K) and secondary lysosomes (Figure 3.14 L).

In the case of mPEG-coated AuNSs and AuNRs internalized by Balb/c 3T3 cells, the star-shaped nanostructures were predominantly located in autophagosomes (Figure 3.14 M-N), suggesting uptake through autophagic pathways in which the cell engulfs and processes cellular components. In contrast, AuNRs-mPEG were mainly found within lysosomes (Figure 3.14 O-P), indicating potential entrapment and degradation within these organelles.

Thus, this study highlights the importance of employing multiple imaging techniques to accurately assess the cellular uptake of nanomaterials. The previously performed confocal microscopy characterization has been well-complemented with the obtained TEM images to better elucidate the bio-interaction between cells and NPs.

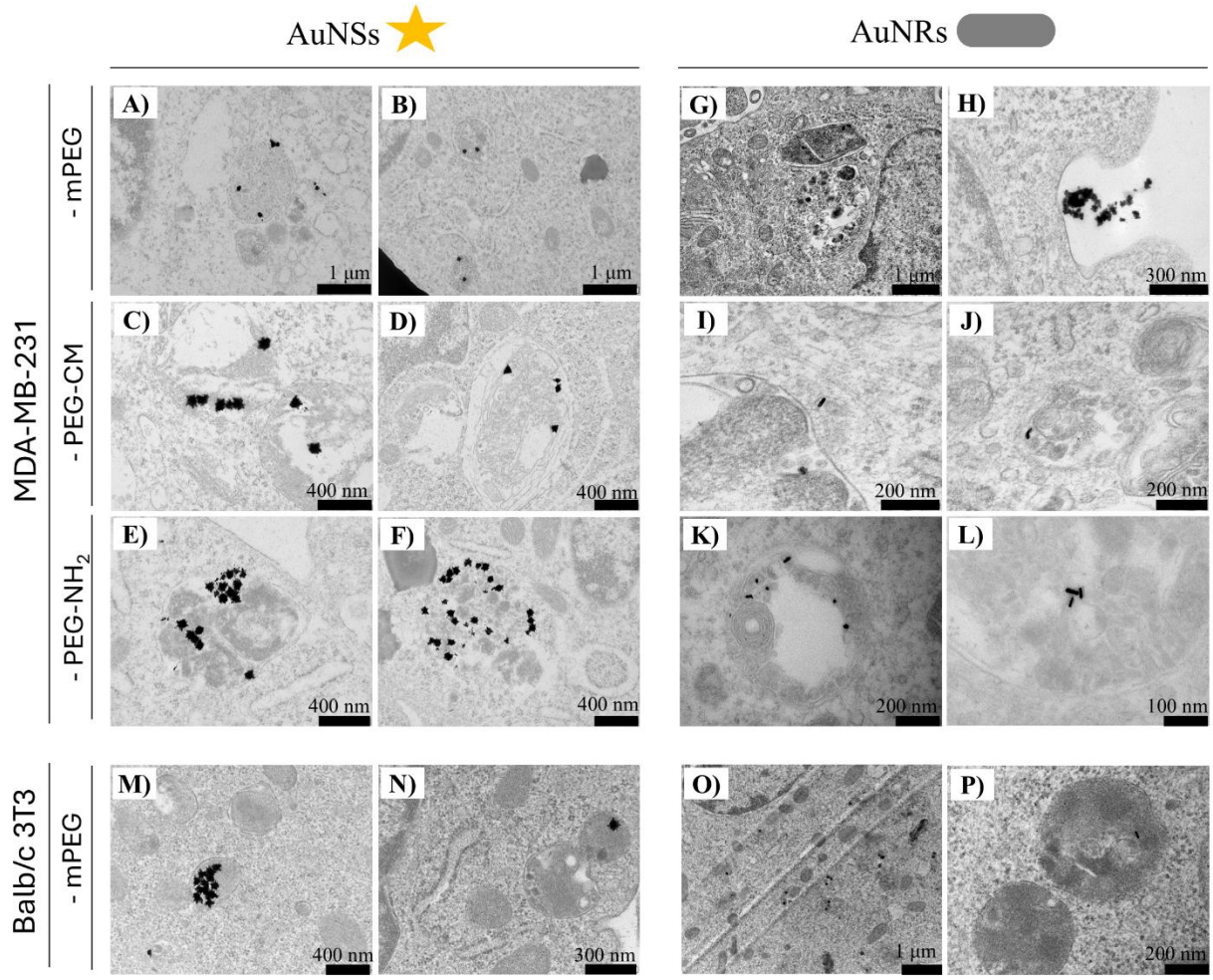

Figure 3.14. TEM images after 24 h incubation of MDA-MB-231 cells and: AuNSs coated with A-B) mPEG, C-D) PEG-CM, and E-F) PEG-NH_2; AuNRs coated with G-H) mPEG, I-J) PEG-CM, and K-L) PEG-NH_2. TEM images after 24 h incubation of Balb/c 3T3 cells and: M-N) AuNSs coated with mPEG, and O-P) AuNRs coated with mPEG.

3.7.1.3 Quantitative Analysis of Cellular Internalization by ICP-MS

After performing a qualitative analysis of the cellular internalization of gold NPs through confocal microscopy and TEM, ICP-MS was used to quantitatively assess the uptake of PEG-coated AuNRs and AuNSs by MDA-MB-231 and Balb/c 3T3 cells. ICP-MS is an elemental analysis technique that ionizes samples using high-temperature plasma and measures the ion mass-to-charge ratio. In our study, ICP-MS allowed precise quantification of the amount of

gold inside the cells, which then can be related to the internalization degree of both AuNRs and AuNSs.

For this analysis, MDA-MB-231 and Balb/c 3T3 cells were incubated for 24 h with PEG-coated gold NPs at four different concentrations ranging from 1.0 x 10^{11} to 1.2 x 10^{12} NP·mL^{-1} in the case of AuNRs, and from 1.5 x 10^{9} to 1.5 x 10^{10} NP·mL^{-1} in the case of AuNSs. After incubation, the cells were washed with PBS to remove any non-internalized gold NPs. The cells were then detached using trypsin, collected, and prepared for gold concentration measurements *via* ICP-MS (see the detailed procedure in Chapter 2).

As shown in Figure 3.15 A-D, the cellular uptake of both AuNRs and AuNSs, increased when increasing the initial administered NPs concentration; however, beyond a certain threshold, the NP uptake reached a plateau, and no additional particle internalization was observed. This trend was consistent across all types of NPs, regardless of the cell type interacting with. This behavior can be attributed to metabolic alterations within the cells, which begin to interfere with their ability to internalize additional NPs.[205] As the cells become saturated, various metabolic processes, including energy production and receptor availability, may be disrupted, leading to a halt in NPs uptake. Furthermore, cells may activate protective mechanisms such as exocytosis to expel accumulated NPs, thereby mitigating potential toxicity and maintaining cellular homeostasis. These adaptive responses highlight the dynamic interplay between nanoparticle exposure and cellular defense mechanisms.[206, 207]

The general trend previously described, which correlates gold NPs concentration in the incubation procedures with the amount of gold detected inside cells, was observed for both AuNRs and AuNSs, as well as for both cell lines analyzed, and the three types of PEGs used for NPs functionalization. However, in terms of absolute values, the performed ICP-MS measurements revealed that the amount of gold inside cells was higher upon incubation with AuNSs compared to AuNRs. Regarding the type of coating, cell incubation with PEG-NH_2-coated NPs resulted in higher gold amounts inside cells than those measured upon incubation with mPEG or PEG-CM-coated nanostructures in both Balb/c 3T3 and MDA-MB-231 cells (Figure 3.15 A-D). In this way, and since the amount of gold inside cells after incubation correlates with the internalization degree of gold NPs, the ICP-MS data obtained align well with previous confocal and TEM results, which showed the higher cellular internalization capability of AuNSs compared to AuNRs, as well as for PEG-NH_2-coated gold NPs.

As mentioned, the performed compositional analysis enables the calculation of the percentage of AuNRs and AuNSs successfully internalized by the cells during the incubation processes. To determine this, the amounts of gold measured within the cells after the 24 h incubation period were normalized to the initial gold content in the NPs dispersions, with both values quantified using ICP-MS (Table 3.1). In this way, it was established that the highest internalization percentages of gold NPs within MDA-MB-231 cells occurred at the lowest concentrations of both AuNRs and AuNSs here analyzed (1.0 x 10^{11} NP·mL^{-1} and 1.5 x 10^{9} NP·mL^{-1}, respectively). Specifically, the NPs uptake percentages for -mPEG, -PEG-CM, and -PEG-NH_2-coated AuNRs were 0.10% (21 μg·L^{-1}), 0.12% (25 μg·L^{-1}), and 0.20% (40 μg·L^{-1}), respectively, while for AuNSs coated with mPEG, PEG-CM, and PEG-NH_2, the obtained values were ca. 0.10 % (60 μg·L^{-1}), 0.18% (110 μg·L^{-1}), and 0.36% (220 μg·L^{-1}), respectively. On the other hand, the correlation between the internalization percentages of AuNRs and AuNSs within the other type of cells here analyzed (Balb/c 3T3), and the initial concentration of gold NPs showed a slightly different pattern. In this case, the highest uptake percentages were observed at the third-highest concentration for both typologies of gold nanostructures (6.0 x 10^{11} NP·mL^{-1} for AuNRs and 7.5 x 10^{9} NP·mL^{-1} for AuNSs, respectively). At this concentration, AuNRs functionalized with mPEG, PEG-CM, and PEG-NH_2 exhibited internalization degrees with Balb/c 3T3 cells of 0.01% (12.5 μg·L^{-1}), 0.03% (38 μg·L^{-1}), and 0.06% (79 μg·L^{-1}), respectively. For AuNSs coated with mPEG, PEG-CM, and PEG-NH_2, these uptake percentages were *ca*. 0.014% (41 μg·L^{-1}), 0.019% (58 μg·L^{-1}), and 0.033% (100 μg·L^{-1}), respectively (Table 3.1).

These observations indicate that increasing the concentration of NPs does not necessarily result in higher cellular internalization. On the contrary, in some cases the highest uptake was observed at the lowest NPs concentration, which could be advantageous for minimizing potential cytotoxic effects of the nanostructures, making them more suitable for biomedical applications.

Table 3.1. ICP-MS quantification of gold concentration (gold uptake percentages) for various PEG-terminated AuNRs and AuNSs internalized by Balb/c 3T3 and MDA-MB-231 cells.

		Balb/c 3T3			MDA-MB-231		
Concentration [NPs·mL^{-1}]		**mPEG**	**PEG-CM**	**PEG-NH_2**	**mPEG**	**PEG-CM**	**PEG-NH_2**
AuNRs	1.0 x 10^{11}	0.003	0.004	0.050	**0.105**	**0.125**	**0.200**
	3.0 x 10^{11}	0.003	0.002	0.053	0.060	0.075	0.150
	6.0 x 10^{11}	**0.010**	**0.032**	**0.066**	0.060	0.070	0.200
	1.2 x 10^{12}	0.005	0.017	0.033	0.007	0.010	0.017
AuNSs	1.0 x 10^{9}	0.008	0.012	0.033	**0.100**	**0.180**	**0.360**
	3.0 x 10^{9}	0.008	0.011	0.033	0.060	0.100	0.225
	6.0 x 10^{9}	**0.014**	**0.019**	**0.033**	0.049	0.060	0.106
	1.2 x 10^{10}	0.007	0.010	0.017	0.025	0.030	0.050

The higher cell uptake observed for PEG-NH_2-coated NPs (Figure 3.15 A-D) can be related to the attractive electrostatic forces between the positively charged NH_2-functional groups and the negatively charged cell membranes. Additionally, the results confirmed that MDA-MB-231 cells internalized a larger amount of both NP types with various PEG coatings at all analyzed concentrations when compared to Balb/c 3T3 ones. These findings are consistent with the results obtained by TEM and confocal microscopy, and also agree with recent studies as that of, for example, Xiao-jiao *et al.* who investigated the effect of nanoparticle surface charge on cellular uptake. This work demonstrated that positively charged polyethylene glycol-block-polylactic acid (PEG-PLA) NPs were taken up by Caco-2 cells in vitro and intestinal epithelial cells in vivo, in greater amounts and through multiple internalization pathways compared to their zwitterionic and negatively charged counterparts.[208]

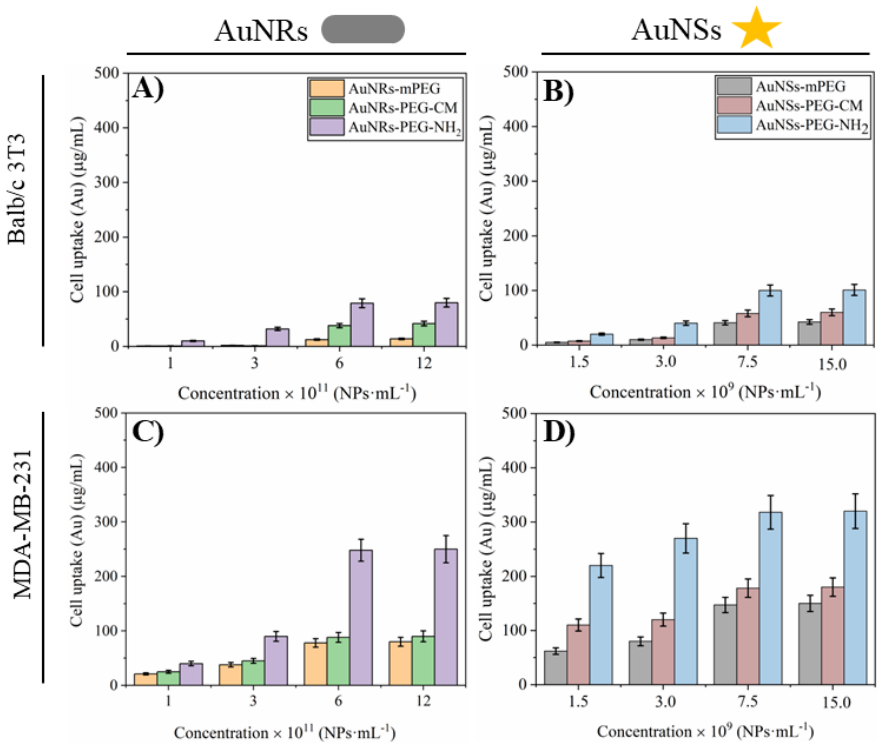

Figure 3.15. ICP-MS measurements to determine gold concentration inside cells upon 24 h incubation with PEG-coated gold NPs at different concentrations: Balb/c 3T3 cells incubated in the presence of A) AuNRs and B) AuNSs; and MDA-MB-231 cells incubated in the presence of C) AuNRs and D) AuNSs.

3.7.2 Cell Viability Before and After CW Laser Irradiation

The bio-interaction of metallic nanostructures with cells is influenced by several factors, including the physiochemical characteristics of the NPs, the type of cells, or the endocytic pathways involved.[209] Among these, the surface chemistry of nanosystems is undoubtedly one of the most critical aspects that dictates their biological interactions and biocompatibility. In this regard, as discussed above, PEGylation is a widely explored functionalization strategy to enhance the colloidal stability of gold-based NPs while preserving their plasmonic properties. Additionally, attaching PEG chains to the surface of gold NPs improves their ability to target specific sites, minimizes potential adverse side effects, and enhances their biocompatibility. Moreover, in the specific case of the AuNRs designed in this work, the as-synthesized rod-shaped NPs were stabilized with an inherently cytotoxic surfactant such as CTAB, making their PEGylation essential to render them non-cytotoxic.

After evaluating the cellular internalization of PEG-coated gold NPs, in this section we assessed their *in vitro* biocompatibility in both Balb/c 3T3 and MDA-MB-231 cell lines. For this, AuNRs and AuNSs functionalized with mPEG, PEG-CM, or PEG-NH_2 were incubated with cells at different concentrations for 24 h. Specifically, the concentration ranges evaluated were 3.2 x 10^9 - 4.0 x 10^{11} NP·mL^{-1} for AuNRs and 1.0 x 10^8 - 5.0 x 10^9 NP·mL^{-1} for AuNSs, thus matching the OD values of both types of dispersions. The effect of CW laser irradiation (2.0 W·cm^{-2} for 5 min) was also analyzed by irradiating the cells after 24 h incubation with NPs, followed by a 24 h post-irradiation incubation period.

As shown in Figure 3.16 A-D, AuNRs and AuNSs coated with the three different types of PEGs were not cytotoxic for both Balb/c 3T3 and MDA-MB-231 cell lines in the absence of laser irradiation, with cell viabilities exceeding 90% after 24 h incubation in all cases. This confirms that the designed PEG-coated gold nanostructures are highly biocompatible within the tested concentration ranges. The high biocompatibility of both AuNRs and AuNSs arises from the chemically inert nature of gold, that does not undergo oxidation or other reactions that could produce harmful by-products.[210] On the other hand, as already discussed, the PEGs used to functionalize the NPs rarely provoke harmful biological reactions and are FDA-approved for medical applications.[211]

However, NIR light irradiation of cells after 24 h incubation with gold NPs led to significant decreases in cell viabilities, with the degree of cytotoxicity depending on the NPs morphology and concentration, the type of PEG coating, and the cell line evaluated. Thus, the viability of both Balb/c 3T3 and MDA-MB-231 cells decreased further with increasing concentrations of gold nanostructures following laser irradiation (Figure 3.16 E-H). This was attributed to the larger amount of heat generated during laser irradiation at higher concentrations of plasmonic NPs, leading to localized hyperthermia which causes protein denaturation, disruption of cellular metabolism, and ultimately cell death.[212] Regarding the effect of gold NPs morphology, it was observed that cells incubated with AuNSs exhibited greater decreases in viability than those treated with AuNRs upon laser irradiation. This distinct behavior was attributed to the higher internalization degree of AuNSs, as confirmed by microscopy images and ICP-MS measurements (see Section 3.7.1).

Focusing on the specific effect of different PEG coatings, it was established that PEG-NH_2-coated gold NPs induced the largest decrease in cell viability following laser irradiation. For

instance, the viability of Balb/c 3T3 cells incubated with the highest concentrations of AuNRs-PEG-NH_2 and AuNSs-PEG-NH_2 decreased by 76% ± 6 and 70% ± 8, respectively, while in the case of MDA-MB-231 cells these values decreased even more, reaching 70% ± 2 and 61% ± 4, respectively (Figure 3.16 E-H). This heightened cytotoxicity was due to the already discussed protonation of the terminal groups of PEG-NH_2 chains, facilitating stronger electrostatic interactions with negatively charged cell membranes and leading to higher NP internalization and a more pronounced photothermal effect. On the other hand, AuNRs and AuNSs with PEG-CM and mPEG coatings showed less cytotoxicity, with lower reductions in cell viability. The slightly higher biocompatibility after CW laser irradiations of NPs coated with mPEG when compared to those coated with PEG-CM also arises from the different cell internalization degrees of the nanostructures depending on the performed functionalization.

Finally, a direct comparison between cell lines revealed that, in general, the viability of MDA-MB-231 cells decreased more significantly than that of Balb/c 3T3 cells after incubation with gold NPs and light irradiation. This was due to the well-established accelerated metabolism of cancer cells, such as MDA-MB-231, which led to higher levels of NPs uptake compared to those observed in healthy cells like Balb/c 3T3.[213] This higher metabolic activity of cancer cells was first described nearly a century ago by Otto Warburg, who found that tumors consume more glucose than normal tissues and typically convert it to lactate, rather than oxidizing it in the mitochondria, even in the presence of abundant oxygen.[214]

In conclusion, in the absence of laser irradiation, PEG-coated AuNRs and AuNSs demonstrated extremely high biocompatibility, with cell viabilities exceeding 90% in both Balb/c 3T3 and MDA-MB-231 cells across the analyzed concentration ranges. Upon CW laser irradiation, cell viabilities decreased in a concentration-dependent manner, with AuNSs being more cytotoxic than AuNRs due to their higher internalization levels. PEG-NH_2-coated gold NPs, in particular, exhibited greater cytotoxicity due to enhanced internalization *via* electrostatic interactions, while cancer cells displayed increased sensitivity due to their higher metabolic activity.

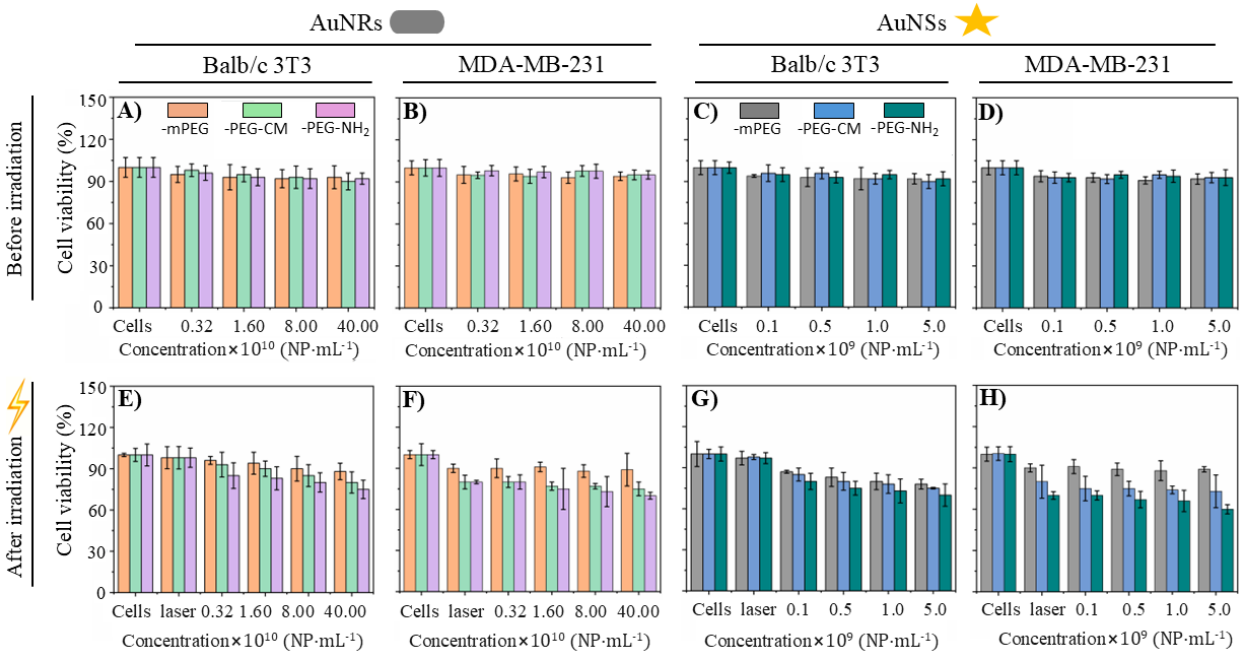

Figure 3.16. Cell viability in the absence of laser irradiation of A) Balb/c 3T3 and B) MDA-MB-231 cells incubated PEG-coated AuNRs, and C) Balb/c 3T3 and D) MDA-MB-231 cells incubated PEG-coated AuNSs. Cell viability after CW laser irradiation (2.0 $W \cdot cm^{-2}$, 5 min) of E) Balb/c 3T3 and F) MDA-MB-231 cells incubated PEG-coated AuNRs, and G) Balb/c 3T3 and H) MDA-MB-231 cells incubated PEG-coated AuNSs.

3.7.3 Cell Death Mechanisms Induced by AuNRs and AuNSs Upon CW Laser Irradiation

The specific cell death mechanisms induced by gold-based NPs during photothermal treatments are pivotal in determining the effectiveness and specificity of the therapeutic procedures. Analyzing in detail how cells respond to temperature increases generated by plasmonic NPs upon light irradiation is essential for optimizing therapies, enhancing the efficacy of cancer cells destruction while minimizing damage to surrounding healthy tissues. Furthermore, understanding the pathways of cell death can provide insights into overcoming resistance mechanisms in cancer cells, leading to more effective treatment outcomes.[215] Interestingly, the activation of the different cell death pathways is highly dependent on the intensity and duration of heat exposure, which are dictated by the physicochemical properties of the plasmonic nanostructures and the irradiation conditions.

In this study, we evaluated the cell death mechanisms induced by the designed AuNRs and AuNSs upon irradiation with CW laser using flow cytometry with an Annexin V/Propidium Iodide assay. Specifically, the cell death mechanism induced by mPEG- and PEG-NH_2-coated AuNRs and AuNSs were assessed in Balb/c 3T3 and MDA-MB-231 cells. In all cases, the cells were incubated with the different nanostructures for 24 h, followed by irradiation at 2.0 $W \cdot cm^{-2}$ for 5 min, and finally performing flow cytometry measurements after an additional 24 h incubation period post-irradiation to allow sufficient time for cell death to occur. Untreated cells were used as a negative (live) control, while cells incubated with 5 µM Doxorubicin (Doxo) served as positive controls for apoptosis and cells treated with Triton X-100 were used as a control for necrosis.

As expected, both the Balb/c 3T3 and MDA-MB-231 cells that were not treated or incubated with gold NPs exhibited very high viability (> 94.1% in all cases) after the incubation period (Figure 3.17A and 3.18 A). Following laser irradiation, the viability of these untreated cells decreased only marginally, remaining above 91.3% for both cell types (Figure 3.17 B and 3.18 B). These minimal reductions in cell viability were attributed to slight temperature increases in the biological solutions induced by the laser irradiation itself, which may cause minor damage to cellular components such as proteins and lipids.[216] In contrast, significant decreases in viability were observed when cells were incubated with Doxo as a positive control. Specifically, Doxo-treated Balb/c 3T3 cells exhibited a viability of 43.1%, with 13.7% of cells in late apoptosis (Figure 3.17 C). In the case of MDA-MB-231 cells treated with the chemotherapeutic drug, they showed a remarkably lower viability of 73.8 % upon their incubation with the chemotherapeutic drug, with 22.0 % of cells undergoing apoptosis (Figure 3.18 C). These percentages increased when Doxo treatment was combined with CW laser irradiation; under these conditions, the proportion of apoptotic cells in Balb/c 3T3 cells rose to approximately 15.5 %, while the percentage of apoptotic cells in MDA-MB-231 cells increased to *ca*. 50% (Figures 3.17 D and 3.18 D). Moreover, a much higher rate of necrotic cells rate upon Doxo administration was observed in Balb/c 3T3 cells (46.8%) compared to MDA-MB-231 (4.9%). These results can be attributed to the increased sensitivity of Balb/c 3T3 cells to chemical agents. This cell line is particularly sensitive to toxic compounds and, for this reason, is widely used in the cosmetic, dermatological, and pharmaceutical industries. Conversely, MDA-MB-231 cells, a triple-negative breast cancer cell line, are known for their

aggressive phenotype and notable resistance to chemotherapeutic drugs. Moreover, their exceptionally high proliferation rate may further enhance their ability to withstand cytotoxic stress, making them more resilient to treatments that are, otherwise, highly toxic in other cell lines.[217–222]

On the other hand, both Balb/c 3T3 and MDA-MB-231 cells undergo lysis following the Triton X-100 treatment used as necrosis control (Figure 3.17 E and 3.18 E). This is due to the disruption of hydrogen bonding within the lipid membranes by the polar head groups of Triton, compromising membrane integrity and causing cell lysis.[223] Hence, the scarce number of events detected by flow cytometry is a consequence of the high level of cell mortality induced by necrosis, and those detected are mainly related to the presence of live and/or apoptotic cells.

Upon CW laser illumination, Balb/c 3T3 cells incubated with either AuNRs or AuNSs exhibited important apoptosis, with rates of *ca*. 10.5 % and 18.2 % for AuNRs-mPEG and AuNRs-PEG-NH_2, and 22.2 % and 28.9 % for AuNSs-mPEG and AuNSs-PEG-NH_2, respectively (Figure 3.17 F-I). In contrast, MDA-MB-231 cells primarily underwent necrosis following exposure to these functionalized NPs and following CW laser illumination, with necrosis rates of approximately 14.7 % and 21.7 % for AuNRs-mPEG and AuNRs-PEG-NH_2, and 24.4 % and 32.9 % for AuNSs-mPEG and AuNSs-PEG-NH_2, respectively (Figure 3.18 F-I).

A smaller proportion of MDA-MB-231 cells exhibited apoptosis, with rates of 14.1 % and 10.9 % for AuNRs-PEG-NH_2 and AuNSs-PEG-NH_2, respectively (Figure 3.18 G, I). This higher necrosis rate for MDA-MB-231 cells incubated in the presence of plasmonic gold NPs could be originated from plasmonic heating, which generates localized high temperatures leading to protein denaturation, membrane rupture, and organelle damage, resulting in necrotic cell death.[224]

In summary, flow cytometry analysis revealed distinct cell death pathways between Balb/c 3T3 and MDA-MB-231 cells following incubation with gold nanostructures and CW laser irradiation. Balb/c 3T3 cells incubated with either AuNRs or AuNSs coated with different PEG terminal groups, exhibited a higher proportion of apoptosis than necrosis after 24 h of incubation and subsequent laser exposure. In contrast, MDA-MB-231 cells displayed predominant necrosis over apoptosis after treatment with either AuNRs or AuNSs coated with

the same PEG terminal groups and exposure to CW laser irradiation. Furthermore, in both cell lines, greater overall cell death was observed in cells incubated with AuNSs compared to those incubated with AuNRs, consistent with the viability data presented in Section 3.7.2.

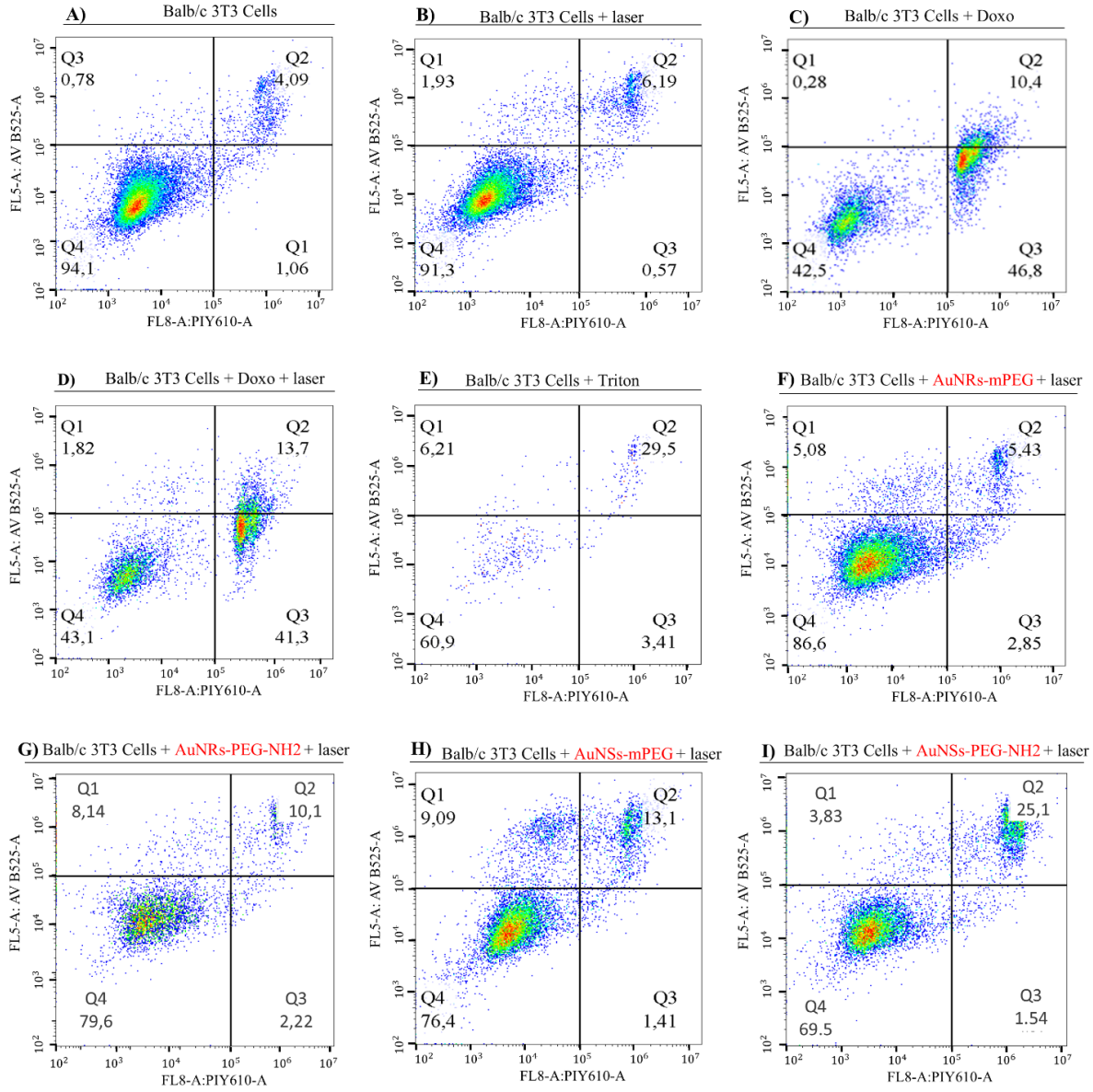

Figure 3.17. Flow cytometry analysis of Balb/c 3T3 cells under various conditions. The controls included: A) untreated cells, B) irradiation with CW laser, C) incubation with 5 µM Doxo, D) incubation with 5 µM Doxo following irradiation, and E) treatment with Triton X-100. The studies involving incubation with gold NPs following irradiation included: F) AuNRs-mPEG, G) AuNRs-PEG-NH_2, H) AuNSs-mPEG, I) AuNSs-PEG-NH_2. CW irradiations were performed at 2.0 $W \cdot cm^{-2}$ for 5 min. Quadrants: Q1 (early apoptosis), Q2 (late apoptosis), Q3 (necrotic cells), and Q4 (live cells).

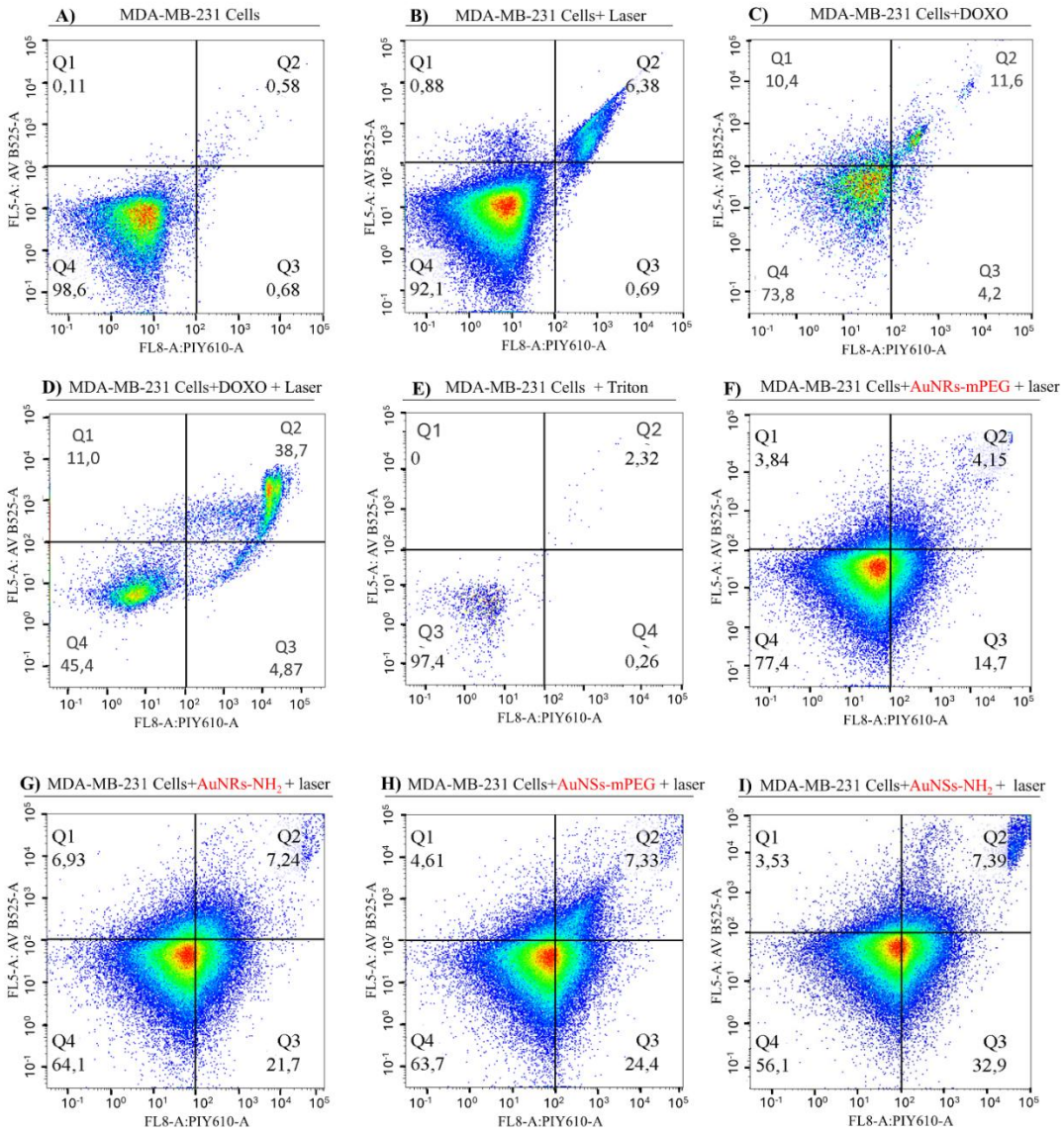

Figure 3.18. Flow cytometry analysis of MDA-MB-231 cells under various conditions. The controls included: A) untreated cells, B) irradiation with CW laser, C) incubation with 5 µM Doxo, D) incubation with 5 µM Doxo following irradiation, and E) treatment with Triton X-100. The studies involving incubation with gold NPs following irradiation included: F) AuNRs-mPEG, G) AuNRs-PEG-NH_2, H) AuNSs-mPEG, I) AuNSs-PEG-NH_2. CW irradiations were performed at 2.0 W·cm^{-2} for 5 min. Quadrants: Q1 (early apoptosis), Q2 (late apoptosis), Q3 (necrotic cells), and Q4 (live cells).

3.7.4 Pulsed Laser Irradiation of Cells Incubated with Gold NPs: Impact on Viability and Cell Death Mechanisms

As previously highlighted, fs lasers emit extremely short light pulses, resulting in very high peak powers. The combination of this intense irradiation and the brief duration of the pulses allows for more precise and localized energy deposition at the target site. This is particularly critical in applications such as photothermal therapy using plasmonic NPs, where minimizing damage to surrounding healthy tissues is essential. In contrast, CW lasers can cause significant thermal diffusion and collateral tissue damage due to their prolonged exposure times.[225]

Given these characteristics, pulsed lasers are often considered more advantageous than CW lasers in various biomedical applications. In this section, we assess the effects of pulsed laser irradiation on cultured cells in the presence of the designed gold NPs, and compare these results to those previously obtained under CW irradiation conditions.

3.7.4.1 Cell viability After Pulsed Laser Irradiation

A preliminary evaluation of the effect of pulsed laser irradiation on cell viability was conducted using the MDA-MB-231 cancer cell line. The cells were incubated for 24 h with PEG-coated AuNRs and AuNSs dispersions at concentrations of 1.50 x 10^{11} and 1.50 x 10^{9} NP·mL^{-1}, respectively. After this incubation period, the systems were irradiated with an 800 nm fs laser for either 2 or 4 min at power densities of 1.0 and 3.0 W·cm^{-2}. These irradiation times and laser power densities were selected to match the energy absorption conditions of CW laser irradiation experiments performed in section 3.7.2. Following irradiation, the cells were incubated under standard culture conditions for an additional 24 h before assessing their viability. Control samples included cells incubated in the absence of gold NPs, both with and without pulsed laser irradiation.

As shown in Figure 3.19, MDA-MB-231 cells incubated in the absence of gold nanostructures exhibited high viability (> 95%) even when irradiated with the pulsed lased source at 3.0 W·cm^{-2} for 4 min. However, a reduction in viability was observed when the cells were incubated with AuNRs or AuNSs followed by pulsed irradiation, with the extent of reduction depending on the type of gold nanostructure, irradiation time, and applied laser power density. Specifically, increasing the irradiation time from 2 to 4 min and raising the power density from 1.0 to 3.0 W·cm^{-2} resulted in slight decreases in the viability of cells incubated with both AuNSs and

AuNRs. Considering the lowest cell viability after pulsed laser irradiation, MDA-MB-231 cells incubated with AuNRs coated with mPEG, PEG-CM, and PEG-NH_2 and irradiated at 3 $W \cdot cm^{-2}$ for 4 min exhibited survival rates of 90.3%, 84.2%, and 80.3%, respectively. Under the same conditions, cells treated with AuNSs coated with mPEG, PEG-CM, and PEG-NH_2 showed slightly lower viabilities, with values of 85.2%, 80.5%, and 76.1%, respectively.

This effect can be attributed to the enhanced photothermal response of the designed plasmonic NPs at higher intensities or longer irradiation durations. Furthermore, the also previously confirmed greater degree of cellular internalization of AuNSs compared to AuNRs led to more pronounced cytotoxicity for the star-shaped gold NPs under pulsed laser irradiation. In a similar way, the effect of coating was also consistent with our previous cellular internalization experiments, with PEG-NH_2-coated gold NPs showing increased cytotoxicity due to their higher cellular uptake.

It is noteworthy that under most irradiation conditions here analyzed, MDA-MB-231 cells incubated with PEG-coated AuNRs and AuNSs exhibited high viability, indicating the favorable biocompatibility of pulsed laser irradiation. Specifically, cells incubated with AuNRs displayed viabilities exceeding 80% across all irradiation conditions and for all three PEG coatings analyzed (Figure 3.19 A). When incubated with AuNSs, the highest cytotoxic effect was observed for PEG-NH_2-coated nanostructures under the maximum laser power density and exposure time, with cell viability decreasing to 76.2% ± 5.1 (Figure 3.19 B). Therefore, in all cases, the observed cell viabilities exceeded the typical threshold of 70-75%, which is commonly used to classify a nanosystem as non-cytotoxic under the evaluated conditions.

A direct comparison of cell viability data from CW and pulsed laser irradiation further highlighted the more reduced damage caused by non-continuous lasers. For example, when MDA-MB-231 cells were incubated with PEG-NH_2-coated AuNRs and AuNSs and exposed to a CW laser (2.0 $W \cdot cm^{-2}$, 5 min), the measured cell viabilities were *ca*. 71.2% and 60.1%, respectively. In contrast, under identical incubation conditions and equivalent energy exposure using a pulsed laser, cell viabilities increased up to *ca*. 82% for AuNRs-PEG-NH_2 and 76.3% for AuNSs-PEG-NH_2. As previously stated, CW lasers deliver energy continuously over time, resulting in greater heat accumulation and more extensive cellular damage, including cellular membranes disruption, protein denaturation, and apoptosis. In contrast, fs lasers deliver energy in very short, intense pulses and, although these can cause localized effects,

such as plasma formation or photomechanical damage, they do not produce the same prolonged heating effect as CW lasers. In more detail, in fs laser irradiations the pulse duration is significantly shorter than the thermal diffusion time of the surrounding medium, satisfying the conditions for thermal confinement. This ensures that heat remains localized near the NPs during each pulse and dissipates before subsequent pulses arrive, thereby preventing cumulative heating. Consequently, the overall thermal energy on the cells remains low, favoring apoptosis *via* non-thermal or sub-lethal pathways. In contrast, CW laser irradiation does not fulfill thermal confinement conditions, as it delivers continuous energy that accumulates over time.[226, 227]

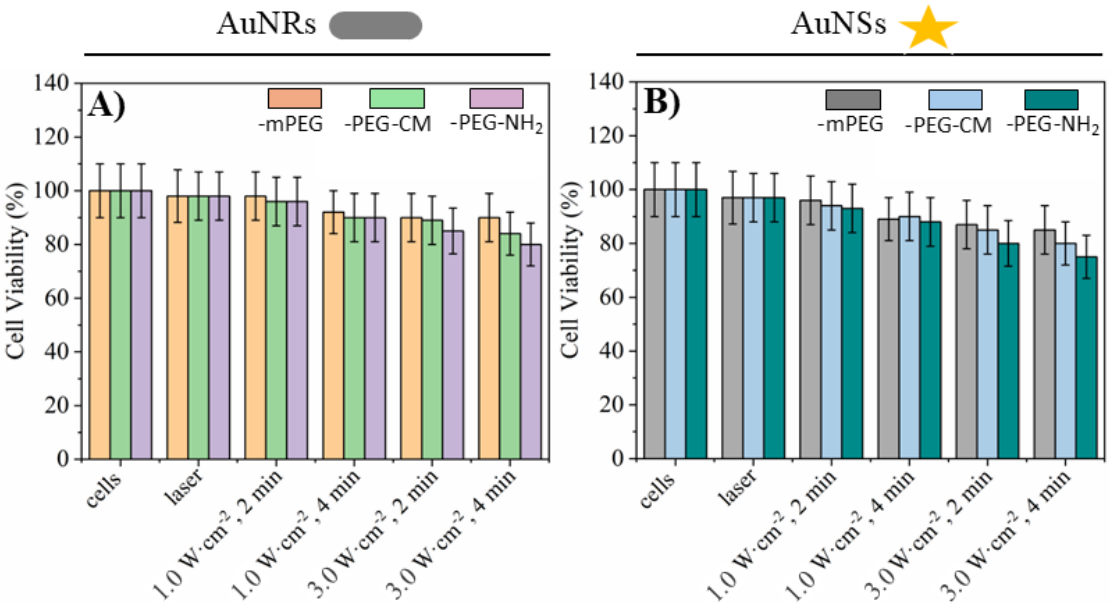

Figure 3.19. Cell viability of MDA-MB-231 cells incubated with PEG-coated A) AuNRs and B) AuNSs, after their irradiation using a fs pulsed laser. The laser power densities evaluated were 1.0 and 3.0 W·cm^{-2}, with exposure times of 2 and 4 min in each case.

3.7.4.2 Cell Death Mechanism Induced by AuNRs and AuNSs after Pulsed Laser Irradiation

After evaluating the viability of MDA-MB-231 cells upon their irradiation with a fs pulsed laser in the presence of gold NPs under various conditions, the underlying mechanisms of cell death were further investigated by flow cytometry.

To ensure an adequate number of dead cells for analysis, the irradiation conditions that previously resulted in lower cell viabilities were selected for this study. Thus, MDA-MB-231

cells were incubated with PEG-NH_2-coated AuNRs and AuNSs dispersions at the typical concentrations of 1.50 x 10^{11} and 1.50 x 10^9 NP·mL^{-1} for 24 h, followed by irradiation at 3.0 W·cm^{-2} for either 2 or 4 min with the pulsed laser. Untreated cells served as negative controls, while cells incubated with Doxo were used as positive controls for apoptosis.

The performed flow cytometry measurements showed that MDA-MB-231 cells incubated without gold NPs exhibited a viability up to 94.0% when not irradiated (Figure 3.20 A). Upon pulsed irradiation (3.0 W·cm^{-2}, 4 min), the viability slightly decreased to 89.1%, with 9.0 % of apoptosis (Figure 3.20 B). As occurred in the study using a CW laser, this minor increase in the number of apoptotic cells upon their irradiation without plasmonic NPs was attributed to energy provided by the laser source, which can affect cellular membrane proteins and lipids, leading to cell damage. On the other hand, incubation with Doxo induced a very significant increase in the apoptosis and necrosis rate of MDA-MB-231 cells, whether combined with pulsed laser irradiation or not. Specifically, Doxo treatment led to apoptosis and necrosis rates of 14.5% and 42.2%, respectively. When combined with pulsed laser irradiation (3.0 W·cm^{-2}, 4 min), these rates varied to 9.1% and 48.1%, respectively, with cell viability dropping to *ca*. 43% in both cases (Figure 3.20 C-D). This increase in early apoptotic cells in samples irradiated in the presence of Doxo was likely due to the synergistic effect of the laser's photothermal heating, which enhances the chemotherapeutic activity of the drug.

When MDA-MB-231 were incubated with the designed gold NPs cells and irradiated with the pulsed laser, the obtained results were in good agreement with cell viability assays under CW irradiation conducted in the previous section. For MDA-MB-231 cells incubated with AuNRs-PEG-NH_2, cell viabilities remained above 82.6% after both 2 and 4 min of pulse irradiation (Figure 3.20 F, G). Interestingly, the mechanism of cell death was not strongly dependent on the irradiation time for cells incubated with rod-shaped nanostructures. Specifically, 9.5% of cells underwent apoptosis after 2 min of irradiation, with this value increasing to 14.5% when the light exposure was extended to 4 min. Additionally, MDA-MB-231 cells incubated with these AuNRs-PEG-NH_2 showed a low necrosis rate of *ca*. 2.9% even after 4 min of pulsed laser irradiation.

A similar pattern was observed when cells were incubated with AuNSs-PEG-NH_2 prior irradiation, where apoptotic cell rates were also higher. Precisely, cell viabilities of 76.7% and 70.2% were recorded after irradiating MDA-MB-231 cells incubated with star-shaped gold NPs

for 2 and 4 min, respectively (Figure 3.20 H-I). After 2 min of irradiation, the apoptotic rate was *ca*. 21.5%, increasing up to 28.5% after 4 min of laser exposure, with minimal necrosis rate regardless of irradiation time.

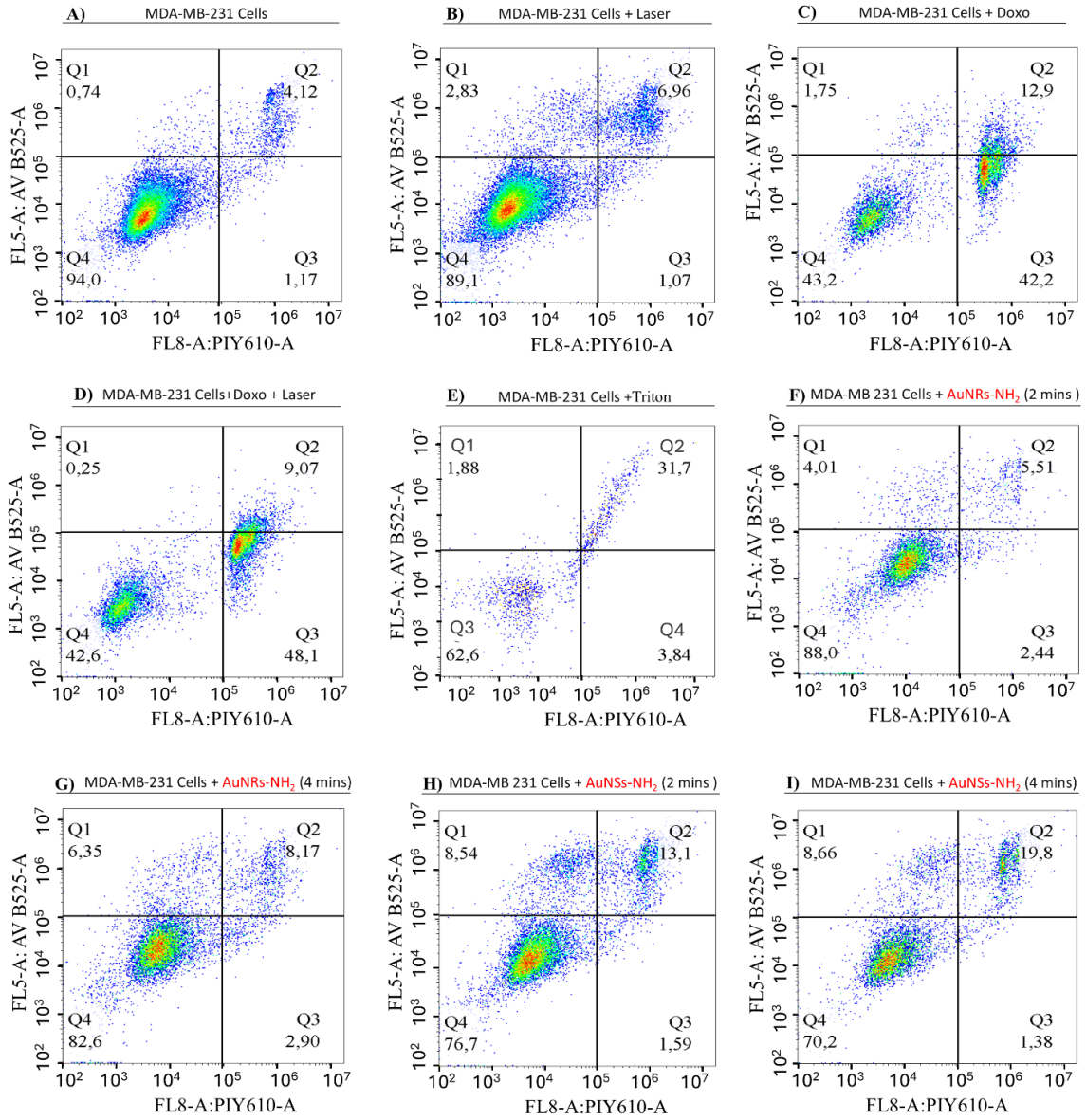

Figure 3.20. Flow cytometry analysis of MDA-MB-231 cells under various conditions. The controls included: A) untreated cells, B) irradiation with pulsed fs laser (4 min), C) incubation with 5 µM Doxo, D) incubation with 5 µM Doxo following irradiation (4 min), and E) treatment with Triton X-100. The studies involving incubation with gold NPs following irradiation included: F) AuNRs-PEG-NH_2 (2 min), G) AuNRs-PEG-NH_2 (4 min), H) AuNSs-PEG-NH_2 (2 min), I) AuNSs-PEG-NH_2 (4 min). All pulsed fs laser irradiations were performed at 3.0 $W \cdot cm^{-2}$. Quadrants: Q1 (early apoptosis), Q2 (late apoptosis), Q3 (necrotic cells), and Q4 (live cells).

Comparison of MDA-MB-231 cells irradiated with a CW laser (2.0 W·cm^{-2}, 5 min) and a pulsed laser (3.0 W·cm^{-2}, 4 min) in the presence of PEG-NH_2-coated AuNRs and AuNSs using a similar total energy input in both cases revealed distinct cell death mechanisms. Thus, after irradiation with the CW laser, cell death was predominantly driven by necrosis, whereas irradiation with the pulsed laser resulted in a higher apoptosis rate. This difference is attributed to the distinct interaction mechanisms between the lasers and the gold nanostructures. While the CW laser generates continuous heating and extensive thermal diffusion leading to necrosis, the non-continuous light exposure induces thermal confinement, minimizing heat diffusion and promoting more localized and controlled cellular effects.

3.7.5 Concluding Remarks on the *In Vitro* Biological Evaluation of Gold NPs

Cell internalization of the designed gold nanostructures was initially examined using confocal microscopy, which confirmed the uptake of AuNSs coated with differently terminated PEGs by both MDA-MB-231 and Balb/c 3T3 cells. However, in reflectance mode confocal microscopy, the uptake of AuNRs was not observed in either cell type, likely due to their smaller size and insufficient light scattering. To further investigate AuNRs internalization, TEM microscopy was used, thus being confirmed their uptake by both cell lines and also demonstrated a higher internalization for AuNSs compared to AuNRs.

For a quantitative assessment of cellular uptake, ICP-MS was used to measure intracellular gold concentration after internalization of gold NPs. Results indicated that MDA-MB-231 cells internalized higher amounts of both AuNRs and AuNSs than Balb/c 3T3 cells. Furthermore, ICP-MS data confirmed a higher uptake of AuNSs relative to AuNRs in both cell lines. Among the different surface modifications, PEG-NH_2-coated gold NPs exhibited the highest levels of cellular internalization.

Subsequent cell viability assays were performed across a concentration range of PEGylated AuNRs and AuNSs, both before and after CW laser irradiation. Prior to irradiation, both cell lines exhibited over 90% viability upon incubation with all types of PEG-coated AuNRs and AuNSs. However, following exposure to CW laser, cell viability decreased in a manner dependent on cell type and gold NPs morphology and functionalization. Notably, cells exposed to PEG-NH_2-coated AuNRs and AuNSs exhibited the greatest reduction in viability, aligning with the internalization data.

To explore the mechanisms of cell death post-irradiation, further analyses were conducted, with the obtained results showing that Balb/c 3T3 cells predominantly underwent apoptosis, indicative of a regulated cell death pathway. In contrast, MDA-MB-231 cells displayed a higher incidence of necrosis, suggesting a less controlled and more damaging cell death response, likely due to their greater sensitivity to photothermal effects.

Finally, the impact of fs pulsed laser irradiation on MDA-MB-231 cells post-internalization of AuNRs and AuNSs were analyzed. The observed trends in cell viability were consistent with those following CW laser exposure, with incubation of cells in the presence of AuNSs-PEG-NH2 and AuNRs-PEG-NH2 leading to the most significant viability reductions. However, overall cell death was lower following fs laser irradiation, likely due to the reduced heat accumulation associated with ultrashort pulse durations compared to the continuous exposure of CW lasers. Flow cytometry analysis confirmed that apoptosis was the predominant cell death pathway in MDA-MB-231 cells treated with both NP types and irradiated with the pulsed laser.

4. Protein Corona Formation on Gold NPs: Focus on the Effect of Plasmonic Heating

When nanostructured materials are incubated in biological fluids such as blood plasma, a dynamic layer of adsorbed proteins, termed as *protein corona*, is spontaneously formed on their surface. This corona remarkably alters the physicochemical properties and biological identity of the NPs, thereby influencing their biodistribution, immune recognition, cellular uptake, and overall biological fate. The composition and structure of the protein corona are dictated by multiple factors, including NPs size, morphology, and surface chemistry, temperature, or the specific proteins milieu of the surrounding environment.[228]

In the case of plasmonic NPs, an additional critical factor that influences biocorona formation is the plasmonic heating resulting from their excitation at LSPR wavelengths. This leads to localized temperature increases near the NPs surfaces, which can induce structural and compositional changes in the adsorbed proteins. Such heating may affect protein unfolding, aggregation, and binding dynamics, thereby impacting NPs stability and biological behavior. Thus, a deeper understanding of how plasmonic heating modulates plasmonic protein corona dynamics is essential for the rational design of gold NPs for biomedical purposes.

In this section, we evaluate the composition and behavior of the corona formed by two model proteins, bovine serum albumin (BSA) and bovine fibrinogen (Fib), on the surface of the designed AuNRs and AuNSs, with a particular emphasis on the impact of plasmonic heating.[228] BSA and Fib were selected due to their high abundance in blood plasma and their distinct characteristics in terms of molecular weight, structure, and surface binding affinity for comparison. Moreover, both proteins have been identified as among the most prevalent constituents of the biocorona formed on gold NPs after exposure to human plasma or serum when parentally administered.[229] BSA is a globular, heart-shaped protein with a molecular weight of *ca*. 66 kDa and dimensions of 4 × 4 × 14 nm^3. In contrast, Fib is an elongated glycoprotein, featuring a cylindrical morphology with dimensions of 45 × 5 × 5 nm^3 and a molecular weight of *ca*. 340 kDa. It plays a key physiological role in hemostasis, undergoing enzymatic conversion by thrombin into fibrin, which polymerizes to form blood clots.[230]

4.1 Protein Corona Formation on AuNRs Incubated with BSA and Fib

The dynamics of protein corona formation on the surface of previously synthesized AuNRs when incubated in the presence of BSA and Fib, were investigated under three different experimental conditions: no light irradiation, *simultaneous* light irradiation, and *sequential* light irradiation. In the *no light irradiation* mode, protein adsorption onto the metallic NPs in the absence of laser light application was analyzed, serving as the control for native protein corona formation. On the other hand, in the *simultaneous mode*, the protein-NPs dispersions were irradiated during the adsorption process, allowing plasmonic heating to influence early-stage particle-protein interactions, including protein binding kinetics, orientation, and structural integrity. Finally, in the *sequential mode*, light irradiation was applied after a 2-h incubation period, targeting the thermal stability and potential rearrangement of the pre-formed protein biocorona. Comparison of these modes should provide insights into how plasmonic heating modulates protein-NPs biointeractions. Thus, while *simultaneous* irradiation may result in a corona with altered composition or conformation due to heat-induced effects during adsorption, *sequential* irradiation study might reveal post-formation restructuring, desorption, or stabilization phenomena of protein corona.

4.1.1 UV-Vis and DLS Characterization of AuNRs Incubated in the Presence of BSA and Fib

Protein adsorption onto the surfaces of plasmonic NPs can induce shifts in the LSPR wavelength, changes in peak intensity, and broadening of the LSPR band. These spectral changes, observable *via* UV-Vis spectroscopy, reflect variations in NPs–protein interactions, colloidal stability, and corona thickness, offering indirect insight into the physicochemical characteristics of the protein layer. [228] In particular, these optical alterations primarily arise from an increase in the local refractive index near the NP surface, affecting the plasmonic resonance behavior. Moreover, adsorbed proteins can introduce non-radiative damping mechanisms—such as vibrational or rotational energy losses—that interfere with the coherent oscillation of conduction electrons, thereby reducing peak intensity. The heterogeneity in protein coverage, orientation, and conformational state further contributes to spectral broadening by introducing variability in the local dielectric environment.[231,232] In parallel, DLS provides complementary information by tracking changes in hydrodynamic diameter and NP aggregation behavior.[233] Together, UV-Vis and DLS offer a robust analytical

framework for evaluating the structural and functional evolution of protein coronas formed on the designed AuNRs.

In this study, AuNRs functionalized with either PEG-NH_2 and PEG-CM at a concentration of 5.0 x 10^{11} NP·mL^{-1} were incubated in the presence of BSA and Fib at a concentration of 2.0 µM (saturation concentration) in PBS pH 7.4. In the irradiation *simultaneous* mode, protein-AuNRs dispersions were irradiated at 3.0 W·cm^{-2} until reaching 45 °C. In the *sequential* mode, irradiation was applied under the same conditions after a 2-h incubation period. UV–Vis spectroscopy and DLS were subsequently used to assess protein-NPs interactions and characterize biocorona formation.

4.1.1.1 AuNRs Incubated with BSA

As shown in Figure 4.1 A, AuNRs-PEG-CM incubated in the presence of BSA exhibited negligible shifts in the longitudinal LSPR peak for all three tested conditions, suggesting minimal interaction between BSA and this kind of AuNRs. In contrast, AuNRs-PEG-NH_2 displayed a red-shift of *ca.* 6 nm in the LSPR band under both *simultaneous* and *sequential* irradiation conditions (Figure 4.1 B). These differences in the interaction behavior between BSA and the AuNRs coated with PEG-CM or PEG-NH_2 can be related to their different surface electrical charges. The terminal group of PEG-NH_2 chains carries a positive charged group at physiological pH (pK_a *ca*. 9), facilitating electrostatic attraction with negatively charged residues of BSA (pK_a *ca*. 6).Conversely AuNRs-PEG-CM shows a negatively charged surface under similar solutions conditions, which enhances colloidal stability but reduces electrostatic interaction with BSA due to charge repulsion.[234] In this way, the slight red shifts in the LSPR peak of AuNRs-PEG-NH_2 incubated in BSA was attributed to changes in the local dielectric environment surrounding the NPs arising from protein adsorption, conformational rearrangements, and/or alterations in surface charge, all of which can influence the optical response of plasmonic NPs.[235] No broadening of the UV-Vis spectra was observed for AuNRs with both types of PEG coating, indicating that the rod-shaped nanostructures retained their plasmonic stability following protein adsorption.

On the other hand, the hydrodynamic size distributions of AuNRs incubated in the presence of BSA showed two peaks corresponding to rotational and translational diffusion coefficients,[177] arising from the anisotropic rod-shaped morphology of the metallic NPs. In the

case of AuNRs-PEG-CM, no significant changes in the hydrodynamic width population distribution were observed across the three analyzed experimental conditions but, in contrast, slight length increases of *ca*. 4, 10, and 4 nm were observed for the no irradiation, *simultaneous*, and *sequential* modes, respectively (Figure 4.1 C).

Conversely, AuNRs-PEG-NH_2 exhibited more pronounced changes in both width and length hydrodynamic dimensions following BSA incubation (Figure 4.1 D). Again, no width change was observed under no irradiation, but non-negligible increases of *ca*. 2 and 1 nm were recorded under *simultaneous* and *sequential* irradiation, respectively. More notably, the hydrodynamic length of PEG-NH_2-coated AuNRs increased by *ca.* 3 nm (no irradiation), 16 nm (*simultaneous* irradiation), and 3 nm (*sequential* irradiation) under the different tested conditions. The substantial increase in the hydrodynamic dimensions of AuNRs-PEG-NH_2 under *simultaneous* irradiation suggests that the localized heating effect enhances corona formation and its thickness in the early stages of incubation by probably promoting BSA unfolding (see below) and facilitating more extensive surface coverage. In contrast, under *sequential* irradiation conditions, BSA adsorbed on the surface of AuNRs-PEG-NH_2 likely reached a quasi-equilibrium conformation prior to induced heating, limiting further protein adsorption or desorption and resulting in only minor changes in NPs hydrodynamic dimensions.[228, 235]

4.1.1.2 AuNRs Incubated with Fib

The formation of a protein corona around PEGylated AuNRs upon their incubation in Fib induced changes in their optical response and hydrodynamic dimensions, particularly under plasmonic heating conditions. As shown in Figure 4.1 E-F, significant decreases in UV–Vis absorption intensity was observed for Fib-incubated samples following laser irradiation, more pronounced than in those previously established for AuNRs incubated in BSA. More specifically, in the case of AuNRs-PEG-CM this intensity loss was most significant under *simultaneous* irradiation, which is accompanied by a red shift of *ca.* 9 nm in the longitudinal LSPR peak, while smaller changes were observed under no-irradiation and *sequential* irradiation modes (Figure 4.1 E). On the other hand, AuNRs-PEG-NH_2 exhibited a strong absorbance reduction in both *simultaneous* and *sequential* irradiation modes, with red shifts of *ca.* 9 and 4 nm in their longitudinal LSPR peaks, respectively (Figure 4.1 F). Minimal changes

were seen in the absence of laser irradiation. These spectral shifts and absorbance losses by plasmonic heating suggest significant Fib-AuNRs interactions and changes in the local dielectric environment of the particles, likely resulting from protein adsorption, unfolding, and possible NPs aggregation.[236]

The performed DLS measurements further supported these findings. In particular, there were observed more significant changes in the hydrodynamic size distributions of Fib-incubated AuNRs than in their BSA counterparts. Thus, AuNRs-PEG-CM exhibited increases in both hydrodynamic length and width: the width increased by approximately 5 nm and 3 nm, and the length by about 10 nm and 9 nm under *simultaneous* and *sequential* irradiation, respectively (Figure 4.1 G). However, no changes in the hydrodynamic dimensions of the plasmonic nanostructures were observed when they were incubated in Fib in the absence of laser irradiation, confirming the important role of light-induced heating on protein binding and corona formation. On the other hand, AuNRs-PEG-NH_2 exhibited more pronounced hydrodynamic changes than their PEG-CM-coated counterparts, with substantial increases in the measured hydrodynamic lengths of up to *ca*. 9 (no-laser), 28 (*simultaneous*), and 13 nm (*sequential*). Slight increases in the hydrodynamic widths were also observed for AuNRs-PEG-NH_2 incubated in Fib under all irradiation conditions (Figure 4.1 H).

Notably, more pronounced increases in the longitudinal dimension were observed for AuNRs-PEG-NH_2 compared to AuNRs-PEG-CM. This suggests a stronger or more extensive interaction between Fib and the amino-functionalized surface, likely due to electrostatic attraction or enhanced protein adsorption. In contrast, the AuNRs-PEG-CM exhibited comparatively minor changes, indicating a weaker interaction or reduced protein binding affinity. These findings highlight the role of surface chemistry in modulating protein-nanoparticle interactions and suggest that the presence of terminal amine groups promotes greater conformational changes or aggregation along the longitudinal axis.[234, 237]

On the other hand, the pronounced increase in hydrodynamic dimensions observed in the *simultaneous* irradiation mode suggests that plasmonic-induced heating during the early stage of Fib incubation with PEG-NH_2-coated AuNRs promotes the formation of NPs–protein clusters, likely driven by enhanced protein-protein interactions and partial aggregation triggered by heating.[238] In addition, these more pronounced changes in the optical and hydrodynamic dimensions of AuNRs incubated with Fib under irradiation can be attributed to

the heat sensitivity of this protein. Localized heating is known to accelerate Fib structural alterations and aggregation,[239] which, in turn, promote AuNRs clustering, as reflected in the reduction of UV-Vis intensity and alteration of hydrodynamic profiles. Aggregation disrupts the characteristic plasmonic response of the designed rod-shaped nanostructures, potentially compromising their optical performance in biomedical applications.[240]

In summary, both UV-Vis and DLS measurements confirmed that AuNRs-protein interactions are strongly dictated by the surface chemistry of the NPs and irradiation mode. While AuNRs-PEG-CM generally maintained colloidal and optical stability in the absence of heating, irradiation led to measurable corona formation and aggregation, particularly when incubated in Fib. AuNRs-PEG-NH_2, owing to their positively charged surface, exhibited stronger interactions with both proteins, particularly under heating conditions. The *simultaneous* irradiation mode consistently induced the most pronounced changes, highlighting the key role of plasmonic heating in the early stages of incubation to modulate protein corona formation and NPs behavior.

4.1.2 Fluorescence Quenching Study of BSA on AuNRs

To complement previous DLS and UV-Vis characterization of protein-NPs interactions, a preliminary fluorescence spectroscopy study was conducted to evaluate the conformational behavior of BSA upon adsorption to PEGylated AuNRs. This analysis was limited to BSA due to its well-characterized fluorescence properties and serves as an initial probe of protein orientation and accessibility on the AuNRs surfaces during corona formation.

Gold NPs are known to quench protein fluorescence *via* energy transfer mechanisms, making this a valuable approach for assessing the proximity of fluorophores (particularly tryptophan residues) to the surface of the nanostructures and characterize protein-NPs interactions.[241] BSA contains two tryptophan residues: Trp134, which is located in subdomain IB on the protein surface, and Trp213, found in the subdomain IIA.[242] BSA polypeptide structure also includes 18 tyrosine residues, with only Tyr263 positioned within subdomain IIA.[243] The extent of fluorescence quenching reflects how accessible these residues are to the AuNRs surface, offering insight into protein orientation and conformational changes.

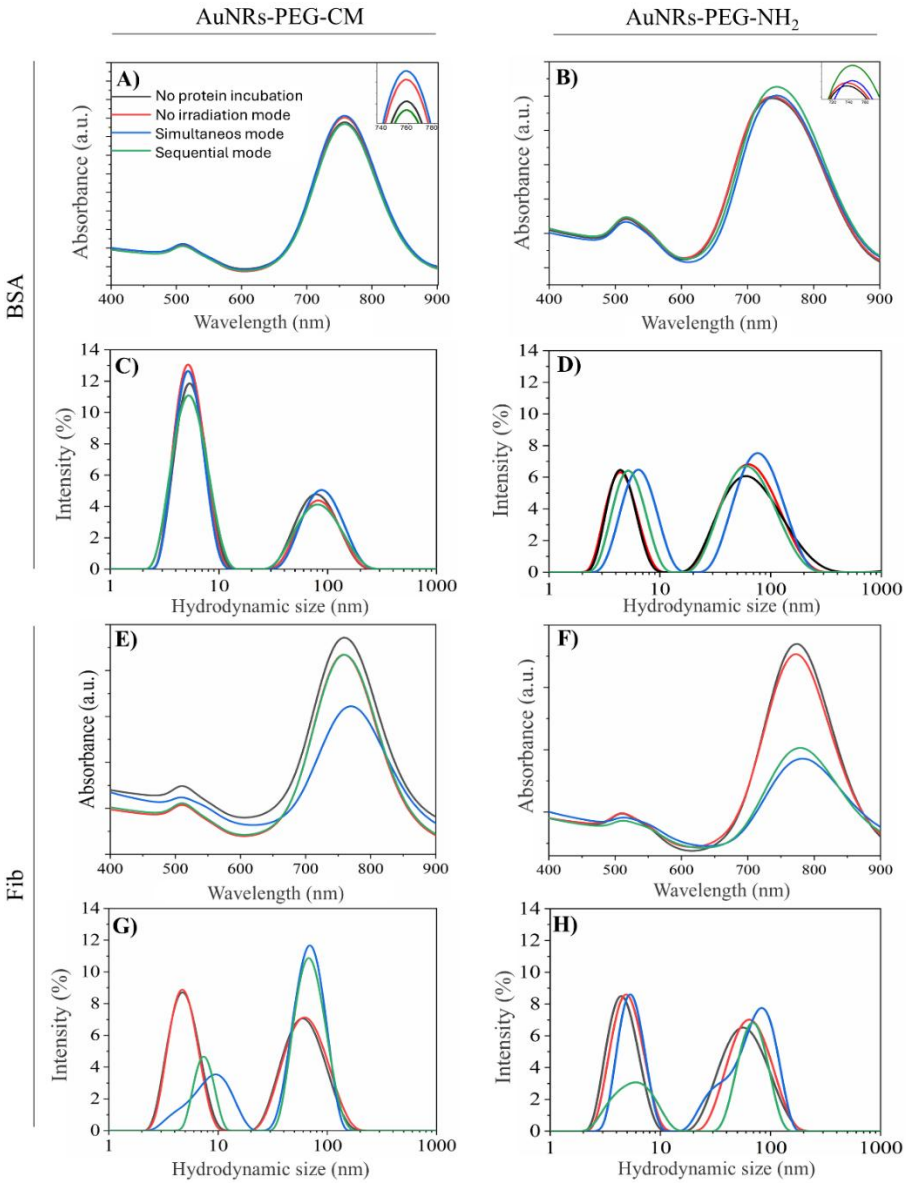

Figure 4.1. DLS and UV-Vis characterization of PEG-coated AuNRs after protein incubation under different irradiation modes. BSA incubation: UV-Vis spectra of AuNRs coated with A) PEG-CM and B) PEG-NH_2; population hydrodynamic size distributions of AuNRs coated with C) PEG-CM and D) PEG-NH_2. Fib incubation: UV-Vis spectra of AuNRs coated with E) PEG-CM and F) PEG-NH_2; population hydrodynamic size distributions of AuNRs coated with G) PEG-CM and H) PEG-NH_2.

For this study, BSA (2µM) was incubated with either AuNRs-PEG-NH_2 or AuNRs-PEG-CM at concentrations ranging from 0 to 1.2 x 10^{12} NP·mL^{-1}. Fluorescence spectra were recorded in the 300-400 nm range, both in the absence of irradiation and under laser exposure at 1.0 and

3.0 W·cm^{-2} for 5 min. The quenching effect was analyzed using the Stern-Volmer model (equation 9):

$$\frac{F_0}{F} = 1 + k_q \tau_0 [Q] = 1 + K_{sv}[Q] \quad (9)$$

where, F_0 and F are the fluorescence intensities of BSA before and after incubation with AuNRs, K_q and K_{sv} are the biomolecular quenching rate constant and the Stern-Volmer quenching constant, respectively. *[Q]* denotes de concentration of AuNRs, and τ_0 is the average excited-state lifetime of BSA in the absence of quencher (1.0×10^{-8} s).[244]

Linear regression was applied to plot of F_0/F *vs*. [Q] to determine the quenching constants (Figure 4.2), the extracted values for K_q and K_{sv} under each condition summarized in Table 4.1.

Thus, it was established that AuNRs-PEG-NH_2/BSA complexes exhibited higher K_{sv} and K_q values than their AuNRs-PEG-CM counterparts under all experimental conditions (irradiation and no irradiation modes), indicating stronger interactions between BSA and positively charged AuNRs-PEG-NH_2, being this consistent with previous DLS and UV-Vis data. Furthermore, both AuNRs-PEG-NH_2/BSA and AuNRs-PEG-CM/BSA nanoconjugates showed increased K_{sv} and K_q upon laser irradiation, with higher values at 3.0 W·cm^{-2} compared to 1.0 W·cm^{-2} (Table 4.1). These enhancements indicate that plasmonic heating promotes stronger NPs-protein binding, likely by inducing conformational flexibility in BSA, exposing tryptophan residues, and facilitating closer contact with AuNRs.[245]

To further evaluate the interaction between BSA and the dispersed PEG-coated AuNRs, the fluorescence data were analyzed using the Hill equation (equation 10):[246]

$$Log\left(\frac{F0}{F} - 1\right) = \log K_a - m log[Q] \quad (10)$$

where K_a is the association constant, and m is the Hill coefficient, which reflects the degree of binding cooperation of proteins interacting with NPs. An $m > 1$ indicates positive cooperativity, where initial protein binding facilitates further adsorption; while $m < 1$ reflects negative cooperativity, where subsequent binding becomes less favorable as coverage increases.[247]

As summarized in Table 4.1, the AuNRs-PEG-CM/BSA conjugates exhibited Hill coefficients below 1 under all experimental conditions, indicating negative cooperativity, that is, the binding affinity decreases as subsequent BSA molecules adsorb onto the surface of the PEG-

CM-coated AuNRs. In contrast, AuNRs-PEG-NH_2/BSA exhibited *m* values greater than 1, characteristic of positive cooperativity, where protein adsorption promotes further binding events.[247] These observations are consistent with previous findings reported by Figueroa *et al*., further validating the observed cooperative binding behavior.[234] In agreement with the Hill coefficient data obtained, the association constants (K_a) for AuNRs-PEG-NH_2/BSA bioconjugates were consistently higher than those determined for AuNRs-PEG-CM/BSA along identical experimental conditions, including both in the presence and absence of laser irradiation. As previously stated, this enhanced affinity was attributed to favorable electrostatic interactions between the positively charged terminal groups on the PEG-NH_2-coated AuNRs and the negatively charged domains of BSA.[237]

Collectively, these findings underscore the key role of AuNRs functionalization and, even more critical, plasmonic heating, in modulating NPs-protein interactions. This ability to tune binding affinity *via* laser irradiation provides a valuable strategy for the rational design of bionanoconjugates with controllable interaction profiles, which may be leveraged in their final application.

Table 4.1. Stern-Volmer constant (K_{sv}), quenching rate constant (K_q), association constant (K_a), and Hill coefficient (*m*) for BSA bioconjugates with AuNRs-PEG-CM and AuNRs-PEG-NH_2 under varying experimental conditions.

Gold NPs	Irradiation	K_{sv} [$\times10^{-13}$ mL·NP^{-1}]	K_q [$\times10^{-5}$ mL·NP^{-1}·s^{-1}]	K_a [$\times10^{-13}$ mL·NP^{-1}]	m
AuNRs-PEG-CM	No irradiation	2.31 ± 0.10	2.31 ± 0.10	0.140 ± 0.010	0.931 ± 0.072
	1.0 W·cm^{-2}	2.76 ± 0.12	2.76 ± 0.12	0.632 ± 0.051	0.850 ± 0.091
	3.0 W·cm^{-2}	2.95 ± 0.13	2.95 ± 0.13	1.002 ± 0.101	0.842 ± 0.077
AuNRs-PEG-NH_2	No irradiation	4.30 ± 0.20	4.30 ± 0.20	150 ± 14	1.131 ± 0.060
	1.0 W·cm^{-2}	4.62 ± 0.23	4.62 ± 0.23	1140 ± 89	1.138 ± 0.081
	3.0 W·cm^{-2}	4.83 ± 0.26	4.83 ± 0.26	1500 ± 130	1.192 ± 0.070

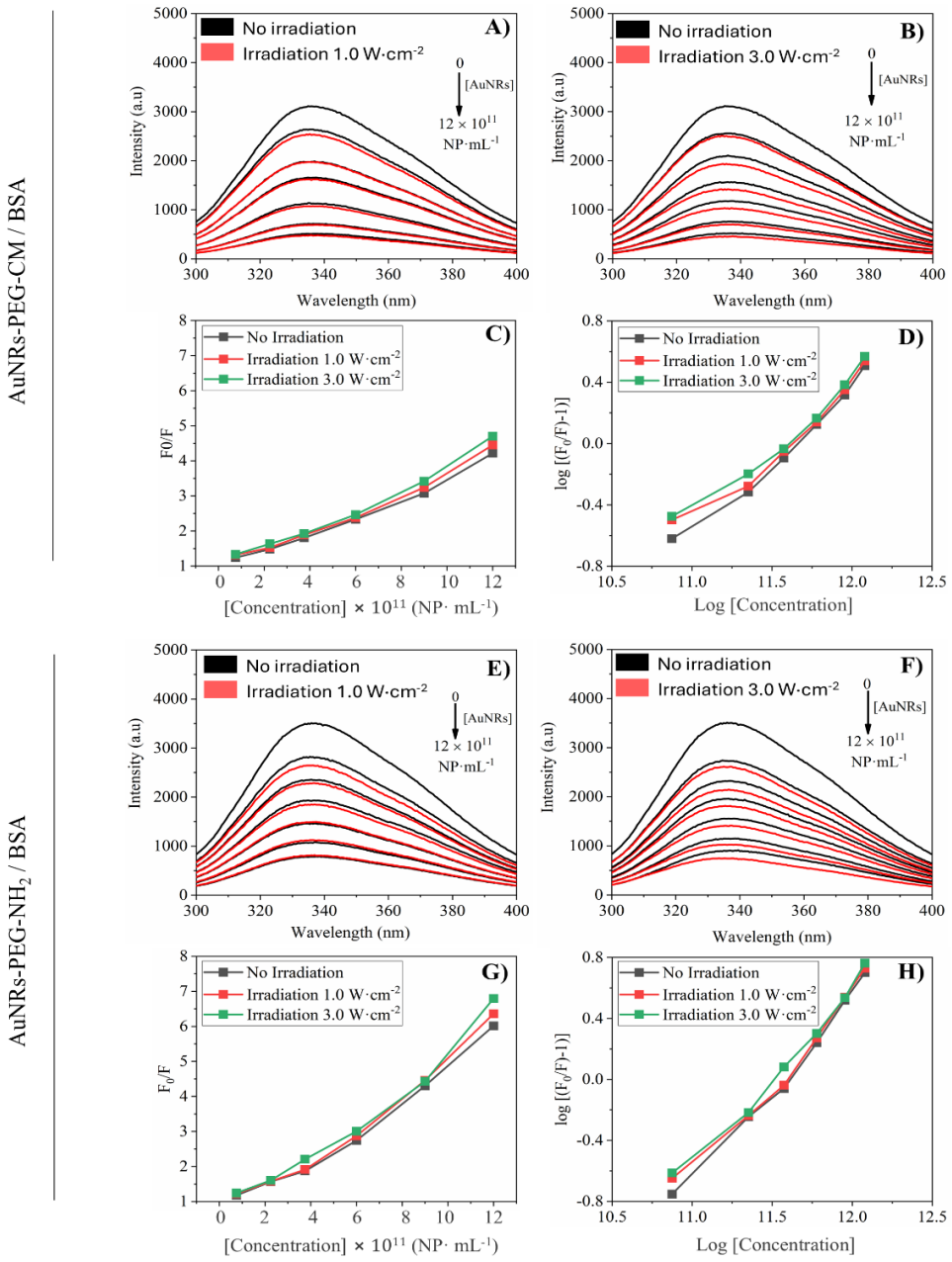

Figure 4.2. Fluorescence quenching spectra of BSA with increasing concentrations of AuNRs-PEG-CM under laser irradiation at A) 1.0 and B) 3.0 W·cm^{-2}. C-D) Corresponding Stern-Volmer and Hill plots under both irradiation conditions of AuNRs-PEG-CM. Fluorescence quenching spectra of BSA with increasing concentrations of AuNRs-PEG-NH_2 under laser irradiation at E) 1.0 and F) 3.0 W·cm^{-2}. G-H) Corresponding Stern-Volmer and Hill plots under both irradiation conditions of AuNRs-PEG-NH_2. The increasing concentrations of PEG-coated AuNRs analyzed were 0, 2, 4, 6, 8,10, and 12 (×10^{11} NP·mL^{-1}).

4.1.3 Conformational Changes of Proteins after Incubation with AuNRs and Plasmonic Heating

Circular dichroism (CD) spectroscopy is a widely used technique for probing the secondary structure and induced conformational changes of proteins, particularly in response to interactions with nanomaterials.[248] Upon adsorption on NPs surfaces, proteins may undergo conformational rearrangements, including unfolding, misfolding, or denaturation, that can significantly impact their biological function. CD spectroscopy, being sensitive to structural motifs such as α-helices, β-sheets, and random coils, enables real-time monitoring of these changes with high specificity, thus helping to better understand protein corona formation dynamics.[249]

Specifically, the changes in protein secondary structure were quantified through the Beta Structure Selection (BeStSel) method. This method allows for the reliable identification of several types of secondary structures, such as α-helices, parallel and antiparallel β-sheets, β-turns, and others.[250] By incorporating the twist angle of β-strands, BeStSel improves prediction accuracy across a wide range of protein conformations, offering critical insight into the structural dynamics of protein-NPs interactions, especially under thermal stimuli such as plasmonic heating.[251]

Here, the CD spectra of BSA and Fib were recorded before and after incubation with either AuNRs-PEG-CM or AuNRs-PEG-NH_2, under the already detailed three different irradiation conditions: no laser exposure, *simultaneous*, and *sequential* irradiation. In both irradiation modes, CW laser exposure at 3.0 $W \cdot cm^{-2}$ was applied until the dispersions reached 45 °C, a value representative of the thermal threshold commonly employed in photothermal cancer therapy.

4.1.3.1 AuNRs Incubated in BSA

As shown in Figure 4.3 A-B, BSA displayed characteristic spectral features consistent with its native secondary structure. Specifically, two negative bands at *ca*. 208 and 222 nm were observed in the CD spectrum, corresponding to α-helical content. In addition, a weak positive signal near 218 nm is indicative of β-sheet structures.[252, 253] These features serve as a baseline for assessing structural alterations induced by NPs interaction and plasmonic heating.

The quantitative analysis of the obtained spectra using the BeStSel algorithm revealed significant reductions in α-helical content following incubation of BSA with either AuNRs-PEG-CM or AuNRs-PEG-NH_2 under *non-irradiation* condition (Figure 4.3 C-D and Table 4.2). This effect was more pronounced after incubation with PEG-NH_2-coated NPs, showing a 24% decrease in α-helices, compared to a 10% reduction observed with AuNRs-PEG-CM.

Comparing the two irradiation modes, *simultaneous* laser exposure conditions induced a greater reduction in α-helical content for both types of AuNRs than *sequential* mode. This trend correlates well with previous UV-Vis and DLS data, where more significant LSPR shifts and hydrodynamic size changes were detected in *simultaneous* irradiation mode. These findings suggest that *in situ* plasmonic heating during protein adsorption intensifies structural alterations, likely by enhancing protein-NPs surface interactions and increasing local temperature gradients. Interestingly, β-sheet content and other structural motifs remained largely unchanged across all conditions, indicating that the structural perturbations in BSA were primarily limited to α-helical domains.

4.1.3.2 AuNRs Incubated with Fib

Similar to BSA, the CD spectra of Fib also displayed distinct signatures characteristic of its native secondary structure (Figure 4.3 G-H and Table 4.2). In the absence of laser irradiation both proteins exhibited comparable behavior, with a reduction in α-helical content following interaction with AuNRs-PEG-CM and AuNRs-PEG-NH_2. However, under laser exposure, Fib underwent more extensive structural alterations than BSA, as evidenced by the pronounced spectral changes observed after plasmonic heating (Figure 4.3 E-H). In the case of *simultaneous* laser irradiation, the α-helical signature disappeared entirely, suggesting near-complete denaturation of the protein native secondary structure. Under *sequential* irradiation, a small but detectable fraction of α-helices still remained, indicating a less severe thermal unfolding process compared to *simultaneous* exposure.

These changes were accompanied by a significant increase in antiparallel β-sheet structures. For Fib incubated with AuNRs-PEG-CM, the increase in antiparallel β-sheets was more pronounced in the *sequential* irradiation mode. In contrast, for AuNRs-PEG-NH_2, the increase in antiparallel β-sheet content was rather similar under both light irradiation regimes, suggesting different mechanisms of structural rearrangement depending on surface

functionalization. These compositional changes in Fib-incubated AuNRs were previously anticipated by, for example, Hashemi *et al.* who demonstrated that plasmonic heating of Fib–AuNRs bioconjugates results in a complete loss of α-helices and a corresponding increase in antiparallel β-sheet structures.[228]

The observed contrasting structural responses of proteins upon interaction with AuNRs were attributed to their native secondary structure compositions and hydrophobicity profiles. BSA predominantly contains α-helices and exhibit great hydrophilicity, whereas Fib is rich in β-sheets, which are intrinsically more hydrophobic. Proteins with exposed hydrophobic domains, such as β-sheets, are more prone to aggregation in aqueous environments, especially under thermal stress. In this context, plasmonic heating likely promotes the exposure of the hydrophobic β-sheet regions of Fib to the surrounding medium, promoting aggregation and extensive conformational rearrangements.[254]

In summary, the results obtained underscore the critical influence of both AuNRs surface chemistry and thermal modulation *via* plasmonic heating on protein structural stability and corona formation. Thus, BSA exhibited significant reductions in α-helical content upon adsorption on NPs surfaces, especially in the case of AuNRs-PEG-NH_2. This structural disruption was further amplified under *simultaneous* laser irradiation. On the other hand, Fib underwent much more dramatic conformational changes, including near-complete loss of α-helices and a significant rise in antiparallel β-sheets, particularly under plasmonic heating. These transformations are consistent with Fib β-sheet-rich structure and higher aggregation propensity in response to localized thermal stress. These results are also consistent with the UV-Vis and DLS measurements, as the AuNRs showed greater changes in LSPR and hydrodynamic size when exposed to Fib compared to BSA. Notably, under plasmonic heating, the AuNRs incubated with Fib exhibited a pronounced red shift and a significant increase in hydrodynamic size. These findings provide valuable insights into the design of nanomaterials for biomedical applications, where protein stability and corona formation critically influence therapeutic efficacy and biocompatibility.

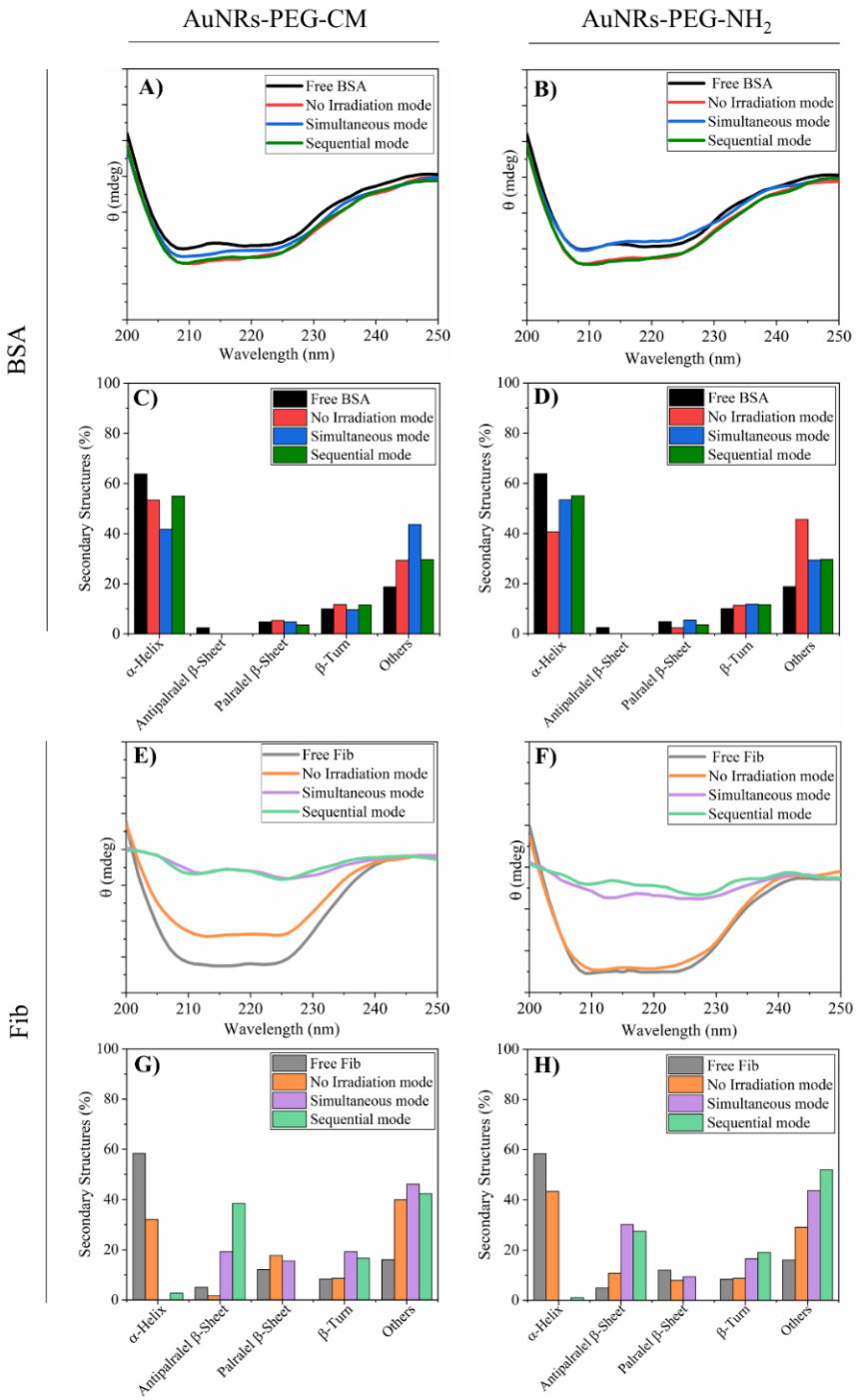

Figure 4.3. CD spectra of BSA adsorbed onto A) AuNRs-PEG-CM and B) and AuNRs-PEG-NH_2; and secondary structure compositions of BSA adsorbed onto C) AuNRs-PEG-CM and D) and AuNRs-PEG-NH_2 under different irradiation modes. CD spectra of Fib adsorbed onto E) AuNRs-PEG-CM and F) and AuNRs-PEG-NH_2; and secondary structure compositions of Fib adsorbed onto G) AuNRs-PEG-CM and H) and AuNRs-PEG-NH_2 under the different irradiation modes.

Table 4.2. Percentages of secondary structure content in BSA and Fib protein coronas formed on PEGylated AuNRs, in the absence of laser exposure and under *simultaneous* and *sequential* irradiation modes.

			Protein Secondary Structures				
Gold NPs	**Protein**	**Irradiation Mode**	**α-helix**	**Anti β-sheet**	**β-sheet**	**β-turn**	**Others**
AuNRs-PEG-CM	BSA	Free BSA	63.8	2.5	4.9	10.0	18.8
		No irradiation	53.4	0	5.4	11.8	29.4
		Simultaneous	51.8	0	4.8	9.7	33.7
		Sequential	55.0	0	3.6	11.6	29.7
AuNRs-PEG-NH_2		Free BSA	63.8	2.5	4.9	10.0	18.8
		No irradiation	40.6	0	2.4	11.4	45.6
		Simultaneous	45.4	0	5.4	12.8	36.4
		Sequential	50	0	3.6	12.6	33.7
AuNRs-PEG-CM	Fib	Free Fib	58.4	5	12.1	8.4	16.1
		No irradiation	32	1.7	17.8	8.6	39.9
		Simultaneous	0	19.2	15.5	19.2	46.1
		Sequential	2.7	38.5	0	16.6	42.3
AuNRs-PEG-NH_2		Free Fib	58.4	5.0	12.1	8.4	16.1
		No irradiation	43.4	10.8	8	8.8	29.1
		Simultaneous	0	30.2	9.4	16.6	43.7
		Sequential	1.1	27.5	0	19.0	52.0

4.2 Protein Corona Formation on AuNSs Incubated in the Presence of BSA and Fib

In order to assess the influence of gold NPs morphology over the dynamics of protein corona formation, the AuNSs here designed were also incubated in the presence of BSA and Fib, and

their behavior in terms of protein biocorona formation and protein conformational states elucidated and compared to that of previously analyzed rod-shaped nanostructures. Following the same procedure applied for AuNRs, the characteristics of the biocorona formed around star-like gold NPs were evaluated under three conditions: no irradiation, *simultaneous* and *sequential* light irradiation. As mentioned previously, in the *no irradiation* mode, protein adsorption occurred in the absence of laser exposure, while *simultaneous and sequential modes* involved light irradiation at the beginning and after a 2-h incubation period, respectively. Given that the objective of this section was just a preliminary assessment of the effect of star-like morphology on the formation of protein corona, only AuNSs coated with PEG-CM were analyzed. Moreover, the characterization study was limited to DLS and UV-Vis measurements, in combination with the evaluation of potential conformational changes in the protein structures *via* CD spectroscopy.

4.2.1 UV-Vis and DLS Characterization of AuNSs Incubated with BSA and Fib

As mentioned before, the combined use of UV-Vis spectroscopy and DLS offers a robust approach for characterizing protein corona formation dynamics on nanostructured materials. By monitoring the effect of protein adsorption over the plasmonic response and the hydrodynamic dimensions of the designed AuNSs, the physicochemical characteristics of biocorona and the nature of NPs-protein interactions can be elucidated.

In this preliminary study, PEG-CM-coated AuNSs at a concentration of 5.0 x 10^9 NP·mL^{-1} were incubated with BSA and Fib solutions (2.0 µM each, in PBS pH 7.4) following the methodology established in analysis of corona formation around AuNRs in this work.

4.2.1.1 AuNSs Incubated with BSA

As shown in Figure 4.4 A–B, incubating PEG-CM-coated AuNSs with BSA did not result in significant changes in either the wavelength or intensity of their LSPR peak nor in their hydrodynamic diameter, under any of the three irradiation conditions evaluated. This suggests a minimal interaction between AuNSs and BSA, being the limited binding of proteins to the surface of the nanostructures attributed to the distinctive morphology of the star-shaped gold NPs. Their irregular pointed geometry likely introduced steric hindrance that minimized the adsorption of the protein (a relatively large globular one) in comparison to that observed onto the more uniform surface of AuNRs. Moreover, it is also worth mentioning that the AuNRs

analyzed in previous section could retain trace amounts of positively charged CTAB surfactant even after PEGylation, which could enhance electrostatic interactions between the rod-like nanostructures and BSA.[255, 256]

A more specific comparative analysis of BSA interactions with AuNSs and AuNRs, both coated with PEG-CM, further supports this interpretation. A modest increase in hydrodynamic size was observed for AuNRs, especially under *simultaneous* light irradiation (Figure 4.1 B), consistent with the formation of a slightly more developed protein corona. Nonetheless, the overall binding affinity of BSA to both nanostructures appear weak.

4.2.1.2 AuNSs Incubated with Fib

In contrast to BSA, Fib exhibited more pronounced interactions with the designed AuNSs-PEG-CM. As shown in Figure 4.4 C, the recorded UV-Vis spectra revealed a decrease in peak intensity under all irradiation modes, with the most significant reduction occurring under *simultaneous* irradiation. However, no significant LSPR shifts were detected under any condition. As previously stated, the observed decreases in UV-Vis absorption intensities can be associated with the formation of a protein layer that alters the local dielectric environment of the NPs, thereby modulating their optical response. DLS measurements further confirmed the formation of a protein corona, as indicated by an increase in the hydrodynamic size of AuNSs from 134 ± 13 nm to 140 ± 13 nm, 153 ± 15 nm, and 146 ± 14 nm under no irradiation, *sequential* irradiation, and *simultaneous* irradiation conditions, respectively (Figure 4.4 D). In good agreement with UV-Vis measurements, this behavior was more relevant when irradiation was applied at the onset of incubation (*simultaneous* mode), corroborating the key role of plasmonic heating in early stages of incubation to enhance protein-NPs interactions.

Comparatively, both AuNRs and AuNSs, functionalized with PEG-CM, exhibited distinct behaviors in protein corona formation when incubated with Fib, followed by irradiation. AuNRs-PEG-CM did not show any LSPR shifts under no *irradiation* or *sequential irradiation* conditions. However, under *simultaneous irradiation*, AuNRs-PEG-CM exhibited more pronounced red shifts and a greater reduction in UV–Vis absorbance intensity compared to AuNSs (Figure 4.1 E).

DLS analysis of the population size distributions revealed that both AuNRs-PEG-CM and AuNSs-PEG-CM experienced increases in hydrodynamic sizes under the different corona

formation modes. In both *simultaneous and sequential modes*, AuNSs exhibited larger increases in hydrodynamic size. However, when comparing relative changes from the bare nanoparticle sizes (prior to corona formation), AuNSs showed slightly greater size ratio increases in the *simultaneous mode*, whereas AuNRs seems to exhibit more pronounced size increases in the *sequential one*.

These increases in hydrodynamic size of AuNRs and AuNSs coated with PEG-CM after incubation with Fib, indicate formation of protein corona under the respective conditions. Importantly, the absence of significant peak broadening indicates that the observed size increases do not originate from aggregation or clustering and also suggests that the bioconjugates remain rather monodisperse. However, a noticeable broadening in the hydrodynamic size distribution of AuNRs (width) under the *simultaneous mode* was observed, which may be attributed to the presence of protein oligomers in the solution, as they typically fall within the 1–10 nm size range.[257]

In summary, the performed UV-Vis and DLS measurements revealed minimal interaction between AuNSs-PEG-CM and BSA, with negligible changes observed in both hydrodynamic size and optical properties. In contrast, incubation with Fib led to a large increase in hydrodynamic diameter and alterations in the UV-Vis spectra, particularly under irradiation, indicating the formation of a protein corona. Comparatively, AuNRs-PEG-CM exhibited greater red shifts and UV–Vis intensity loss than AuNSs-PEG-CM under the *simultaneous* irradiation mode. Both nanoparticle types showed increased hydrodynamic sizes after Fib incubation, with AuNSs showing greater changes in the *simultaneous* mode and AuNRs in the *sequential* mode. These findings emphasize the critical role of nanoparticle morphology in dictating protein binding affinity and demonstrate the enhanced interaction of Fib with both nanostructures, particularly under plasmonic heating conditions.

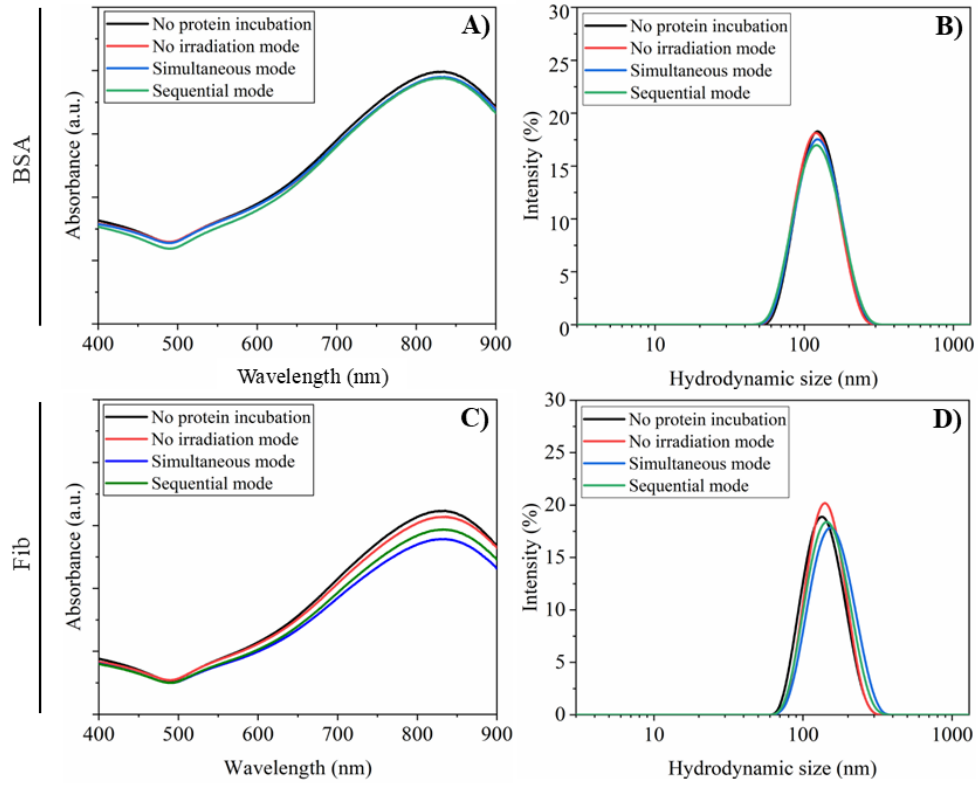

Figure 4.4. DLS and UV-Vis characterization of AuNSs-PEG-CM upon incubation with proteins under different irradiation modes: A) UV-Vis spectra and B) population hydrodynamic size distribution upon incubation with BSA; and C) UV-Vis spectra and D) population hydrodynamic size distribution upon incubation with Fib.

4.2.2 Conformational Changes of Proteins after Incubation with AuNSs and Plasmonic Heating

As previously described in Section 4.1.3, BSA and Fib also exhibited characteristic CD spectra upon incubation with AuNSs. Again, they showed two negative bands near 208 and 222 nm, indicative of α-helical structures, and a positive band around 218 nm, associated with β-sheet content (Figure 4.5). Interestingly, remarkable structural changes were observed for both proteins upon their incubation with AuNSs-PEG-CM under the application of the different irradiation conditions. Thus, in the case of star-shaped nanostructures incubated with BSA, the protein exhibited a notable increase in α-helical content under both *simultaneous* and *sequential* irradiation modes. Moreover, parallel and antiparallel β-sheets were completely absent after irradiation, suggesting a substantial structural reorganization of BSA induced by

plasmonic heating. β-turn content, however, remained largely unchanged along all experimental conditions (Figure 4.5 B and Table 4.3).

In contrast, plasmonic heating of Fib-AuNSs-PEG-CM dispersions led to a marked reduction in the α-helices, with complete loss observed in the *sequential* irradiation mode. Compared to free Fib, antiparallel β-sheet content increased by 16.0%, 23.5%, and 27.4% in the non-irradiated, *simultaneous*, and *sequential* modes, respectively. Meanwhile, parallel β-sheets were eliminated following both irradiation protocols, indicating selective unfolding or rearrangement of secondary structures under plasmonic-induced temperature increases (Figure 4.5 C-D, Table 4.3). These structural findings are in good agreement with UV–Vis and DLS measurements discussed in Section 4.2.1, where incubation of BSA with AuNSs–PEG-CM under various irradiation conditions resulted in only minor changes in LSPR peak position, UV–Vis absorbance intensity, and hydrodynamic sizes.

These data suggest a relatively stable NPs-protein interaction at the colloidal level, despite notable conformational rearrangements at the molecular scale—highlighting that subtle structural changes may occur without significantly affecting the bulk physicochemical properties of the nanostructures. In contrast, under all irradiation conditions, a pronounced decrease in UV–Vis absorbance and a substantial increase in hydrodynamic size were observed for AuNSs incubated Fib. These changes are consistent with CD data and support the conclusion that Fib undergoes significant conformational alterations and forms a more extensive protein corona upon binding and plasmonic stimulation.

When comparing these protein structural changes induced by AuNSs to those previously observed with AuNRs with the same surface coating, clear morphology-dependent differences emerge. Thus, BSA showed increased α-helicity upon incubation with star-shaped gold NPs, whereas incubation with AuNRs-PEG-CM followed by irradiation led to a decrease in α-helical content.

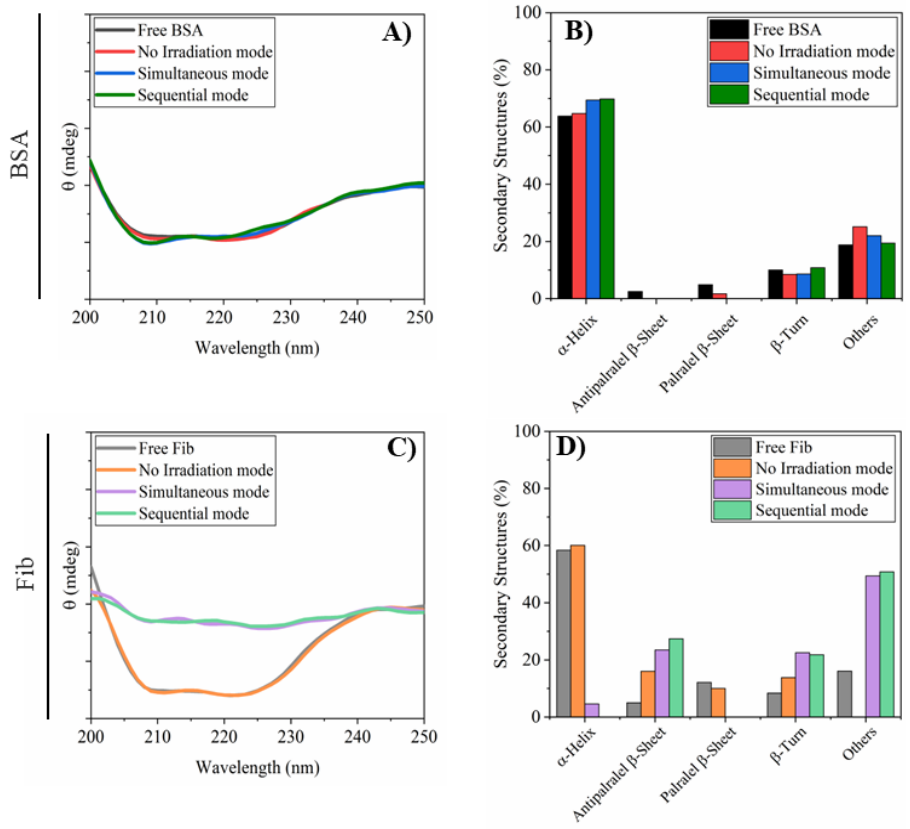

Figure 4.5. CD Spectra and B) corresponding secondary structure composition of BSA after adsorption onto AuNSs-PEG-CM. C) CD spectra and D) corresponding secondary structure compositions of Fib after adsorption onto AuNRs-PEG-CM.

Additionally, the disappearance of parallel β-sheets was exclusive to the BSA-AuNSs system and was not observed in the presence of AuNRs. In contrast, Fib showed comparable conformational changes with both typologies of NPs: a loss of α-helical content accompanied by an increase in antiparallel β-sheets and β-turns under plasmonic heating.

In summary, the performed analysis of the structural changes of BSA and Fib upon incubation/irradiation in the presence of AuNSs-PEG-CM showed significant conformational variations for both proteins. However, Fib exhibited a more pronounced response, suggesting a higher structural sensitivity to NPs interaction and thermal perturbation. This differential behavior may stem from intrinsic differences in protein architecture and flexibility, with the extended and multi-domain structure of Fib rendering it more susceptible to plasmonic-induced unfolding than BSA.

Table 4.3. Percentages of secondary structure content in BSA and Fib protein coronas formed on AuNSs-PEG-CM, in the absence of laser exposure and under *simultaneous* and *sequential* irradiation modes.

			Protein Secondary Structures				
Gold NPs	**Protein**	**Irradiation Mode**	**α-helix**	**Anti β-sheet**	**β-sheet**	**β-turn**	**Others**
AuNSs-PEG-CM	BSA	Free BSA	63.8	2.5	4.9	10.0	18.8
		No irradiation	64.7	0	1.7	8.5	25.1
		Simultaneous	64.4	0	0	9.6	26
		Sequential	64.8	0	0	10.8	24.4
	Fib	Free Fib	58.4	5.0	12.1	8.4	16.1
		No irradiation	60.1	16.0	10	13.8	0
		Simultaneous	4.6	23.5	0	22.5	49.4
		Sequential	0	27.4	0	21.8	50.8

4.3 Concluding Remarks on Protein Corona Characterization under Plasmonic Heating

This study explores how plasmonic heating influences protein corona formation on gold NPs, using BSA and Fib as model proteins. AuNRs and AuNSs, functionalized with either PEG-CM or PEG-NH_2, were incubated with the proteins under three conditions: no irradiation, *simultaneous* irradiation, and *sequential* irradiation.

PEG-NH_2-coated AuNRs exhibited stronger binding with both proteins due to favorable electrostatic interactions, particularly under plasmonic heating. BSA adsorption led to moderate conformational changes, primarily a reduction in α-helical content, with more pronounced effects observed under *simultaneous* irradiation. In contrast, Fib showed

extensive unfolding, characterized by near-complete loss of α-helices and an increase in antiparallel β-sheets, indicating higher heat sensitivity and a greater tendency for aggregation.

Fluorescence quenching studies provided further insights into protein-NPs interactions. BSA fluorescence was more effectively quenched by PEG-NH_2-coated AuNRs than by PEG-CM-coated ones, indicating closer proximity and stronger binding. This effect intensified under laser irradiation, especially at higher power, confirming that plasmonic heating promotes conformational flexibility and stronger surface interactions. Stern-Volmer and Hill analyses revealed that BSA binding to PEG-NH_2-coated AuNRs exhibited positive cooperativity, while binding to PEG-CM-coated AuNRs showed negative cooperativity, further emphasizing the impact of both surface chemistry and thermal energy on interaction dynamics.

AuNSs, due to their complex star-like geometry, showed limited BSA binding but greater affinity for Fib. Protein adsorption on AuNSs induced less intense structural and optical changes compared to AuNRs, although plasmonic heating still triggered conformational rearrangements, particularly in Fib. Notably, BSA showed an increase in α-helical content upon irradiation with AuNSs, in contrast to its behavior with AuNRs.

Collectively, these findings demonstrate that protein corona formation and protein structural integrity are strongly influenced by NPs morphology, surface chemistry, and thermal exposure. These observations are essential for designing nanomaterials with well-controlled bio-nano interfaces, ultimately improving biocompatibility and therapeutic efficacy.

Conclusions

AuNRs were successfully synthesized *via* a seed-mediated growth method using CTAB as a stabilizing surfactant and $AgNO_3$ as an anisotropy-directing agent. The resulting AuNRs exhibited high monodispersity and well-defined rod-like morphologies. In parallel, AuNSs were synthesized through an alternative seed-mediated route employing PVP as a stabilizing agent and DMF as both solvent and reducing agent, yielding star-shaped gold nanostructures with uniform particle size and morphology.

Both typologies of anisotropic gold NPs, AuNRs-PSS and AuNSs-PVP, demonstrated efficient photothermal conversion under CW laser irradiation. The extent of the photothermal response varied depending on the type of NPs, their concentration, or the applied laser power density, indicating the potential of the nanosystems for application in localized hyperthermia or as thermal sensitizers to enhance chemotherapeutic efficacy and selectively ablate malignant cells.

When exposed to fs laser pulses, both AuNRs and AuNSs generated lower temperature increases in dispersion compared to CW irradiation. This behavior was attributed to the ultrashort pulse duration of the fs laser, which fulfilled the thermal confinement condition by being shorter than the heat diffusion time of the surrounding medium.

Photostability studies under CW laser exposure revealed minimal changes in LSPR peaks, hydrodynamic sizes, and morphologies for both AuNRs and AuNSs, indicating the strong stability of both types of gold NPs. Under fs laser irradiation, AuNSs retained similar stability, while AuNRs exhibited a notable blue shift in LSPR, reduced hydrodynamic size, and pronounced morphological reshaping.

The successful PEGylation of the designed gold NPs was confirmed by characteristic red shifts in their LSPR peaks, increased hydrodynamic diameters, and altered zeta potentials. These physicochemical changes were consistent with an effective attachment of PEG chains to the NPs surfaces, which enhances their colloidal stability and modifies their interfacial properties.

PEGylated AuNRs and AuNSs remained highly stable in PBS, acetate buffer, and at low ionic strengths. However, incubation in higher NaCl concentrations induced notable shifts in the LSPR peaks and changes in the hydrodynamic dimensions of the NPs, indicating decreased

stability. Despite this, their average hydrodynamic size remained below *ca*. 200 nm across all tested conditions, supporting their potential suitability for cellular uptake required in several biomedical applications.

When dispersed in DMEM, the observed significant LSPR red-shifts and size increases—especially for AuNRs—indicated aggregation due to destabilizing components. Conversely, incubation in 10% FBS solution stabilized the designed gold NPs *via* protein corona formation, minimizing spectral and size changes. At higher FBS concentrations, increased protein adsorption led to greater aggregation, more prominently in AuNRs. The extent of these effects was modulated by the chemical nature of PEG terminal groups, affecting proteins-NPs interactions.

Cellular uptake studies using ICP-MS, TEM, and reflectance confocal microscopy confirmed the internalization PEG-coated AuNSs with various terminal groups by MDA-MB-231 and Balb/c 3T3 cells. In contrast, AuNRs were not detectable by reflectance imaging, likely due to their smaller size and weaker light scattering properties. Gold NPs coated with PEG-NH_2 showed the highest cellular internalization degrees, likely due to their enhanced electrostatic interactions with negatively charged cell membranes.

The performed *in vitro* cytotoxicity assays revealed high biocompatibility of PEGylated AuNRs and AuNSs in the absence of laser exposure, maintaining over 90% cell viability in both Balb/c 3T3 and MDA-MB-231 cell lines. Under CW laser irradiation, cytotoxicity increased with NPs concentration, with PEG-NH_2-coated nanostructures, especially in the case of AuNSs, inducing lower cell viability degrees due to higher internalization. Notably, cancer cells were more susceptible to photothermal treatment than healthy cells. Under fs laser irradiation, MDA-MB-231 cells incubated with PEGylated AuNRs and AuNSs exhibited significantly higher viability compared to CW laser conditions, due to more localized heat generation and reduced bulk heating—characteristic of thermal confinement.

Flow cytometry studies revealed that Balb/c 3T3 cells predominantly underwent apoptosis after CW laser exposure in the presence of mPEG- or PEG-NH_2-functionalized NPs, whereas MDA-MB-231 cells primarily experienced necrosis. Overall, cell death was more pronounced with AuNSs than with AuNRs in both cell types. Interestingly, exposure of PEG-NH_2 coated NPs

to pulsed fs laser led to a shift toward apoptotic pathways in MDA-MB-231 cells, indicating laser-dependent modulation of cell death mechanisms.

The characterization of the protein corona formed by BSA and Fib around AuNRs following plasmonic heating revealed a stronger affinity of proteins for AuNRs functionalized with PEG-NH_2 than for those coated with PEG-CM. Simultaneous laser irradiation of these bioconjugates led to denser corona formation, LSPR red shifts, increases in hydrodynamic size, and more extensive changes in protein secondary structure compared to sequential laser exposure. Fib was more structurally altered than BSA, suggesting higher sensitivity to plasmonic heating.

On the other hand, AuNSs coated with PEG-CM exhibited weak binding affinity with BSA, but stronger interactions with Fib. Although protein adsorption on the surface of star-shaped NPs induced less pronounced changes than those established in the case of AuNRs, significant secondary structure alterations in Fib were still observed following plasmonic heating of AuNSs.

References

1. Baig, N., Kammakakam, I. & Falath, W. Nanomaterials: a review of synthesis methods, properties, recent progress, and challenges. *Mater Adv* **2**, 1821–1871 (2021).

2. Bayda, S., Adeel, M., Tuccinardi, T., Cordani, M. & Rizzolio, F. The History of Nanoscience and Nanotechnology: From Chemical–Physical Applications to Nanomedicine. *Molecules* **25**, (2020).

3. Gnach, A., Lipinski, T., Bednarkiewicz, A., Rybka, J. & Capobianco, J. A. Upconverting nanoparticles: assessing the toxicity. *Chem Soc Rev* **44**, 1561–1584 (2015).

4. https://www.britishmuseum.org/research/collection_online/collection.

5. Asha, A. B. & Narain, R. Chapter 15 - Nanomaterials properties. in Polymer Science and Nanotechnology (ed. Narain, R.) 343–359 (Elsevier, 2020).

6. Neikov, O. D. & Yefimov, N. A. Chapter 9 - Nanopowders. in *Handbook of Non-Ferrous Metal Powders (Second Edition)* (eds. Neikov, O. D., Naboychenko, S. S. & Yefimov, N. A.) 271–311 (Elsevier, Oxford, 2019).

7. Noginov, M. M. *et al.* Magnetic resonance in iron oxide nanoparticles: Quantum features and effect of size. *J Magn Magn Mater* **320**, 2228–2232 (2008).

8. Li, Q. *et al.* Charge Transfer from Quantum-Confined 0D, 1D, and 2D Nanocrystals. *Chem Rev* **124**, 5695–5763 (2024).

9. Navya, P. N. & Daima, H. K. Rational engineering of physicochemical properties of nanomaterials for biomedical applications with nanotoxicological perspectives. *Nano Converg* **3**, 1-z. Epub 2016 Feb 1 (2016).

10. Tang, H., Zhu, C., Meng, G. & Wu, N. Review—Surface-Enhanced Raman Scattering Sensors for Food Safety and Environmental Monitoring. *J Electrochem Soc* **165**, B3098 (2018).

11. Kargozar, S. & Mozafari, M. Nanotechnology and Nanomedicine: Start small, think big. *Mater Today Proc* **5**, 15492–15500 (2018).

12. Saleh, T. A. Nanomaterials: Classification, properties, and environmental toxicities. *Environ Technol Innov* **20**, 101067 (2020).

13. Syduzzaman, M., Hassan, A., Anik, H. R., Akter, M. & Islam, M. R. Nanotechnology for High-Performance Textiles: A Promising Frontier for Innovation. *ChemNanoMat* **9**, e202300205 (2023).

14. Verma, C. *et al.* 3D Nanomaterials: The future of industrial, biological, and environmental applications. *Inorg Chem Commun* **156**, 111163 (2023).

15. Joudeh, N. & Linke, D. Nanoparticle classification, physicochemical properties, characterization, and applications: a comprehensive review for biologists. *J Nanobiotechnology* **20**, 262 (2022).

16. Zhang, X.-L. *et al.* One-pot synthesis of gold nanostars using plant polyphenols for cancer photoacoustic imaging and photothermal therapy. *Journal of Nanoparticle Research* **18**, 174 (2016).

17. Salata, O. V. Applications of nanoparticles in biology and medicine. *J Nanobiotechnology* **2**, 3 (2004).

18. Mhetre, H., Kanse, D. & Patil, D. Nanomaterials: Applications in Electronics. *Int J Adv Eng Nano Technol* **4**, 7–19 (2021).

19. Gohar, O. *et al.* Nanomaterials for advanced energy applications: Recent advancements and future trends. *Mater Des* **241**, 112930 (2024).

20. Aghababai Beni, A. & Jabbari, H. Nanomaterials for Environmental Applications. *Results in Engineering* **15**, 100467 (2022).

21. Subhan, M. A., Choudhury, K. P. & Neogi, N. Advances with Molecular Nanomaterials in Industrial Manufacturing Applications. *Nanomanufacturing* **1**, 97 (2021).

22. Kabir, D. *et al.* Dye-sensitized solar cell with plasmonic gold nanoparticles modified photoanode. *Nano-Structures & Nano-Objects* **26**, 100698 (2021).

23. Kashyap, K., Maheswata, M., Subrat Kumar, P. & and Khan, F. Adsorptive removal of heavy metal ions from aqueous solution by using green synthesized copper oxide nanoparticles. *Inorganic and Nano-Metal Chemistry* 1–12.

24. Jiang, S., Lin, K. & Cai, M. ZnO Nanomaterials: Current Advancements in Antibacterial Mechanisms and Applications. *Front Chem* **Volume 8-2020**, (2020).

25. Gong, B. *et al.* Thermo-responsive polymer encapsulated gold nanorods for single continuous wave laser-induced photodynamic/photothermal tumour therapy. *J Nanobiotechnology* **19**, 41 (2021).

26. Namgung, S. D. *et al.* Circularly polarized light-sensitive, hot electron transistor with chiral plasmonic nanoparticles. *Nat Commun* **13**, 5081 (2022).

27. Jain, S., Hirst, D. G. & O'Sullivan, J. M. Gold nanoparticles as novel agents for cancer therapy. *BJR* **85**, 101–113 (2012).

28. Khan, Y. *et al.* Classification, Synthetic, and Characterization Approaches to Nanoparticles, and Their Applications in Various Fields of Nanotechnology: A Review. *Catalysts* **12**, (2022).

29. Alkilany, A. M., Thompson, L. B., Boulos, S. P., Sisco, P. N. & Murphy, C. J. Gold nanorods: Their potential for photothermal therapeutics and drug delivery, tempered by the complexity of their biological interactions. *Adv Drug Deliv Rev* **64**, 190–199 (2012).

30. Khan, I., Saeed, K. & Khan, I. Nanoparticles: Properties, applications and toxicities. *Arabian Journal of Chemistry* **12**, 908–931 (2019).

31. Deshmukh, A., Bhaiswar, J., Kapse, V. & Meghe, D. 2 - Quantum dots: a brief review. in *Quantum Dots* (eds. Thejo Kalyani, N. et al.) 41–66 (Woodhead Publishing, 2023).

32. Chen, L., Wang, N., Wang, X. & Ai, S. Protein-directed in situ synthesis of platinum nanoparticles with superior peroxidase-like activity, and their use for photometric determination of hydrogen peroxide. *Microchimica Acta* **180**, 1517–1522 (2013).

33. Karikalan, N., Velmurugan, M., Chen, S.-M. & Karuppiah, C. Modern Approach to the Synthesis of Ni(OH)2 Decorated Sulfur Doped Carbon Nanoparticles for the Nonenzymatic Glucose Sensor. *ACS Appl Mater Interfaces* **8**, 22545–22553 (2016).

34. Şahin, B., Demir, E., Aygün, A., Gündüz, H. & Şen, F. Investigation of the effect of pomegranate extract and monodisperse silver nanoparticle combination on MCF-7 cell line. *J Biotechnol* **260**, 79–83 (2017).

35. Thakkar, K. N., Mhatre, S. S. & Parikh, R. Y. Biological synthesis of metallic nanoparticles. *Nanomedicine* **6**, 257–262 (2010).

36. Haes, A. J., Stuart, D. A., Nie, S. & Van Duyne, R. P. Using solution-phase nanoparticles, surface-confined nanoparticle arrays and single nanoparticles as biological sensing platforms. *J Fluoresc* **14**, 355–367 (2004).

37. Nadaf, N. Y. & Kanase, S. S. Biosynthesis of gold nanoparticles by Bacillus marisflavi and its potential in catalytic dye degradation. *Arabian Journal of Chemistry* **12**, 4806–4814 (2019).

38. Santhoshkumar, J., Rajeshkumar, S. & Venkat Kumar, S. Phyto-assisted synthesis, characterization and applications of gold nanoparticles – A review. *Biochem Biophys Rep* **11**, 46–57 (2017).

39. Jain, P. K., Huang, X., El-Sayed, I. & El-Sayed, M. Noble Metals on the Nanoscale: Optical and Photothermal Properties and Some Applications in Imaging, Sensing, Biology, and Medicine. *Acc Chem Res* **41**, 1578–1586 (2008).

40. Nikoobakht, B. & El-Sayed, M. Preparation and Growth Mechanism of Gold Nanorods (NRs) Using Seed-Mediated Growth Method. *Chemistry of Materials* **15**, 1957–1962 (2003).

41. Huang, X. & El-Sayed, M. A. Gold nanoparticles: Optical properties and implementations in cancer diagnosis and photothermal therapy. *J Adv Res* **1**, 13–28 (2010).

42. Link, S., Mohamed, M. B. & El-Sayed, M. Simulation of the Optical Absorption Spectra of Gold Nanorods as a Function of Their Aspect Ratio and the Effect of the Medium Dielectric Constant. *J Phys Chem B* **103**, 3073–3077 (1999).

43. Draine, B. T. The discrete-dipole approximation and its application to interstellar graphite grains. *Astrophysical Journal, Part 1 (ISSN 0004-637X), vol.333, Oct.15, 1988, p.848-872.* **333**, 848–872 (1988).

44. Garcia, M. A. Surface plasmons in metallic nanoparticles: fundamentals and applications. *J Phys D Appl Phys* **44**, 283001 (2011).

45. Lee, K.-S. & El-Sayed, M. Gold and Silver Nanoparticles in Sensing and Imaging: Sensitivity of Plasmon Response to Size, Shape, and Metal Composition. *J Phys Chem B* **110**, 19220–19225 (2006).

46. Andreiuk, B. *et al.* Design and synthesis of gold nanostars-based SERS nanotags for bioimaging applications. *Nanotheranostics* **6**, 10–30 (2022).

47. Becerril-Castro, I. *et al.* Gold Nanostars: Synthesis, Optical and SERS Analytical Properties. *Analysis & Sensing* **2**, e202200005 (2022).

48. Morton, W. *et al.* Modeling Au Nanostar Geometry in Bulk Solutions. *The Journal of Physical Chemistry C* **127**, 1680–1686 (2023).

49. Burda, C., Chen, X., Narayanan, R. & El-Sayed, M. Chemistry and Properties of Nanocrystals of Different Shapes. *Chem Rev* **105**, 1025–1102 (2005).

50. Senthil Kumar, P., Pastoriza-Santos, I., Rodríguez-González, B., Javier García de Abajo, F. & Liz-Marzán M., L. High-yield synthesis and optical response of gold nanostars. *Nanotechnology* **19**, 015606 (2007).

51. Hao, F., Nehl, C. L., Hafner, J. H. & Nordlander, P. Plasmon Resonances of a Gold Nanostar. *Nano Lett* **7**, 729–732 (2007).

52. Hao, E., Bailey, R. C., Schatz, G. C., Hupp, J. T. & Li, S. Synthesis and Optical Properties of "Branched" Gold Nanocrystals. *Nano Lett* **4**, 327–330 (2004).

53. de Puig, H., Tam, J. O., Yen, C.-W., Gehrke, L. & Hamad-Schifferli, K. Extinction Coefficient of Gold Nanostars. *The Journal of Physical Chemistry C* **119**, 17408–17415 (2015).

54. Chen, S. *et al.* Tunable nonlinear absorption of gold nanostars and application as a saturable absorber. *Opt Laser Technol* **168**, 109873 (2024).

55. Santhosh, P. B., Genova, J. & Chamati, H. Green Synthesis of Gold Nanoparticles: An Eco-Friendly Approach. *Chemistry (Easton)* **4**, 369 (2022).

56. Lu, H. *et al.* Modular and Integrated Systems for Nanoparticle and Microparticle Synthesis—A Review. *Biosensors (Basel)* **10**,165, (2020).

57. Szczyglewska, P., Feliczak-Guzik, A. & Nowak, I. Nanotechnology–General Aspects: A Chemical Reduction Approach to the Synthesis of Nanoparticles. *Molecules* **28**,13, (2023).

58. Iqbal, M. *et al.* Preparation of gold nanoparticles and determination of their particles size via different methods. *Mater Res Bull* **79**, 97–104 (2016).

59. Mafuné, F., Kohno, J., Takeda, Y., Kondow, T. & Sawabe, H. Formation of Gold Nanoparticles by Laser Ablation in Aqueous Solution of Surfactant. *J Phys Chem B* **105**, 5114–5120 (2001).

60. Sylvestre, J.-P. *et al.* Surface Chemistry of Gold Nanoparticles Produced by Laser Ablation in Aqueous Media. *J Phys Chem B* **108**, 16864–16869 (2004).

61. Chen, Y.-H. & Yeh, C.-S. Laser ablation method: use of surfactants to form the dispersed Ag nanoparticles. *Colloids Surf A Physicochem Eng Asp* **197**, 133–139 (2002).

62. Abou El-Nour, K. M. M., Eftaiha, A., Al-Warthan, A. & Ammar, R. A. A. Synthesis and applications of silver nanoparticles. *Arabian Journal of Chemistry* **3**, 135–140 (2010).

63. Parial, D., Patra, H. K., Roychoudhury, P., Dasgupta, A. K. & Pal, R. Gold nanorod production by cyanobacteria—a green chemistry approach. *J Appl Phycol* **24**, 55–60 (2012).

64. Sasidharan, S., Bahadur, D. & Srivastava, R. Rapid, One-Pot, Protein-Mediated Green Synthesis of Gold Nanostars for Computed Tomographic Imaging and Photothermal Therapy of Cancer. *ACS Sustain Chem Eng* **5**, 10163–10175 (2017).

65. Lassenberger, A. *et al.* Monodisperse Iron Oxide Nanoparticles by Thermal Decomposition: Elucidating Particle Formation by Second-Resolved in Situ Small-Angle X-ray Scattering. *Chemistry of Materials* **29**, 4511–4522 (2017).

66. Lu, A.-H., Salabas, E. L. & Schüth, F. Magnetic Nanoparticles: Synthesis, Protection, Functionalization, and Application. *Angewandte Chemie International Edition* **46**, 1222–1244 (2007).

67. Majidi, S., Zeinali Sehrig, F., Farkhani, S. M., Soleymani Goloujeh, M. & Akbarzadeh, A. Current methods for synthesis of magnetic nanoparticles. *Artif Cells Nanomed Biotechnol* **44**, 722–734 (2016).

68. Otto, K., Oja Acik, I., Krunks, M., Tõnsuaadu, K. & Mere, A. Thermal decomposition study of HAuCl4·3H2O and AgNO3 as precursors for plasmonic metal nanoparticles. *J Therm Anal Calorim* **118**, 1065–1072 (2014).

69. Zhang, J., Gao, Y., Alvarez-Puebla, R., Buriak, J. M. & Fenniri, H. Synthesis and SERS Properties of Nanocrystalline Gold Octahedra Generated from Thermal Decomposition of HAuCl4 in Block Copolymers. *Advanced Materials* **18**, 3233–3237 (2006).

70. Nasirpouri, F. Fundamentals and Principles of Electrode-Position. in *Electrodeposition of Nanostructured Materials* (ed. Nasirpouri, F.) 75–121 (Springer International Publishing, Cham, 2017).

71. Burlec, A. F. *et al.* Current Overview of Metal Nanoparticles' Synthesis, Characterization, and Biomedical Applications, with a Focus on Silver and Gold Nanoparticles. *Pharmaceuticals* **16**,10, (2023).

72. Anik, M. *et al.* Recent progress of magnetic nanoparticles in biomedical applications: A review. *Nano Select* **2**, 1146–1186 (2021).

73. Wu, S. *et al.* Nucleation Mechanism of Electrochemical Deposition of Cu on Reduced Graphene Oxide Electrodes. *The Journal of Physical Chemistry C* **115**, 15973–15979 (2011).

74. Herizchi, R., Abbasi, E., Milani, M. & Akbarzadeh, A. Current methods for synthesis of gold nanoparticles. *Artif Cells Nanomed Biotechnol* **44**, 596–602 (2016).

75. Kimling, J. *et al.* Turkevich Method for Gold Nanoparticle Synthesis Revisited. *J Phys Chem B* **110**, 15700–15707 (2006).

76. Ji, X. *et al.* Size Control of Gold Nanocrystals in Citrate Reduction: The Third Role of Citrate. *J Am Chem Soc* **129**, 13939–13948 (2007).

77. Ojea-Jiménez, I., Bastús, N. G. & Puntes, V. Influence of the Sequence of the Reagents Addition in the Citrate-Mediated Synthesis of Gold Nanoparticles. *The Journal of Physical Chemistry C* **115**, 15752–15757 (2011).

78. Brust, M., Walker, M., Bethell, D., Schiffrin, D. J. & Whyman, R. Synthesis of thiol-derivatised gold nanoparticles in a two-phase liquid–liquid system. *J Chem Soc Chem Commun* **7**,801–802 (1994).

79. Uson, L., Sebastian, V., Arruebo, M. & Santamaria, J. Continuous microfluidic synthesis and functionalization of gold nanorods. *Chemical Engineering Journal* **285**, 286–292 (2016).

80. Jana, N. R., Gearheart, L. & Murphy, C. J. Evidence for Seed-Mediated Nucleation in the Chemical Reduction of Gold Salts to Gold Nanoparticles. *Chemistry of Materials* **13**, 2313–2322 (2001).

81. Brown, K. R. & Natan, M. J. Hydroxylamine Seeding of Colloidal Au Nanoparticles in Solution and on Surfaces. *Langmuir* **14**, 726–728 (1998).

82. Priyadarshni, N. & Chanda, N. Gold Nanoparticle-Based Colorimetric Sensing of Metal Toxins. in *Miniaturized Biosensing Devices: Fabrication and Applications* (eds. Chandra, P. & Mahato, K.) 273–308 (Springer Nature Singapore, Singapore, 2022).

83. Wang, W. & Mattoussi, H. Engineering the Bio–Nano Interface Using a Multifunctional Coordinating Polymer Coating. *Acc Chem Res* **53**, 1124–1138 (2020).

84. Chen, Y., Xianyu, Y. & Jiang, X. Surface Modification of Gold Nanoparticles with Small Molecules for Biochemical Analysis. *Acc Chem Res* **50**, 310–319 (2017).

85. Komsthöft, T., Bovone, G., Bernhard, S. & Tibbitt, M. W. Polymer functionalization of inorganic nanoparticles for biomedical applications. *Curr Opin Chem Eng* **37**, 100849 (2022).

86. Kumar, Y., Sinha, A. S. K., Nigam, K. D. P., Dwivedi, D. & Sangwai, J. S. Functionalized nanoparticles: Tailoring properties through surface energetics and coordination chemistry for advanced biomedical applications. *Nanoscale* **15**, 6075–6104 (2023).

87. Danhier, F. *et al.* PLGA-based nanoparticles: an overview of biomedical applications. *J Control Release* **161**, 505–522 (2012).

88. Shi, L. *et al.* Effects of polyethylene glycol on the surface of nanoparticles for targeted drug delivery. *Nanoscale* **13**, 10748-10764 (2021).

89. Fam, S. Y. *et al.* Stealth Coating of Nanoparticles in Drug-Delivery Systems. *Nanomaterials (Basel)* **10**, 787 (2020).

90. Suk, J. S., Xu, Q., Kim, N., Hanes, J. & Ensign, L. M. PEGylation as a strategy for improving nanoparticle-based drug and gene delivery. *Adv Drug Deliv Rev* **99**, 28–51 (2016).

91. Levin, C. S., Bishnoi, S. W., Grady, N. K. & Halas, N. J. Determining the conformation of thiolated poly(ethylene glycol) on Au nanoshells by surface-enhanced Raman scattering spectroscopic assay. *Anal Chem* **78**, 3277–3281 (2006).

92. Padín González, E. *et al.* Understanding the Role and Impact of Poly (Ethylene Glycol) (PEG) on Nanoparticle Formulation: Implications for COVID-19 Vaccines. *Front Bioeng Biotechnol* **10**, (2022).

93. Butterworth, M. D., Illum, L. & Davis, S. S. Preparation of ultrafine silica- and PEG-coated magnetite particles. *Colloids Surf A Physicochem Eng Asp* **179**, 93–102 (2001).

94. Otsuka, H., Nagasaki, Y. & Kataoka, K. PEGylated nanoparticles for biological and pharmaceutical applications. *Adv Drug Deliv Rev* **55**, 403–419 (2003).

95. Xie, J., Xu, C., Kohler, N., Hou, Y. & Sun, S. Controlled PEGylation of Monodisperse Fe3O4 Nanoparticles for Reduced Non-Specific Uptake by Macrophage Cells. *Advanced Materials* **19**, 3163–3166 (2007).

96. Hirsch, L. R. *et al.* Nanoshell-mediated near-infrared thermal therapy of tumors under magnetic resonance guidance. *Proceedings of the National Academy of Sciences* **100**, 13549–13554 (2003).

97. Peracchia, M. T. *et al.* Visualization of in vitro protein-rejecting properties of PEGylated stealth polycyanoacrylate nanoparticles. *Biomaterials* **20**, 1269–1275 (1999).

98. Peracchia, M. T. *et al.* Stealth PEGylated polycyanoacrylate nanoparticles for intravenous administration and splenic targeting. *J Control Release* **60**, 121–128 (1999).

99. Bazile, D. *et al.* Stealth Me. PEG-PLA Nanoparticles Avoid Uptake by the Mononuclear Phagocytes System. *J Pharm Sci* **84**, 493–498 (1995).

100. Alexis, F., Pridgen, E., Molnar, L. K. & Farokhzad, O. C. Factors Affecting the Clearance and Biodistribution of Polymeric Nanoparticles. *Mol Pharm* **5**, 505–515 (2008).

101. Lim, J., Yeap, S. P., Che, H. X. & Low, S. C. Characterization of magnetic nanoparticle by dynamic light scattering. *Nanoscale Res Lett* **8**, 381 (2013).

102. Mudalige, T. *et al.* Chapter 11 - Characterization of Nanomaterials: Tools and Challenges. in *Nanomaterials for Food Applications* (eds. López Rubio, A., Fabra Rovira, M. J., martínez Sanz, M. & Gómez-Mascaraque, L. G.) 313–353 (Elsevier, 2019).

103. Filipe, V., Hawe, A. & Jiskoot, W. Critical evaluation of Nanoparticle Tracking Analysis (NTA) by NanoSight for the measurement of nanoparticles and protein aggregates. *Pharm Res* **27**, 796–810 (2010).

104. Mourdikoudis, S., Pallares, R. M. & Thanh, N. T. K. Characterization techniques for nanoparticles: comparison and complementarity upon studying nanoparticle properties. *Nanoscale* **10**, 12871–12934 (2018).

105. Pate, K. & Safier, P. 12 - Chemical metrology methods for CMP quality. in *Advances in Chemical Mechanical Planarization (CMP)* (ed. Babu, S.) 299–325 (Woodhead Publishing, 2016).

106. Polo, E. *et al.* Colloidal bioplasmonics. *Nano Today* **20**, 58–73 (2018).

107. Zook, J. M., Rastogi, V., MacCuspie, R. I., Keene, A. M. & Fagan, J. Measuring Agglomerate Size Distribution and Dependence of Localized Surface Plasmon Resonance Absorbance on Gold Nanoparticle Agglomerate Size Using Analytical Ultracentrifugation. *ACS Nano* **5**, 8070–8079 (2011).

108. Ostermeyer, A.-K., Kostigen Mumuper, C., Semprini, L. & Radniecki, T. Influence of Bovine Serum Albumin and Alginate on Silver Nanoparticle Dissolution and Toxicity to Nitrosomonas europaea. *Environ Sci Technol* **47**, 14403–14410 (2013).

109. Njoki, P. N. *et al.* Size Correlation of Optical and Spectroscopic Properties for Gold Nanoparticles. *The Journal of Physical Chemistry C* **111**, 14664–14669 (2007).

110. Myroshnychenko, V. *et al.* Modelling the optical response of gold nanoparticles. *Chem Soc Rev* **37**, 1792–1805 (2008).

111. Blanco-Andujar, C. *et al.* Real-time tracking of delayed-onset cellular apoptosis induced by intracellular magnetic hyperthermia. *Nanomedicine (Lond)* **11**, 121–136 (2016).

112. Gontier, E. *et al.* Is there penetration of titania nanoparticles in sunscreens through skin? A comparative electron and ion microscopy study. *Nanotoxicology* **2**, 218–231 (2008).

113. Elliott, A. D. Confocal Microscopy: Principles and Modern Practices. *Curr Protoc Cytom* **92**, e68 (2020).

114. Rigby, P. J. & Goldie, R. G. Confocal microscopy in biomedical research. *Croat Med J* **40**, 346–352 (1999).

115. Mahmoudi, M., Landry, M. P., Moore, A. & Coreas, R. The protein corona from nanomedicine to environmental science. *Nat Rev Mater* **8**, 422–438 (2023).

116. Pan, H., Qin, M., Meng, W., Cao, Y. & Wang, W. How Do Proteins Unfold upon Adsorption on Nanoparticle Surfaces? *Langmuir* **28**, 12779–12787 (2012).

117. Castagnola, V. *et al.* Biological recognition of graphene nanoflakes. *Nat Commun* **9**, 1577 (2018).

118. Casals, E., Pfaller, T., Duschl, A., Oostingh, G. J. & Puntes, V. Time Evolution of the Nanoparticle Protein Corona. *ACS Nano* **4**, 3623–3632 (2010).

119. Milani, S., Baldelli Bombelli, F., Pitek, A. S., Dawson, K. A. & Rädler, J. Reversible versus Irreversible Binding of Transferrin to Polystyrene Nanoparticles: Soft and Hard Corona. *ACS Nano* **6**, 2532–2541 (2012).

120. Kokkinopoulou, M., Simon, J., Landfester, K., Mailänder, V. & Lieberwirth, I. Visualization of the protein corona: towards a biomolecular understanding of nanoparticle-cell-interactions. *Nanoscale* **9**, 8858–8870 (2017).

121. De, M., You, C.-C., Srivastava, S. & Rotello, V. M. Biomimetic Interactions of Proteins with Functionalized Nanoparticles: A Thermodynamic Study. *J Am Chem Soc* **129**, 10747–10753 (2007).

122. Zhang, Y., Wu, J. L. Y., Lazarovits, J. & Chan, W. C. W. An Analysis of the Binding Function and Structural Organization of the Protein Corona. *J Am Chem Soc* **142**, 8827–8836 (2020).

123. García-Álvarez, R. & Vallet-Regí, M. Hard and Soft Protein Corona of Nanomaterials: Analysis and Relevance. *Nanomaterials* **11**,888, (2021).

124. Soenen, S. J. *et al.* Cellular toxicity of inorganic nanoparticles: Common aspects and guidelines for improved nanotoxicity evaluation. *Nano Today* **6**, 446–465 (2011).

125. Deng, J. & Gao, C. Recent advances in interactions of designed nanoparticles and cells with respect to cellular uptake, intracellular fate, degradation and cytotoxicity. *Nanotechnology* **27**, 412002 (2016).

126. Xia, T. *et al.* Comparison of the Mechanism of Toxicity of Zinc Oxide and Cerium Oxide Nanoparticles Based on Dissolution and Oxidative Stress Properties. *ACS Nano* **2**, 2121–2134 (2008).

127. Derfus, A. M., Chan, W. C. W. & Bhatia, S. N. Probing the Cytotoxicity of Semiconductor Quantum Dots. *Nano Lett* **4**, 11–18 (2004).

128. Barnard, P. J. & Berners-Price, S. J. Targeting the mitochondrial cell death pathway with gold compounds. *Coord Chem Rev* **251**, 1889–1902 (2007).

129. Tait, S. W. G. & Green, D. R. Mitochondria and cell death: outer membrane permeabilization and beyond. *Nat Rev Mol Cell Biol* **11**, 621–632 (2010).

130. Larsen, A. *et al.* Gold ions bio-released from metallic gold particles reduce inflammation and apoptosis and increase the regenerative responses in focal brain injury. *Histochem Cell Biol* **130**, 681–692 (2008).

131. Kang, M. S. *et al.* Biosafety of inorganic nanomaterials for theranostic applications. *Emergent Mater* **5**, 1995–2029 (2022).

132. Awashra, M. & Młynarz, P. The toxicity of nanoparticles and their interaction with cells: an in vitro metabolomic perspective. *Nanoscale Adv* **5**, 2674–2723 (2023).

133. Zhao, Z., Ukidve, A., Krishnan, V. & Mitragotri, S. Effect of physicochemical and surface properties on in vivo fate of drug nanocarriers. *Adv Drug Deliv Rev* **143**, 3–21 (2019).

134. Yohan, D., Cruje, C., Lu, X. & Chithrani, D. B. Size-Dependent Gold Nanoparticle Interaction at Nano–Micro Interface Using Both Monolayer and Multilayer (Tissue-Like) Cell Models. *Nanomicro Lett* **8**, 44–53 (2016).

135. Chithrani, B. D., Ghazani, A. A. & Chan, W. C. W. Determining the Size and Shape Dependence of Gold Nanoparticle Uptake into Mammalian Cells. *Nano Lett* **6**, 662–668 (2006).

136. Xie, X., Liao, J., Shao, X., Li, Q. & Lin, Y. The Effect of shape on Cellular Uptake of Gold Nanoparticles in the forms of Stars, Rods, and Triangles. *Sci Rep* **7**, 3827 (2017).

137. Donahue, N. D., Acar, H. & Wilhelm, S. Concepts of nanoparticle cellular uptake, intracellular trafficking, and kinetics in nanomedicine. *Adv Drug Deliv Rev* **143**, 68–96 (2019).

138. Bartneck, M. *et al.* Rapid Uptake of Gold Nanorods by Primary Human Blood Phagocytes and Immunomodulatory Effects of Surface Chemistry. *ACS Nano* **4**, 3073–3086 (2010).

139. Kedmi, R., Ben-Arie, N. & Peer, D. The systemic toxicity of positively charged lipid nanoparticles and the role of Toll-like receptor 4 in immune activation. *Biomaterials* **31**, 6867–6875 (2010).

140. Cao, H. *et al.* Hydrophobic interaction mediating self-assembled nanoparticles of succinobucol suppress lung metastasis of breast cancer by inhibition of VCAM-1 expression. *Journal of Controlled Release* **205**, 162–171 (2015).

141. Sun, S. *et al.* Effect of Hydrophobicity on Nano-Bio Interactions of Zwitterionic Luminescent Gold Nanoparticles at the Cellular Level. *Bioconjug Chem* **29**, 1841–1846 (2018).

142. Augustine, R. *et al.* Cellular uptake and retention of nanoparticles: Insights on particle properties and interaction with cellular components. *Mater Today Commun* **25**, 101692 (2020).

143. Giner-Casares, J. J., Henriksen-Lacey, M., Coronado-Puchau, M. & Liz-Marzán, L. M. Inorganic nanoparticles for biomedicine: where materials scientists meet medical research. *Materials Today* **19**, 19–28 (2016).

144. Aishwaryadev Banerjee, S. and C. H. M. Nanostructures for Biosensing, with a Brief Overview on Cancer Detection, IoT, and the Role of Machine Learning in Smart Biosensors. *sensors* **21**, 1–33 (2021).

145. Beniwal, N., Verma, A., Putta, C. L. & Rengan, A. K. Recent Trends in Bio-nanomaterials and Non-invasive Combinatorial Approaches of Photothermal Therapy against Cancer. *Nanotheranostics* **8**, 219–238 (2024).

146. Szwed, M. & Marczak, A. Application of Nanoparticles for Magnetic Hyperthermia for Cancer Treatment—The Current State of Knowledge. *Cancers (Basel)* **16**, 1156 (2024).

147. del Pino, P. & Pelaz, B. Chapter 13 - Hyperthermia Using Inorganic Nanoparticles. in *Frontiers of Nanoscience* (eds. de la Fuente, J. M. & Grazu, V.) vol. 4 309–335 (Elsevier, 2012).

148. Kacem, M., Essoumhi, A. & Dib, M. Magnetic iron oxide-based materials and their hyperthermia application: A review. *Inorg Chem Commun* **166**, 112510 (2024).

149. Kairdolf, B. *et al.* Semiconductor Quantum Dots for Bioimaging and Biodiagnostic Applications. *Annu Rev Anal Chem (Palo Alto Calif)* **6**,143–162, (2013).

150. Si, P. *et al.* Gold nanomaterials for optical biosensing and bioimaging. *Nanoscale Adv* **3**, 2679–2698 (2021).

151. Liba, O., SoRelle, E. D., Sen, D. & de La Zerda, A. Contrast-enhanced optical coherence tomography with picomolar sensitivity for functional in vivo imaging. *Sci Rep* **6**, 23337 (2016).

152. SoRelle, E. D., Liba, O., Hussain, Z., Gambhir, M. & de la Zerda, A. Biofunctionalization of Large Gold Nanorods Realizes Ultrahigh-Sensitivity Optical Imaging Agents. *Langmuir* **31**, 12339–12347 (2015).

153. Kim, C. *et al.* In vivo photoacoustic mapping of lymphatic systems with plasmon-resonant nanostars. *J Mater Chem* **21**, 2841–2844 (2011).

154. Harmsen, S. *et al.* Surface-Enhanced Resonance Raman Scattering Nanostars for High Precision Cancer Imaging. *Sci Transl Med* **7**, 271ra7 (2015).

155. Ou, Y.-C. *et al.* Diagnosis of immunomarkers in vivo via multiplexed surface enhanced Raman spectroscopy with gold nanostars. *Nanoscale* **10**, 13092–13105 (2018).

156. Pissuwan, D. & Hattori, Y. Detection of Adhesion Molecules on Inflamed Macrophages at Early-Stage Using SERS Probe Gold Nanorods. *Nanomicro Lett* **9**, 8 (2016).

157. Fales, A. M., Yuan, H. & Vo-Dinh, T. Silica-Coated Gold Nanostars for Combined Surface-Enhanced Raman Scattering (SERS) Detection and Singlet-Oxygen Generation: A Potential Nanoplatform for Theranostics. *Langmuir* **27**, 12186–12190 (2011).

158. Khalbas, A. H., Albayati, T. M., Ali, N. S. & Salih, I. K. Drug loading methods and kinetic release models using of mesoporous silica nanoparticles as a drug delivery system: A review. *S Afr J Chem Eng* **50**, 261–280 (2024).

159. Vallet-Regi, M., Rámila, A., del Real, R. P. & Pérez-Pariente, J. A New Property of MCM-41: Drug Delivery System. *Chemistry of Materials* **13**, 308–311 (2001).

160. Meireles, I. B. da C. J., Oliveira, A. F., Rodrigues, M. A. & Sousa, E. M. B. de. A platform of gold nanoparticles coated with silica as controlled drug delivery for application in cancer treatment. *J Mater Sci* **59**, 22181–22205 (2024).

161. Arellano, L. G. *et al.* Light excitation of gold Nanorod-Based hybrid nanoplatforms for simultaneous bimodal phototherapy. *J Mol Liq* **377**, 121511 (2023).

162. Vankayala, R., Huang, Y.-K., Kalluru, P., Chiang, C.-S. & Hwang, K. C. First Demonstration of Gold Nanorods-Mediated Photodynamic Therapeutic Destruction of Tumors via Near Infra-Red Light Activation. *Small* **10**, 1612–1622 (2014).

163. Huang, X., El-Sayed, I., Qian, W. & El-Sayed, M. Cancer Cell Imaging and Photothermal Therapy in the Near-Infrared Region by Using Gold Nanorods. *J Am Chem Soc* **128**, 2115–2120 (2006).

164. Dickerson, E. *et al.* Gold nanorod assisted near-infrared plasmonic photothermal therapy (PPTT) of squamous cell carcinoma in mice. *Cancer Lett* **269**, 57–66 (2008).

165. Espinosa, A. *et al.* Cancer Cell Internalization of Gold Nanostars Impacts Their Photothermal Efficiency In Vitro and In Vivo: Toward a Plasmonic Thermal Fingerprint in Tumoral Environment. *Adv Healthc Mater* **5**, 1040–1048 (2016).

166. Bao, C. *et al.* Gold nanoprisms as a hybrid in vivo cancer theranostic platform for in situ photoacoustic imaging, angiography, and localized hyperthermia. *Nano Res* **9**, 1043–1056 (2016).

167. Khlebtsov, B. *et al.* Nanocomposites Containing Silica-Coated Gold–Silver Nanocages and Yb–2,4-Dimethoxyhematoporphyrin: Multifunctional Capability of IR-Luminescence Detection, Photosensitization, and Photothermolysis. *ACS Nano* **5**, 7077–7089 (2011).

168. Liu, Y. *et al.* Tumor-triggered drug release from calcium carbonate-encapsulated gold nanostars for near-infrared photodynamic/photothermal combination antitumor therapy. *Theranostics* **7**, 1650–1662 (2017).

169. Hühn, J. *et al.* Selected Standard Protocols for the Synthesis, Phase Transfer, and Characterization of Inorganic Colloidal Nanoparticles. *Chemistry of Materials* **29**, 399–461 (2017).

170. Graf, C., Vossen, D. L. J., Imhof, A. & van Blaaderen, A. A General Method To Coat Colloidal Particles with Silica. *Langmuir* **19**, 6693–6700 (2003).

171. Barbosa, S. *et al.* Tuning size and sensing properties in colloidal gold nanostars. *Langmuir* **26**, 14943–14950 (2010).

172. Roper, D. K., Ahn, W. & Hoepfner, M. Microscale Heat Transfer Transduced by Surface Plasmon Resonant Gold Nanoparticles. *The Journal of Physical Chemistry C* **111**, 3636–3641 (2007).

173. Das, N. Ch. *et al.* Shape and Size of Highly Concentrated Micelles in CTAB/NaSal Solutions by Small Angle Neutron Scattering (SANS). *Langmuir* **28**, 11962–11968 (2012).

174. Qin, Z. & Bischof, J. C. Thermophysical and biological responses of gold nanoparticle laser heating. *Chem Soc Rev* **41**, 1191–1217 (2012).

175. Chen, H., Shao, L., Li, Q. & Wang, J. Gold nanorods and their plasmonic properties. *Chem Soc Rev* **42**, 2679–2724 (2013).

176. Kekicheff, P. & Spalla, O. Refractive Index of Thin Aqueous Films Confined between Two Hydrophobic Surfaces. *Langmuir* **10**, 1584–1591 (1994).

177. Liu, H., Pierre-Pierre, N. & Huo, Q. Dynamic light scattering for gold nanorod size characterization and study of nanorod–protein interactions. *Gold Bull* **45**, 187–195 (2012).

178. Hassan, P. A., Rana, S. & Verma, G. Making Sense of Brownian Motion: Colloid Characterization by Dynamic Light Scattering. *Langmuir* **31**, 3–12 (2015).

179. Nikoobakht, B. & El-Sayed, M. A. Evidence for Bilayer Assembly of Cationic Surfactants on the Surface of Gold Nanorods. *Langmuir* **17**, 6368–6374 (2001).

180. Mirza, A. Z. & Shamshad, H. Fabrication and characterization of doxorubicin functionalized PSS coated gold nanorod. *Arabian Journal of Chemistry* **12**, 146–150 (2019).

181. Pastoriza-Santos, I. & Liz-Marzán, L. M. N,N-Dimethylformamide as a Reaction Medium for Metal Nanoparticle Synthesis. *Adv Funct Mater* **19**, 679–688 (2009).

182. Kereselidze, Z., Romero Arellano, V. H., Peralta, X. & Santamaria, F. Gold Nanostar Synthesis with a Silver Seed Mediated Growth Method. *J Vis Exp,* **59,**3570 (2012).

183. Theodorou, I. G. *et al.* Fluorescence enhancement from single gold nanostars: towards ultra-bright emission in the first and second near-infrared biological windows. *Nanoscale* **10**, 15854–15864 (2018).

184. Filippov, S. K. *et al.* Dynamic light scattering and transmission electron microscopy in drug delivery: a roadmap for correct characterization of nanoparticles and interpretation of results. *Mater Horiz* **10**, 5354–5370 (2023).

185. Pattani, V. P. & Tunnell, J. W. Nanoparticle-mediated photothermal therapy: A comparative study of heating for different particle types. *Lasers Surg Med* **44**, 675–684 (2012).

186. Cole, J. R., Mirin, N. A., Knight, M. W., Goodrich, G. P. & Halas, N. J. Photothermal Efficiencies of Nanoshells and Nanorods for Clinical Therapeutic Applications. *The Journal of Physical Chemistry C* **113**, 12090–12094 (2009).

187. Almada, M. *et al.* Photothermal conversion efficiency and cytotoxic effect of gold nanorods stabilized with chitosan, alginate and poly(vinyl alcohol). *Materials Science and Engineering C* **77**, 583–593 (2017).

188. Horiguchi, Y., Honda, K., Kato, Y., Nakashima, N. & Niidome, Y. Photothermal Reshaping of Gold Nanorods Depends on the Passivating Layers of the Nanorod Surfaces. *Langmuir* **24**, 12026–12031 (2008).

189. Taha, S., Mohamed, W. R., Elhemely, M. A., El-Gendy, A. O. & Mohamed, T. Tunable femtosecond laser suppresses the proliferation of breast cancer in vitro. *J Photochem Photobiol B* **240**, 112665 (2023).

190. Ekici, O. *et al.* Thermal analysis of gold nanorods heated with femtosecond laser pulses. *J Phys D Appl Phys* **41**, 185501 (2008).

191. Reznickova, A. *et al.* PEGylated gold nanoparticles: Stability, cytotoxicity and antibacterial activity. *Colloids Surf A Physicochem Eng Asp* **560**, 26–34 (2019).

192. Kopwitthaya, A. *et al.* Biocompatible PEGylated gold nanorods as colored contrast agents for targeted in vivo cancer applications. *Nanotechnology* **21**, 315101 (2010).

193. Zygouri, E. *et al.* pH-Sensitive Gold Nanorods for Non-Steroidal Anti-Inflammatory Drugs (NSAIDs) Delivery and DNA-Binding Studies. *Molecules* **28**,3780, (2023).

194. Sperling, R. A. *et al.* Size Determination of (Bio)conjugated Water-Soluble Colloidal Nanoparticles: A Comparison of Different Techniques. *The Journal of Physical Chemistry C* **111**, 11552–11559 (2007).

195. Lee, S.-Y. & Shieh, M.-J. Platinum(II) Drug-Loaded Gold Nanoshells for Chemo-Photothermal Therapy in Colorectal Cancer. *ACS Appl Mater Interfaces* **12**, 4254–4264 (2020).

196. Chen, H. *et al.* 'Living' PEGylation on gold nanoparticles to optimize cancer cell uptake by controlling targeting ligand and charge densities. *Nanotechnology* **24**, 355101 (2013).

197. Schmalenberg, K. E., Frauchiger, L., Nikkhouy-Albers, L. & Uhrich, K. E. Cytotoxicity of a Unimolecular Polymeric Micelle and Its Degradation Products. *Biomacromolecules* **2**, 851–855 (2001).

198. Chávez, M. *et al.* Distinct thermoresponsive behaviour of oligo- and poly-ethylene glycol protected gold nanoparticles in concentrated salt solutions. *Nanoscale Adv* **3**, 4767–4779 (2021).

199. Emilsson, G. *et al.* Strongly Stretched Protein Resistant Poly(ethylene glycol) Brushes Prepared by Grafting-To. *ACS Appl Mater Interfaces* **7**, 7505–7515 (2015).

200. Mahmoud, N. N. *et al.* Interaction of gold nanorods with cell culture media: Colloidal stability, cytotoxicity and cellular death modality. *J Drug Deliv Sci Technol* **60**, 101965 (2020).

201. Masoudi, A., Madaah Hosseini, H. R., Shokrgozar, M. A., Ahmadi, R. & Oghabian, M. A. The effect of poly(ethylene glycol) coating on colloidal stability of superparamagnetic iron oxide nanoparticles as potential MRI contrast agent. *Int J Pharm* **433**, 129–141 (2012).

202. Areias, L. R. P., Mariz, I., Maçôas, E. & Farinha, J. P. S. Reflectance Confocal Microscopy: A Powerful Tool for Large Scale Characterization of Ordered/Disordered Morphology in Colloidal Photonic Structures. *ACS Nano* **15**, 11779–11788 (2021).

203. Pakravan, A., Salehi, R. & Mahkam, M. Comparison study on the effect of gold nanoparticles shape in the forms of star, hallow, cage, rods, and Si-Au and Fe-Au core-shell on photothermal cancer treatment. *Photodiagnosis Photodyn Ther* **33**, 102144 (2021).

204. Wang, W. *et al.* Facile Synthesis of Uniform Virus-like Mesoporous Silica Nanoparticles for Enhanced Cellular Internalization. *ACS Cent Sci* **3**, 839–846 (2017).

205. Behzadi, S. *et al.* Cellular uptake of nanoparticles: journey inside the cell. *Chem Soc Rev* **46**, 4218–4244 (2017).

206. Li, B. & Tang, M. Research progress of nanoparticle toxicity signaling pathway. *Life Sci* **263**, 118542 (2020).

207. Sakhtianchi, R. *et al.* Exocytosis of nanoparticles from cells: Role in cellular retention and toxicity. *Adv Colloid Interface Sci* **201–202**, 18–29 (2013).

208. Du, X.-J. *et al.* The effect of surface charge on oral absorption of polymeric nanoparticles. *Biomater Sci* **6**, 642–650 (2018).

209. Awashra, M. & Młynarz, P. The toxicity of nanoparticles and their interaction with cells: an in vitro metabolomic perspective. *Nanoscale Adv* **5**, 2674–2723 (2023).

210. Hassan, H. *et al.* Gold nanomaterials – The golden approach from synthesis to applications. *Mater Sci Energy Technol* **5**, 375–390 (2022).

211. Yao, X., Qi, C., Sun, C., Huo, F. & Jiang, X. Poly(ethylene glycol) alternatives in biomedical applications. *Nano Today* **48**, 101738 (2023).

212. Huang, X., Jain, P. K., El-Sayed, I. H. & El-Sayed, M. A. Determination of the Minimum Temperature Required for Selective Photothermal Destruction of Cancer Cells with the Use of Immunotargeted Gold Nanoparticles. *Photochem Photobiol* **82**, 412–417 (2006).

213. Jang, M., Kim, S. S. & Lee, J. Cancer cell metabolism: implications for therapeutic targets. *Exp Mol Med* **45**, e45–e45 (2013).

214. Pavlova, N. N., Zhu, J. & Thompson, C. B. The hallmarks of cancer metabolism: Still emerging. *Cell Metab* **34**, 355–377 (2022).

215. Melamed, J. R., Edelstein, R. S. & Day, E. S. Elucidating the Fundamental Mechanisms of Cell Death Triggered by Photothermal Therapy. *ACS Nano* **9**, 6–11 (2015).

216. Xiaofei, Y. *et al.* Effect of Laser Irradiation on Cell Function and Its Implications in Raman Spectroscopy. *Appl Environ Microbiol* **84**, e02508-17 (2018).

217. Smith, C. N. & Alexander, B. R. The relative cytotoxicity of personal care preservative systems in Balb/C 3T3 clone A31 embryonic mouse cells and the effect of selected preservative systems upon the toxicity of a standard rinse-off formulation. *Toxicology in Vitro* **19**, 963–969 (2005).

218. Salinas-Jazmín, N. *et al.* Continuous exposure to doxorubicin induces stem cell-like characteristics and plasticity in MDA-MB-231 breast cancer cells identified with the SORE6 reporter. *Cancer Chemother Pharmacol* **94**, 571–583 (2024).

219. Smith, L. *et al.* The analysis of doxorubicin resistance in human breast cancer cells using antibody microarrays. *Mol Cancer Ther* **5**, 2115–2120 (2006).

220. Mascolo, M. G. *et al.* BALB/c 3T3 cell transformation assay for the prediction of carcinogenic potential of chemicals and environmental mixtures. *Toxicology in Vitro* **24**, 1292–1300 (2010).

221. Fang, Y., Sullivan, R. & Graham, C. H. Confluence-dependent resistance to doxorubicin in human MDA-MB-231 breast carcinoma cells requires hypoxia-inducible factor-1 activity. *Exp Cell Res* **313**, 867–877 (2007).

222. Cudazzo, G., Smart, D. J., McHugh, D. & Vanscheeuwijck, P. Lysosomotropic-related limitations of the BALB/c 3T3 cell-based neutral red uptake assay and an alternative testing approach for assessing e-liquid cytotoxicity. *Toxicology in Vitro* **61**, 104647 (2019).

223. Koley, D. & Bard, A. J. Triton X-100 concentration effects on membrane permeability of a single HeLa cell by scanning electrochemical microscopy (SECM). *Proceedings of the National Academy of Sciences* **107**, 16783–16787 (2010).

224. Pattani, V. P., Shah, J., Atalis, A., Sharma, A. & Tunnell, J. W. Role of apoptosis and necrosis in cell death induced by nanoparticle-mediated photothermal therapy. *Journal of Nanoparticle Research* **17**, 20 (2015).

225. Dheyab, M. A. *et al.* Gold nanoparticles-based photothermal therapy for breast cancer. *Photodiagnosis Photodyn Ther* **42**, 103312 (2023).

226. Zhigilei, L. V & Garrison, B. J. Microscopic mechanisms of laser ablation of organic solids in the thermal and stress confinement irradiation regimes. *J Appl Phys* **88**, 1281–1298 (2000).

227. Mustafa, H., Matthews, D. T. A. & Römer, G. R. B. E. Influence of the pulse duration at near-infrared wavelengths on the laser-induced material removal of hot-dipped galvanized steel. *J Laser Appl* **32**, 022015 (2020).

228. Hashemi, F. *et al.* Laser irradiation affects the biological identity and cellular uptake of plasmonic nanoparticles. *Nanoscale* **11**, 5974–5981 (2019).

229. Nandakumar, A. *et al.* Dynamic Protein Corona of Gold Nanoparticles with an Evolving Morphology. *ACS Appl Mater Interfaces* **13**, 58238–58251 (2021).

230. Weisel, J. W. & Litvinov, R. I. Fibrin Formation, Structure and Properties. in *Fibrous Proteins: Structures and Mechanisms* (eds. Parry, D. A. D. & Squire, J. M.) 405–456 (Springer International Publishing, Cham, 2017).

231. Kharazian, B., Hadipour, N. L. & Ejtehadi, M. R. Understanding the nanoparticle–protein corona complexes using computational and experimental methods. *Int J Biochem Cell Biol* **75**, 162–174 (2016).

232. Hooshmand, N., Thoutam, A., Anikovskiy, M., Labouta, H. I. & El-Sayed, M. Localized Surface Plasmon Resonance as a Tool to Study Protein Corona Formation on Nanoparticles. *The Journal of Physical Chemistry C* **125**, 24765–24776 (2021).

233. Cui, M. *et al.* Quantitative study of protein coronas on gold nanoparticles with different surface modifications. *Nano Res* **7**, 345–352 (2014).

234. Figueroa, V. *et al.* Role of surface functionalization and biomolecule structure on protein corona adsorption and conformation onto anisotropic metallic nanoparticles. *J Mol Liq* **398**, 124240 (2024).

235. Mahmoudi, M. *et al.* Variation of Protein Corona Composition of Gold Nanoparticles Following Plasmonic Heating.**14**, 6−12 (2014).

236. Dominguez-Medina, S. *et al.* Adsorption and Unfolding of a Single Protein Triggers Nanoparticle Aggregation. *ACS Nano* **10**, 2103–2112 (2016).

237. Johnston, B. D. *et al.* Colloidal Stability and Surface Chemistry Are Key Factors for the Composition of the Protein Corona of Inorganic Gold Nanoparticles. *Adv Funct Mater* **27**, 1701956 (2017).

238. Mahmoudi, M., Lohse, S. E., Murphy, C. J. & Fathizadeh, A. Variation of Protein Corona Composition of Gold Nanoparticles Following Plasmonic Heating. 1–11.

239. Marx, G. *et al.* Heat denaturation of fibrinogen to develop a biomedical matrix. *J Biomed Mater Res B Appl Biomater* **84B**, 49–57 (2008).

240. Kinnear, C. *et al.* Gold Nanorods: Controlling Their Surface Chemistry and Complete Detoxification by a Two-Step Place Exchange. *Angewandte Chemie International Edition* **52**, 1934–1938 (2013).

241. Lopez, M. M. & Kosk-Kosicka, D. Spectroscopic Analysis of Halothane Binding to the Plasma Membrane Ca2+-ATPase. *Biophys J* **74**, 974–980 (1998).

242. Ruankham, W. *et al.* In silico and multi-spectroscopic analyses on the interaction of 5-amino-8-hydroxyquinoline and bovine serum albumin as a potential anticancer agent. *Sci Rep* **11**, 20187 (2021).

243. Sandros, M. G., Gao, D., Gokdemir, C. & Benson, D. E. General, high-affinity approach for the synthesis of fluorophore appended protein nanoparticle assemblies. *Chemical Communications,***22**, 2832–2834 (2005).244. Roach, P., Farrar, D. & Perry, C. C. Surface Tailoring for Controlled Protein Adsorption: Effect of Topography at the Nanometer Scale and Chemistry. *J Am Chem Soc* **128**, 3939–3945 (2006).

245. Maleki, S. *et al.* Surface plasmon resonance, fluorescence, and molecular docking studies of bovine serum albumin interactions with natural coumarin diversin. *Spectrochim Acta A Mol Biomol Spectrosc* **230**, 118063 (2020).

246. Shang, W. *et al.* Cytochrome c on Silica Nanoparticles: Influence of Nanoparticle Size on Protein Structure, Stability, and Activity. *Small* **5**, 470–476 (2009).

247. Deng, Z. J., Liang, M., Toth, I., Monteiro, M. J. & Minchin, R. F. Molecular Interaction of Poly(acrylic acid) Gold Nanoparticles with Human Fibrinogen. *ACS Nano* **6**, 8962–8969 (2012).

248. Micsonai, A. *et al.* Accurate secondary structure prediction and fold recognition for circular dichroism spectroscopy. *Proc Natl Acad Sci U S A* **112**,E3095-103, (2015).

249. Linhares, L. A. & Ramos, C. H. I. Unlocking Insights into Folding, Structure, and Function of Proteins through Circular Dichroism Spectroscopy—A Short Review. *Applied Biosciences* **2**, 639–655 (2023).

250. Micsonai, A. *et al.* Accurate secondary structure prediction and fold recognition for circular dichroism spectroscopy. *Proceedings of the National Academy of Sciences* **112**, E3095–E3103 (2015).

251. Micsonai, A., Bulyáki, É. & Kardos, J. BeStSel: From Secondary Structure Analysis to Protein Fold Prediction by Circular Dichroism Spectroscopy. in *Structural Genomics: General Applications* (eds. Chen, Y. W. & Yiu, C.-P. B.) 175–189 (Springer US, New York, NY, 2021).

252. Juárez, J. *et al.* Additional Supra-Self-Assembly of Human Serum Albumin under Amyloid-Like-Forming Solution Conditions. *J Phys Chem B* **113**, 12391–12399 (2009).

253. Juárez, J. *et al.* Hydration effects on the fibrillation process of a globular protein: the case of human serum albumin. *Soft Matter* **8**, 3608–3619 (2012).

254. Wang, W. Protein Aggregation and its inhibition in biopharmaceuticals. *Int J Pharm* **289**, 1–30 (2005).

255. Alam, S. & Mukhopadhyay, A. Conjugation of Gold Nanorods with Bovine Serum Albumin Protein. *The Journal of Physical Chemistry C* **118**, 27459–27464 (2014).

256. Zhao, S. *et al.* BSA-Coated Gold Nanorods for NIR-II Photothermal Therapy. *Nanoscale Res Lett* **16**, 170 (2021).

257. Krainer, G. *et al.* Single-molecule digital sizing of proteins in solution. *Nat Commun* **15**, 7740 (2024).

Annex 1: Permissions to Reproduce Figures

Figure 1.1 A: Representative examples of systems with dimensions ranging from the nanometric to the micrometric scale.

CCC Marketplace

This is a License Agreement between Xaniar Ezmaeilzadeh ("User") and Copyright Clearance Center, Inc. ("CCC") on behalf of the Rightsholder identified in the order details below. The license consists of the order details, the Marketplace Permissions General Terms and Conditions below, and any Rightsholder Terms and Conditions which are included below.

All payments must be made in full to CCC in accordance with the Marketplace Permissions General Terms and Conditions below.

Order Date	26-Mar-2024	**Type of Use**	Republish in a thesis/dissertation
Order License ID	1466020-1	**Publisher**	ROYAL SOCIETY OF CHEMISTRY, ETC.]
ISSN	0306-0012	**Portion**	Chart/graph/table/figure

LICENSED CONTENT

Publication Title	Chemical Society reviews	**Rightsholder**	Royal Society of Chemistry
Article Title	Upconverting nanoparticles: assessing the toxicity.	**Publication Type**	Journal
Author / Editor	CHEMICAL SOCIETY (GREAT BRITAIN)	**Start Page**	1561
Date	01/01/1972	**End Page**	1584
Language	English	**Issue**	6
Country	United Kingdom of Great Britain and Northern Ireland	**Volume**	44

REQUEST DETAILS

Portion Type	Chart/graph/table/figure	**Distribution**	Worldwide
Number of Charts / Graphs / Tables / Figures Requested	1	**Translation**	Original language of publication
		Copies for the Disabled?	No
Format (select all that apply)	Print, Electronic	**Minor Editing Privileges?**	No
Who Will Republish the Content?	Author of requested content	**Incidental Promotional Use?**	No
Duration of Use	Current edition and up to 5 years	**Currency**	EUR
Lifetime Unit Quantity	Up to 499		
Rights Requested	Main product		

Figure 1.3: Schematic illustration of the applications of nanomaterials across various fields, including biomedicine, energy storage , electronics, environmental protection , and industrial processes.

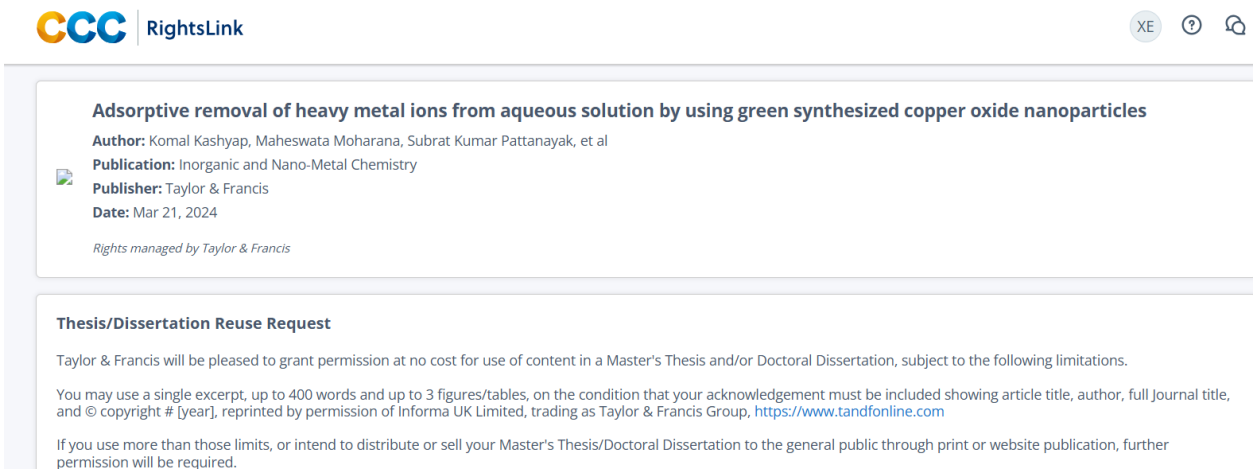

RightsLink

XE

Adsorptive removal of heavy metal ions from aqueous solution by using green synthesized copper oxide nanoparticles

Author: Komal Kashyap, Maheswata Moharana, Subrat Kumar Pattanayak, et al
Publication: Inorganic and Nano-Metal Chemistry
Publisher: Taylor & Francis
Date: Mar 21, 2024

Rights managed by Taylor & Francis

Thesis/Dissertation Reuse Request

Taylor & Francis will be pleased to grant permission at no cost for use of content in a Master's Thesis and/or Doctoral Dissertation, subject to the following limitations.

You may use a single excerpt, up to 400 words and up to 3 figures/tables, on the condition that your acknowledgement must be included showing article title, author, full Journal title, and © copyright # [year], reprinted by permission of Informa UK Limited, trading as Taylor & Francis Group, https://www.tandfonline.com

If you use more than those limits, or intend to distribute or sell your Master's Thesis/Doctoral Dissertation to the general public through print or website publication, further permission will be required.

Figure 1.5: A) TEM images of AuNRs with different aspect ratios. B) Color change and C) LSPR red shifting of AuNRs dispersions with different aspect ratios between 2.4 and 6.6 . D) DDA simulation of AuNRs with different sizes. E) Correlation between the aspect ratio of AuNRs and their LSPR wavelength (top) and scattering yield (down) . Under creative commons CC BY-NC-ND 3.0 license.

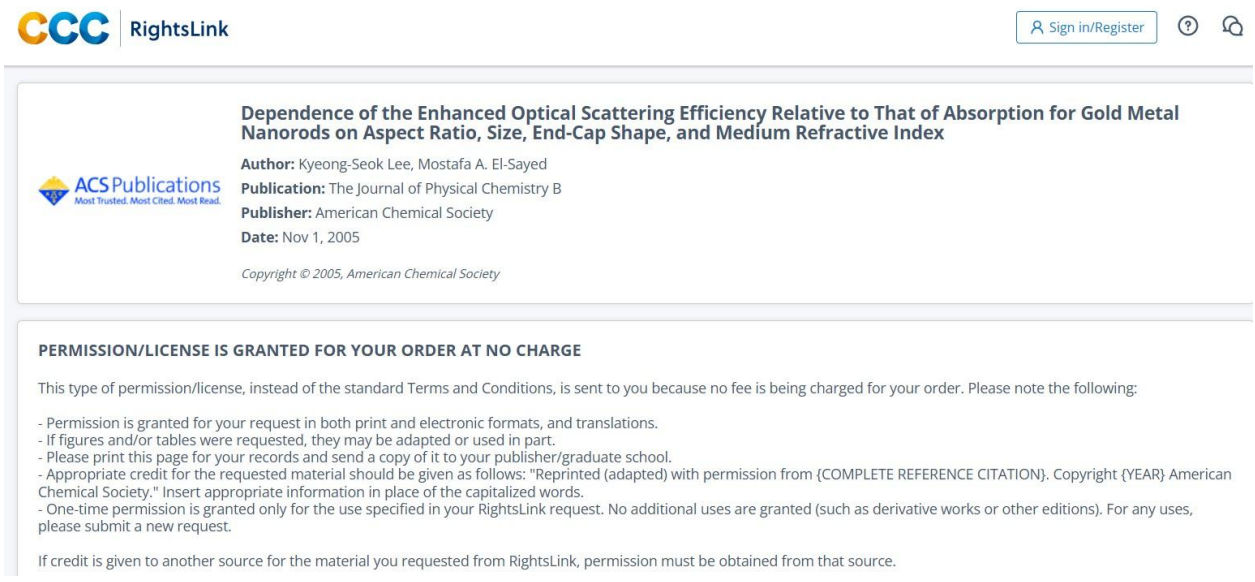

RightsLink

Sign in/Register

ACS Publications
Most Trusted. Most Cited. Most Read.

Dependence of the Enhanced Optical Scattering Efficiency Relative to That of Absorption for Gold Metal Nanorods on Aspect Ratio, Size, End-Cap Shape, and Medium Refractive Index

Author: Kyeong-Seok Lee, Mostafa A. El-Sayed
Publication: The Journal of Physical Chemistry B
Publisher: American Chemical Society
Date: Nov 1, 2005

Copyright © 2005, American Chemical Society

PERMISSION/LICENSE IS GRANTED FOR YOUR ORDER AT NO CHARGE

This type of permission/license, instead of the standard Terms and Conditions, is sent to you because no fee is being charged for your order. Please note the following:

- Permission is granted for your request in both print and electronic formats, and translations.
- If figures and/or tables were requested, they may be adapted or used in part.
- Please print this page for your records and send a copy of it to your publisher/graduate school.
- Appropriate credit for the requested material should be given as follows: "Reprinted (adapted) with permission from {COMPLETE REFERENCE CITATION}. Copyright {YEAR} American Chemical Society." Insert appropriate information in place of the capitalized words.
- One-time permission is granted only for the use specified in your RightsLink request. No additional uses are granted (such as derivative works or other editions). For any uses, please submit a new request.

If credit is given to another source for the material you requested from RightsLink, permission must be obtained from that source.

Figure 1.6: Representative UV-Vis absorbance spectra illustrating the key influence of structural characteristics of AuNSs on their plasmonic response, including A) number of tips, B) tip length, and C) diameter of the central core.

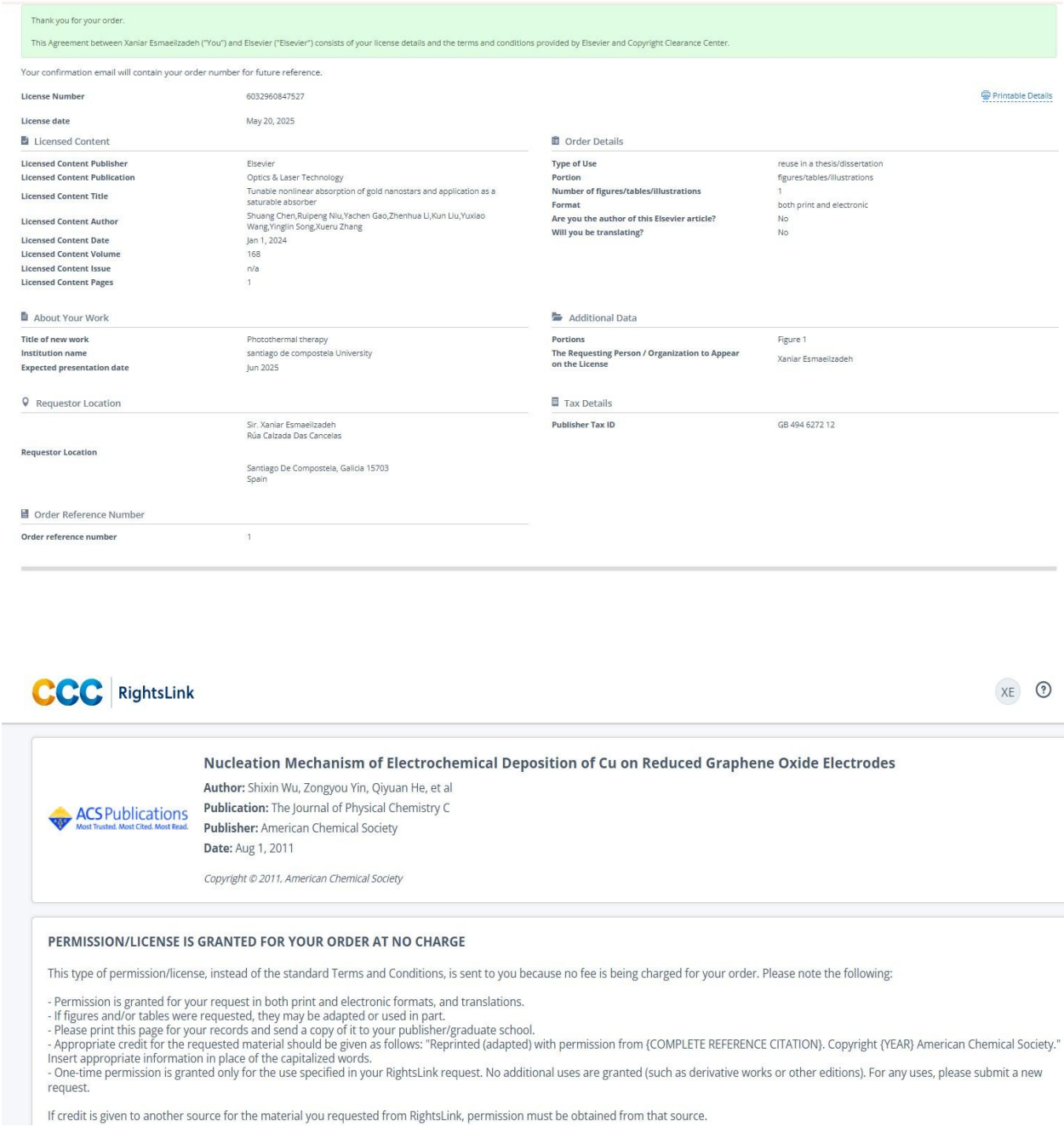

Thank you for your order.

This Agreement between Xaniar Esmaeilzadeh ("You") and Elsevier ("Elsevier") consists of your license details and the terms and conditions provided by Elsevier and Copyright Clearance Center.

Your confirmation email will contain your order number for future reference.

License Number	6032960847527
License date	May 20, 2025

Printable Details

Licensed Content

Licensed Content Publisher	Elsevier
Licensed Content Publication	Optics & Laser Technology
Licensed Content Title	Tunable nonlinear absorption of gold nanostars and application as a saturable absorber
Licensed Content Author	Shuang Chen,Ruipeng Niu,Yachen Gao,Zhenhua Li,Kun Liu,Yuxiao Wang,Yinglin Song,Xueru Zhang
Licensed Content Date	Jan 1, 2024
Licensed Content Volume	168
Licensed Content Issue	n/a
Licensed Content Pages	1

Order Details

Type of Use	reuse in a thesis/dissertation
Portion	figures/tables/illustrations
Number of figures/tables/illustrations	1
Format	both print and electronic
Are you the author of this Elsevier article?	No
Will you be translating?	No

About Your Work

Title of new work	Photothermal therapy
Institution name	santiago de compostela University
Expected presentation date	Jun 2025

Additional Data

Portions	Figure 1
The Requesting Person / Organization to Appear on the License	Xaniar Esmaeilzadeh

Requestor Location

Sir. Xaniar Esmaeilzadeh
Rúa Calzada Das Cancelas

Requestor Location

Santiago De Compostela, Galicia 15703
Spain

Tax Details

Publisher Tax ID	GB 494 6272 12

Order Reference Number

Order reference number	1

CCC RightsLink

XE

Nucleation Mechanism of Electrochemical Deposition of Cu on Reduced Graphene Oxide Electrodes

Author: Shixin Wu, Zongyou Yin, Qiyuan He, et al
Publication: The Journal of Physical Chemistry C
Publisher: American Chemical Society
Date: Aug 1, 2011

Copyright © 2011, American Chemical Society

PERMISSION/LICENSE IS GRANTED FOR YOUR ORDER AT NO CHARGE

This type of permission/license, instead of the standard Terms and Conditions, is sent to you because no fee is being charged for your order. Please note the following:

- Permission is granted for your request in both print and electronic formats, and translations.
- If figures and/or tables were requested, they may be adapted or used in part.
- Please print this page for your records and send a copy of it to your publisher/graduate school.
- Appropriate credit for the requested material should be given as follows: "Reprinted (adapted) with permission from {COMPLETE REFERENCE CITATION}. Copyright {YEAR} American Chemical Society." Insert appropriate information in place of the capitalized words.
- One-time permission is granted only for the use specified in your RightsLink request. No additional uses are granted (such as derivative works or other editions). For any uses, please submit a new request.

If credit is given to another source for the material you requested from RightsLink, permission must be obtained from that source.

Figure 1.9: Schematic illustration of the three fundamental chemical reduction strategies for the synthesis of gold NPs: A) Turkevich, B) Brust-Schiffrin, and C) seed-mediated growth methods.

SPRINGER NATURE LICENSE
TERMS AND CONDITIONS

May 20, 2025

This Agreement between Xaniar Esmailzadeh ("You") and Springer Nature ("Springer Nature") consists of your license details and the terms and conditions provided by Springer Nature and Copyright Clearance Center.

The publisher has provided special terms related to this request that can be found at the end of the Publisher's Terms and Conditions.

License Number	5961810529520
License date	Feb 04, 2025
Licensed Content Publisher	Springer Nature
Licensed Content Publication	Springer eBook
Licensed Content Title	Gold Nanoparticle-Based Colorimetric Sensing of Metal Toxins
Licensed Content Author	Nivedita Priyadarshni, Nripen Chanda
Licensed Content Date	Jan 1, 2022
Type of Use	Thesis/Dissertation
Requestor type	academic/university or research institute
Format	electronic

Figure 1.14 A: Energy and LSPR position of plasmonic NPs with different morphologies and compositions.

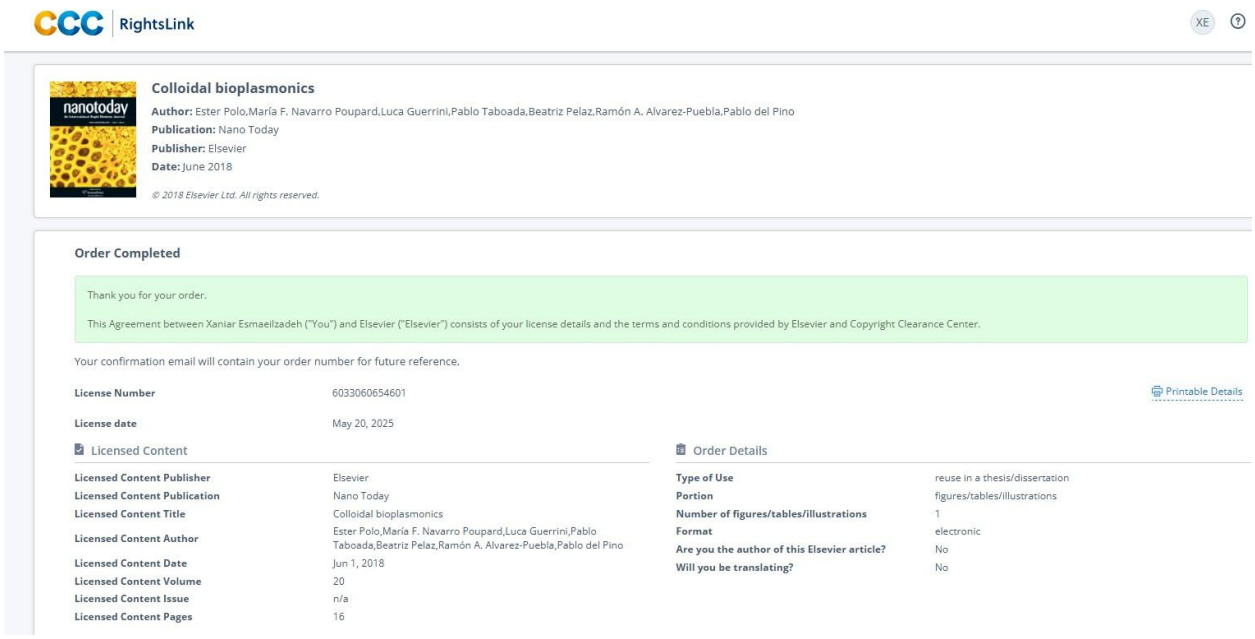

CCC RightsLink

Colloidal bioplasmonics

Author: Ester Polo,María F. Navarro Poupard,Luca Guerrini,Pablo Taboada,Beatriz Pelaz,Ramón A. Alvarez-Puebla,Pablo del Pino
Publication: Nano Today
Publisher: Elsevier
Date: June 2018

© 2018 Elsevier Ltd. All rights reserved.

Order Completed

Thank you for your order.

This Agreement between Xaniar Esmaeilzadeh ("You") and Elsevier ("Elsevier") consists of your license details and the terms and conditions provided by Elsevier and Copyright Clearance Center.

Your confirmation email will contain your order number for future reference.

License Number	6033060654601
License date	May 20, 2025

Printable Details

Licensed Content

Licensed Content Publisher	Elsevier
Licensed Content Publication	Nano Today
Licensed Content Title	Colloidal bioplasmonics
Licensed Content Author	Ester Polo,María F. Navarro Poupard,Luca Guerrini,Pablo Taboada,Beatriz Pelaz,Ramón A. Alvarez-Puebla,Pablo del Pino
Licensed Content Date	Jun 1, 2018
Licensed Content Volume	20
Licensed Content Issue	n/a
Licensed Content Pages	16

Order Details

Type of Use	reuse in a thesis/dissertation
Portion	figures/tables/illustrations
Number of figures/tables/illustrations	1
Format	electronic
Are you the author of this Elsevier article?	No
Will you be translating?	No

Figure 1.14 B: Position of LSPR in gold NPs with different sizes.

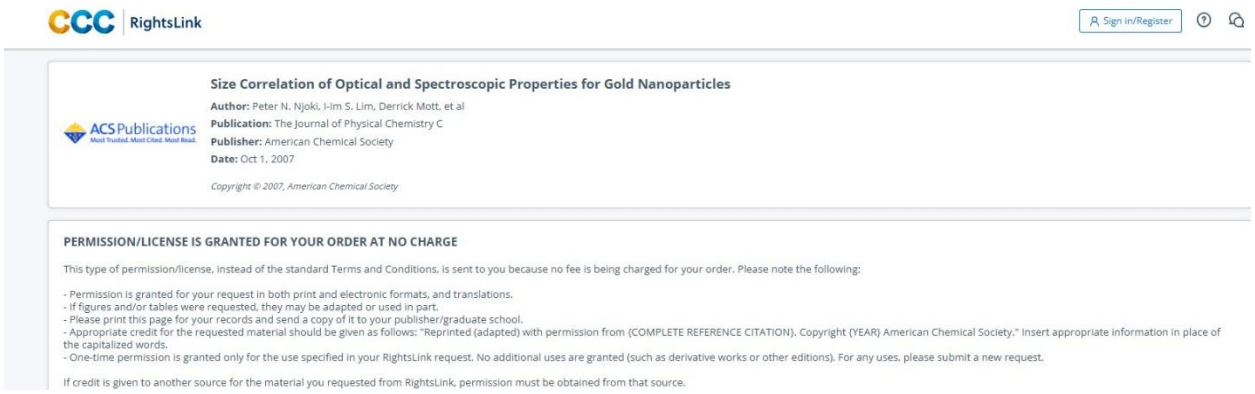

CCC RightsLink

Sign in/Register

Size Correlation of Optical and Spectroscopic Properties for Gold Nanoparticles

Author: Peter N. Njoki, I-Im S. Lim, Derrick Mott, et al
Publication: The Journal of Physical Chemistry C
Publisher: American Chemical Society
Date: Oct 1, 2007

Copyright © 2007, American Chemical Society

PERMISSION/LICENSE IS GRANTED FOR YOUR ORDER AT NO CHARGE

This type of permission/license, instead of the standard Terms and Conditions, is sent to you because no fee is being charged for your order. Please note the following:

- Permission is granted for your request in both print and electronic formats, and translations.
- If figures and/or tables were requested, they may be adapted or used in part.
- Please print this page for your records and send a copy of it to your publisher/graduate school.
- Appropriate credit for the requested material should be given as follows: "Reprinted (adapted) with permission from (COMPLETE REFERENCE CITATION). Copyright (YEAR) American Chemical Society." Insert appropriate information in place of the capitalized words.
- One-time permission is granted only for the use specified in your RightsLink request. No additional uses are granted (such as derivative works or other editions). For any uses, please submit a new request.

If credit is given to another source for the material you requested from RightsLink, permission must be obtained from that source.

Figure 1.14 C: Plasmonic response (LSPR position and extinction cross-section) of two gold spherical NPs interacting as a function of their interparticle distance.

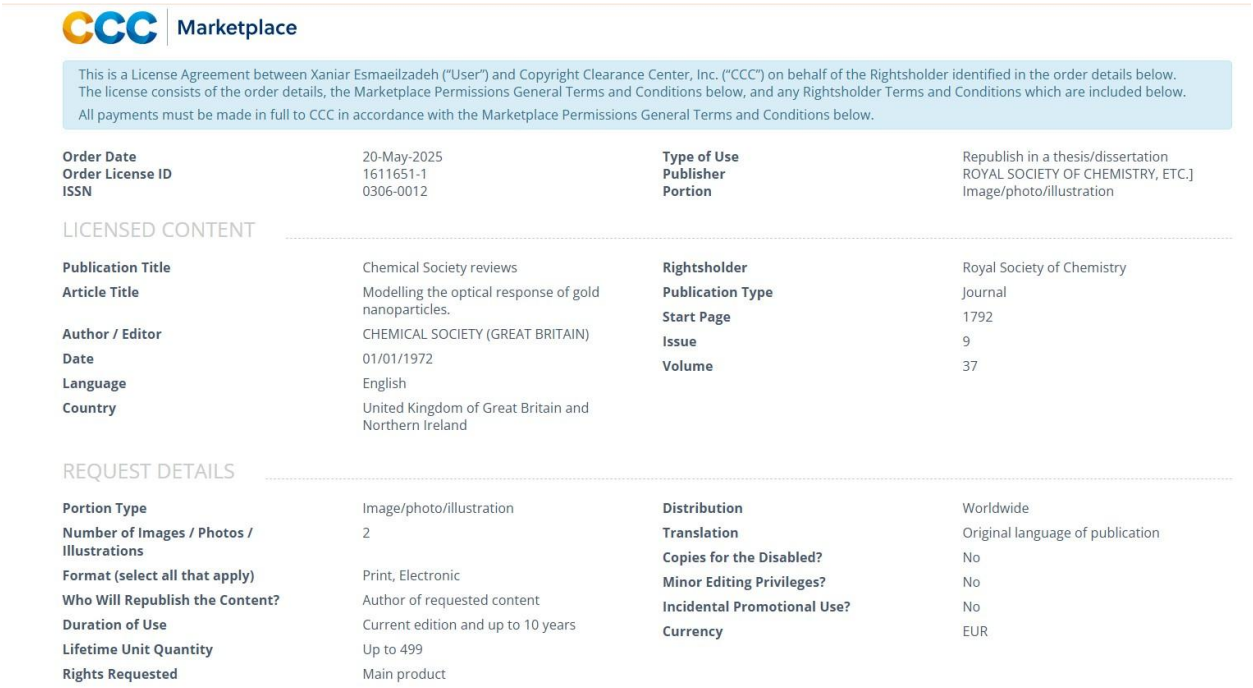

CCC Marketplace

This is a License Agreement between Xaniar Esmaeilzadeh ("User") and Copyright Clearance Center, Inc. ("CCC") on behalf of the Rightsholder identified in the order details below. The license consists of the order details, the Marketplace Permissions General Terms and Conditions below, and any Rightsholder Terms and Conditions which are included below.

All payments must be made in full to CCC in accordance with the Marketplace Permissions General Terms and Conditions below.

Order Date	20-May-2025	**Type of Use**	Republish in a thesis/dissertation
Order License ID	1611651-1	**Publisher**	ROYAL SOCIETY OF CHEMISTRY, ETC.]
ISSN	0306-0012	**Portion**	Image/photo/illustration

LICENSED CONTENT

Publication Title	Chemical Society reviews	**Rightsholder**	Royal Society of Chemistry
Article Title	Modelling the optical response of gold nanoparticles.	**Publication Type**	Journal
		Start Page	1792
Author / Editor	CHEMICAL SOCIETY (GREAT BRITAIN)	**Issue**	9
Date	01/01/1972	**Volume**	37
Language	English		
Country	United Kingdom of Great Britain and Northern Ireland		

REQUEST DETAILS

Portion Type	Image/photo/illustration	**Distribution**	Worldwide
Number of Images / Photos / Illustrations	2	**Translation**	Original language of publication
		Copies for the Disabled?	No
Format (select all that apply)	Print, Electronic	**Minor Editing Privileges?**	No
Who Will Republish the Content?	Author of requested content	**Incidental Promotional Use?**	No
Duration of Use	Current edition and up to 10 years	**Currency**	EUR
Lifetime Unit Quantity	Up to 499		
Rights Requested	Main product		

Figure 1.18 A: Comparative cellular uptake study showing greater internalization of spherical gold NPs with 14 and 74 nm in diameter compared to rod-shaped NPs with 14x40 and 14x74 nm dimensions.

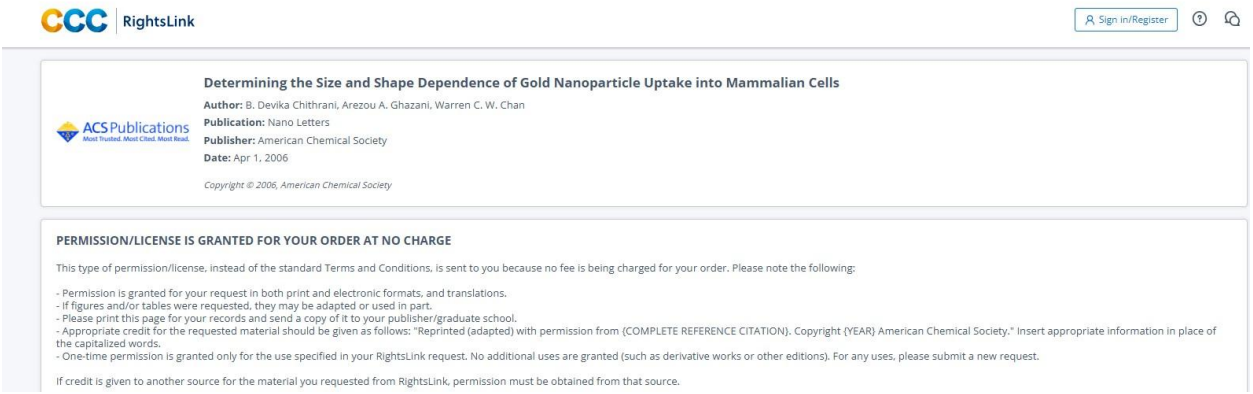

CCC RightsLink

Sign in/Register

ACS Publications

Determining the Size and Shape Dependence of Gold Nanoparticle Uptake into Mammalian Cells

Author: B. Devika Chithrani, Arezou A. Ghazani, Warren C. W. Chan
Publication: Nano Letters
Publisher: American Chemical Society
Date: Apr 1, 2006

Copyright © 2006, American Chemical Society

PERMISSION/LICENSE IS GRANTED FOR YOUR ORDER AT NO CHARGE

This type of permission/license, instead of the standard Terms and Conditions, is sent to you because no fee is being charged for your order. Please note the following:

- Permission is granted for your request in both print and electronic formats, and translations.
- If figures and/or tables were requested, they may be adapted or used in part.
- Please print this page for your records and send a copy of it to your publisher/graduate school.
- Appropriate credit for the requested material should be given as follows: "Reprinted (adapted) with permission from {COMPLETE REFERENCE CITATION). Copyright {YEAR} American Chemical Society." Insert appropriate information in place of the capitalized words.
- One-time permission is granted only for the use specified in your RightsLink request. No additional uses are granted (such as derivative works or other editions). For any uses, please submit a new request.

If credit is given to another source for the material you requested from RightsLink, permission must be obtained from that source.

Figure 1.19 A: Schematic representation of the effect of surface charge on the cellular uptake of positively, negatively, and neutrally charged NPs.

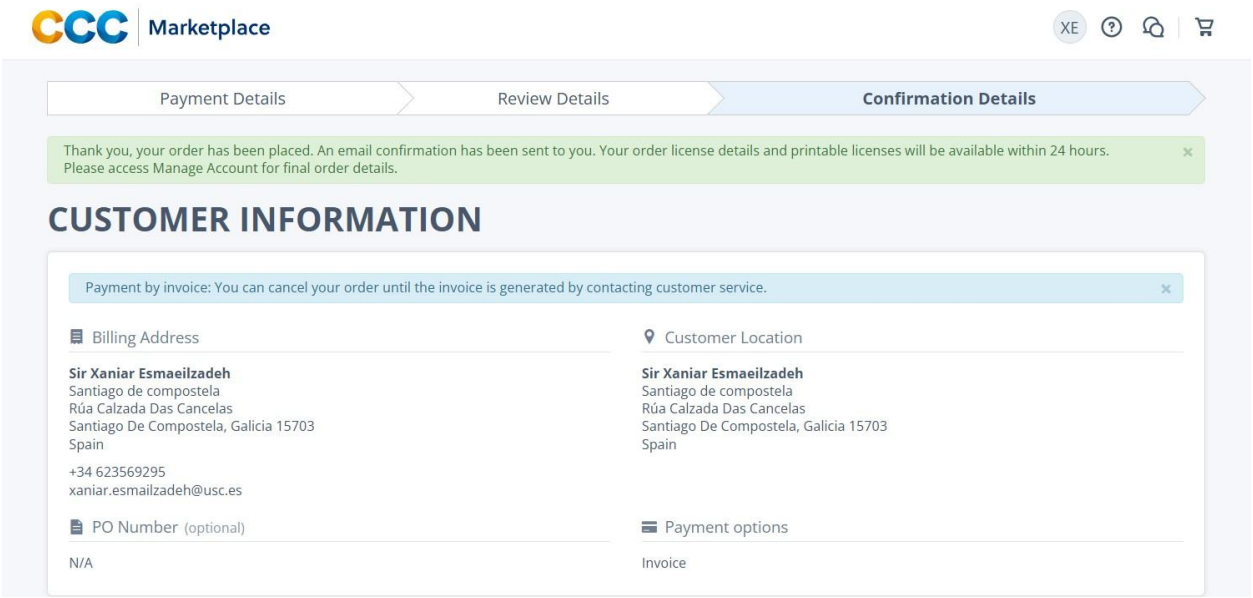

Figure 1.19 B-C: Expressions of B) CD163, indicative of an anti-inflammatory response, and C) 27E10, associated with a pro-inflammatory phenotype, obtained through the flow cytometry analysis of macrophages after 7 days of incubation with different functionalized AuNRs.

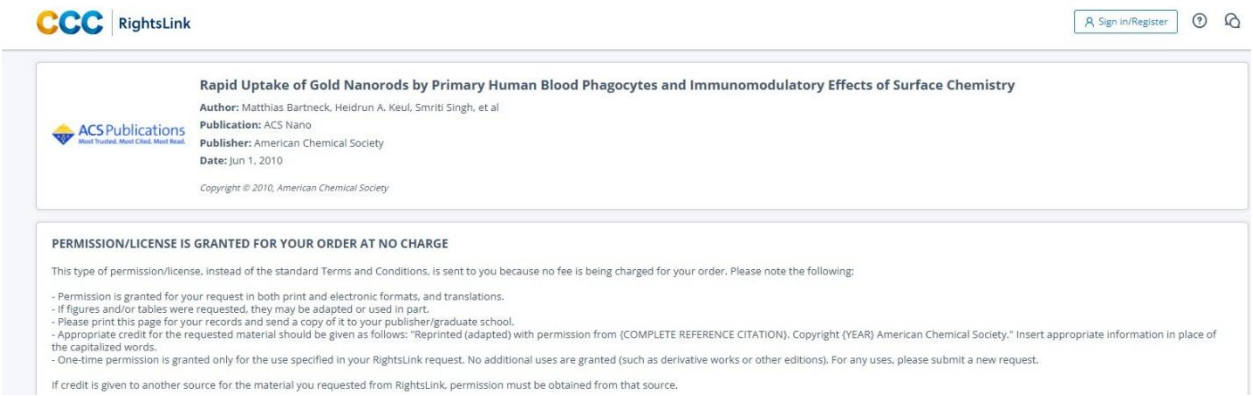

Figure 1.20: Graphical representation of the main biomedical applications of anisotropic gold NPs, including bioimaging, targeted drug delivery, biosensing, PTT and PDT. Under creative commons CC BY-NC 4.0 license.

ELSEVIER LICENSE
TERMS AND CONDITIONS

May 21, 2025

This Agreement between Xaniar Esmaeilzadeh ("You") and Elsevier ("Elsevier") consists of your license details and the terms and conditions provided by Elsevier and Copyright Clearance Center.

License Number	6010900375317
License date	Apr 16, 2025
Licensed Content Publisher	Elsevier
Licensed Content Publication	Journal of Photochemistry and Photobiology B: Biology
Licensed Content Title	Gold nanoclusters modified mesoporous silica coated gold nanorods: Enhanced photothermal properties and fluorescence imaging
Licensed Content Author	Qianqian Duan,Min Yang,Boye Zhang,Yi Li,Yixia Zhang,Xiaoning Li,Jianming Wang,Wendong Zhang,Shengbo Sang
Licensed Content Date	Feb 1, 2021
Licensed Content Volume	215
Licensed Content Issue	n/a
Licensed Content Pages	1

Figure 1.21 A: Representative example of the use of gold NPs for bioimaging applications: OCT signal intensity comparison between large AuNRs and two concentrations of small AuNRs.

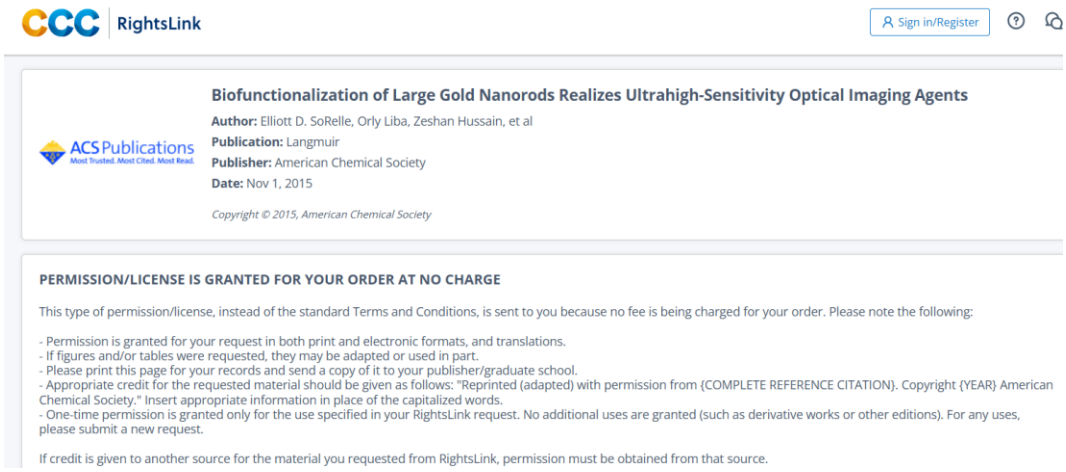

CCC RightsLink

Sign in/Register

ACS Publications
Most Trusted. Most Cited. Most Read.

Biofunctionalization of Large Gold Nanorods Realizes Ultrahigh-Sensitivity Optical Imaging Agents

Author: Elliott D. SoRelle, Orly Liba, Zeshan Hussain, et al
Publication: Langmuir
Publisher: American Chemical Society
Date: Nov 1, 2015

Copyright © 2015, American Chemical Society

PERMISSION/LICENSE IS GRANTED FOR YOUR ORDER AT NO CHARGE

This type of permission/license, instead of the standard Terms and Conditions, is sent to you because no fee is being charged for your order. Please note the following:

- Permission is granted for your request in both print and electronic formats, and translations.
- If figures and/or tables were requested, they may be adapted or used in part.
- Please print this page for your records and send a copy of it to your publisher/graduate school.
- Appropriate credit for the requested material should be given as follows: "Reprinted (adapted) with permission from {COMPLETE REFERENCE CITATION}. Copyright {YEAR} American Chemical Society." Insert appropriate information in place of the capitalized words.
- One-time permission is granted only for the use specified in your RightsLink request. No additional uses are granted (such as derivative works or other editions). For any uses, please submit a new request.

If credit is given to another source for the material you requested from RightsLink, permission must be obtained from that source.

Figure 1.21 C-D-E: Representative example of the use of gold NPs for bioimaging applications: C) *In vivo* PA imaging of the rat axillary region before (top) and after (bottom) AuNSs injection, showing selective accumulation in the sentinel lymph node (SLN). D) Photograph (top) and corresponding ex vivo PA image (bottom) of left and right SLNs, revealing a stronger PA signal on the side proximal to the injection site. E) Spectroscopic PA signal quantification in vivo and ex vivo within the SLNs, demonstrating robust AuNSs accumulation and signal retention.

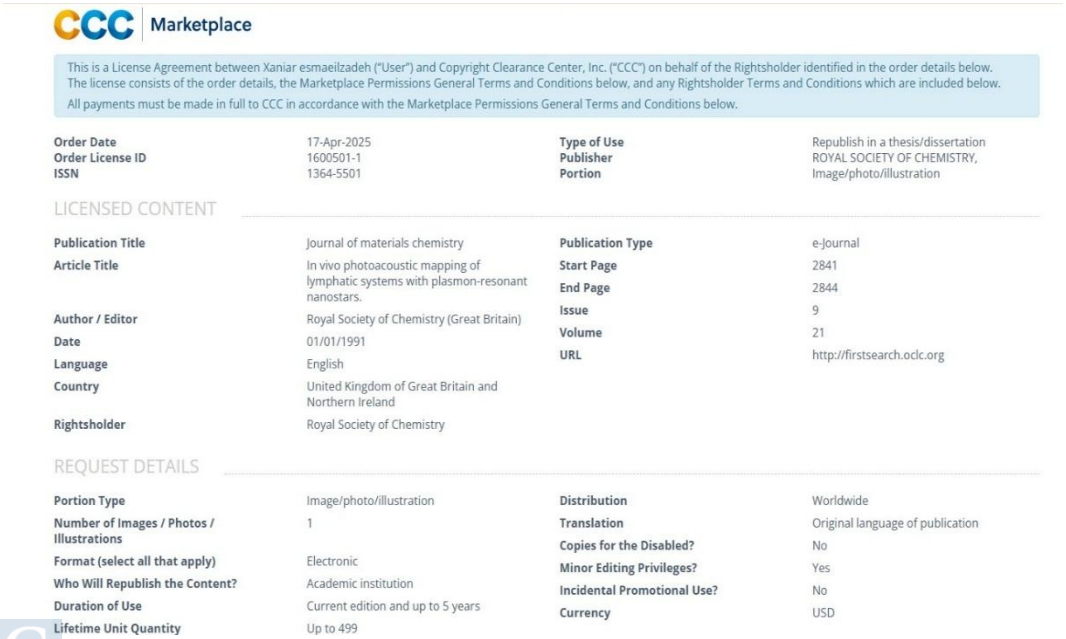

CCC Marketplace

This is a License Agreement between Xaniar esmaeilzadeh ("User") and Copyright Clearance Center, Inc. ("CCC") on behalf of the Rightsholder identified in the order details below. The license consists of the order details, the Marketplace Permissions General Terms and Conditions below, and any Rightsholder Terms and Conditions which are included below.

All payments must be made in full to CCC in accordance with the Marketplace Permissions General Terms and Conditions below.

Order Date	17-Apr-2025	**Type of Use**	Republish in a thesis/dissertation
Order License ID	1600501-1	**Publisher**	ROYAL SOCIETY OF CHEMISTRY,
ISSN	1364-5501	**Portion**	Image/photo/illustration

LICENSED CONTENT

Publication Title	Journal of materials chemistry	**Publication Type**	e-Journal
Article Title	In vivo photoacoustic mapping of lymphatic systems with plasmon-resonant nanostars.	**Start Page**	2841
		End Page	2844
Author / Editor	Royal Society of Chemistry (Great Britain)	**Issue**	9
Date	01/01/1991	**Volume**	21
Language	English	**URL**	http://firstsearch.oclc.org
Country	United Kingdom of Great Britain and Northern Ireland		
Rightsholder	Royal Society of Chemistry		

REQUEST DETAILS

Portion Type	Image/photo/illustration	**Distribution**	Worldwide
Number of Images / Photos / Illustrations	1	**Translation**	Original language of publication
		Copies for the Disabled?	No
Format (select all that apply)	Electronic	**Minor Editing Privileges?**	Yes
Who Will Republish the Content?	Academic institution	**Incidental Promotional Use?**	No
Duration of Use	Current edition and up to 5 years	**Currency**	USD
Lifetime Unit Quantity	Up to 499		

Figure 1.23: Representative example of the use of gold NPs for drug delivery applications: A) schematic illustration of the application of silica-coated AuNRs for the controlled delivery of MTX in cancer treatments. B) MTX release curves and percentage of MTX released over 30 h from the designed gold-based nanoplatforms.

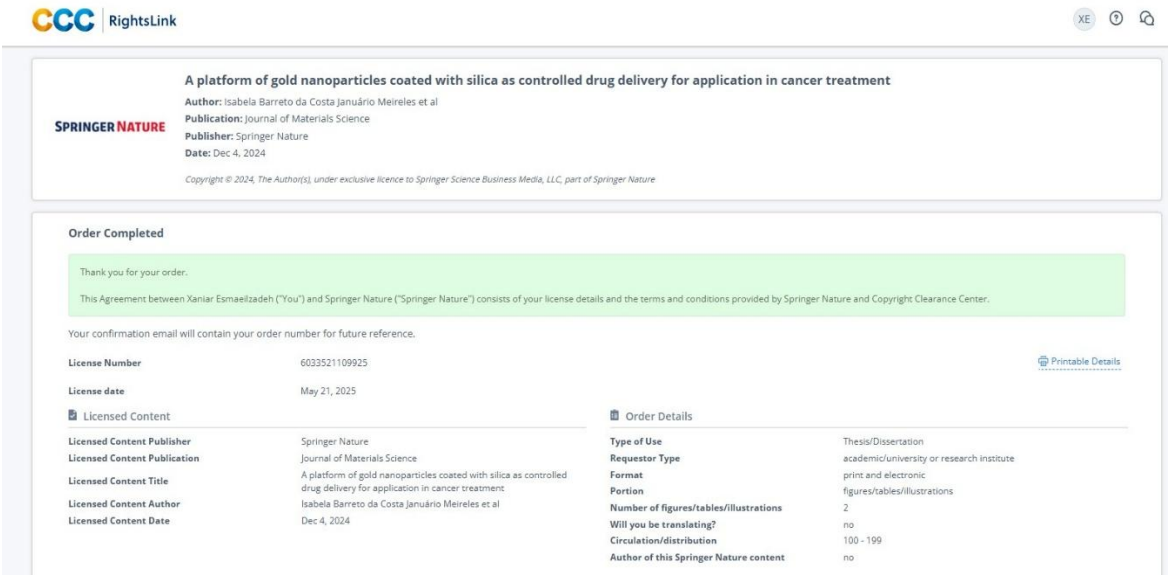

CCC | RightsLink

SPRINGER NATURE

A platform of gold nanoparticles coated with silica as controlled drug delivery for application in cancer treatment

Author: Isabela Barreto da Costa Januário Meireles et al
Publication: Journal of Materials Science
Publisher: Springer Nature
Date: Dec 4, 2024

Copyright © 2024, The Author(s), under exclusive licence to Springer Science Business Media, LLC, part of Springer Nature

Order Completed

Thank you for your order.

This Agreement between Xaniar Esmaeilzadeh ("You") and Springer Nature ("Springer Nature") consists of your license details and the terms and conditions provided by Springer Nature and Copyright Clearance Center.

Your confirmation email will contain your order number for future reference.

License Number	6033521109925
License date	May 21, 2025

Printable Details

Licensed Content

Licensed Content Publisher	Springer Nature
Licensed Content Publication	Journal of Materials Science
Licensed Content Title	A platform of gold nanoparticles coated with silica as controlled drug delivery for application in cancer treatment
Licensed Content Author	Isabela Barreto da Costa Januário Meireles et al
Licensed Content Date	Dec 4, 2024

Order Details

Type of Use	Thesis/Dissertation
Requestor Type	academic/university or research institute
Format	print and electronic
Portion	figures/tables/illustrations
Number of figures/tables/illustrations	2
Will you be translating?	no
Circulation/distribution	100 - 199
Author of this Springer Nature content	no

All other figures presented in this thesis have been independently developed by the author.

Annex 2: Calculation of Photothermal Conversion Efficiency of Plasmonic Gold NPs

The photothermal conversion efficiency was calculated following the method reported by Roper *et al.* [172] Briefly, the temperature increase of the NPs dispersions can be analyzed by considering the thermal equilibrium between the heat generated by laser irradiation of the nanostructures (Q_I), the heat absorbed by the system components (quartz cell and water) (Q_0), and the heat dissipated to the surroundings through convection (Q_{ext}). This equilibrium is expressed as follows:

$$\sum m_i C_i \left(\frac{dT}{dt}\right) = Q_I + Q_0 - Q_{EXT} \quad (1)$$

where m_i and C_i are the mass and heat capacity of the components of the system (6.9 g and 0.89 $J \cdot g^{-1} \cdot K^{-1}$ for quartz cell; 2.0 g and 4.20 $J \cdot g^{-1} \cdot K^{-1}$ for water), *T* is the temperature, and *t* is time.

The term Q_I (heat produced by gold NPs after irradiation) can be expressed by the following equation:

$$Q_I = I\left(1 - 10^{-A\lambda}\right)\eta \quad (2)$$

where *I* is the power of the laser, η represents the efficiency of converting incident light into thermal energy (photothermal conversion efficiency), and A_λ is the absorbance of gold NPs at the wavelength of the laser (808 nm).

On the other hand, Q_{ext} (heat dissipated to the surrounding environment) can be expressed as:

$$Q_{ext} = hA(T - T_{amb}) \quad (3)$$

where *h* is the convective heat transfer coefficient, and *A* the area of the quartz cell (1 cm^2).

A dimensionless driving force temperature, θ, is introduced, scaled using the maximum system temperature, T_{max}:

$$\theta = \frac{T_{amb} - T}{T_{amb} - T_{max}} \quad (4)$$

In this model, a parameter known as the characteristic velocity constant or the system time constant (τ_s) is calculated as:

$$\tau_s = \frac{\sum_i m_i c_i}{hA} \quad (5)$$

which can be substituted into equation 1 and then rearranged to obtain:

$$\frac{d\theta}{dt} = \frac{1}{\tau_s}\left[\frac{Q_I + Q_0}{hA(T_{max} - T_{amb})} - \theta\right] \quad (6)$$

When laser irradiation stops, $Q_I + Q_0 = 0$ and the system cools, simplifying equation 6 to:

$$\frac{d\theta}{dt} = -\frac{\theta}{\tau_s} \quad (7)$$

By applying the initial condition $\theta = 1$ at $t = 0$, the equation 7 could be substituted with:

$$-Ln\ \theta = \frac{t}{\tau_s} \quad (8)$$

Thus, plotting the curve of $-Ln\ \theta$ *vs. t*, τ_s can be determined. Then, using the equation 5, hA can be extracted and substituted into the following equation to obtain the photothermal conversion efficiency (η):

$$\eta = \frac{hA(T_{max} - T_{amb}) - Q_0}{I(1 - 10^{-A_\lambda})} \quad (9)$$

where Q_0, could be calculated by this equation:

$$Q_0 = (hA)_{water}(T_{max} - T_{amb}) \quad (10)$$

This thesis presents a comprehensive investigation into the photothermal properties of gold nanorods and nanostars for their potential application in plasmonic photothermal therapy targeting breast cancer. The study covers the synthesis, surface functionalization, protein corona formation, and in vitro interaction of the designed gold nanostructures with cancer cells. Their photothermal responses were systematically evaluated under continuous and femtosecond laser irradiation, with particular attention to the influence of morphology, surface coating, and concentration. Results demonstrate that both nanorods and nanostars efficiently generate heat upon light exposure, enabling the selective ablation of tumor cells and highlighting their promise for targeted cancer therapy.